UNIVERSITY OF SOUTHAMPTON

Faculty of Engineering
School of Engineering

RANS-Based Mixing Noise Predictions of Installed Asymmetric Jet Flows

by

Matthew Elliott Wellman

MEng

ORCiD: 0000-0003-1984-2710

A thesis for the degree of
Doctor of Philosophy

May 2023

Abstract

As the world's dependency on air travel and transportation increases, the public's concern over noise pollution around airports grows. Engine manufacturers must meet increasingly stringent noise certification targets while designing new products. Traditional noise analysis techniques often assume that jets are axisymmetric which is not true for realistic geometries. Therefore, a more detailed analysis is needed to see how to model complex asymmetric jets.

A method has been previously developed at the University of Southampton, called Lighthill's Acoustic Analogy with Ray Tracing (LRT), to predict the jet mixing noise for civil aircraft engines. In this thesis, the LRT method is used to analyse the change in the jet mixing noise that different geometric features cause. By studying how the mixing noise scales and how the source distribution changes with geometry, this can be used to inform decisions for future commercial aircraft nozzle designs.

The main contributions of this work are as follows: RANS has been shown to predict the flow field of the isolated axisymmetric and asymmetric jets that have been studied. This allows the LRT acoustic model to predict the change in the isolated jet mixing noise to within 0.5dB as the geometry changes. The azimuthal variation in the noise is accounted for in the ray tracing calculation. LRT now includes the ability to predict the reflected mixing noise from solid surfaces. RANS prediction for static installed cases showed good agreement with experimental data underneath the wing, leading to accurate prediction above $St = 2$ of the high-frequency noise. Despite over-predicting the turbulence levels downstream of the wing trailing edge, this has minimal impact on the far-field mixing noise. It is hoped that this work will be used in the future to help understand the jet-surface interaction that dominates installed jet noise below $St = 1$.

Contents

List of Figures

List of Tables

Declaration of Authorship

I declare that this thesis and the work presented in it is my own and has been generated by me as the result of my own original research.

I confirm that:

1. This work was done wholly or mainly while in candidature for a research degree at this University;
2. Where any part of this thesis has previously been submitted for a degree or any other qualification at this University or any other institution, this has been clearly stated;
3. Where I have consulted the published work of others, this is always clearly attributed;
4. Where I have quoted from the work of others, the source is always given. With the exception of such quotations, this thesis is entirely my own work;
5. I have acknowledged all main sources of help;
6. Where the thesis is based on work done by myself jointly with others, I have made clear exactly what was done by others and what I have contributed myself;
7. Parts of this work have been published as: Wellman et al. 2022

Signed:..... Date:.....

Acknowledgements

This research has been carried out at the Rolls-Royce University Technology Centre within the Institute of Sound and Vibration Research (ISVR).

There are several key people that I would like to thank, who without this work would not have been possible. Firstly, my supervisors, Prof. Rod Self and Dr Jack Lawrence, who have given me guidance in times when I have struggled to work out the direction of the research or come across a particularly difficult concept to understand. Also for helping me with my writing of technical documents as this has certainly been one of the biggest challenges of this thesis. Being able to have work that is understandable for those who are not highly familiar with my work is certainly a good thing.

I would also like to express my gratitude to Anderson, whom I have been constantly emailing about experimental data throughout this project. Without his work, I would not know how accurate my simulations are. Thanks should also be given to Erika Quaranta for her help at the beginning of this project in learning how to use Pointwise and her advice on the CFD meshes that I have generated.

My project would not be where it is without the day-to-day discussions with the other students within the research group. Both for helping me solve everyday problems in my work or for simply listening to me complain when my computer or code decides not to work for no apparent reason.

Finally, my family and cats need to be acknowledged as they have given me their love and support throughout the project. Thank you for believing in me!!!

To Mum, Jacob and Peter

Abbreviations

Abbreviation	Meaning
2D	2-Dimensional
3D	3-Dimensional
AOA	Angle of Attack
BPR	Bypass Ratio
CFD	Computational Fluid Dynamics
DNS	Direct Numerical Simulations
EPNL	Effective Perceived Noise Level
FJR	Flight Jet Rig
ICAO	International Civil Aviation Organisation
ISVR	Institute of Sound and Vibration Research
JFI	Jet-Flap Interaction
JSI	Jet-Surface Interaction
JSR	Jet-Surface Reflections
LES	Large Eddy Simulations
LRT	Lighthill's Acoustic Analogy with Ray Tracing
MTOM	Maximum Take-Off Mass
OASPL	Overall Sound Pressure level
OGV	Outlet Guide Vane
PAA	Propulsion Airframe Acoustics
PNL	Perceived Noise Level
PSD	Power Spectral Density
RANS	Reynolds Averaged Navier-Stokes
RMS	Root-mean square
RSTM	Reynolds Stress Turbulence model

SPL	Sound Pressure Level
TE	Trailing Edge
TET	Turbulent Energy Transfer
TI	Turbulent Intensity
TKE	Turbulent Kinetic Energy
UHBR	Ultra High Bypass Ratio

Nomenclature

Roman

Symbol	Meaning
A	Area of ray tube
B_i	Body forces
c_l	Length scale calibration constant
c_{local}	Local speed of sound
c_t	Time scale calibration constant
c_0	Speed of sound in the far field
C_i	Directivity coefficients
D_{eff}	Effective diameter of jet
D_F	Doppler factor
D_J	Diameter of nozzle
f	Frequency
$\mathcal{F}$	Fourier transform
h	Vertical distance to wing
$\mathbf{i}$	Imaginary number
I	Acoustic intensity
I_{ijkl}	Intensity fourth-order correlation tensor
l	Horizontal distance to flap trailing edge
L	Length scale
L_p	Potential core length
L_{vc}	Width of jet at vena-contracta
M_c	Convected Mach number
M_f	Flight-stream Mach number
M_J	Acoustic Jet Mach number

n_i	Normal vector to wave front
N	Number of rays in each far-field bin
p	Pressure
p'	Pressure fluctuation
P	Power Spectral Density
P_a	Acoustic power
Q	Source strength
r	Distance to observer
$\mathbf{r_x}$	Ray position vector
Re	Reynolds number
R_{ijjk}	Lighthill's stress correlation function
s_i	Slowness vector
t	Time
T_{ij}	Lighthill's stress tensor
u_i	Average velocity component
u_i'	Fluctuating velocity
U_f	Flight-stream velocity
U_J	Maximum velocity in jet
v_i	Overall velocity field
V	Volume of the jet
W	Flap length
$\mathbf{x}$	Observer location
x_i	Direction component
$\mathbf{y}$	Source location

Greek letters

Symbol	**Meaning**
α	Nozzle convergence angle
β	Ratio of turbulent velocities
δ	Boundary layer thickness
δ_β	Shear layer half-width
δ_{ij}	Kronecker delta
Δ	Ratio of length scales

ϵ_{ij}	Strain rate tensor
$\boldsymbol{\eta}$	Separation in moving reference frame
γ	Empirical constant
γ_J	Jet Spreading angle
γ_{L_p}	Angle to the edge of the potential core
κ	Wave number
λ	Wavelength
μ	Dynamic viscosity
Π_{ijkl}	Jet directivity
ρ	Density
ρ'	Density Fluctuation
ω	Angular frequency
Ω	Convected frequency
ϕ	Azimuthal observer angle
ϕ_{rel}	Relative azimuthal observer angle
Φ	Flow factor
σ	Vorticity
σ_{ij}	Viscous stress tensor
τ	Retardation time
τ_{ij}	Stress tensor
τ_s	Time scale at source
τ_s^*	Turbulent energy transfer time scale
θ	Polar observer angle
θ_{cos}	Critical polar angle of the cone of silence
$\theta_{deployed}$	Deployed flap angle
θ_{rel}	Relative polar observer angle
ζ_i	Static separation distance

Subscripts

Symbol	**Meaning**
f	Flight-stream variable
i, j, k	Component of variable in local vector coordinates
J	Jet variable

0	Variable in the far field

Chapter 1

Introduction

1.1 Problem specification

As the world's population continues to grow, there is an increasing demand for air transportation. Recently, the issue of noise from aircraft engines has been a source of great debate with the proposed third runway at London's Heathrow Airport. It is argued that Heathrow's capacity is being capped with only two runways for both trade and long-haul flights. An expansion would allow the airport to accommodate the growing number of passengers and goods as shown in Figures 1.1.1 and 1.1.2, respectively.

However, an expansion of Heathrow airport will not only result in an increase in carbon emissions from planes and road traffic, but the public living nearby will also be exposed to greater noise levels. Hearing loss, increased stress levels and sleep disturbance are the main health impacts associated with excessive noise exposure. Clark [1] reports that the elderly, shift workers and children are thought to be most at risk. A higher level of exposure to noise within the school environment was shown to have a detrimental effect on children's reading, comprehension and memory. It is, therefore, imperative for airports and aircraft manufacturers to consider the impact of noise of current and future aircraft.

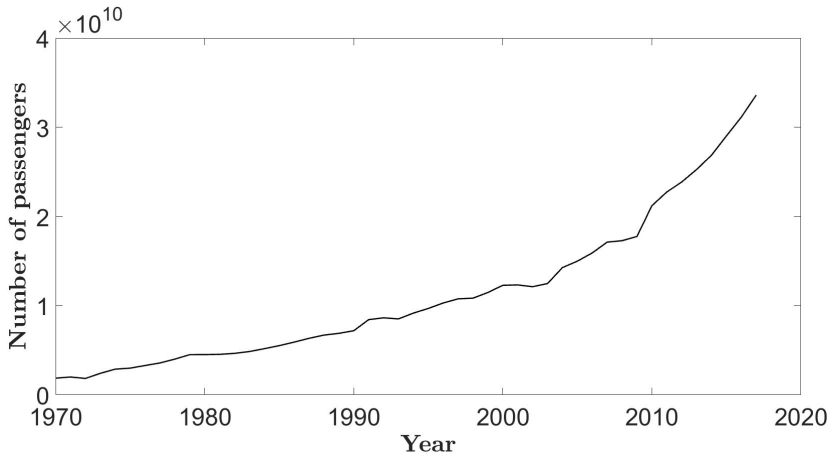

FIGURE 1.1.1: Diagram showing the number of passengers travelling by air transport worldwide. (Data from ICAO [2]).

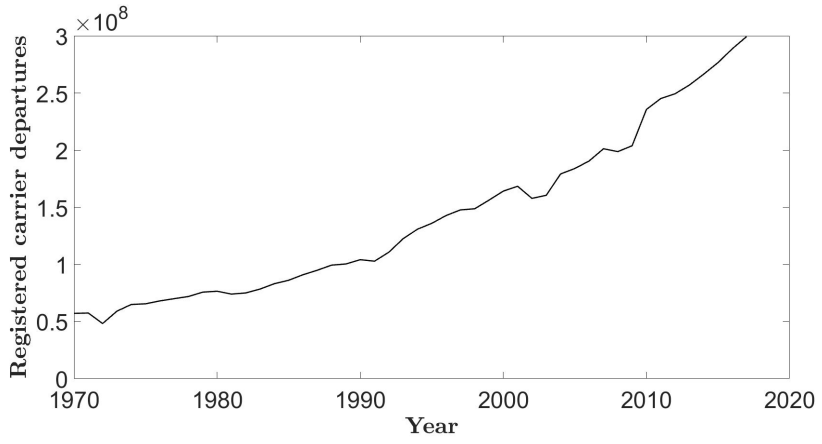

FIGURE 1.1.2: Diagram showing the number of departures of aircraft worldwide. (Data from ICAO [3]).

To combat the increase in noise levels from a growing number of flights, some airports restrict airlines to fly within certain hours or follow flight paths that avoid densely packed urban areas. Heathrow, for instance, does not allow flights to land before 4:30 am [4]. Alternatively, governments have introduced schemes to reduce the ambient level of noise that households experience around airports, such as providing loft insulation and double glazing [5]. The location of some airports outside of city centres, like Washington Dulles, can minimise the impact on the local populous. However, as Smith [6] remarked, this does make it unpopular for commuters.

Since the earliest jet engines entered service in the 1960s, aircraft manufacturers have continued to increase the engine efficiency, capacity of aircraft and produce greater thrust from engines by primarily turning to coaxial engines with increasing bypass

ratios (BPR). One of the consequences of this is a reduction in the overall noise level, seen in Figure 1.1.3, as for a larger engine, the same thrust can be achieved with a lower bypass velocity. As the dominant noise source of large coaxial engines is the shear layer between the bypass and ambient air, a lower noise level is generated with a reduced bypass velocity.

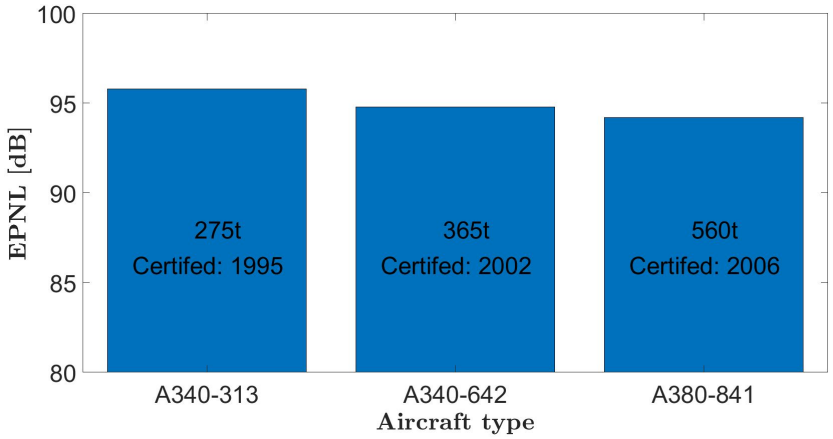

FIGURE 1.1.3: Increase in capacity (Tonnes) against Effective Perceived Noise Level (EPNL) over time (Data from [7]).

Aircraft require certification to demonstrate they meet the required international standards for airworthiness. The International Civil Aviation Organisation (ICAO) has introduced regulations to cut down on the noise produced by aircraft. During certification, a series of microphone measurements are taken at critical points around the aircraft's flight path. This is shown in Figure 1.1.4. These reference points are at the approach, sideline and take-off positions and allow for the variation in noise from different components to be accounted for both airport workers and the surrounding community. The approach reference point is 2000m along the centre line of the extended runway at a position vertically below the 3° glide path. The sideline measurement is taken 450m parallel to the runway while the take-off (fly-over) reference point is 6500m from the start of the roll. One of the ways to reduce noise at the fly-over reference point is to operate the engine at a reduced thrust and angle of climb, called cutback, after the aircraft has reached a minimum altitude. This is done to limit noise exposure for airport workers and local communities around the airport.

During the certification process, the Effective Perceived Noise Level (EPNL) is calculated to ensure the aircraft meets regulations [6]. However, the EPNL is a complex metric as it has to account for the range of frequencies that can be heard by

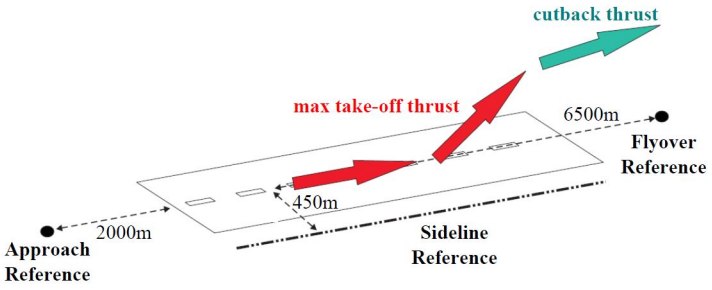

FIGURE 1.1.4: Diagram showing aircraft noise certification reference points according to ICAO Annex 16.

people (normally between 0.02 and 20kHz [8]), tone corrections (discrete tone penalties above the ambient level) and the duration of each event (approach, fly-over and departure). Studies have found that the most annoying frequencies are in the 2.5 - 5.5kHz range [9, 10]. To pass the certification process, the cumulative value of the three reference points needs to be below the allowable levels depending on an aircraft's Maximum Take-Off Mass (MTOM) and the age/chapter of the aircraft. This can be seen in Figure 1.1.5. The certification process measures the noise from the entire aircraft and can be broken down into sources from different components. Figure 1.1.6 shows the typical strength of these sources on take-off and approach. Here it can easily be seen that the fan and jet noise dominate at take-off. Although the jet noise provides a smaller contribution to the total noise on approach, it is still present and mainly contributes to the installation effects.

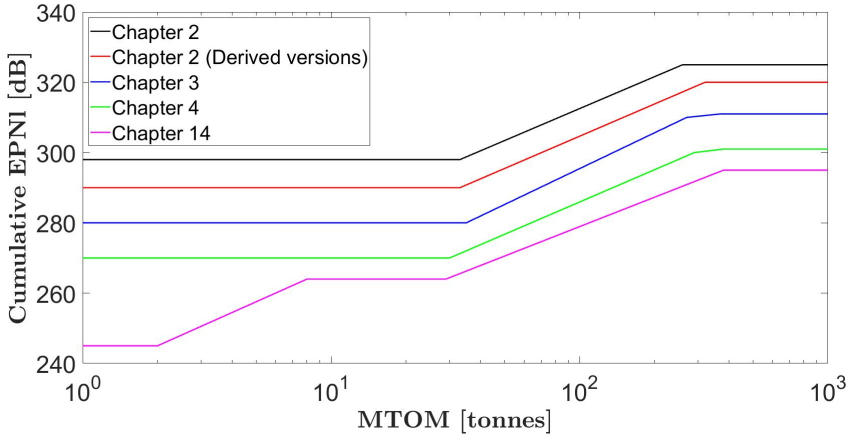

FIGURE 1.1.5: Diagram showing the ICAO cumulative EPNL for each chapter of aircraft against Maximum Take-Off Mass (MTOM) (Data adapted from [11]).

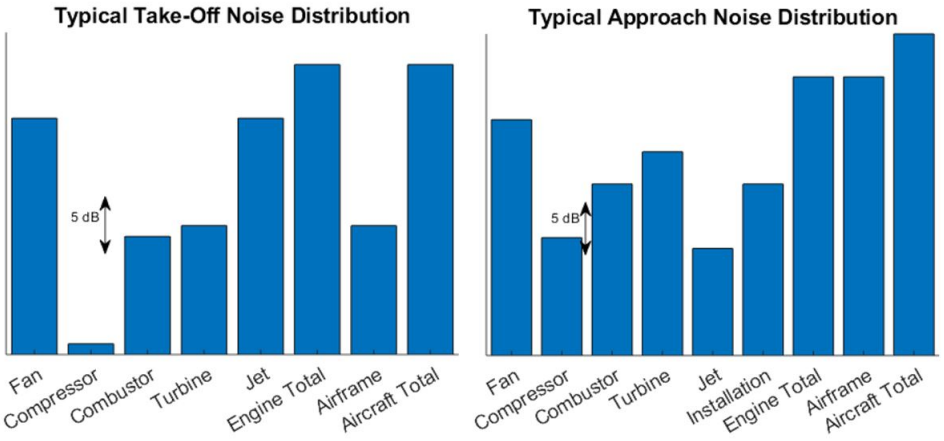

FIGURE 1.1.6: Typical noise distribution for take-off (left) and approach (right). Data adapted from private communication with Roll-Royce (2017).

1.2 Motivation

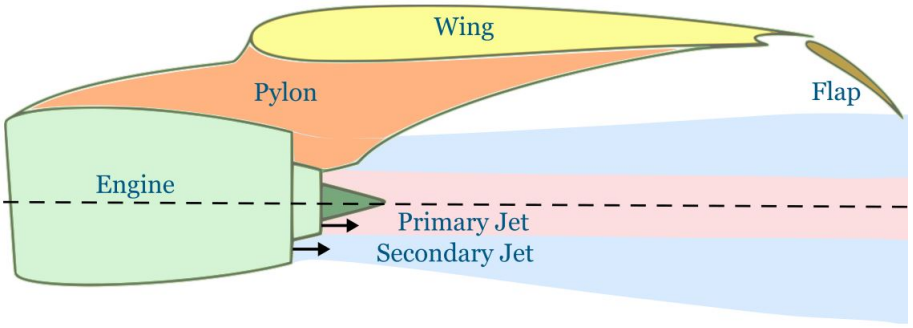

FIGURE 1.2.1: Diagram showing the geometry around the engine.

Most of the noise reductions seen in aircraft engines over the last sixty years have come from increasing the BPR. However, as engines have increased in diameter, their surface area and, therefore, drag have increased. Future engines will encounter ground clearance issues if the engine is kept below the wing and the BPR is increased further. To solve this, the engine can be moved forwards and lifted higher off the ground. This will bring the jet closer to the wing and it is thought that a low-frequency penalty will be introduced due to the increase in the jet-surface interaction with the wing and flap. Therefore, there is a trade-off between increased noise levels and having a larger and more efficient aircraft engine.

Aircraft manufacturers have had to turn to other solutions to continue to reduce the noise. Numerous geometric variations of nozzles have been employed which include

chevrons [12–14], serrations [15], non-concentric nozzles [16] and plugs in the primary nozzle [17]. These geometries cause a reduction in noise either due to the change in the sound propagation path or the mixing rate of the jet. Another area of research [18–20] is the design of low-noise pylons which connect the engine to the wing (Figure 1.2.1). The blockage of the pylon on the flow will obviously cause an asymmetric flow and noise fields to develop even before considering the impact of the wing. Advanced prediction methods are, therefore, needed to be able to study this complex situation at the preliminary design stage.

Taking noise measurements is an expensive and time-consuming process for aircraft. Differences between static and in-flight noise mean that full-scale testing on an airframe is required for the certification procedure. Therefore, companies only carry out noise measurements near the end of the design cycle. Before then, companies need to rely on analytical and numerical procedures to highlight potential noise risks at the early design stages. These are preferred to experimental testing due to the low cost and fast calculation that is possible with modern computers. Traditional analytical noise prediction techniques have often assumed the jet to be axisymmetric. This is clearly no longer valid for more realistic asymmetric geometries. Therefore, there is a need for developments in the simulation techniques used. Computational Fluid Dynamics (CFD) simulations are used to analyse the flow and range from fast calculations from Reynolds Averaged Navier-Stokes (RANS) simulations, to slow Direct Numerical Simulations (DNS). Design teams must find a compromise between computational time and the scale of turbulence that can be simulated. The results of these simulations are then used to help inform the design of future aircraft to meet increasingly demanding requirements. For simulation techniques to be useful at the preliminary design stage, confidence is needed that these techniques can predict the changes in the flow field and noise that different designs produce.

The focus of this work is the change in the mixing noise as the nozzle geometry is changed for subsonic isothermal jets for ultra-high bypass ratio (UHBR) engines. The noise from other sources such as the fan, internal noise sources (combustion and Outlet Guide Vane (OGV) interaction noise), landing gear noise (one of the most significant contributors to airframe noise), and the noise from supersonic jets will not be covered here. The change in noise produced by hot jets will not be discussed in detail since the majority of jet mixing noise from modern large bypass ratio engines

comes from the outer shear layer formed by the cold bypass ratio flow and the ambient air. While installed jets are studied in Chapter 6 of this thesis, the additional energy at low frequency due to the jet-surface interaction is not modelled, and so will not be discussed in much detail.

The co-ordinate system that is used in this thesis is shown below in Figure 1.2.2. The observer polar angle, θ, is measured from the x_1 axis and the observer azimuthal angle, ϕ, from the positive x_3 axis going anti-clockwise when looking upstream. It should be noted that $0 \leq \theta \leq \pi$ and $0 \leq \phi < 2\pi$.

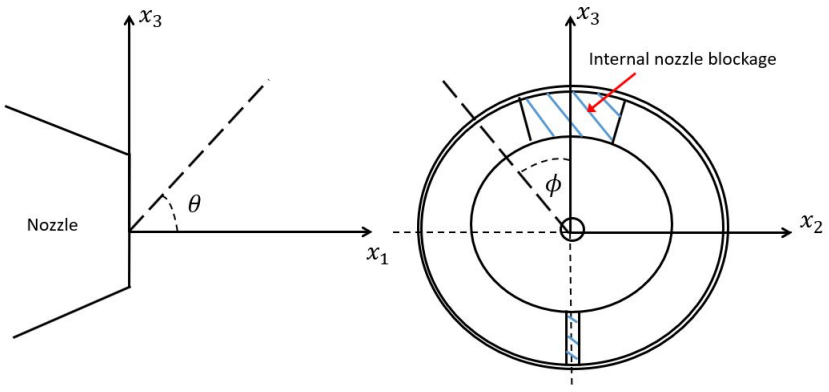

FIGURE 1.2.2: Diagram showing the co-ordinate system used. The jet axis is aligned with the x_1 axis.

1.3 Author's contribution

This project has developed the method called Lighthill's Acoustic Analogy with Ray Tracing (LRT), initially developed by Ilario [21], and implemented several novel ideas to advance the current understanding in aeroacoustics. These include:

- A new derivation of the source equation used in the LRT model to include the convection effect on the axial length scale. This introduces a source compactness term that has not been considered within the LRT method previously.
- Using LRT, in-flight predictions of the far-field jet mixing noise away from $\theta = 90^0$ for isolated jets have been carried out.
- Improved predictions can be made using an anisotropic model for the jet mixing noise instead of assuming isotropic turbulence.

- Analysis has been conducted on pylons of differing internal blockage to ascertain the impact of this variable on the far-field mixing noise.
- Reflections can now be modelled from simple geometries (a cone and flat plate) to allow for installed geometries to be analysed.

The research questions that have been answered in this project are:

- What degree of accuracy can be obtained from a k-ϵ RANS model for predicting the flow of realistic isolated and installed nozzle geometries? What are the limits?
- How does introducing an internal and external blockage to the nozzle (a pylon) affect the far-field mixing noise amplitude and directivity?
- How does the reflected and jet mixing noise change when an installed geometry is considered?
- How does the source strength and distribution change and scale as the geometry is changed from a simple conical nozzle to an installed jet?

1.4 Outline of thesis

The structure of this thesis is as follows: Chapter 2 introduces the background to fluid motion and turbulence, how these are simulated, jet physics, and a literature review of how the mixing noise has been modelled previously. Chapter 3 outlines the methodology of the work with the generation of the CFD meshes, inputs for the CFD simulation, and generation of the inputs for the ray tracing code. An improved source equation is then derived to account for the convection of the axial length scale and source compactness. Although the author has not conducted any experimental work, data from the Doak Laboratory at the University of Southampton has been used to compare against simulations and so the experimental set-up is briefly discussed. The LRT method is validated against results for a simple conical nozzle in Chapter 4 and the sensitivities of the method are discussed, including the impact of the anisotropy on the flow and acoustic results. Within Chapter 5, the complexity of the isolated geometry is increased to understand how different geometric features influence the flow and noise produced. The primary focus is on the impact of the blockage caused

by the pylon on the flow field and mixing noise. Chapter 6 demonstrates how the LRT method can be used to predict the direct jet mixing and reflected mixing noise from installed jets. The reflective code is validated against experimental data for varying wing positions before the LRT method is applied to two installed geometries. Finally, a theoretical deflected jet from a flap is analysed to see how the ray path changes when flaps are deployed during take-off and on approach. The final chapter of this thesis, Chapter 7, presents the conclusions, recommendations and future work for this project. Additional details on some of the mathematical modelling can be found in the Appendix.

Chapter 2

Background

Having discussed in the previous chapter the problems that local communities around the airport face due to excessive noise from jets, this chapter aims to provide the reader with a background to the topics that will be crucial for the rest of the thesis; namely, how can jets be modelled and what research has been done previously.

2.1 Modelling fluid motion

The noise that jets generate, and how that noise propagates, is due to the behaviour of air as a fluid. Fluid motion is governed by the Navier-Stokes equations which are derived from the continuity (Equation 2.1.1) and momentum equations (Equation 2.1.2).

$$\frac{\partial \rho}{\partial t} + \frac{\partial \rho v_i}{\partial x_i} = 0 \tag{2.1.1}$$

$$\frac{\partial v_i}{\partial t} + v_j \frac{\partial v_i}{\partial x_j} = \frac{1}{\rho} \frac{\partial \tau_{ij}}{\partial x_i} + B_i \tag{2.1.2}$$

ρ is the density of the fluid, t is time, v_i is the total velocity of the fluid in the i_{th} direction, x_i is the direction of the component, τ_{ij} is the stress component, and B_i is the body forces that are applied to the fluid (e.g. gravity). By expanding the stress component using the relations for stresses in a Newtonian fluid, the Navier-Stokes equation for an incompressible fluid is written as

$$\rho\Big(\frac{\partial v_i}{\partial t} + v_j\frac{\partial v_i}{\partial x_j}\Big) = -\frac{\partial p}{\partial x_i} + \mu\frac{\partial^2 v_i}{\partial x_j \partial x_j} + \rho B_i \tag{2.1.3}$$

where p is the pressure and μ is the dynamic viscosity. Although compressibility is needed for acoustics, the incompressible equation is shown here for ease of use. The Navier-Stokes equations are essentially Newton's second law applied to a fluid, i.e. the acceleration of a mass of fluid is equal to the forces applied to that fluid.

One way to simplify the Navier-Stokes equations is to use a process called Reynolds decomposition. Here, a flow variable is split into a mean component and a fluctuating component. For example, the turbulent velocity field, v_i, is given by

$$v_i = u_i + u_i' \tag{2.1.4}$$

where the mean velocity is u_i and the fluctuating component of velocity is u_i'. By carrying out this procedure with each variable in Equations 2.1.1 and 2.1.2, the resulting time-averaged equations for an incompressible fluid, neglecting the effect of gravity, are

$$\frac{\partial u_i}{\partial x_i} = 0 \tag{2.1.5}$$

$$\rho\frac{\partial u_i}{\partial t} + \rho\frac{\partial u_i u_j}{\partial x_i} = -\frac{\partial p}{\partial x_i} + \mu\frac{\partial u_i}{\partial x_j \partial x_j} - \rho\frac{\partial u_i' u_j'}{\partial x_j} \tag{2.1.6}$$

The final term in Equation 2.1.6 is known as the Reynolds stress and deals with the turbulence of the flow.

There are a wide range of turbulent scales within a flow, which vary from the largest integral length scale to the Kolmogorov scale (smallest). Eddies between these two sizes are known as the Taylor microscale, as shown in Figure 2.1.1. Most of the energy of the flow is contained within the largest structures of the flow. This turbulent energy is transferred to smaller eddies as the eddies roll-up and break down in size in the inertial subrange. The slope of the inertial subrange (Figure 2.1.1) is constant due to there being an equilibrium between the energy gained from the largest turbulent scales and that which is lost to the smallest scales. Energy is lost in the dissipation range (also called the viscous subrange) as heat due to viscosity.

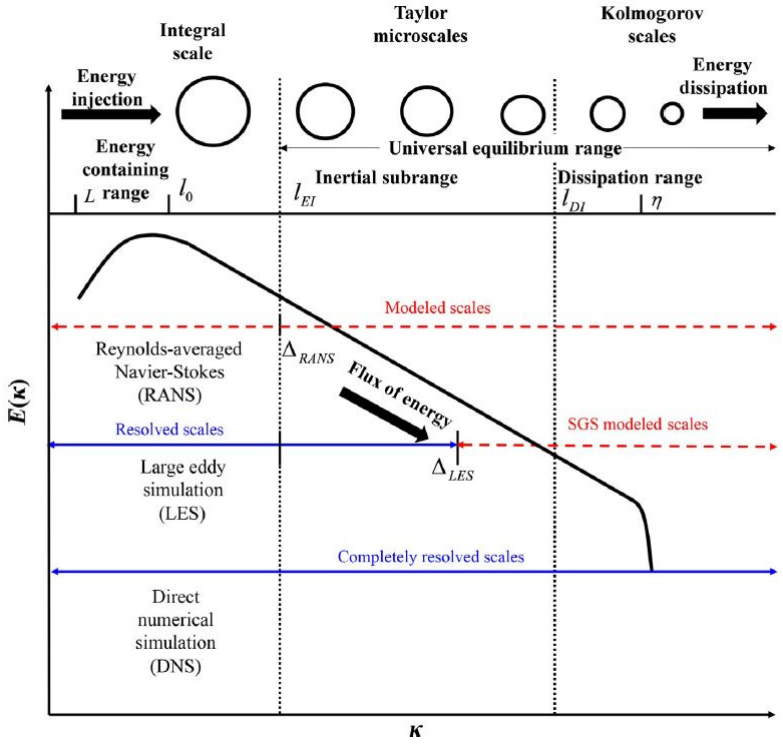

FIGURE 2.1.1: Diagram showing the energy of eddies based on their wavelength. (Diagram from Jyeshtharaj [22]).

In Figure 2.1.1, the wave number, κ, is defined as

$$\kappa = \frac{2\pi}{\lambda} \tag{2.1.7}$$

where λ is the wavelength of the wave.

Due to the non-linear nature of the Navier-Stokes equations and the large range of turbulent length scales that exist in flows, it is not possible to solve the flow fields of complex jets analytically. Instead, several numerical methods have been developed over the years, depending on the level of turbulence that needs to be modelled. These can be split into Reynolds Averaged Navier-Stokes (RANS), Large Eddy Simulations (LES) and Direct Numerical Simulations (DNS). RANS models calculate a time-averaged mean flow and only capture the largest eddies in the energy-containing region. LES simulations model a large proportion of the turbulence in the inertial subrange whereas DNS models the complete range of scales. LES and DNS are more computationally expensive than RANS due to needing a finer mesh to resolve the smaller turbulence scales. Therefore, there is a balance between how much of the

turbulence range is needed to provide results and the limits on the time and computational memory available. Due to this, some researchers have turned to hybrid RANS-LES models. A low Reynolds number RANS model is used close to the wall, to reduce the computational requirements for fine-scale modelling [23].

The advantages and disadvantages of the three main CFD methods are summarised below in Table 2.1. In this thesis, the focus will be on RANS models, but it is useful to have an understanding of other CFD methods when looking at the literature.

Method	Advantages	Disadvantages
RANS	Quick simulation time (hours), low grid requirements, models all scales of turbulence	Results are an average over time, different turbulence models needed to close equations
LES	Simulates a larger range of turbulent length scales than RANS, uses a model for the smallest eddies in the viscous subrange	Higher computational cost than RANS due to using a finer mesh, longer simulation time than RANS (weeks)
DNS	Simulates all turbulence scales	Higher computational cost than LES due to finer mesh, long simulation time (weeks/months)

TABLE 2.1: Advantages and disadvantages of CFD methods.

The problem that CFD models face is that there is no information within the solution to directly calculate the Reynolds stresses from Equation 2.1.6, and hence the equations are not closed. Different turbulence models have been generated to provide closure. One of the most common approaches that CFD models use is the Boussinesq hypothesis which relates the Reynolds stress term to the mean velocity gradient by the eddy viscosity, μ_t. Different turbulence models will solve for this in different ways.

Over the years, different RANS models have been developed, for example, the k-ϵ and k-ω models, to look at a variety of flow regimes. The k-ϵ model [24] is often used when looking at jets and is a two-equation model; one for the turbulent kinetic energy (TKE), k, and one for the turbulent dissipation rate, ϵ. The TKE is modelled by

$$\rho\frac{\partial(k)}{\partial t}+\rho\frac{\partial(ku_i)}{\partial x_i}=\frac{\partial}{\partial x_j}\Big[\frac{\mu_t}{\sigma_k}\frac{\partial k}{\partial x_j}\Big]+\mu_t\Big(\frac{\partial u_i}{\partial x_j}+\frac{\partial u_j}{\partial x_i}\Big)\frac{\partial u_i}{\partial x_j}-\rho\epsilon \tag{2.1.8}$$

$$\mu_t=\rho C_\mu\frac{k^2}{\epsilon} \tag{2.1.9}$$

The dissipation is then calculated by

$$\rho\frac{\partial(\epsilon)}{\partial t}+\rho\frac{\partial(\epsilon u_i)}{\partial x_i}=\frac{\partial}{\partial x_j}\Big[\mu\frac{\mu_t}{\sigma_\epsilon}\frac{\partial\epsilon}{\partial x_j}\Big]+\frac{C_1\mu_t\epsilon}{k}\Big(\frac{\partial u_i}{\partial x_j}+\frac{\partial u_j}{\partial x_i}\Big)\frac{\partial u_i}{\partial x_j}-C_2\rho\frac{\epsilon^2}{k} \tag{2.1.10}$$

The terms involving buoyancy have been neglected from Equations 2.1.8 and 2.1.10 since only a single-phase fluid, air, is being considered. C_μ, C_1, C_2, σ_k and σ_ϵ are numerical constants and the standard values of these are 0.09, 1.44, 1.92, 1 and 1.3 respectively. Equations 2.1.8 and 2.1.10 are transport equations for the kinetic energy and dissipation rates respectively. Both are made up of a time and convection term on the left-hand side of the equations. The right-hand side contains a diffusive term first of all, followed by any sources or sinks of energy. Once the transport equations have been solved, the value of μ_t can be calculated and used to compute the velocity field in Equation 2.1.6. The k-ϵ model was first developed to model turbulent boundary layers and plane shear flows [25], but is also commonly used for jet flows.

One of the limitations of the k-ϵ turbulence model is the fact that it does not produce good results for adverse pressure gradients (for example, the separation of the boundary layer over an airfoil [26]). This is due to the damping functions that are needed in the k-ϵ model to calculate the near-wall region in the viscous sublayer. The damping functions were originally derived for a flat plate with no adverse pressure gradient. Therefore, a new turbulence model was proposed, first by Kolmogorov [27] in 1942 but the modern version is by Wilcox [28], called the k-ω model which addresses this shortcoming.

Like the k-ϵ model, the k-ω model is a two-equation model. The transport equation for k is the same (Equation 2.1.8) but a transport equation for the specific turbulence dissipation rate, ω_s, is used rather than the transport equation for ϵ. ω_s is defined as

$$\omega_s = \frac{\epsilon}{C_\mu k} \tag{2.1.11}$$

The transport equation for ω_s is written as

$$\rho\frac{\partial(\omega_s)}{\partial t} + \rho\frac{\partial(\omega_s u_i)}{\partial x_i} = \frac{\partial}{\partial x_j}\left[(\mu + \frac{\mu_t}{\sigma_{\omega_s}})\frac{\partial \omega_s}{\partial x_j}\right] + 2\mu_t\frac{\omega_s}{k}\epsilon_{ij}\epsilon_{ij} - \beta_i\rho\omega_s^2 \tag{2.1.12}$$

where ϵ_{ij} is the strain rate tensor and there are two empirical constants: $\sigma_\omega = 2$ and $\beta_i = 0.072$. The final two terms on the right-hand side of Equation 2.1.12 account for the generation and dissipation of ω_s, respectively.

Similar to the k-ϵ model, the transport equations for k and ω_s are solved within the k-ω model to allow μ_t to be calculated, and hence the momentum equation is solved. The main differences between the k-ϵ and k-ω models are the values of the empirical constants and the fact that k-ω does not need damping functions in the near-wall region. Hence the suitability for k-ω for adverse pressure gradients. However, it has been shown in the literature that the k-ω model is dependent on the freestream turbulence conditions [29]. One way to get around this is to use a k-ϵ model, which is not dependent on the freestream conditions, away from the wall and a k-ω model close to the wall. A blending function is then used to change between the models. This is the principle behind the SST turbulence model [30] which has been found to give improved predictions of the flow around airfoils compared with other turbulence models [31–33].

So far in this chapter, a brief discussion on how fluids can be modelled has been given. Depending on the problem being studied and any time constraints, an appropriate method will be selected. To proceed with looking into jet noise, an understanding of the physics of jets, how the noise is modelled and what work has been done previously is required.

2.2 The structure of jets

Jets can be broken down into two categories: single and coaxial jets. The structure of each of these will now be discussed.

2.2.1 Single jets

Within a single jet, three main regions can be identified, as shown in Figure 2.2.1. The flow inside the nozzle is assumed to be laminar and exits the nozzle into the initial region. Here, a turbulent shear layer is created between the flow from the nozzle and the ambient air. As the shear layer grows, part of the jet flow outside the nozzle, but not in the shear layer, can still be considered as being laminar. This is called the potential core. The initial region ends at the end of the potential core. The second region of a single jet is the transitional region, where the flow regimes mix. Far downstream of the nozzle exit, the main region exists where the flows have been fully mixed.

Within a jet, the size of an eddy is limited by the shear layer width. Therefore, high-frequency noise is generated very close to the nozzle exit where the shear layer and eddy size are small. As eddies travel downstream, they roll-up, forming larger eddies and lower frequencies. These low frequencies, as mentioned in Chapter 1, are what aircraft manufacturers are most concerned about as they are said to be the most "annoying" to people.

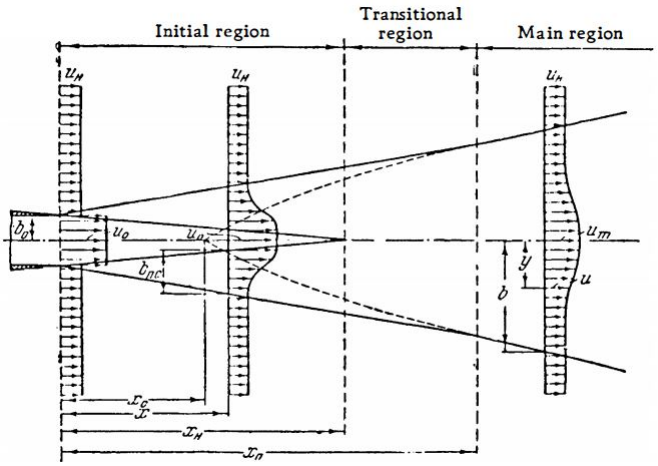

FIGURE 2.2.1: Diagram showing the main regions in a single jet. (Diagram from Abramovich [34]).

By normalising his velocity data by the jet velocity and the radial distance by the distance from the centreline to the point which is half the centreline value, Abramovich [34] showed that the velocity profiles of axisymmetric jets collapsed onto each other. This is called similarity. Two different types of similarity are present in an axisymmetric single jet. Until the end of the potential core, the flow can be considered

as being a two-dimensional (2D) shear flow and once the flow is fully mixed, it becomes axisymmetric. Wygnanski [35] and Hussein [36] showed that the similarity of the jet exists up to seventy diameters downstream of the nozzle exit. The importance of similarity for jets is that it allows for axisymmetric jets of different sizes and jet velocities to be compared, as long as velocities and distances are in a non-dimensional form. This means that analytical models of the velocity profile can be derived [35–37]. However, when an asymmetric jet is considered, similarity conditions cannot be applied to asymmetric flow regions. This means that complex flow fields require expensive computation before analysis of noise can begin, rather than using simple analytical models. Therefore, advanced simulation techniques require development.

2.2.2 Coaxial jets

Modern jet engines are coaxial due to their increased propulsive efficiency and reduced noise levels compared to single-stream jets. However, the larger diameter means a greater drag, heavier fan and larger supporting components, so there is a trade-off here.

The regions of the coaxial jet are defined slightly differently from the single jet and are illustrated in Figure 2.2.2. The initial region contains the secondary jet that issues from the bypass duct of the engine. Starting at the end of the potential core of the secondary flow, the interaction region contains the rest of the potential core from the core of the engine. The potential core of the primary jet is longer than that of a single jet since the secondary flow shields the primary flow from the ambient medium. Far downstream, the flow can be considered as being fully mixed in the mixed flow region.

Unlike a single jet, there are two shear layers present in coaxial jets. The primary shear layer (see Figure 2.2.2) occurs between the potential cores of both nozzles. In modern civil turbofan engines, the flow velocities are fairly similar so this layer is sometimes neglected in studies [38]. The ambient shear layer occurs due to the mixing of the bypass flow with the ambient medium around the engine. This region behaves similarly to the initial region of a single jet. The size of each region is determined by the velocity and area ratios between the primary and secondary nozzles. UHBR engines have a BPR above 9. Due to the secondary to ambient shear layer being the dominant source of mixing noise for UHBR engines, these engines are often considered as single stream jets for the purpose of noise predictions.

One of the other differences between single and coaxial jets is the fact that a temperature difference exists between the flows. The primary nozzle directs the flow that has passed through the combustion chamber and is consequently much hotter than the bypass flow. While heating a jet has been shown to reduce the mixing noise [21], it also introduces a dipole-like source [39,40]. The work in this thesis will focus on UHBR engines, where the mixing from the bypass and ambient fluid dominates, so the heating effect on the primary flow will not be considered further.

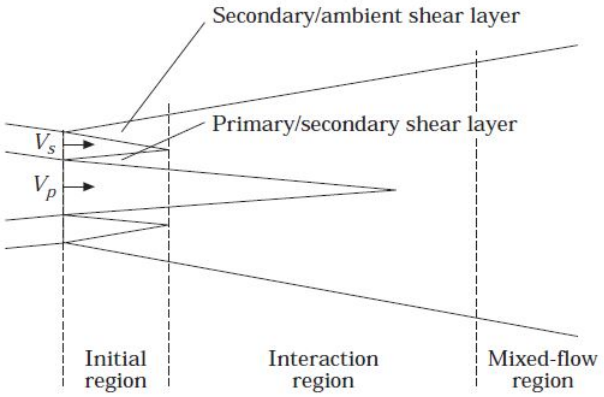

FIGURE 2.2.2: Diagram showing the regions of a coaxial jet. (Diagram from Fisher and Preston [40]).

Early work on coaxial jets was carried out by Ko and Kwan [41,42]. When looking at the turbulence generated, the primary shear layer behaves like a single jet discharging into a moving stream, while the ambient shear layer behaves like a single stream jet. This meant similarity could be achieved in the initial and mixed-flow regions, just like a single stream jet. In terms of the noise produced, the primary shear layer was found to predominately produce the high-frequency noise while the ambient shear layer produced the lower frequencies. The presence of two jet streams did cause two distinct peaks to evolve in the SPL spectra, although the high-frequency peak disappeared as the velocity ratio approached unity. Ko and Kwan concluded by saying that as an agreement in terms of similarity and spectra could be found between single and coaxial jets, then coaxial jets could be modelled by several single jets. Further work by the same authors in [42], provided additional evidence showing that both single and coaxial jets exhibit similar coherent structures using two-point correlation measurements.

Having gained an understanding of how fluids and jets behave, the next step is to look at how the noise from jets can be modelled.

2.3 Modelling jet acoustics

The previous discussion has focused on how the flow field of a jet may be modelled. With this information, the strength of acoustic sources can be determined as well as how noise propagates away from the sources. The next section discusses how the acoustic source strength and propagation of the resultant noise are mathematically modelled.

2.3.1 Lighthill's analogy

The study of noise produced by jets, called aeroacoustics, began with Lighthill in 1952 [43, 44]. In these papers, Lighthill developed his now well-recognised analogy which is a rearrangement of the Navier-Stokes equation into a wave equation-like form. Lighthill considered an isolated jet discharging into a quiescent medium and analysed an eddy generated in a moving frame of reference as seen in Figure 2.3.1.

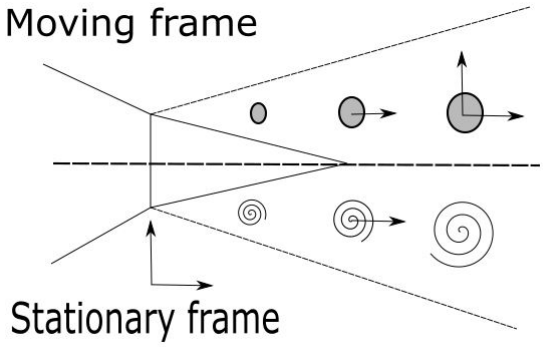

FIGURE 2.3.1: Diagram showing Lighthill's frame of reference moving with an eddy as opposed to a stationary frame of reference in the laboratory.

To derive Lighthill's analogy, one starts from the compressible mass and momentum equations given in Equations 2.1.1 and 2.1.2 but repeated below for convenience. Any effect by the body forces has been neglected.

$$\frac{\partial \rho}{\partial t} + \frac{\partial \rho v_i}{\partial y_i} = 0 \tag{2.3.1}$$

$$\frac{\partial v_i}{\partial t} + v_j \frac{\partial v_i}{\partial y_j} = \frac{1}{\rho} \frac{\partial \tau_{ij}}{\partial y_i} \tag{2.3.2}$$

where ρ is the density of the fluid, t is time, v_i is the velocity of the fluid in the i_{th} direction, y_i is the source location and τ_{ij} is the stress component. Taking the time derivative of Equation 2.3.1 gives

$$\frac{\partial^2 \rho}{\partial t^2} + \frac{\partial^2 \rho v_i}{\partial y_i \partial t} = 0 \tag{2.3.3}$$

If the partial derivative with respect to y_i is taken of Equation 2.3.2, Equation 2.3.3 can be substituted into the results of the spatial derivative to give

$$\frac{\partial^2 \rho}{\partial t^2} = -\frac{\partial^2 \tau_{ij}}{\partial y_i \partial y_j} + \frac{\partial^2 \rho v_i v_j}{\partial y_i \partial y_j} \tag{2.3.4}$$

Subtracting $c_0^2 \frac{\partial^2}{\partial y_i^2} \rho$ from both sides of Equation 2.3.4, where c_0 is the speed of sound in the far field, gives

$$\frac{\partial^2 \rho}{\partial t^2} - c_0^2 \frac{\partial^2 \rho}{\partial y_i^2} = \frac{\partial^2 T_{ij}}{\partial y_i \partial y_j} \tag{2.3.5}$$

where

$$T_{ij} = (p - \rho c_0^2)\delta_{ij} - \sigma_{ij} + \rho v_i v_j \tag{2.3.6}$$

where σ_{ij} is the viscous stress tensor and δ_{ij} is the Kronecker delta. Equation 2.3.5 is Lighthill's equation. T_{ij} is called Lighthill's stress tensor and $\rho v_i v_j$ is the Reynolds stress term.

Given that Lighthill's analogy is a rearrangement of the Navier-Stokes equation, it is, therefore, an exact equation as no approximations have been made. If it is assumed that the right-hand side of Equation 2.3.5 is known, then one can work out the noise generated in a turbulent jet. Lighthill's Acoustic Analogy shows that the aerodynamic noise of a jet creates a distribution of quadrupole-like source terms, $\frac{\partial^2 T_{ij}}{\partial y_i \partial y_j}$.

Lighthill's stress tensor in Equation 2.3.6 can be simplified in certain circumstances. For jets at sufficiently high Reynolds numbers, the viscous stress term (σ_{ij}) is much smaller than the Reynolds stress term ($\rho v_i v_j$) and so can be neglected. For isothermal

jets, the contribution of density fluctuation in $(p - \rho c_0^2)$ can also be ignored. Therefore, Lighthill's stress tensor can be approximated as

$$T_{ij} \approx \rho_0 v_i v_j \tag{2.3.7}$$

There are several issues with Lighthill's analogy which need to be accounted for when looking at the noise from jets.

- Lighthill's analogy assumes that the medium outside the jet is quiescent, so there is no convection of sound by the flow. These effects are assumed to be contained within the T_{ij} term and are, therefore, known. Additional modelling is needed to account for any convection or refraction that happens within the jet.
- The jet is considered to be isothermal. For heated jets, a dipole-like term is introduced [39].
- Analysis is limited to subsonic jets as shock wave production is not accounted for.
- There are no surfaces within the domain and so Lighthill's analogy is only accurate for isolated jets. Curle [45] and Ffowcs Williams [46] extended Lighthill's analogy to include solid boundaries in stationary and moving mediums, respectively, which results in two extra terms being generated; namely a dipole and monopole-like terms.

Lighthill went on to develop an important scaling law which provides a lot of useful information about jet noise. In the far field, a wave emitted from a source will behave like a spherical wave and so the density fluctuation, ρ', without the presence of flow can be written as a free-space Green's function to give

$$\rho'(\mathbf{x}, t) = \frac{1}{4\pi c_o^2} \int_V \frac{1}{r} \left[\frac{\partial^2 T_{ij}}{\partial y_i \partial y_j} \right]_{\tau = t - \frac{r}{c_0}} d^3\mathbf{y} \tag{2.3.8}$$

where $\mathbf{x}$ is the observer position, V is the volume of the jet, r is the distance from the source to an observer ($r = |\mathbf{x} - \mathbf{y}|$) and τ is the retardated time. According to Goldstein [47], T_{ij} can be assumed to be smooth and decays quicker than y^{-1} in the far field. Therefore, Equation 2.3.8 can be written as

$$\rho'(\mathbf{x},t) = \frac{1}{4\pi c_o^2}\int_V \left[\frac{\partial^2}{\partial x_i \partial x_j}\frac{T_{ij}}{r}\right]_{\tau=t-\frac{r}{c_0}} d^3\mathbf{y} \tag{2.3.9}$$

x_i is the direction component as opposed to $\mathbf{x}$ which is the location of the observer in the far field. According to Goldstein, the second derivative of T_{ij} can be approximated as

$$\frac{\partial^2}{\partial x_i \partial x_j}\frac{T_{ij}}{r} \approx \frac{1}{c_0^2}\frac{x_i x_j}{\mathbf{x}^3}\frac{\partial^2}{\partial \tau^2}T_{ij} \tag{2.3.10}$$

Using the ideal gas assumption that the pressure fluctuation, p', is given by $p' = c_0^2\rho'$ and Equation 2.3.10, Equation 2.3.9 becomes

$$p'(\mathbf{x},\tau) = \frac{1}{4\pi c_0^2}\frac{x_i x_j}{\mathbf{x}^3}\int_V \frac{\partial^2 T_{ij}}{\partial \tau^2}(y,\tau)\, d^3\mathbf{y} \tag{2.3.11}$$

The peak frequency, f, of a jet changes with the maximum velocity in the jet, U_J. To link this to Equation 2.3.11, one needs to consider how T_{ij} changes with U_J. Khavaran [48,49] demonstrated that the largest component of T_{ij} comes from the T_{11} part. Given that the turbulence of a jet scales with jet velocity, T_{11} must also scale with U_J. The peak frequency is approximated as

$$f \sim \frac{U_J}{D_J} \tag{2.3.12}$$

where D_J is the nozzle diameter. Equation 2.3.12 shows that the peak frequency of a jet inversely scales with the jet diameter but scales with the jet velocity. This is because both these variables are linked to the size of the shear layer and hence how large eddies are. As $\frac{\partial}{\partial \tau} \sim \frac{1}{\tau} = f$, $\frac{\partial^2}{\partial \tau^2} \sim f^2$, the source term on the right-hand side of Equation 2.3.11, with Equation 2.3.7, becomes

$$\frac{\partial^2 T_{ij}}{\partial \tau^2} \sim \frac{1}{D_J^2}\rho_0 U_J^4 \tag{2.3.13}$$

This means that Equation 2.3.11 can be written as

$$p' \sim \frac{D_J}{\mathbf{x}} \frac{\rho_0}{c_0^2} U_J^4 \tag{2.3.14}$$

Here, it is assumed that $\int d^3y \sim D_J^3$. The far-field acoustic power of a jet, assuming spherical spreading, can now be written as

$$P_a \sim \frac{\rho_0}{c_0^5} D_J^2 U_J^8 \tag{2.3.15}$$

which is Lighthill's famous eighth power law. Experimental data has been taken by a range of authors, including Lush [50] and Harper-Bourne [51], which has confirmed this scaling law. Harper-Bourne [52] also showed that this meant that the turbulent intensity of a jet scales with U_J^4. Lighthill's scaling law can be used to understand how increasing the bypass ratio has led to quieter jets. As thrust scales as $D_J^2 U_J^2$, a higher BPR allows for a greater bypass mass flow and a lower bypass jet velocity for the same thrust. Hence, for a constant level of thrust, a lower noise level is generated.

In order to compare different nozzles or to extrapolate how a nozzle behaves under different conditions, the noise produced by a jet can be scaled. From Lighthill's scaling law in Equation 2.3.15, the noise of jets can be scaled using the jet velocity and diameter. A ratio of $70 \log \frac{U_J}{U_{ref}}$ is used to scale the noise between different Mach number jets [53] from the same nozzle while a ratio of $20 \log \frac{D_J}{D_{ref}}$ can be used to account for the difference in the flow area [54] of the same shape nozzle at $\theta = 90°$. U_{ref} and D_{ref} refer to a reference jet velocity and diameter, respectively. The scaling of noise due to flight-stream effects, however, is a subject with some variation in the literature. Viswanathan [55] showed that the flight velocity exponent changed with the polar angle from 2.9 at $\theta = 50°$ up to 7.6 at $\theta = 150°$ for a cold jet but also varied with temperature [54]. A value of roughly 3 was found at $\theta = 90°$. On the other hand, Michalke [56] found a value of roughly 6 was needed for the flight exponent at $\theta = 90°$. The variations in results are due to the simplifications and approximations that are used to describe the various effects that are combined together on the right-hand side of Lighthill's equation in Equation 2.3.5.

To allow for the convection effects of the flow to be accounted for in Equation 2.3.11, an additional factor needs to be included. Lighthill modelled the amplification of

sound due to convection with a $(1 - M_c \cos\theta)^{-6}$ term where M_c is the convected Mach number and θ is the polar angle. Ffowcs-Williams [57] later corrected this as he found that Lighthill's factor over-predicted the noise intensity. Ffowcs-Williams considered a limited source volume and found that the convection effect could be modelled by $(1 - M_c \cos\theta)^{-5}$.

Convection effects have now been accounted for. However, the refraction effect on the propagation of noise has not. One way of doing this is to use ray theory.

2.3.2 Ray theory

Ray tracing, also known as geometrical acoustics, can be used to quantify the effect of refraction, as shown in Figure 2.3.2. Refraction occurs due to the gradients of velocity and temperature for non-isothermal jets. Ray tracing methods assume the wavelength is much smaller than fluctuations in the flow. This means that ray tracing is a high-frequency approximation. Due to the ease of coding the equations shown in this section, several authors [21,58,59] have used ray-tracing methods to predict jet noise. The derivation of the equations in this section can be found in Pierce [60].

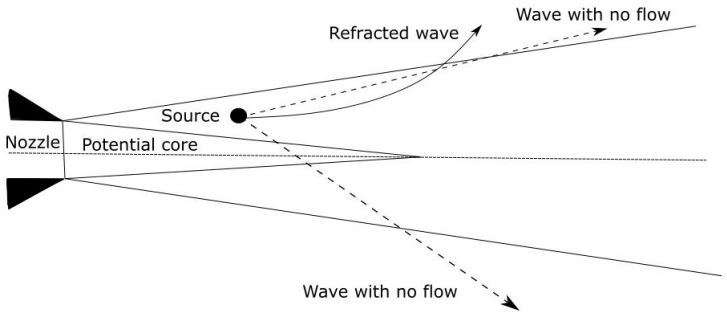

FIGURE 2.3.2: Diagram showing the effect of refraction inside the jet. (Adapted from [21]).

A wavefront is defined as a line on which all points have the same emission time and the same phase. A plane wave moves perpendicular to the wavefront. When a mean flow is present, the wave is also convected. The mean flow may not be constant, however, and this causes the normal of the wavefront to change direction. Hence, the shape of the wavefront changes in space and time.

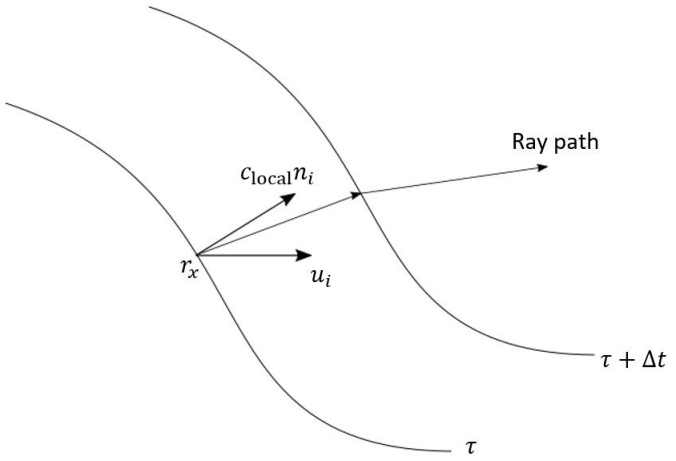

FIGURE 2.3.3: Diagram of a ray path and wave front. (Adapted from Pierce [60]).

Figure 2.3.3 shows the concept of a ray path. The wavefront moves perpendicular to the current position of the wave at the speed of sound but is convected along by the mean flow, u_i, so the actual path of the ray is a combination of these. Pierce shows that the path of a ray at the position, $\mathbf{r_x}$, can be modelled by

$$\frac{ds_i}{dt} = -\frac{\Gamma_i}{c_{\text{local}}}\nabla c_{\text{local}} - s_i \times (\nabla \times u_i) - s_i \cdot (\nabla u_i) \tag{2.3.16}$$

and

$$\frac{d\mathbf{r_x}}{dt} = u_i + \frac{c_{\text{local}}^2 s_i}{\Gamma_i} \tag{2.3.17}$$

where s_i is the slowness vector parallel to the normal vector of the wavefront, n_i, c_{local} is the local speed of sound and $\Gamma_i = 1 - u_i s_i$. Equations 2.3.16 and 2.3.17 allow the propagation of rays through the jet shear layer to be calculated. Furthermore, as there is no assumption of axisymmetry, these equations can be applied to asymmetric flows. Within the LRT, as will be detailed in Chapter 3, rays are released from source points in the jet and traced to the far field. This enables the calculation of the flow factor, outlined in Appendix A.2, which allows for the effect of refraction on the mixing noise to be captured. The flow factor is then used in conjunction with the source equation derived in Chapter 3, to calculate the far-field mixing noise.

When analysis using ray theory is conducted on jets, it is found that the region close to the jet axis has a lower predicted intensity of sound than would be expected from experimental data. This region is called the cone of silence and, unlike the name suggests, is the region where the intensity of noise is the largest. The additional noise that ray theory does not include is generated by evanescent complex rays which decay exponentially. These rays become trapped within the cone of silence and are beamed downstream close to the jet axis (see [61,62] for more details). Ray theory assumes that only the real part of the pressure contributes to the noise created and so under-predictions at low polar angles occur. The edge of the cone of silence, θ_{cos}, and therefore the minimum polar angle that ray theory will give accurate results for, can be calculated using the following expression [63].

$$\theta_{cos} = \sin^{-1}\left(\frac{c_0}{U_J + U_f + c_J}\right) \tag{2.3.18}$$

where U_J is the maximum velocity in the jet, U_f is the flight-stream velocity and c_J is the speed of sound at the nozzle exit. For the static conical nozzle at a jet Mach number of 0.6 that is studied in Chapter 4, $\theta_{cos} = 38.9°$. Increasing either U_J or U_f will reduce θ_{cos}. It should be noted that the edge of the cone of silence is not a definite point, but rather a region where the physics changes. Therefore, analysis in this thesis is conducted above $\theta = 50^0$ to ensure that there are no cone of silence effects within the experimental data. Lilley [64] found that by this polar angle, there was a minimal influence of cone of silence on the far-field mixing noise.

The assumptions and limitations of ray theory are outlined below.

- The acoustic source is compact which means that the wavelength of the acoustic wave is small compared to the variations within the flow. This means that ray theory is a high-frequency approximation.
- For high frequencies, the wavelength is small enough that the flow can be considered as being a uniform mean flow.
- Rays are considered as spherically spreading plane waves.
- Ray theory is not capable of capturing the effects within the cone of silence.

2.4 Literature review of noise modelling

So far, an understanding of the problem that jet noise poses to those around airports has been gained, as well as mathematical descriptions of how fluids behave and how the jet mixing noise can be modelled. The next step is to understand the different ways that previous researchers have used simulation techniques to predict jet noise. With over sixty years of research into aeroacoustics, there is a vast amount of literature available, so a summary is presented here. This will be split into three investigations: an investigation into jet mixing noise, how the jet mixing noise is changed by the pylon and the additional noise sources of an installed jet.

2.4.1 Jet mixing noise

Before looking at the noise models that have been developed over the years, it is worth taking a bit of time to understand some of the common simplifications that are used to generate noise predictions. These include splitting the noise into its self and shear components, modelling the fourth-order correlation function as a sum of second-order components and the use of Gaussian functions to approximate those second-order functions.

The idea of splitting the mixing noise into the self (that which comes from the turbulence alone) and shear noise (which comes from the turbulence and mean shear flow) was originally proposed by Ribner [65]. Ribner showed that the self noise has nine non-zero components which make up the quadrupole directivity for individual eddies within an axisymmetric jet. As each quadrupole is oriented randomly, the overall effect is a uniform directivity to the whole jet mixing noise. At $\theta = 90^\circ$, only the self noise is present as there is no shear. Away from this polar angle, the shear noise contributes to the overall directivity of the jet as shown in Figure 2.4.1. This directivity does not include the effects of convection or refraction, which were accounted for separately. Ribner showed good agreement with experimental data outside of the cone of silence when $\theta \geq 40^\circ$.

Experimental data is often quoted as a pressure squared term, which having squared Equation 2.3.11, will generate a fourth-order correlation term, $\frac{\partial^2 T_{ij}}{\partial \tau^2}\frac{\partial^2 T_{ij}}{\partial \tau^2}$.
Batchelor [66, 67] found that the fourth-order correlation function could be modelled as a sum of second-order components. This ignores the non-linear effects that arise

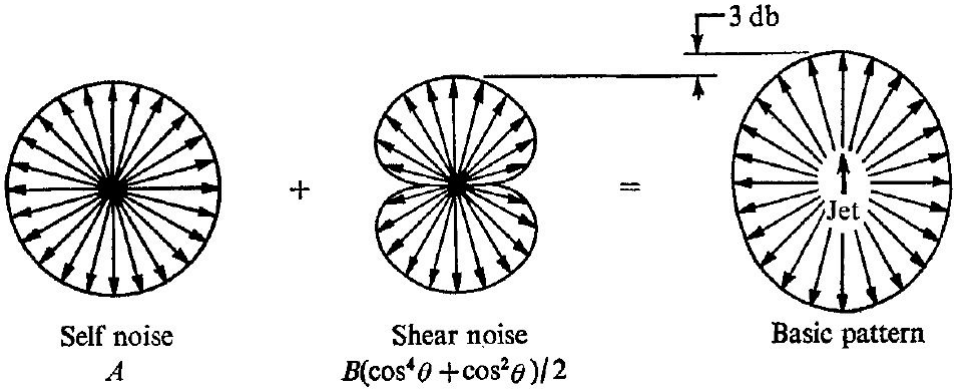

FIGURE 2.4.1: Directivity of self and shear noise without convection or refraction (Diagram from Ribner [65]).

from the triple-velocity correlations, but as Batchelor noted, these non-linear effects only dominate for the smallest eddies which contain little energy. Therefore, this approximation is valid for the energy-containing region of the jet.

The next step is to determine mathematical models that can be used for the second-order components. Ribner [65] showed that the second-order components were independent of each other in terms of space and time. Therefore, separate functions can be used to model the spatial and temporal decay of eddies. The most commonly used functions are Gaussian [51, 68, 69] which have been found to match experimental data [52]. The exact form of the Gaussian function varies between authors depending on the assumptions or simplifications that each researcher uses. However, it should be pointed out that the magnitude of the overall pressure field, and therefore the value of any calibration constants, is dependent on the choice of Gaussian function.

Now that some of the common aspects of different mixing noise models have been explored, attention can be turned to those models. With seventy years of research into this area, several different noise models are outlined in the literature. The main differences between them are what assumptions and simplifications are used to determine the right-hand side of Lighthill's equation (Equation 2.3.5). One of the limitations of Lighthill's equation is the fact that the refraction effects that take place within a jet, are not explicitly defined. An alternative formulation of Lighthill's equation was proposed by Lilley [70], who rearranged the mass and conservation equations to obtain a new wave equation with the refraction effect included within the

propagation operator. Due to the complex nature of the Lilley equation, this is not widely used. One successful application of Lilley's equation is in the MGBK method.

The method referred to as the MGBK method, was developed by Mani, Gliebe and Balsa [71] in the 1970s with improvements being made later on by Khavaran [72]. Lilley's equation is solved for a point source in an axisymmetric jet being convected by the flow using a high-frequency Green's function. Shielding coefficients, which depend on the case being studied, are used to model the refraction effects. The jet is assumed to be parallel and so the refraction effect can be modelled as the velocity and temperature profile only varies in the radial direction. The advantage of this method is the fact that different flow conditions or source terms like source compactness, different correlation functions, refraction and shielding effects can be investigated for both subsonic and supersonic flows [68]. However, the MGBK model also assumes that the jet is axisymmetric and so is of limited use for realistic jets.

Another method was proposed by Tam [73–75] when Tam noticed that he could split the experimental spectra of jet mixing noise into a summation of large and fine-scale turbulence. The fine-scale turbulence was found to dominate at high polar angles. Tam developed a semi-empirical prediction method based on kinetic gas theory for the fine-scale noise based on input data from a k-ϵ RANS model. Three empirical coefficients were found; the length and time scale coefficients and a kinetic energy constant for the fine-scale turbulence. The jet was divided up into slices every 0.5 diameters to work out the volume integral. Analysis was conducted on a large range of subsonic jet conditions and nozzle geometries which covered all known operating conditions during flight. Tam's method provided good agreement for both the symmetric and a few asymmetric jets, apart from at high frequency due to the high-frequency cut-off of the microphones. Morris and Farassat [76] analysed Tam's method and found that it was identical to Lighthill's Acoustic Analogy at $\theta = 90^\circ$ if an isotropic turbulence model was used.

A more general approach was taken by Goldstein [77] by solving linearised Euler equations. The Reynolds stress terms were then included in the source terms. Within his analysis, Goldstein assumed the jet was axisymmetric rather than the more restrictive assumption of isotropic turbulence that Ribner used. This allowed for the

anisotropy of the jet to be modelled. The details of anisotropy will be discussed shortly.

So far, several different acoustic models have been introduced which differ in how they treat the source term on the right-hand side of Lighthill's equation. The difference between these models was the focus of the work by Samanta [78] who found that models which explicitly modelled the propagation effects, like Goldstein's model, provided more accurate predictions than simpler models. Samanta showed that the simpler models were more sensitive to errors within the large-scale structures, while similar predictions were made between all models studied at high frequencies. He concluded by saying that more analysis was needed for heated and complex jets.

While a lot of work has focused on single-stream jets, coaxial jets offer an increase in propulsive efficiency and so are used for modern engines. One method of predicting the noise of coaxial jets was proposed by Fisher [38] and developed the work of Ko and Kwan into an acoustic model called the 4-source model. For an isothermal coaxial jet, Fisher found that the noise could be modelled as a superposition of single jet noise spectra, confirming what Ko and Kwan thought. Four regions, or sources, were identified and are as follows:

- The noise from the ambient shear layer in the initial region. This has the same flow characteristics as the initial region for a single stream jet using the secondary nozzle diameter and flow velocity.
- The noise from the primary shear layer in the initial region. It should be noted that although this is a source of noise, it is sometimes neglected as the secondary to ambient shear layer is the dominant noise source for certain applications (e.g. UHBR engines).
- An effective jet from the interaction region.
- The noise from the mixed flow region can be modelled as a single stream jet characterised by a mixed velocity and diameter which take into account the area and velocity ratios of both nozzles. This region is primarily responsible for the low-frequency content of the jet noise spectra.

When modelling the noise from the interaction region, the effective jet was found to use a lower turbulence level than was typical for single jets (10% instead of 15%). This

is due to a change in flow conditions at the end of the potential core of the primary jet. Overall, this causes the noise in the interaction region to be under-predicted but is compensated by an additional contribution from the mixed flow region. In general, good agreement to within 1dB was found with experimental data, but it was noted that at low polar angles and high-velocity ratios, there was an under-prediction at high frequency. This was thought to be due to the large change in velocities that occur between the primary jet velocity and fully mixed jet velocity which does not occur for single stream jets. Fisher [40] later extended his analysis to look at a heated primary stream. A change in the noise level in the interaction region was put down to the density variations within a heated jet giving rise to a dipole-like term. This dipole term scales with jet velocity differently to the quadrupole mixing noise. Therefore, an attenuation factor was required to change between having a quadrupole and dipole-dominated field. The noise in the secondary shear layer and fully mixed regions did not need to be changed for the heated case. Again, a match to within 1dB was found with experimental data. Further work on the 4-source model was carried out by Bryce [79] who looked into in-flight predictions using static data. The in-flight predictions were achieved by modifying the spreading rate of the secondary jet which meant that expensive in-flight testing was not needed for preliminary designs.

The work by Fisher and Bryce has shown that despite coaxial jets being more realistic than single-stream jets, the simplification of the situation can still provide useful insight into the complex problems of jet noise predictions.

The models mentioned previously require information about the turbulent nature of jets which is often extracted from numerical simulations. Due to the lack of computing power, until recently, as Lilley [64] pointed out, researchers have often turned to RANS simulations for this data. As early as 1976, RANS was used as the input for calculations in the MGBK method by Mani, Gliebe and Balsa [71] and Khavaran [72]. Both Béchara [80] and Bailley [81,82] used k-ϵ RANS simulations to analyse subsonic and supersonic jets. Ribner's model was compared against Goldstein's model and it was found that similar predictions could be made at $\theta = 90^{\circ}$, but Ribner's model over-predicted the noise in the rear arc. This was attributed to the improvements in the turbulence modelling within Goldstein's model.

Morris [83] used a hybrid k-ϵ RANS and acoustic model to look at an isothermal

axisymmetric jet. He found that the convective amplification effect, where the relative source motion to the observer is important, was only true if a Gaussian model was used for the space and time correlation functions. Morris assumed that the length scale of an eddy was independent of frequency, however, does present an alternative method for a frequency-dependent length scale. This second model gave nearly perfect agreement with experimental data at $\theta = 90^\circ$ while the model with a length scale independent of frequency under-predicted the high frequency. Morris concluded that the high-frequency predictions are, therefore, sensitive to changes in the modelling of the source statistics.

Ilario [21,84] developed a novel method called Lighthill's analogy with Ray Tracing (LRT). A RANS CFD model was used to provide the mean flow inputs to an acoustic ray tracing model. Good agreement was found with experimental data for a large range of single and coaxial engines. It was shown to provide better predictions than the MGBK method, especially at high polar angles. The results were only applicable outside of the cone of silence due to the limitations of the ray tracing method.

Given the advancements in computational power and simulation techniques in the last couple of decades, more detailed analysis can be undertaken on the flow field. Within a jet, the axial component of the flow is dominant over the transverse components. This causes eddies in the shear layer to be stretched along the jet axis, as seen by Townsend [85] and is called anisotropy. Given that the shear is the greatest close to the nozzle exit where the shear layer is the thinnest, high-frequency eddies are more affected than larger eddies which occur further downstream. The stretching of eddies causes the axial length scale, L_1, to become greater than the transverse length scale, L_2, and so a ratio between the two is defined as $\Delta = \frac{L_2}{L_1}$. This stretching also causes the turbulent fluctuations in the axial and transverse directions to change and so this is taken into account with the expression $\beta = 1 - \frac{\overline{u_2^2}}{\overline{u_1^2}}$.

Due to anisotropy mainly influencing the fine-scale turbulence which has little energy, RANS models based on the Boussinesq hypothesis assume that the turbulence is isotropic as this will be the case for the large energy-containing structures of the flow. Therefore, the stretching of the eddy and the change that this introduces to the mixing noise directivity is ignored. The question that must now be asked is, how much does this influence noise predictions?

Proudman [86] was one of the first to consider how an isotropic turbulence model would be applied to jet noise. As Proudman found that the power output of a jet was not critically dependent on the correlation function used, he concluded that the assumption of isotropy could be applied to jets, but should only be used to give a rough estimate of the order of magnitude of acoustic noise. This was confirmed by Lilley [64, 87] for both cold and hot jets.

However, not all authors have assumed isotropic turbulence. Almeida [88] noted that neglecting the impact of anisotropy has very little impact on the magnitude of shear stresses which dominate the mixing process and hence will have little impact on the magnitude of turbulence and noise generated. Therefore, a rough estimation can be found using an isotropic model. Almeida also noted that the anisotropy changed through the jet but there is a lack of mathematical and experimental investigations to implement a more accurate description of anisotropic turbulence.

Khavaran [48, 49] also studied the influence of anisotropy on jet noise using a RANS simulation with a k-ϵ turbulence model to provide the input to a source model based on Lilley's equation. Although both self and shear noise were modelled, the shear noise was found to have a greater impact at lower values of θ. Khavaran selected values of 0.4 and 0.5 for β and Δ, respectively, which were assumed to be constant across the whole jet. He noted that, although decreasing Δ reduced the noise intensity, increasing β had a much larger effect. The overall effect of anisotropy was to increase the noise produced by about 5dB across all polar angles. This increase was, however, sensitive to the values of β and Δ that were chosen. Khavaran concludes by saying that, although an anisotropic model would be ideal, an axisymmetric model with constant β and Δ values may be accurate enough for most applications.

Jordan and Gervais [89] included the inhomogeneous and anisotropic effects of turbulence within their analysis by adapting the spatial and temporal correlation functions. Unlike other authors who only considered the effect of anisotropy on the length scales, Jordan split the time scale into its axial and radial components to better match experimental data. A rough factor of two was found between the two. Jordan found that an anisotropic turbulence model reduced the characteristic length scales in both the axial and radial directions over which the turbulence is correlated. The reduction in correlation also led to the shear noise efficiency decreasing with the

anisotropic model. This means that an isotropic model will likely over-predict the noise from the shear noise source. On the other hand, the self noise was seen to increase in magnitude when anisotropy was introduced. The self noise was, therefore, shown to be dependent on the intensity of turbulence as opposed to the spatial extent of correlated turbulence for the shear noise. This changed the proportions of noise from each source, with the self noise becoming more dominant. Good general agreement was found with experimental data but the model did not include acoustic to hydrodynamic interactions, leading to a poor agreement at high frequencies and low polar angles. Jordan and Gervais concluded by saying that the assumptions of isotropy and homogeneity of flow are an oversimplification of reality.

Self [90] developed a jet noise model based on Lighthill's Acoustic Analogy but decided to include frequency-dependent length and time scales. The flow anisotropy was modelled with different length scales parallel and perpendicular to the jet axis. Only the self noise term was modelled to avoid the flow-acoustic interaction of the shear noise term. Due to this limitation, predictions were limited to $\theta = 90^{\circ}$. Self used a moving-axis time scale which was dependent on frequency to better model the characteristic length and time scales. This is different to other authors who assumed these scales are independent of frequency. The reason for doing this was to better match experimental data gathered by Harper-Bourne [51]. Harper-Bourne showed that the low-frequency length scale was independent of frequency but there was an inverse dependency on frequency for higher frequency length scales. Self also pointed out that the high frequencies see a uniform shear as they are small compared to the shear layer width. On the other hand, the large-scale turbulence is limited by the shear layer width and so decays more rapidly. A good match was found with experimental data from the EDSU database for single stream jets and demonstrated the improvement of using a frequency-dependent length scale within the model.

The study of jet mixing noise is a complex and not fully understood subject as evident above. Different authors have proposed variations of models to overcome the limitations of other methods. Some of these limitations have been necessary in the past due to computational limits, however, with more computing power available, researchers can now start modelling more complex geometries.

2.4.2 Changes to the jet mixing noise caused by the pylon

All the jets studied in the previous section were axisymmetric. Although these simple geometries are useful to understand the underlying mechanism of jet mixing noise, realistic civil aircraft engines are asymmetric. This is because the pylon attaches the core of the engine to the wing and so blocks part of the flow through the nozzle (see Figure 2.4.2). Hence the flow and noise become asymmetric. The question that now arises is how much does the mixing noise change due to the pylon? This area of research is often referred to as Propulsion Airframe Aeroacoustics (PAA) within the literature. A lot of research in this area has focused on coaxial pylon jets. Thus, it is not clear what effect such a blockage has on the primary-to-secondary compared to the secondary-to-ambient shear layer. Given that the secondary to ambient shear layer is dominant for UHBR engines, which is the focus of this work, it is believed that the trends seen for a single-stream pylon jet will be relevant.

The main change to the flow field that is introduced by the pylon, or bifurcation, is the introduction of a wake (low-pressure region) behind the pylon tip causing the jet to be drawn towards the pylon (a "rooster-tail" flow field). This has been seen experimentally by Doty [91] and in CFD simulations by Vuillot [92], Hunter et al [93] and Massey [94]. Vuillot showed that the pylon wake redistributed the turbulent energy of the jet, with twice the amount of energy behind the pylon as in the shear layer on the opposite side. This effect was also noted by Hunter et al [93]. Furthermore, the pylon only affected the flow field within the first ten diameters of the nozzle exit and "jump-started" the mixing process. He noted that the pylon induced counter-rotating streamwise vortices which would explain the extra mixing effect present near the nozzle exit. This resulted in higher turbulence and noise levels close to the nozzle exit but a reduction downstream. The overall effect is, therefore, a reduction in noise from the whole jet.

Acoustically, the change in the distribution of the turbulence within the jet will create an azimuthal variation in the jet mixing noise. Figure 2.4.2 has been included to remind the reader of how the azimuthal angle is defined relative to the pylon. The increase in turbulence behind the pylon seen in the CFD simulations will cause an increase in noise at $\phi = 0^\circ$ while observers at $\phi = 180^\circ$ will be shielded by the jet and so see a noise reduction. This is similar to non-concentric jets [95].

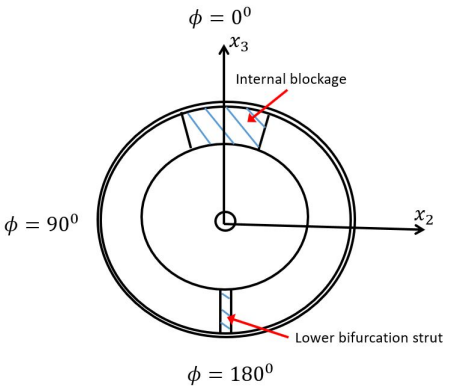

FIGURE 2.4.2: Diagram of azimuthal angles relative to the blockage from the pylon.

The azimuthal variation in real jet geometries was noted by Viswanathan [18]. He found that engine power, engine angle and aircraft speed altered the directivity of noise. When the secondary stream was seen to dominate (i.e. when the area or velocity ratios were high between the secondary and core flows), Viswanathan found there was no azimuthal variation. However, when the velocity and area ratios were low, there was an increase of around 3dB at low polar angles. In these conditions, the primary flow would be the dominant noise source. When compared to an axisymmetric jet, it was noted that the pylon reduced the noise at small polar angles between 2 and 4dB while a 2dB increase was seen at higher polar angles. Therefore, it is important not to view the pylon as simply a noise-reducing component as it redistributes the noise. Similar trends were observed going in-flight, although the absolute levels again changed with velocity and area ratios. This work highlights the fact that the influence of the pylon on the mixing noise can vary drastically as the geometry and operating conditions are changed.

Zaman [95,96] studied the impact of the pylon on static jets. He split his analysis into two parts: one looking at the effect of the internal blockage of the pylon and the second into the effect of the external pylon fairing. A substantial decrease, of around 5dB, was seen in the Overall Sound Pressure Level (OASPL) at the sideline and fly-over positions at low polar angles when the internal blockage was included. There was virtually no change in the forward arc. The external pylon was seen to have a negligible impact on the results, possibly due to only static tests being carried out. Zaman also found that changing the nozzle changed the impact of the internal pylon on the far-field results. It was thought that the change in flow lines from straight in a conical case to converging with an annular nozzle was the cause, however, further

analysis was required to be certain. A noise reduction was generally seen at $\phi = 180°$ and low polar angles.

Ilario [21] found that the modification of the flow field by the pylon caused an increase in the attenuation of sources at $\phi = 90°$. This was particularly strong for the high-frequency noise at low angles outside of the cone of silence. An increase in noise was seen at high polar angles at the sideline. Despite a high-frequency cut-off at 5kHz due to starting the computational domain at the end of the pylon, Ilario showed that his novel method predicted the mixing noise below this limit well.

As seen above, the amount of change in mixing noise introduced by the pylon is subject to contention in the literature. Looking through more literature, Bhat [97] reported that more noise was generated at the sideline position and in the rearward arc. This was true for static and in-flight cases. Azimuthal variation of up to 3.5dB was found. Similarly, White [20] found an increase at the sideline position by 1-1.5dB but a decrease in peak Perceived Noise Level (PNL) by 1dB at the fly-over position. The largest decrease in noise was found at low polar angles. The azimuthal variation that Bhat and White saw was not seen, however, by Thomas [14] who found very little azimuthal variation but did see that the pylon reduced the mixing noise by 1EPNdB overall. Another set of experimental data by Meloni [98] found that the pylon created an increase in noise in the forward arc at the fly-over position.

Part of the reason for the variation in results could come from the different ways in which authors report experimental results. It is not clear if Zaman and Thomas corrected their results for the change in the flow area introduced by the pylon. Therefore, it is difficult to discern if the change in noise is a geometric effect of the pylon or simply due to a difference in flow area and thrust. Meloni acknowledges this point but does not correct for it due to not being certain of the correct way of doing so. On the other hand, Bhat accounted for this by producing geometries with the same flow areas but different nozzle diameters. All the authors mentioned in this section also present results in terms of frequency rather than a non-dimensional Strouhal number. This makes the comparison between different authors' results extremely difficult as either one or neither of the axis of data have been corrected for flow area variations.

Despite the variations in how results are reported, it is thought that this will not account for all the variations seen in results in the literature. The sensitivity of the pylon to small changes, as suggested by Papamoschou [99], is dependent on the repeatability of experimental test runs while the wear and tear or material defects [100] may also play a part. Furthermore, Tam [101] suggested that the large scales of turbulence, which have dimensions comparable to the mean flow, are dependent on the specific flows generated by each geometry. Therefore, by the nature of authors looking at different nozzles, a variety of results are generated.

More research is required to understand the change in the jet mixing noise caused by the pylon blockage. The eventual goal is to be able to look at the change in mixing noise in a closely installed case where Semiletov [102] noted that there was a large increase in the turbulent kinetic energy due to the interaction of the pylon and wing. The ability to predict the jet mixing noise of the installed jet will allow a more detailed analysis of the more prominent jet surface interaction noise source for installed geometries.

2.4.3 Jet-surface interaction and jet-surface reflection

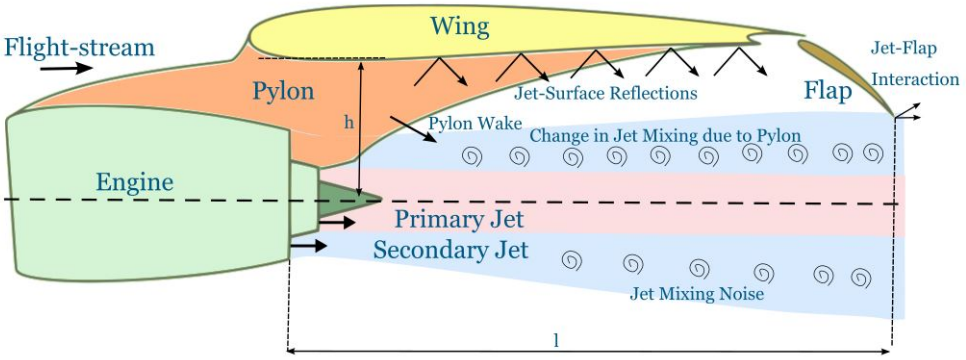

FIGURE 2.4.3: Diagram showing the geometry and acoustic sources around the engine.

Much of the research over the past seventy years in aeroacoustics has focused on the jet mixing noise of isolated jets. However, the solid surfaces close to the jet introduce two additional noise sources; Jet-Surface Reflections (JSR) from the wing and Jet-Surface Interaction (JSI). As the focus of this thesis is on the mixing noise of jets, a summary of these noise sources and how they can be modelled will now be given.

JSR is caused by waves being reflected off solid surfaces, like the wing and flaps, before the wave is propagated to the far field. Given the shear layer width is small under the wing, the high frequencies generated here are the most affected and so the JSR is primarily a high-frequency effect. Looking at an example of an installed spectra in Figure 2.4.4, one can see a constant increase in the installed spectra above the isolated spectra at high frequency. This is due to the JSR. The increase is due to a mirror-image source being created by the wing, and so there is a theoretical maximum increase in noise of 3dB. The pylon will create some additional reflective noise, primarily at the sideline, but this will be limited to higher frequencies than the reflected noise from the wing. As the contribution of the reflections from the wing will be most prevalent directly below the wing, where the public is, this is the primary reflective source studied. Due to the simplicity of modelling reflections, most of the research on installed jet noise has focused on the JSI noise source.

The JSI noise source is caused by the interaction of the near-field pressure fluctuations interacting with solid surfaces. In the near-field of a jet, pressure fluctuations are generated which decay exponentially. These fluctuations do not contribute strongly to the isolated far-field mixing noise. However, when a surface with a sharp trailing edge is introduced, these near-field pressure fluctuations can be scattered more efficiently to produce a large contribution to noise at low frequencies. This can be seen in Figure 2.4.4. If the noise generated in this way comes from the flap rather than the wing, it is called Jet-Flap Interaction (JFI) noise. Although the JSI noise source is not modelled within this work, it is important to understand the influence of the JSI on installed noise spectra. Lawrence [103] studied the effect of wing position on installed jet noise. He varied the vertical, h, and horizontal, l, distance to the wing trailing edge in a parametric study, as defined in Figure 2.4.3. Lawrence found that decreasing h led to an increase in the peak amplitude and frequency of the JSI noise. However, up to 15dB variation in noise was seen in the JSI when l was varied. Although the absolute levels of JSR noise were found to be dependent on the wing position, especially the horizontal distance l, it was found to be independent of jet Mach number.

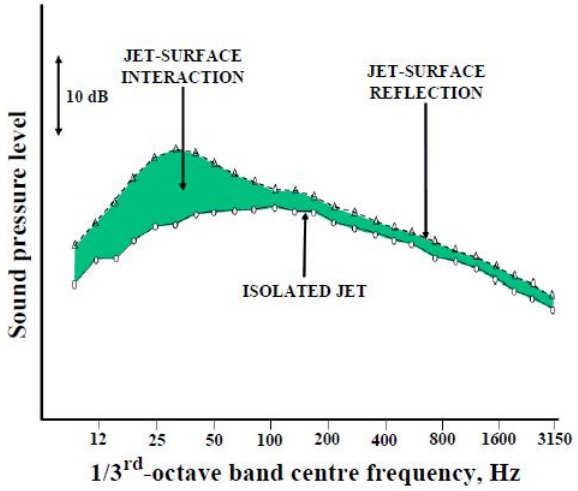

FIGURE 2.4.4: Installed jet noise spectrum at $\theta = 90^o$ (Diagram from Lawrence [103]).

Early work on installation noise was carried out by Curle [45] and Ffowcs-Williams [46]. Curle extended Lighthill's analogy to show that a stationary solid boundary acts on the flow to cause a dipole term to arise in addition to the quadrupole jet mixing noise term. The dipole term becomes increasingly important as the jet velocity decreases. The acoustic power of these dipoles was found to vary as U_j^6 whereas the mixing noise from isolated jet varies as U_j^8. Ffowcs-Williams extended Curle's work to account for the flight-stream past the solid surface. Later on, Amiet [104] used the pressure on the surface of an airfoil to derive a method for scattering the dipole noise source from the trailing edge. The work by these three authors forms the basis for much of the work on simulating the JSI noise source. A few of these noise models for the JSI noise source will now be reviewed. The point of including these is to make the reader aware that the JSI can be modelled, rather than an in-depth study of the literature.

Using ray theory, McLaughlin [58] studied the installation effects of jets by modelling the wing as a flat plate. His model included a semi-empirical blockage model to deal with refractions of noise in hot jets caused by the temperature and velocity gradients. Although accurate predictions could be made on the cases studied, due to the semi-empirical nature of the model, there was some doubt over its applicability to other geometries. Lyu [105] proposed a semi-analytical model for installed jet noise which combined Lighthill's Acoustic Analogy for modelling the quadrupole mixing noise sources and a trailing edge scattering using Amiet's approach. The effects of the

mean flow refraction on the installed jet were not taken into account, so Lyu's model was only accurate at $\theta = 90°$. Good agreement was found with the isolated and installed results at $\theta = 90°$. Lyu demonstrated the low-frequency enhancement that the jet-flap scattering introduces to the noise spectrum was predicted well by his model. Building on Lyu's work, Dawson [106] used near-field experimental data to predict the far-field JSI of in-flight installed model jets. Good agreement between the model and experimental data up to a flight Mach number of 0.2. Dawson's model was also seen to account for the decrease in JSI seen as θ increased. However, a consistent under-prediction of the high-frequency noise was seen in the forward arc as the JSR noise source was not modelled.

The literature reviewed in this section has shown that numerical models exist which can be used to predict the individual noise sources of the jet mixing and the JSI. It is assumed that each noise source is independent of the others. Within the literature, there are a variety of models available for each noise source which differ in the assumptions that have been used to derive them. Although isolated axisymmetric jets are well understood, the variation in reported results for isolated asymmetric jets would suggest a change in the underlying physics. More work is, therefore, needed to understand how current models need to be adapted to predict isolated asymmetric jets. As the pylon will affect the flow, and therefore noise, generated close to the wing, it is important to be able to understand and then model this. This is the focus of the work in this thesis.

2.5 Summary of chapter

In this chapter:

- The background to turbulence and how fluid flows are modelled have been outlined.
- The structure of jets has been described.
- The fundamental equations for modelling the acoustics of jets have been derived.
- A literature review of jet mixing noise modelling, the change in the mixing noise with the introduction of the pylon, JSI and JSR noise sources has been conducted.

Chapter 3

LRT Methodology

The work in this thesis is a continuation of work done by Ilario [21] and Rosa [107]. Ilario [21] developed a hybrid method called Lighthill's analogy with Ray Tracing (LRT). It relies on a CFD RANS calculation to work out the mean flow physics and then the acoustic field is calculated separately. This method was then extended by Rosa [107] to include the thermodynamic effect of heated jets by separating the momentum and enthalpy terms. In this current work, the enthalpy term has been neglected as analysis is only being undertaken on cold jets.

Within the LRT method, several assumptions are made and are outlined below.

- An infinite flight-stream is assumed to exist between where a ray exits the acoustic domain and the far field.
- When $M_f > 0$, the free-stream flow is in the same direction as the jet stream (i.e. the aircraft is moving forward) and is parallel to the jet axis (i.e. the angle of attack (AOA) of the engine is 0°).
- Jet mixing noise and jet surface reflective noise are the only noise sources that are modelled. Other noise sources may be present (e.g., vortex shedding or jet surface interaction) in experimental data, but are not modelled.
- There is no noise generated inside the nozzle.

For reference, the co-ordinate system used in this thesis is repeated below. It should be noted that $0 \leq \theta \leq \pi$ and $0 \leq \phi \leq 2\pi$.

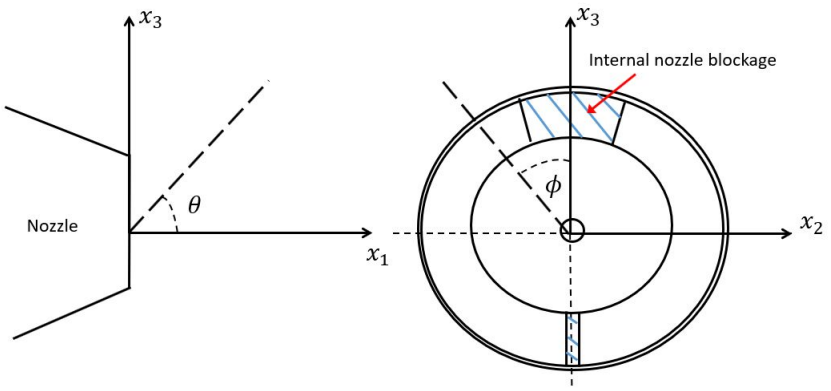

FIGURE 3.0.1: Diagram showing the co-ordinate system used. The jet axis is aligned with the x_1 axis.

3.1 Mathematical modelling

3.1.1 Numerical procedure

An overview of the methodology of LRT can be seen in the block diagram in Figure 3.1.1. The geometry is exported into a software called Pointwise used to produce the CFD mesh before it is run using ANSYS Fluent. After the CFD simulation has converged, an orthogonal grid with constant spacing is generated. The CFD data are interpolated onto this orthogonal grid. Acoustic source points are generated from which the ray tracing is performed. The ray tracing code used in this thesis has been developed previously at the University of Southampton. With the results of the ray tracing, the source equation that will be derived in Section 3.1.4 is used to calculate the Sound Pressure Level (SPL). More detail on each of these steps will now be given in this chapter.

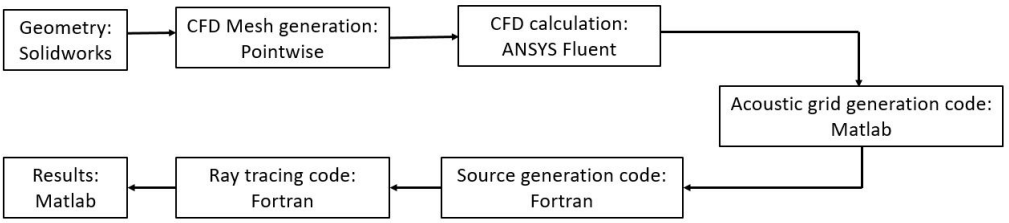

FIGURE 3.1.1: Work flow of the LRT method.

3.1.2 CFD model

This section describes the CFD setup for each of the geometries that have been studied in this thesis. CFD meshes have been generated using Pointwise V18.4. In all simulations, ANSYS Fluent 19.1 has been used to calculate the mean flow data. The CFD model has a domain size of 50 x 20 x $20D_J$ downstream of the nozzle exit. It was found that an extra-long section ($10D_J$) of the nozzle was needed before the nozzle exit for a turbulent boundary layer at the nozzle exit to be achieved. As most of the mixing noise is generated within the first $20D_J$, the domain is sufficiently large to capture most of the mixing noise.

Details of the CFD meshes and their quality can be found below in Table 3.1. The average aspect ratio and maximum centroid skewness values have been collected from the structured parts of the meshes only. Some of the meshes in Table 3.1 have an average $y^+ \approx 1$, while others have a $y^+ \approx 35$. The meshes with a $y^+ \approx 1$ were made by a consultant to the ISVR and were designed so that LES could be run on them if it was thought necessary. These fine meshes used a structured grid within the jet and an unstructured grid outside of this to help reduce the mesh size. This is the reason for the coarse mesh for the annular nozzle having more grid points than the fine mesh.

To reduce the complexity of the mesh in the annular nozzle, the three internal struts that hold the bullet in place were removed. As the struts are thin and aerodynamically shaped, it was thought that their impact on the flow field would be minimal. Part of the mesh for the annular nozzle can be seen in Figure 3.1.2.

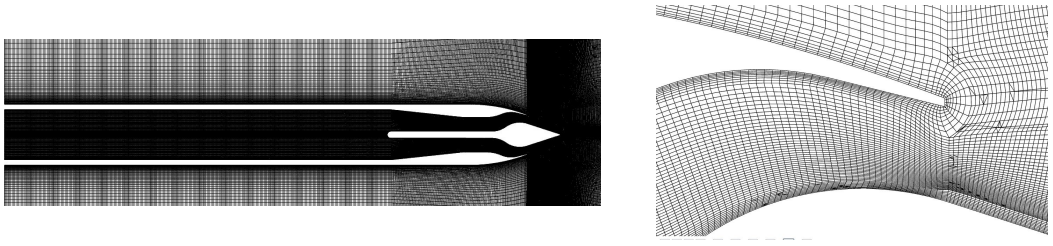

FIGURE 3.1.2: Diagram of the CFD domain inside the annular nozzle (left) and at the nozzle exit (right) in the x_1-x_3 plane

Although the use of structured grids enables fast run times for simulation, the complex geometry of asymmetric nozzles means that this is a time-consuming process to generate the mesh. The solution is to use an unstructured region of mesh around complex geometric features. Dippold [108] studied the impact of unstructured grids

on jet plume development. He discovered that structured grids in the jet plume more accurately predicted the velocity and turbulence profiles than unstructured grids.

Geometry	Average y^+	Cell count (million)	Average Aspect ratio	Max centroid skewness (Majority<0.8)
Conical	35	17.7	3.7	0.44
Isolated Annular (coarse)	35	22.4	7.3	0.68
Isolated Annular (fine)	1	18.4	9.62	0.47
5% Internally Blocked	35	15.8	4.4	0.45
10% Internally Blocked	35	16.7	3.27	0.76
10% Externally Blocked	1	24.5	9.80	0.77
20% Internally Blocked	35	15.0	3.49	0.34
Installed Annular	35	30.7	7.53	0.47
Jet-pylon-wing	1	27.5	9.1	0.77

TABLE 3.1: CFD mesh size and quality.

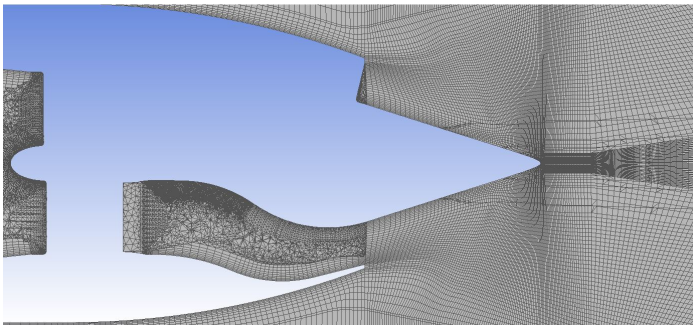

FIGURE 3.1.3: Diagram of the CFD domain of the 10% internally blocked nozzle in the x_1-x_3 plane.

Unstructured grids could be used outside the jet plume to enable a reduction in the computational cost of the simulations without loss of accuracy. Unstructured grids in the jet plume led to an under-prediction of the thrust and momentum of the jet, even if

the mesh was significantly refined. Therefore, in this thesis, an unstructured grid has been used inside the asymmetric geometries while a structured grid is used externally. An example grid near the nozzle exit of the 10% internally blocked nozzle can be seen in Figure 3.1.3.

Having generated the above meshes, the flow solution could then be calculated. ANSYS Fluent 2019 was used as the CFD solver. A density-based solver, with a k-ϵ turbulence model employing the coefficients found by Thies and Tam [25], was used. Thies and Tam found that by changing the model coefficients within the k-ϵ model, a better agreement could be found between CFD simulations and experimental data. More detail on this will be given in Chapter 4. Second-order schemes were used to model the flow, kinetic energy, and dissipation rate. The pressure at the nozzle inlet was matched to that set in the experiment to achieve the correct acoustic Mach number (M_J) at the nozzle exit. Two acoustic Mach numbers are studied in this thesis, $M_J = 0.6$ and 0.8, which give a Reynolds number ($Re = \frac{\rho U_J D_J}{\mu}$) of 0.56 and 0.74×10^6. This is where ρ is the density of the fluid, U_J is the maximum velocity in the jet, D_J is the jet diameter and μ is the dynamic viscosity. Therefore, the jets are fully turbulent.

The pressure values at the flight-stream inlet boundary condition were found using the isentropic flow relations and a small temperature difference of 2K between the jet and the free-stream inlets was used. To help with convergence, a small flight-stream Mach number ($M_f = 0.005$) was applied at the free-stream boundary of the CFD domain for any static cases reported in this thesis. All CFD simulations were run until the residuals were reduced by at least two orders of magnitude and when no change was observed in the velocity and TKE profiles.

3.1.3 Acoustic grid and source generation

Having determined the flow field of a particular simulation condition, the impact of the flow on the propagation of sound needs to be determined using a ray-tracing code. The ray-tracing code requires an orthogonal mesh and given that the CFD mesh is not orthogonal, an interpolation onto a new grid was needed using a Matlab script. For the simulations in this thesis, a grid of $400 \times 161 \times 161$ grid points was used over a domain of $40 \times 12.5 \times 12.5$ jet diameters (D_J) from the nozzle exit. The odd number of grid points in the x_2 and x_3 directions means that there is a grid point on the centre line of the jet. This gives a frequency range that the grid can capture up to 0.425-42.5kHz

which is within the 0.4-40kHz limit of the experimental data. A constant grid spacing was used in each direction. This was to speed up the ray-tracing calculation as the distances between grid points do not need to be calculated at each ray tracing step.

The final input needed for the ray-tracing code is the position of the acoustic source points from which rays will be released. Sources are distributed in radial rings down the jet based on the RANS data and concentrated within the shear layer. An example source distribution can be seen below in Figures 3.1.4 and 3.1.5. Here, 6,636 sources are distributed within the jet plume, whereas Ilario used 1700 in [84]. The original code distributed the first two rings of sources at 0.01 and $2D_J$ downstream from the nozzle exit. It was thought that this spacing was too big and so would not be able to capture changes in the flow field close to the nozzle exit, especially for asymmetric geometries. Source planes are now spread axially downstream based on a growth rate of 1.1 times the distance between the previous planes as far as $25D_J$ downstream of the nozzle exit. The first ring of sources is placed $0.01D_J$ from the nozzle exit. Some of the geometries studied in this thesis contain a centre-body "bullet" or pylon that protrudes into the acoustic domain. Any sources located inside the solid surfaces are, therefore, removed.

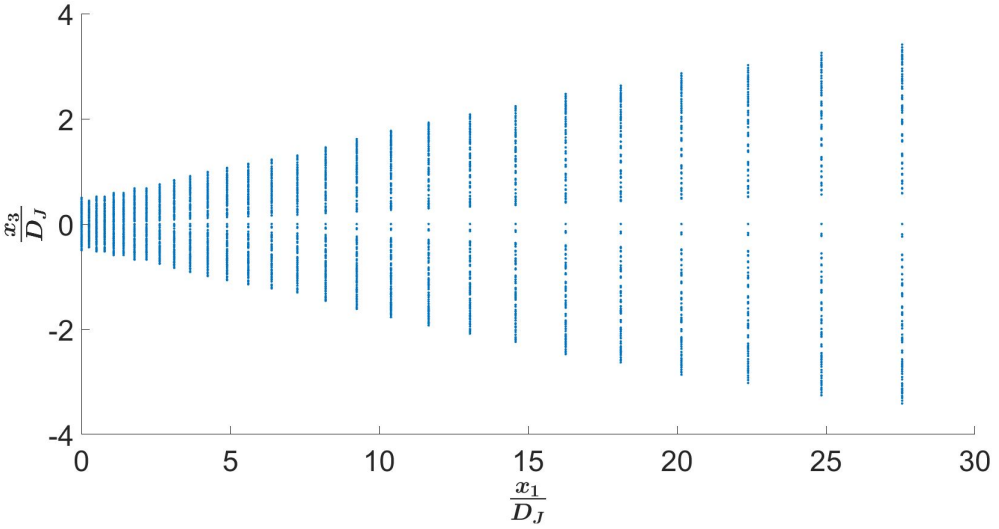

FIGURE 3.1.4: Sources are distributed down the jet and are concentrated in the shear layer.

The interpolated CFD data and the source positions are then used as the input to the ray-tracing code following the method shown by Pierce [60]. 655,000 rays are released from each source and traced to the far field where they are collected in bins. These

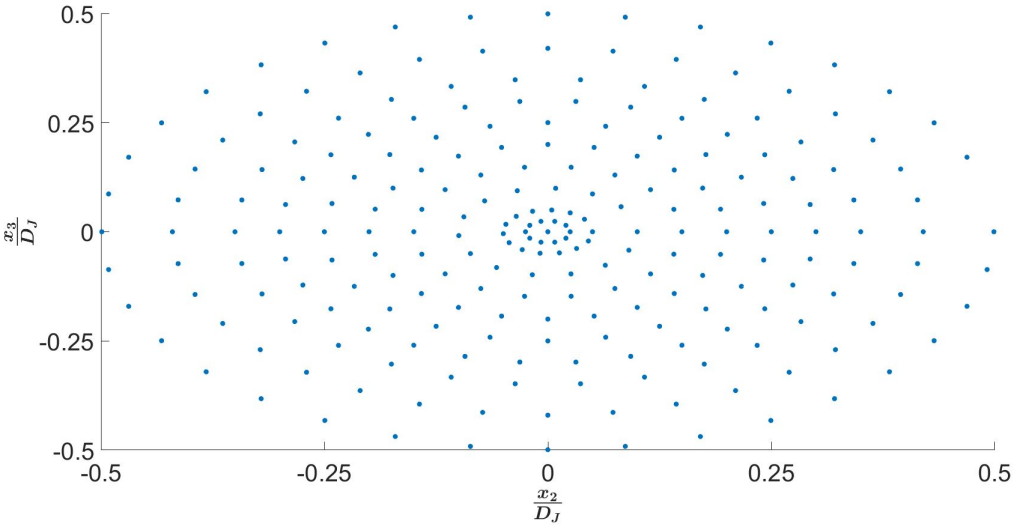

FIGURE 3.1.5: 1^{st} ring of sources.

bins are formed from a geodesic sphere consisting of 10,200 faces. The number of rays that are traced to each bin allows the flow factor Φ - a measure of flow-acoustic refraction - to be calculated. The source equation, which will be derived in Section 3.1.4, can then be used to compute the SPL as a function of frequency. Data is calculated for a Strouhal number range of 0.08-8.

3.1.4 Source equation of LRT

The LRT source equation is derived from Lighthill's equation. This section follows the derivation by Azarpeyvand [68] and is reproduced below. Starting from Lighthill's equation, the steps found previously between Equations 2.3.8 and 2.3.11 are used. For convenience, Equation 2.3.11 is repeated below.

$$p'(\mathbf{x},\tau) = \frac{1}{4\pi c_0^2}\frac{x_i x_j}{\mathbf{x}^3}\int_V \frac{\partial^2 T_{ij}}{\partial \tau^2}(\mathbf{y},\tau)\, d^3\mathbf{y} \tag{3.1.1}$$

where $\mathbf{x}$ and $\mathbf{y}$ are the observer and source locations, respectively, r is the distance from the source to the observer given by $r = |\mathbf{x} - \mathbf{y}|$, c_0 is the speed of sound in the far field, V is the volume of the jet, τ is the retarded time and T_{ij} is Lighthill's stress tensor. Any bold terms denote vector quantities.

The intensity in the far field, I, assuming spherical spreading, is then given by

$$
\begin{aligned}
I(\mathbf{x},t) &= \frac{1}{\rho_0 c_0}\overline{p'(\mathbf{x},\tau)p'(\mathbf{x},t+\tau)} \\
&= \frac{1}{16\pi^2\rho_0 c_0^5}\frac{x_i x_j x_k x_l}{\mathbf{x}^6}\int\int \frac{\partial^4}{\partial\tau^4}\overline{T_{ij}(\mathbf{y_A},\tau)T_{kl}(\mathbf{y_B},t+\tau)}\; d^3\mathbf{y_A}d^3\mathbf{y_B} \\
&= \frac{1}{16\pi^2\rho_0 c_0^5\mathbf{x}^2}\frac{x_i x_j x_k x_l}{\mathbf{x}^4}\int\int \frac{\partial^4}{\partial\tau^4}R_{ijkl}(\mathbf{y_A},\boldsymbol{\eta},\tau+\frac{\hat{\mathbf{x}}}{\mathbf{x}}\cdot\frac{\boldsymbol{\eta}}{c_0})\; d\mathbf{y_A}d\boldsymbol{\eta}
\end{aligned}
\tag{3.1.2}
$$

where ρ_0 is the density in the far field, $\hat{\mathbf{x}}$ is the position of the wavefront, $\boldsymbol{\eta}$ is the separation distance in the moving reference frame between two source locations, $\mathbf{y_A}$ and $\mathbf{y_B}$, and the over-bar represents a time-averaged quantity. Furthermore,

$$
R_{ijkl}(\mathbf{y_A},\boldsymbol{\eta},\tau+\frac{\hat{\mathbf{x}}}{\mathbf{x}}\frac{\boldsymbol{\eta}}{c_0}) = \overline{T_{ij}(\mathbf{y_A},\tau)T_{kl}(\mathbf{y_A}+\boldsymbol{\eta},t+\tau)}
\tag{3.1.3}
$$

where R_{ijkl} is Lighthill's stress correlation function in a frame of reference that moves with the eddy. This has used a transformation of coordinates with the expression $\boldsymbol{\eta} = \mathbf{y_B} - \mathbf{y_A}$. Taking the Fourier transform to convert into frequency space, Equation 3.1.2 becomes

$$
I(\mathbf{x},\omega) = \frac{\Pi_{ijkl}}{16\pi^2\rho_0 c_0^5 r^2}\int_{-\infty}^{\infty}\frac{\partial^4}{\partial\tau^4}\int_{\mathbf{y_A}}\int_{\eta}R_{ijkl}(\mathbf{y_A},\boldsymbol{\eta},\tau+\frac{\hat{\mathbf{x}}}{\mathbf{x}}\frac{\boldsymbol{\eta}}{c_0})e^{\mathbf{i}\omega(\tau-\frac{\hat{\mathbf{x}}}{\mathbf{x}}\cdot\frac{\boldsymbol{\eta}}{c_0})}\; d\boldsymbol{\eta}d\mathbf{y_A}d\tau
\tag{3.1.4}
$$

where $\mathbf{i} = \sqrt{-1}$, ω is the angular frequency and directivity of the jet is given by

$$
\Pi_{ijkl}(\theta,\phi) = \frac{1}{2\pi}\int_0^{2\pi}\frac{x_i x_j x_k x_l}{\mathbf{x}^4}d\phi
\tag{3.1.5}
$$

While Π_{ijkl} is a tensor, it has been shown by Khavaran [48] and Ilario [21] that the directivity of an axisymmetric jet can be linked to the intensity along the jet axis, R_{1111}. Each of the tensor components can be represented as a multiple of the R_{1111}. This is detailed in Appendix A.1. Thus, Π_{ijkl} becomes a scalar component and the indices will be dropped hereafter. Equation 3.1.5 includes a integral over ϕ which is not present in the previous steps. This is due to the fact that Equation 3.1.2 is valid for any single

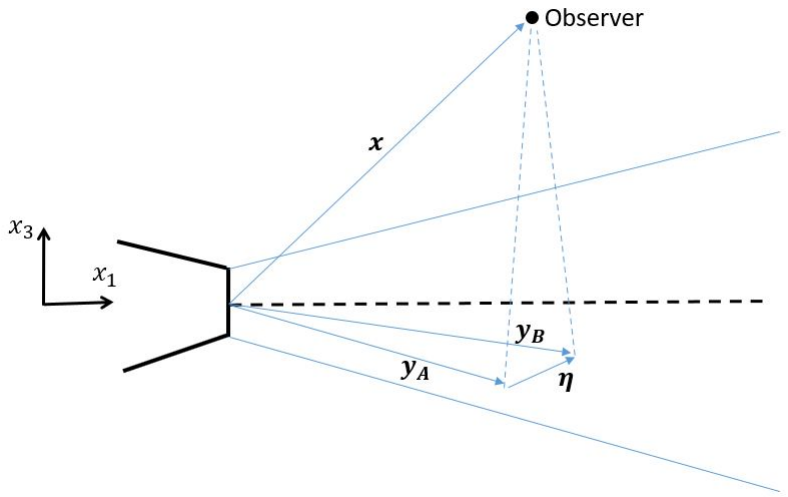

FIGURE 3.1.6: Transformation of co-ordinate frames. Diagram adapted from [68].

point in space but one is interested in a range of angles in the far field and so an additional integration over space is carried out.

So far, the noise produced by an eddy in the moving frame of reference has been considered. To transform into the static laboratory coordinate system, the following equation will be used

$$\zeta_i = \eta_i - \mathbf{U_c}\tau \tag{3.1.6}$$

where ζ_i is the separation in the static laboratory coordinate system, $\mathbf{U_c} = [u_1\, 0\, 0]$ and u_1 is the axial velocity. Equation 3.1.6 allows for the convection of the eddy by the mean flow to be accounted for. It is assumed, here, that the axial component of velocity is much larger than the transverse components, thus the jet can be considered to be parallel. Using Equation 3.1.6, Equation 3.1.4 becomes

$$I(\mathbf{x},\omega) = \frac{\Pi}{16\pi^2\rho_0 c_0^5 r^2 D_F^5}\int_{-\infty}^{\infty}\frac{\partial^4}{\partial\tau^4}\int_{\mathbf{y_A}}\int_{\zeta_i} R^m_{ijkl}(\mathbf{y_A},\zeta_i,\tau)e^{\mathbf{i}\omega((1-M_c cos\theta)\tau-\frac{\hat{\mathbf{x}}}{\mathbf{x}}\cdot\frac{\zeta_i}{c_0})}\,d\zeta_i d\mathbf{y_A}d\tau \tag{3.1.7}$$

R^m_{ijkl} is R_{ijkl} in the static frame and so the eddy is moving relative to this reference frame. The Doppler factor, D_F, is defined by

$$D_F = (1 - M_c \cos\theta) \tag{3.1.8}$$

where θ is the observer polar angle to the jet axis and the convective Mach number, M_c, is given by Ilario [84] as

$$M_c = \frac{1}{4}\left(\frac{u_1}{c_{\text{local}}}\right) + \frac{1}{3}\left(\frac{U_J}{c_0}\right) \tag{3.1.9}$$

where c_{local} is the local speed of sound and U_J is the maximum velocity of the jet. Equation 3.1.9 is not a unique solution of how the convected Mach number can be modelled. Different variations of Equation 3.1.9 are present within the literature (e.g. [21, 52]) but causes very little difference in the final far-field noise predictions.

Since one can swap the order of elements of multiplication, the integration over time in Equation 3.1.7 can be written as

$$\begin{aligned}
&\int_{-\infty}^{\infty} R^m_{ijkl}(\mathbf{y_A}, \zeta_i, \tau) \frac{\partial^4}{\partial \tau^4} e^{\mathbf{i}\omega((1-M_c cos\theta)\tau - \frac{\hat{\mathbf{x}}}{\mathbf{x}}\cdot\frac{\zeta_i}{c_0})}\, d\tau \\
&= \omega^4 (1 - M_c \cos\theta)^4 \int_{-\infty}^{\infty} R^m_{ijkl}(\mathbf{y_A}, \zeta_i, \tau) e^{\mathbf{i}\omega((1-M_c cos\theta)\tau - \frac{\hat{\mathbf{x}}}{\mathbf{x}}\cdot\frac{\zeta_i}{c_0})}\, d\tau \\
&\approx \Omega^4 \int_{-\infty}^{\infty} R^m_{ijkl}(\mathbf{y_A}, \zeta_i, \tau) e^{\mathbf{i}\omega((1-M_c cos\theta)\tau - \frac{\hat{\mathbf{x}}}{\mathbf{x}}\cdot\frac{\zeta_i}{c_0})}\, d\tau
\end{aligned} \tag{3.1.10}$$

where Ω is the convected angular frequency and is given by

$$\Omega = 2\pi f \sqrt{(1 - M_c cos\theta)^2 + \left(\frac{\gamma k^{0.5}}{c_0}\right)^2} \tag{3.1.11}$$

Here k is the turbulent kinetic energy and γ is an empirical constant that needs to be determined experimentally. Ilario [84] reported that $\gamma = 0.5$. This definition of the convected frequency allows for a numerically stable solution to be obtained when $M_c \to 1$ at the sonic condition. The γ term is much smaller than the $(1 - M_c \cos\theta)^2$ term ($\mathcal{O}[1 \times 10^{-3}]$ compared to $\mathcal{O}(1)$). Therefore, the overall value of Ω will not change significantly with this additional term. The definition for D_F will be updated from Equation 3.1.8 to

$$D_F = \sqrt{(1 - M_c cos\theta)^2 + \left(\frac{\gamma k^{0.5}}{c_0}\right)^2} \tag{3.1.12}$$

Using the result of Equation 3.1.10, Equation 3.1.7 becomes

$$I(\mathbf{x},\omega) = \frac{\Pi\Omega^4}{16\pi^2\rho_0 c_0^5 r^2 D_F^5} \int_{-\infty}^{\infty} \int_{\mathbf{y_A}} \int_{\zeta_i} R^m_{ijkl}(\mathbf{y_A},\zeta_i,\tau) e^{\mathbf{i}\omega((1-M_c cos\theta)\tau - \frac{\hat{\mathbf{x}}}{\mathbf{x}}\cdot\frac{\zeta_i}{c_0})}\, d\zeta_i d\mathbf{y_A} d\tau \tag{3.1.13}$$

To continue, an accurate model of R^m_{ijkl} is required. It has been shown in Appendix A.1 that the largest contribution to jet noise comes from the axial component, i.e. the R^m_{1111} term. If one assumes the length and time separations can be modelled using Gaussian curves, R^m_{1111} can take the form

$$R^m_{1111}(\mathbf{y},\zeta_i,\tau) = \rho_0^2 \overline{u_1'^2}^2 e^{-(\frac{\tau}{\tau_s})^2} e^{-((\frac{\zeta_1 - \mathbf{U_c}\tau}{L_1})^2 + (\frac{\zeta_2}{L_2})^2 + (\frac{\zeta_3}{L_3})^2)} \tag{3.1.14}$$

L_1, L_2 and L_3 are the length scales of the eddy along each of the direction axes, $\overline{u_1'}$ is the average turbulent fluctuations in the x_1 direction and τ_s is the time scale at the source. Equation 3.1.14 is not a unique way of modelling how turbulence behaves in space and time. A number of other functions are listed by Azarpeyvand [68].

For the integration to be carried out in Equation 3.1.13, the following co-ordinate transformation for the convected eddy, as given by Azarpeyvand [68], is used

$$\frac{\hat{\mathbf{x}}}{\mathbf{x}} \cdot \zeta_i = \zeta_1 \cos\theta_{rel} + \zeta_2 \sin\theta_{rel} \cos\phi_{rel} - \zeta_3 \sin\theta_{rel} \sin\phi_{rel} \tag{3.1.15}$$

where θ_{rel} and ϕ_{rel} are the relative polar and azimuthal angles of the randomly orientated eddies. The $\frac{\hat{\mathbf{x}}}{\mathbf{x}} \cdot \zeta_i$ term accounts for the difference in retarded time from one side of the eddy to the other as pointed out by Goldstein [47]. Goldstein explains that this difference in time will be much less than the decay time of the eddy for subsonic jets and so ignores this difference. If this approach is taken, the integration of Equation 3.1.13 will reduce to the LRT source equation found by Ilario [21]. In this derivation, the difference in time across the eddy will be accounted for.

Although the inclusion of the relative polar and azimuthal angles is a more accurate description of the physics, it does present issues with how to carry out the integration of Equation 3.1.13. To solve this, one needs to consider what is happening during the integration steps. If one considers a single randomly orientated eddy or point in space, as one integrates over time, that eddy or point in space will exhibit a uniform directivity. In other words, there is no preferred directivity. Therefore, any terms which include relative angles will tend to zero during an integration over time.

When considering the integration over space (i.e. the jet volume), one needs to consider the energy that a far-field observer is receiving. When one of the lobes of the quadrupole is aligned with the mean path that the rays take to reach an observer in the far field, that quadrupole will contribute the most to the overall noise for the observer. The angle of the lobe to the horizontal will tend to the global polar or azimuthal angle in the far field. Therefore, during the integration over space, the relative angle can be replaced with the global equivalent.

Combining Equations 3.1.13, 3.1.14 and 3.1.15, the integration can be carried out using the general result for the integration of an arbitrary Gaussian function of

$$\int_{-\infty}^{\infty} \exp(-a(x+b)^2)\, dx = \sqrt{\frac{\pi}{a}} \tag{3.1.16}$$

Due to the complexity of each integration, the integrations over ζ_i and τ are shown separately below, starting with ζ_1.

$$\begin{aligned}
&\int e^{-\left(\frac{\zeta_1^2 - 2\mathbf{U_c}\tau\zeta_1 + \mathbf{U_c}^2\tau^2}{L_1^2}\right)} e^{-\left(\frac{\mathbf{i}\omega}{c_0}\cos\theta_{rel}\zeta_1\right)} d\zeta_1 \\
&= e^{-\frac{\mathbf{U_c}^2\tau^2}{L_1^2}} \int e^{-\left(\frac{1}{L_1^2}\zeta_1^2 - \frac{2\mathbf{U_c}\tau}{L_1^2}\zeta_1 + \frac{\mathbf{i}\omega}{c_0}\cos\theta_{rel}\zeta_1\right)} d\zeta_1 \\
&= e^{-\frac{\mathbf{U_c}^2\tau^2}{L_1^2}} \int e^{-\frac{1}{L_1^2}\left(\zeta_1^2 + \left(\frac{L_1^2\mathbf{i}\omega\cos\theta_{rel} - 2\mathbf{U_c}c_0\tau}{c_0}\right)\zeta_1\right)} d\zeta_1 \\
&= e^{-\frac{\mathbf{U_c}^2\tau^2}{L_1^2}} \int e^{-\frac{1}{L_1^2}\left[\left(\zeta_1 + \left(\frac{L_1^2\mathbf{i}\omega\cos\theta_{rel} - 2\mathbf{U_c}c_0\tau}{2c_0}\right)\right)^2 - \left(\frac{L_1^2\mathbf{i}\omega\cos\theta_{rel} - 2\mathbf{U_c}c_0\tau}{2c_0}\right)^2\right]} d\zeta_1 \\
&= e^{-\frac{\mathbf{U_c}^2\tau^2}{L_1^2}} \int e^{-\frac{1}{L_1^2}\left(\zeta_1 + \left(\frac{L_1^2\mathbf{i}\omega\cos\theta_{rel} - 2\mathbf{U_c}c_0\tau}{2c_0}\right)\right)^2} e^{\frac{1}{L_1^2}\left(\frac{L_1^2\mathbf{i}\omega\cos\theta_{rel} - 2\mathbf{U_c}c_0\tau}{2c_0}\right)^2} d\zeta_1 \\
&= L_1\sqrt{\pi} e^{-\frac{\mathbf{U_c}^2\tau^2}{L_1^2}} e^{\left(\frac{-L_1^4\omega^2\cos^2\theta + 4\mathbf{U_c}^2c_0^2\tau^2 - 4\mathbf{U_c}c_0L_1^2\mathbf{i}\omega\tau\cos\theta}{4c_0^2L_1^2}\right)} \\
&= L_1\sqrt{\pi} e^{-\left(\frac{L_1\omega\cos\theta}{2c_0}\right)^2} e^{-\left(\frac{\mathbf{U_c}\mathbf{i}\omega\tau\cos\theta}{c_0}\right)}
\end{aligned} \tag{3.1.17}$$

The integration of ζ_2 is much simpler than that of ζ_1 and is written as

$$\begin{aligned}
&\int e^{-(\frac{1}{L_2^2}\zeta_2^2+(\frac{\mathbf{i}\omega}{c_0}\sin\theta_{rel}\cos\phi_{rel})\zeta_2)}d\zeta_2 \\
&= \int e^{-\left[\frac{1}{L_2^2}(\zeta_2+\frac{\mathbf{i}\omega L_2^2}{2c_0}\sin\theta_{rel}\cos\phi_{rel})^2-\frac{1}{L_2^2}(\frac{\mathbf{i}\omega L_2^2}{2c_0}\sin\theta_{rel}\cos\phi_{rel})^2\right]}d\zeta_2 \\
&= \int e^{-\left[\frac{1}{L_2^2}(\zeta_2+\frac{\mathbf{i}\omega L_2^2}{2c_0}\sin\theta_{rel}\cos\phi_{rel})^2+(\frac{\omega L_2}{2c_0}\sin\theta_{rel}\cos\phi_{rel})^2\right]}d\zeta_2 \\
&= \int e^{-\left[\frac{1}{L_2^2}(\zeta_2+\frac{\mathbf{i}\omega L_2^2}{2c_0}\sin\theta_{rel}\cos\phi_{rel})^2\right]}e^{-(\frac{\omega L_2}{2c_0}\sin\theta_{rel}\cos\phi_{rel})^2}d\zeta_2 \\
&= L_2\sqrt{\pi}e^{-(\frac{\omega L_2}{2c_0}\sin\theta\cos\phi)^2}
\end{aligned} \tag{3.1.18}$$

A similar procedure to the integration of ζ_2 takes place for ζ_3 and gives

$$\begin{aligned}
&\int e^{-(\frac{1}{L_3^2}\zeta_3^2-(\frac{\mathbf{i}\omega}{c_0}\sin\theta_{rel}\sin\phi_{rel})\zeta_3)}d\zeta_3 \\
&= L_3\sqrt{\pi}e^{-(\frac{\omega L_3}{2c_0}\sin\theta\sin\phi)^2}
\end{aligned} \tag{3.1.19}$$

When considering the integration over τ, the second exponential in Equation 3.1.17 needs to be included. The integration becomes

$$\begin{aligned}
&\int e^{-(\frac{1}{\tau_s^2}\tau^2-\mathbf{i}\omega D_F\tau+\frac{\mathbf{U_c}\mathbf{i}\omega\cos\theta_{rel}}{c_0}\tau)}d\tau \\
&= \int e^{-\frac{1}{\tau_s^2}\left[\tau^2+(\frac{\mathbf{U_c}\mathbf{i}\omega\tau_s^2\cos\theta_{rel}-\mathbf{i}\omega D_F\tau_s^2c_0}{c_0})\tau\right]}d\tau \\
&= \int e^{-\frac{1}{\tau_s^2}\left[(\tau+\frac{\mathbf{U_c}\mathbf{i}\omega\tau_s^2\cos\theta_{rel}-\mathbf{i}\omega D_F\tau_s^2c_0}{2c_0})^2-(\frac{\mathbf{U_c}\mathbf{i}\omega\tau_s^2\cos\theta_{rel}-\mathbf{i}\omega D_F\tau_s^2c_0}{2c_0})^2\right]}d\tau \\
&= \sqrt{\pi}\tau_s e^{-\frac{\omega^2D_F^2\tau_s^2}{4}}
\end{aligned} \tag{3.1.20}$$

Combining Equations 3.1.17, 3.1.18, 3.1.19 and 3.1.20 together, and if $L_2 = L_3$, gives

$$\begin{aligned}
&L_1L_2^2\tau_s\pi^2e^{-(\frac{\omega^2L_1^2\cos^2\theta+\omega^2L_2^2\sin^2\theta\cos^2\phi+\omega^2L_2^2\sin^2\theta\sin^2\phi}{4c_0^2})}e^{-\frac{\omega^2D_F^2\tau_s^2}{4}} \\
&= L_1L_2^2\tau_s\pi^2e^{-(\frac{\omega^2L_1^2\cos^2\theta+\omega^2L_2^2\sin^2\theta(\cos^2\phi+\sin^2\phi)}{4c_0^2})}e^{-\frac{\omega^2D_F^2\tau_s^2}{4}} \\
&= L_1^3\Delta^2\tau_s\pi^2e^{-(\frac{\omega^2L_1^2(\cos^2\theta+\Delta^2\sin^2\theta)}{4c_0^2})}e^{-\frac{\omega^2D_F^2\tau_s^2}{4}}
\end{aligned} \tag{3.1.21}$$

where the ratio of length scales, Δ, is defined as

$$\Delta = \frac{L_2}{L_1} \tag{3.1.22}$$

Substituting Equation 3.1.21 back into Equation 3.1.13 gives

$$I(\mathbf{x},\omega) = \frac{\rho_0 \Omega^4 \Pi}{16 c_0^5 r^2 D_F^5} \int_{\mathbf{y_A}} L_1^3 \Delta^2 \tau_s \overline{u_1'^2} e^{-\left(\frac{\omega^2 L_1^2 (\cos^2\theta + \Delta^2 \sin^2\theta)}{4c_0^2}\right)} e^{-\frac{\omega^2 D_F^2 \tau_s^2}{4}} \, d^3\mathbf{y_A} \tag{3.1.23}$$

Equation 3.1.23 reduces to that found by Azarpeyvand [68] if one assumes that the flow is isotropic.

Until now, the effects of refraction have been neglected. Equation 3.1.23 can be multiplied by the flow factor, Φ, to incorporate this effect. The flow factor is given by

$$\Phi(\mathbf{x},\mathbf{y}) = \frac{I_{\text{jet}}}{I_{\text{free field}}} \tag{3.1.24}$$

where I_{jet} and $I_{\text{free field}}$ are the intensities of the source seen by an observer in the far field when the jet is present and when there is just a free field, respectively. Therefore, the flow factor includes both the effects of refraction and reflection. Furthermore, no assumptions are made as to whether the jet is symmetric or in-flight. This term is evaluated by using the results from the ray-tracing calculation. Further details of this can be found in Appendix A.2.

To proceed with the source model derivation, the distribution of turbulent energy when an eddy is stretched (i.e. the anisotropy) must be considered. It is assumed that the turbulence in the transverse directions is equal (i.e. $\overline{u_2'^2} = \overline{u_3'^2}$). This allows the turbulence ratio between the longitudinal and transverse directions, β, to be defined as

$$\beta = 1 - \frac{\overline{u_2'^2}}{\overline{u_1'^2}} \tag{3.1.25}$$

Thus turbulent kinetic energy, k, is now defined as

$$k = \frac{1}{2}\left(\overline{u_1'^2} + \overline{u_2'^2} + \overline{u_3'^2}\right)$$

$$= \overline{u_1'^2}\left(\frac{3}{2} - \beta\right) \tag{3.1.26}$$

Substituting Equation 3.1.26 into Equation 3.1.23 gives

$$I(\mathbf{x},\omega) = \frac{\rho_0 \Omega^4 \Pi}{16 c_0^5 r^2 D_F^5} \int_{\mathbf{y_A}} L_1^3 \tau_s k^2 \Phi(\mathbf{x},\mathbf{y}) \left(\frac{\Delta}{\frac{3}{2}-\beta}\right)^2 e^{-\left(\frac{\omega^2 L_1^2(\cos^2\theta + \Delta^2 \sin^2\theta)}{4c_0^2}\right)} e^{-\frac{\omega^2 D_F^2 \tau_s^2}{4}} \, d^3\mathbf{y_A} \tag{3.1.27}$$

The axial length, L_1, and time, τ_s, scales of an eddy are given by

$$\begin{aligned} L_1 &= c_l \frac{\overline{u_1'^2}^{\frac{3}{2}}}{\epsilon} \\ &= c_l \frac{k^{\frac{3}{2}}}{\epsilon(\frac{3}{2}-\beta)^{\frac{3}{2}}} \end{aligned} \tag{3.1.28}$$

$$\begin{aligned} \tau_s &= c_t \frac{\overline{u_1'^2}}{\epsilon} \\ &= c_t \frac{k}{\epsilon(\frac{3}{2}-\beta)} \end{aligned} \tag{3.1.29}$$

where c_l and c_t are the length and time calibration constants, ϵ is the turbulent dissipation rate and L_1 is the integral length scale of the eddy in the direction of the jet axis. As the integral scales contain most of the energy in the flow, this is a good approximation to make when looking at the jet mixing noise. L_1 can now be written in terms of τ_s and the result substituted into Equation 3.1.27 to give

$$I(\mathbf{x},\omega) = \frac{\rho_0 \Omega^4 \Pi}{16 c_0^5 r^2 D_F^5} \int_{\mathbf{y_A}} \tau_s^4 k^{\frac{7}{2}} \frac{c_l^3}{c_t^3} \Phi(\mathbf{x},\mathbf{y}) \frac{\Delta^2}{(\frac{3}{2}-\beta)^{\frac{7}{2}}} e^{-\left(\frac{\omega^2 L_1^2(\cos^2\theta + \Delta^2 \sin^2\theta)}{4c_0^2}\right)} e^{-\frac{\omega^2 D_F^2 \tau_s^2}{4}} \, d^3\mathbf{y_A} \tag{3.1.30}$$

A new time scale was found by Azarpeyvand [109], called the Turbulent Energy Transfer (TET) time scale. This is shown in Equation 3.1.31. τ_s^* is the time scale (or lifetime) of the largest eddies, which is linked to their size. The ratio $\frac{L_1}{D_J}$, where D_J is the jet diameter, shows how large an eddy is relative to the shear layer width, which scales with nozzle diameter. High-frequency eddies generated near the nozzle exit, where the shear layer is the thinnest, will see a higher shear rate and so will have a

shorter lifetime. Azarpeyvand showed that using this definition for τ_s^* yields an improved prediction compared to experimental data.

$$\tau_s^* = \tau_s \left(\frac{L_1}{D_J} \right)^{\frac{2}{3}} \tag{3.1.31}$$

Replacing τ_s with τ_s^*, Equation 3.1.30 is written in terms of the Power Spectral Density (PSD), P, to give the final source equation as

$$\boxed{P(\mathbf{x},\omega) = \frac{\rho_0^2 \Omega^4 \Pi}{16 c_0^4 r^2 D_F^5} \int_{\mathbf{y_A}} \tau_s^{*4} k^{\frac{7}{2}} \Phi(\mathbf{x},\mathbf{y}) \frac{c_l^3}{c_t^3} \frac{\Delta^2}{(\frac{3}{2}-\beta)^{\frac{7}{2}}} e^{-\frac{\omega^2 L_1^2 (\cos^2\theta + \Delta^2 \sin^2\theta)}{4c_0^2}} e^{-\frac{\omega^2 D_F^2 \tau_s^{*2}}{4}} d^3\mathbf{y_A}} \tag{3.1.32}$$

Equation 3.1.32 is the final source equation used within the LRT acoustic model. From this equation, several different physical effects can be seen. The anisotropy that is induced by the shear layer is present in the $\frac{\Delta^2}{(\frac{3}{2}-\beta)^{\frac{7}{2}}}$ term. This will be discussed in more detail in Section 4.3.3. It is worth noting that the minimal value of $\frac{3}{2} - \beta$ is $\frac{1}{2}$ and so the PSD is always a finite value. The decay rate of each frequency is dependent on the values of the two exponentials, as seen in Figure 3.1.7. Within Figure 3.1.7, the Strouhal number, which is a non-dimensional frequency, is defined as

$$St = \frac{f D_J}{U_J} \tag{3.1.33}$$

where f is the frequency, D_J is the jet diameter and U_J is the maximum jet velocity.

The first exponential in Equation 3.1.32 can be thought of as a source compactness term. This is because $\frac{\omega L_1}{c_0} = \frac{2\pi L_1}{\lambda}$, with λ being the wavelength of noise produced by an eddy. If $L_1 \ll \lambda$, then the first exponential will tend to one. This term, therefore, only becomes relevant when the source is non-compact (i.e. $L_1 \geq \lambda$). The compactness term is multiplied by a directivity factor based on the anisotropy of the eddy $(\cos^2\theta + \Delta^2 \sin^2\theta)$. Δ tells us how stretched an eddy is due to the shear force exerted on it. The stretching of eddies (a decrease in Δ) will result in the source compactness term being relevant for a larger proportion of the flow field.

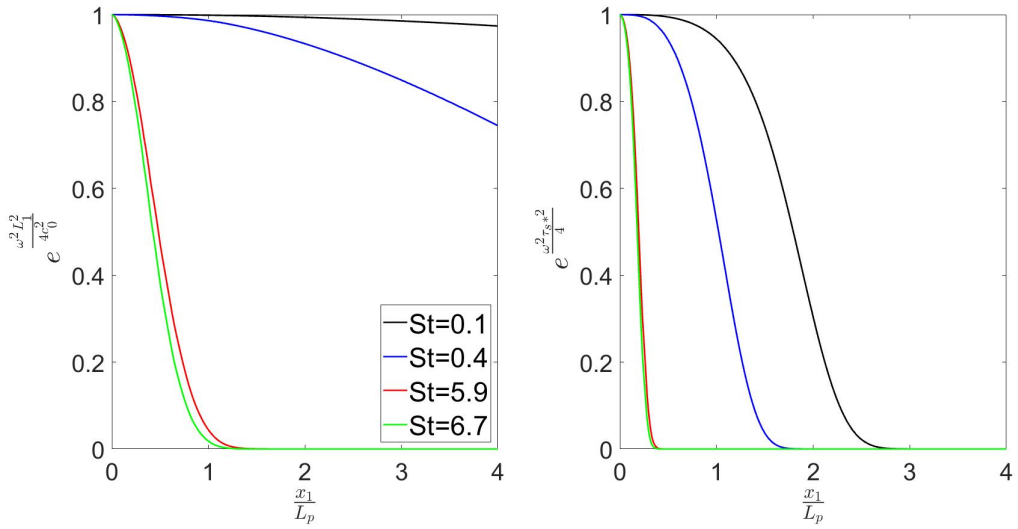

FIGURE 3.1.7: Variation in the exponential terms with frequency along the lip-line of the static conical nozzle studied in Chapter 4 at $M_J = 0.6$, $\theta = 90^\circ$ and assuming isotropic turbulence.

The second exponential determines the decay rate based on an eddies life span and how it is being convected. The larger the eddy is, the longer the life span will be and hence the slower it will decay by this exponential. This term will be the dominant factor for most frequencies when the source can be considered non-compact and so the first exponential will have little effect, as seen in Figure 3.1.7.

It should be noted that both exponentials are dependent on the frequency of the eddy in the moving frame, ω, rather than the convected wavelength that an observer sees, Ω. There are two effects that need to be separated here. Although the frequency that is observed at different locations will change due to the Doppler effect, eddies decay based on their local shear rates. The D_F^{-5} term accounts for the variation in observed frequency, while the exponentials model the change based on the local shear rates. These shear rates are represented by the relationships between k and ϵ in the length and time scales.

The source equation (Equation 3.1.32) gives the PSD for a jet. Results in this thesis are presented in terms of an SPL. To convert the PSD into an SPL, the bandwidth (which is 100Hz) needs to be accounted for by using the following formula

$$SPL = PSD + 10\log(\text{bandwidth}) \tag{3.1.34}$$

The acoustic model requires calibration using the two constants, c_l and c_t, which correspond to the length and time scale calibration constants. These are empirical constants which allow the average energy found at a point in space to be linked to a particular frequency. Given that this average energy is a sum across all frequencies, the calibration constants allow the specific energy per frequency to be recovered. It should be noted that the calibration constants are dependent on the choice of functions used to model the stress correlation factor, R_{ijkl}, and so the values of these constants cannot be compared between authors with different models.

The experimental data at $\theta = 90^\circ$ is often used to calibrate prediction models. This is the simplest case to analyse as the convection and refraction effects from the jet are negligible at this angle. To calibrate the LRT model, the static conical nozzle described in Chapter 4 at $M_J = 0.6$ is used. The first step is to select whether an isotropic or anisotropic turbulence model is being used. This will be discussed in more detail at the end of Chapter 4. Next, the peak frequency is matched by changing the time scale calibration constant c_t. Once the peak frequency is matched, the final step is to match the peak amplitude by adjusting the length scale calibration constant, c_l. Minor adjustments may be needed to c_t as c_l also has an impact on the frequency response. For an isotropic turbulence model, this procedure gives $c_l = 0.43$ and $c_t = 0.8$.

The effect of changing the values of the calibration constants is highlighted in Figure 3.1.8 where the calibration constants have been independently increased by 0.1 from their isotropic values. This increase in c_l leads to a 2.7dB increase in noise but a decrease in the peak frequency by 200Hz while the increase in c_t leads to a decrease in noise level by 1.5dB and a decrease in peak frequency by 200Hz. There is no noticeable change in the shape of the curves when the calibration constants are changed. Due to the opposite directions that the magnitude of noise moves when the calibration constants are increased, it is easy to see how multiple pairs of constants could provide the same prediction. This will be discussed in more detail in Section 4.3.2.

The derivation of the LRT source model in this thesis is different to the one originally proposed by Ilario [21] as the new source equation in Equation 3.1.32 has the source compactness exponential. The difference that including this term has on predictions is illustrated in Figure 3.1.9. Here, no difference is seen at very low frequencies, but above $St = 0.5$, the old model starts to over-predict the high-frequency noise. By

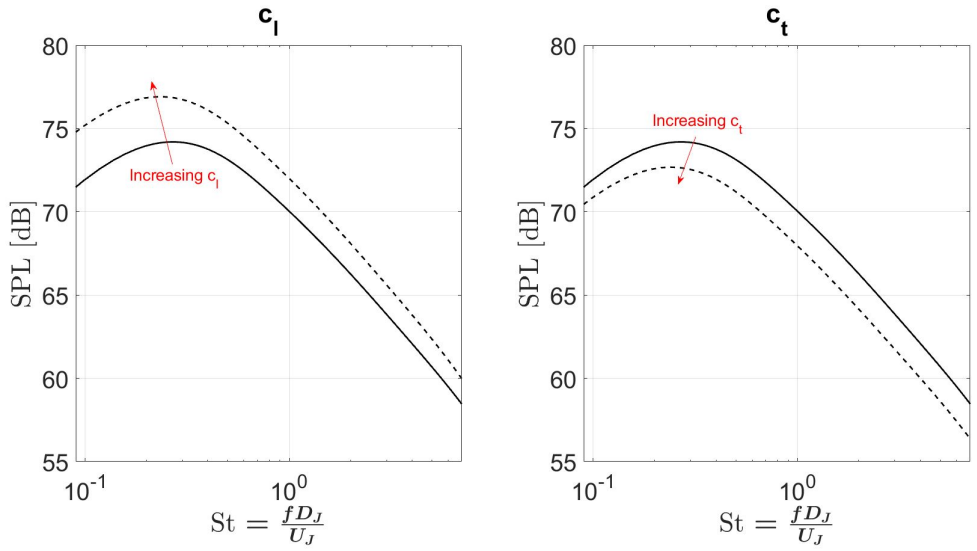

FIGURE 3.1.8: Variation in the SPL values as the calibration constants are changed individually by 0.1 for the static conical nozzle studied in Chapter 4 at $M_J = 0.6$ and $\theta = 90^0$ from their isotropic values.

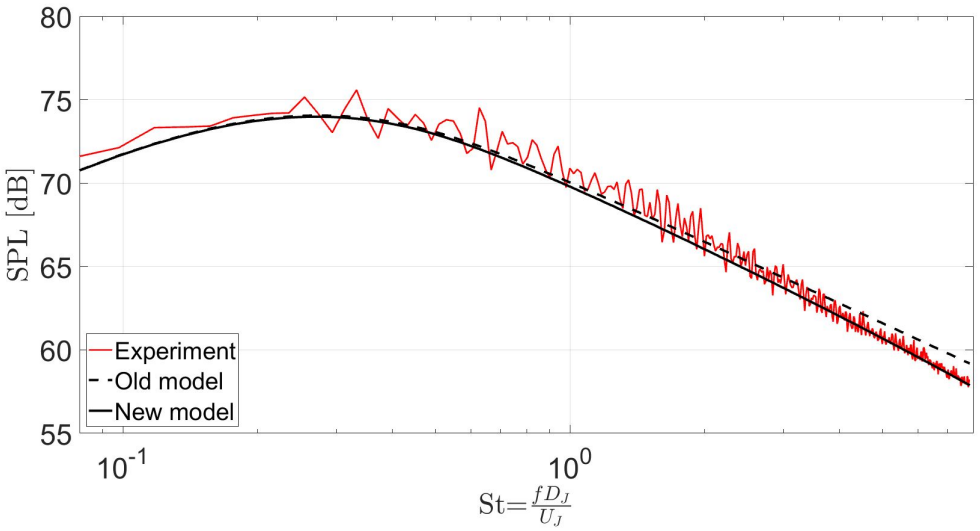

FIGURE 3.1.9: Comparison of the old and new LRT models for the static conical nozzle studied in Chapter 4 at $M_J = 0.6$ and $\theta = 90^\circ$. The new model has an additional decay rate due to the source compactness.

$St = 7.8$, there is a 1.2dB over-prediction while the new model matches the experimental data well. Therefore, the inclusion of the source compactness term allows for the fall-off at high frequency to be better modelled and for a more accurate prediction to be made.

3.2 Experimental set-up

Although experimental results are presented in the following results chapters, the author did not take part in this work. However, an overview of the experimental set-up and data acquisition is given below.

The experimental data was generated using the Flight Jet Rig (FJR) in the Doak Laboratory, at the University of Southampton. Full details of the rig and measurement data uncertainty are outlined by Proenca [53, 110–112]. The Doak Laboratory is an anechoic chamber, approximately 15m-long, 7m-wide and 5m-high. The laboratory is fully anechoic down to 400Hz. A high-pressure reservoir supplies the flow through the nozzle. An upright labyrinth silencer plenum ensures that the flow is quiet and has a uniform pressure distribution. The FJR can support in-flight isolated and installed jet testing at flight-stream Mach numbers (M_f) in the range of 0.05 to 0.3. The laboratory setup can be seen in Figure 3.2.1 and 3.2.2. Although the Doak laboratory is capable of running the flight-stream at $M_f = 0.3$, it was found that noise from the finite flight-stream mixing with the ambient air contaminated experimental data when $\frac{M_J}{M_f} < 3$, where M_J is the acoustic jet Mach number. This led to a large increase in noise at low frequencies and so analysis has been limited to $M_f = 0.2$ in this thesis.

The acoustic jet Mach number is defined as

$$M_J = \frac{u_{max}}{c_0} \tag{3.2.1}$$

where u_{max} is the maximum velocity in the jet and c_0 is the speed of sound in the far field.

Aerodynamic data were recorded using a constant temperature anemometry single-component, single-point hot-wire probe. The probe measured the instantaneous resultant velocity field. For the far-field acoustic measurements, both azimuthal and fly-over arrays were used to gather the data. The fly-over array was situated $58D_J$ above the nozzle. 1/4-inch GRAS Type 40BF condenser microphones with B&K Falcon Type 2670 pre-amplifiers were used on both arrays. A 24-bit National Instruments PCI-4472 dynamic signal acquisition system was used to sample the data at 100kHz. The data was passed through a low-pass filter set at 40kHz to

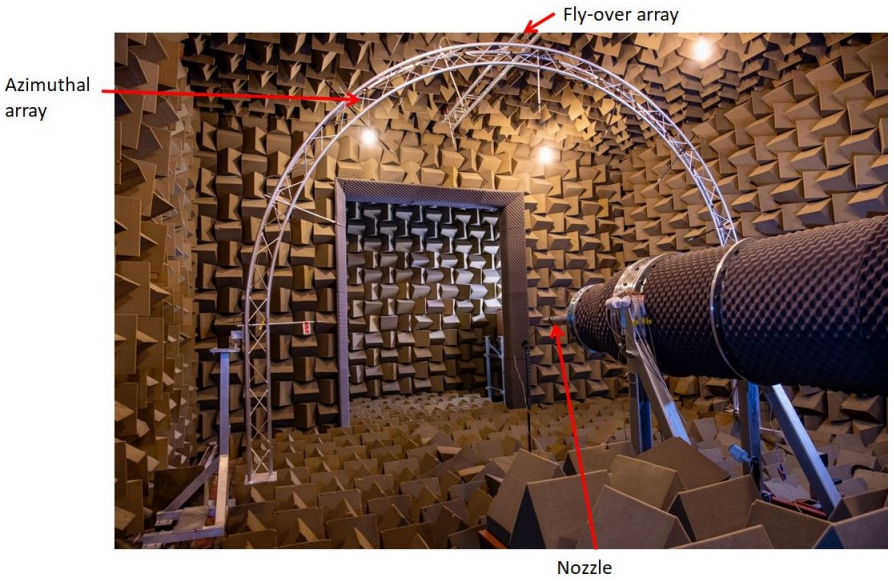

FIGURE 3.2.1: Experimental set-up of the Doak laboratory, University of Southampton.

avoid any aliasing effects. For the conical nozzle at $M_J = 0.6$ studied in Chapter 4, this gives a Strouhal number range of 0.08-8.

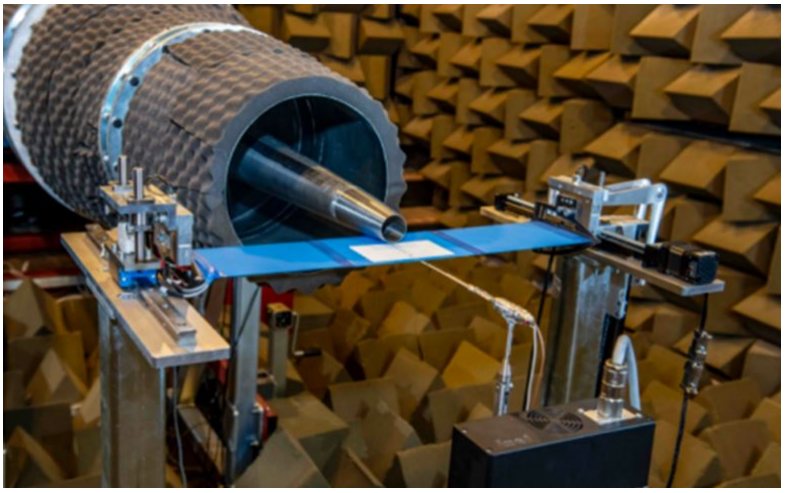

FIGURE 3.2.2: Experimental set-up of the Doak laboratory when looking at an installed case.

The experimental acoustic data taken in the Doak laboratory has had several corrections applied to it. Firstly, the data has been corrected for any background noise on the day of the experiment. When looking at in-flight cases, corrections have been made for the refraction of the shear layer of the finite flight-stream. Finally, the Doppler shift due to the convection of sound has also been accounted for. It should be noted that the experimental data used has an error of $\pm$0.25dB. Therefore, it is

important when looking at small changes in noise from experiments and predictions to take this into account.

3.3 Summary of chapter

In this chapter:

- The numerical implementation of the LRT method has been described and the assumptions and limitations of the method are outlined.
- The source equation used in the LRT acoustic model is derived from Lighthill's equation and includes the anisotropy of the turbulence and the compactness of the source. The final equations are as follows:

$$\boxed{P(\mathbf{x},\omega) = \frac{\rho_0^2 \Omega^4 \Pi}{16 c_0^4 r^2 D_F^5} \int_{\mathbf{y_A}} \tau_s^{*4} k^{\frac{7}{2}} \Phi(\mathbf{x},\mathbf{y}) \frac{c_l^3}{c_t^3} \frac{\Delta^2}{(\frac{3}{2}-\beta)^{\frac{7}{2}}} e^{-\frac{\omega^2 L_1^2 (\cos^2\theta + \Delta^2 \sin^2\theta)}{4c_0^2}} e^{-\frac{\omega^2 D_F^2 \tau_s^{*2}}{4}} \, d^3\mathbf{y_A}} \tag{3.3.1}$$

$$\Omega = 2\pi f \sqrt{D_F^2 + \left(\frac{\gamma k^{0.5}}{c_0}\right)^2} \tag{3.3.2}$$

$$D_F = \sqrt{(1 - M_c cos\theta)^2 + \left(\frac{\gamma k^{0.5}}{c_0}\right)^2} \tag{3.3.3}$$

$$M_c = \frac{1}{4}\left(\frac{u_1}{c_y}\right) + \frac{1}{3}\left(\frac{U_J}{c_0}\right) \tag{3.3.4}$$

$$L_1 = c_l \frac{k^{\frac{3}{2}}}{\epsilon(\frac{3}{2}-\beta)^{\frac{3}{2}}} \tag{3.3.5}$$

$$\tau_s^* = c_t \frac{k}{\epsilon(\frac{3}{2}-\beta)} \left(\frac{L_1}{D_J}\right)^{\frac{2}{3}} \tag{3.3.6}$$

$$\Delta = \frac{L_2}{L_1} \tag{3.3.7}$$

$$\beta = 1 - \frac{\overline{u_2^2}}{\overline{u_1^2}} \tag{3.3.8}$$

$$\Phi(\mathbf{x},\mathbf{y}) = \frac{I_{\text{jet}}}{I_{\text{free field}}} \tag{3.3.9}$$

$$\Pi = \frac{1}{2\pi} \int_0^{2\pi} \frac{x_i x_j x_k x_l}{x^4} d\phi \tag{3.3.10}$$

Further details on $\Phi(\mathbf{x},\mathbf{y})$ and Π can be found in Appendix A.1 and A.2, respectively.

Chapter 4

Method Validation

In previous chapters, the issue of jet noise has been explained and the background to how simulation techniques have been used to help mitigate noise has been explored. A method called LRT has then been explained and is being developed to understand how the asymmetric nature of jet flows affects the mixing noise produced. In this chapter, a simple round nozzle has been analysed to gain confidence with the method and to allow for the sensitivities of the model to be investigated. This nozzle has a 40mm diameter (D_J) with a 2.5° convergence angle (α) as shown in Figure 4.0.1. The nozzle has been run at different acoustic jet, M_J, and flight, M_f, Mach numbers as seen in Table 4.1. These cases have been selected as they are representative of jet speeds at take-off, when the noise problem will be greatest for those around the airport.

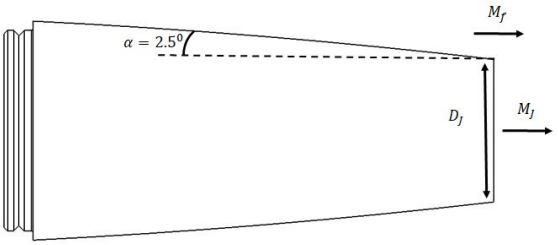

FIGURE 4.0.1: Conical nozzle geometry.

M_J	M_f
0.6 and 0.8	$0.0 \rightarrow 0.2$ (0.1 intervals)

TABLE 4.1: Cases simulated for the conical nozzle.

4.1 CFD results

The first question to ask is which turbulence model should be used for predicting the flow of jets. Within the literature shown in Chapter 2, the k-ϵ turbulence model is the most commonly used and so this turbulence model has been primarily used in this work. The sensitivity of the CFD results to the turbulence model will be investigated in more detail in Section 4.3.4. For now, the degree to which the CFD profiles match experimental data will provide evidence for the choice of turbulence model.

One of the sources of error that occurs with the k-ϵ RANS models of jets is the over-prediction of the potential core length, L_p, as seen in [75, 113, 114]. This means that the physical location of the maximum turbulence, which occurs just after the end of the potential core, is different between the experiment and the simulation. Previous work [107] has shown that normalising by the potential core length allows the isolated CFD results to collapse. For isolated jets, this difference in potential core length will not cause much difference in the far-field mixing noise as the difference in position and angle is negligible in the far field. However, for an installed case, the flow field will be affected by the presence of solid bodies around the jet and the relative position of the acoustic sources compared to the surface will clearly also be important for the reflected mixing noise problem.

Thies and Tam [25] looked into the over-prediction of the potential core and found that the error arises from the assumptions used to derive the k-ϵ turbulence model. When the model was first proposed, it was assumed that the characteristics of turbulence were universal. The early applications of the k-ϵ model were on turbulent boundary layers and plane shear flows rather than spreading jets. It has since been realised that, as the large-scale turbulent structures are of the same order of magnitude as the flow field, they are dependent on the geometry being studied. Fine-scale turbulence, on the other hand, is more universal. Thies and Tam studied a large number of isolated single and coaxial jets at subsonic and supersonic conditions. They found that by changing the values of the constants used in the k-ϵ model in Equations 2.1.8 and 2.1.10, a much better set of predictions for the velocity profiles, and hence more accurate potential core length prediction, could be achieved. The work by Thies and Tam has since been used by Weaver [115] and Tam [75] to give more accurate

predictions using the k-ϵ model. The standard coefficients, together with those used by Thies and Tam, are shown below in Table 4.2.

Coefficient	Standard model	Thies and Tam's model
C_μ	0.09	0.0874
C_1	1.44	1.4
C_2	1.92	2.02
σ_k	1	0.324
σ_ϵ	1.3	0.377

TABLE 4.2: k-ϵ turbulence model coefficients.

The conical nozzle was analysed with both sets of coefficients and the results are shown in Table 4.3. Proença [53] found that the experimental potential core length for this particular nozzle could be calculated using the equation

$$\frac{L_p}{D_J} = \frac{0.7}{(0.16 - 0.16^2 M_J)\frac{\rho_0}{\rho_J}^{0.28}} \tag{4.1.1}$$

where ρ_0 is the density in the far field and ρ_J is the density of the jet at the nozzle exit. This equation is based on the definition that the end of the potential core is the point on the centreline where the velocity decreases below 98% of the maximum velocity.

	Potential Core length [$\frac{L_p}{D_J}$]	% Error
Experiment	4.86	
RANS: Standard k-ϵ coefficients	7.99	64
RANS: Thies and Tam's coefficients	5.86	20

TABLE 4.3: Potential core lengths of the static conical nozzle at $M_J = 0.6$ with different k-ϵ turbulence models.

Using the Thies and Tam coefficients, the error in the potential core length has been reduced from 64% down to 20%. This implies that the velocity and turbulence distributions in the shear layer are now much closer to reality.

To check the sensitivity of the potential core length to the CFD mesh, the mesh density at the nozzle wall (y^+) was investigated on a 2D simulation. The results can be seen in

Figure 4.1.1. Here, the 2D RANS converges away from the experimental value as the mesh density increases rather than towards it. Figure 4.1.1 shows that increasing the y^+ by a factor of ten from 35 to 3 has a minor impact on the overall potential core length for a considerable increase in computational cost. This will be even greater for running three-dimensional (3D) cases with the finer mesh. Therefore, a mesh density with a $y^+ \approx 35$ will be used for future simulations. The small increase in potential core length going from 2D to 3D RANS is thought to be due to the extra degree of freedom within equations. No data has been taken for y^+ values between 5 and 30 because there is a cross-over region between the viscous sublayer ($y^+ \leq 5$) and the log-law region ($y^+ \geq 30$). This cross-over region is called the buffer region and neither of the equations that are used to model the velocity in the other two regions holds for the buffer region. There is, therefore, limited accuracy of CFD grids that have a y^+ in this region. Hence, no calculations are presented for grids with $5 \leq y^+ \leq 30$.

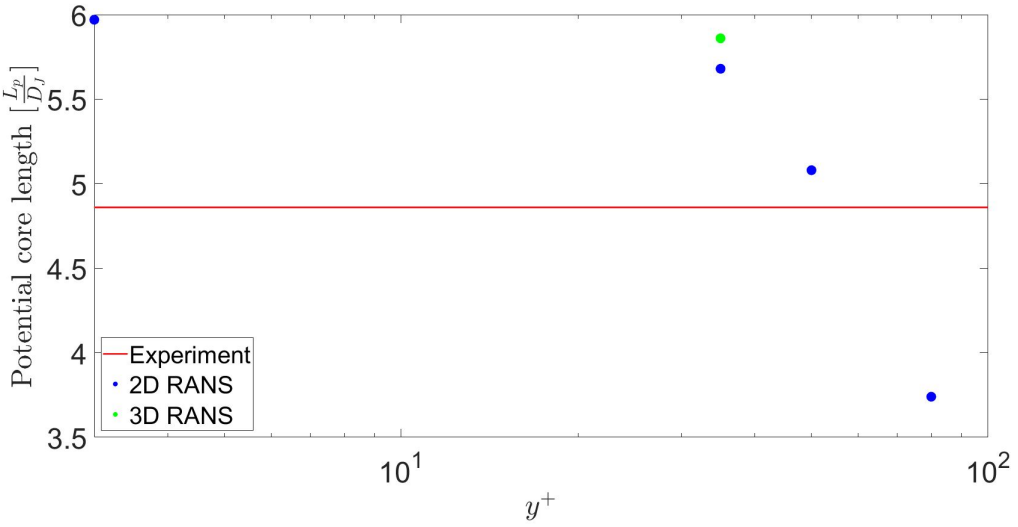

FIGURE 4.1.1: Variation in potential core length as the y^+ of the mesh is changed.

Having shown that the prediction of the potential core length has been improved by using the Thies and Tam coefficients, comparisons of the RANS flow field to model experimental data can be undertaken. Radial profiles of axial velocity are shown below in Figure 4.1.2 and show excellent agreement with the experimental data. The peak velocity is predicted to within 5% until $\frac{x_1}{D_J} = 10$, where there is a 6% under-prediction. This error will now be investigated further.

The blue dashed line marks the edge of the jet where the velocity has fallen to 10% of the maximum velocity, U_J. This allows the spreading angle, γ_J, to be calculated. This

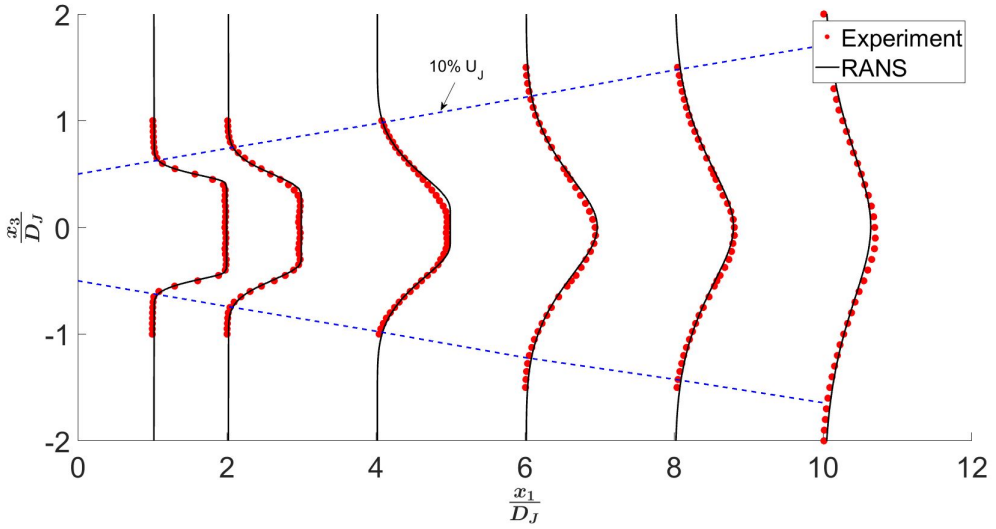

FIGURE 4.1.2: Radial profiles of axial velocity for the static conical nozzle at $M_J = 0.6$.

is the angle from the edge of the jet to the horizontal as seen in Figure 4.1.3. The shear layer half-width, δ_β, was found by Proença [53] to follow the relationship

$$\begin{aligned}\delta_\beta &= \frac{x_1 \sin(\gamma_J + \gamma_{L_p})}{\cos(\gamma_J)\cos(\gamma_{L_p})} \text{ when } x_1 < L_p \\ &= x_1 \tan(\gamma_J) + 0.5 D_J \text{ when } x_1 \geq L_p \end{aligned} \tag{4.1.2}$$

where γ_{L_p} is the angle between the horizontal and the edge of the potential core.

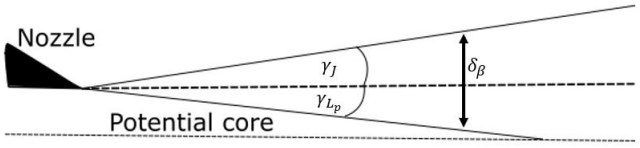

FIGURE 4.1.3: Diagram to show the definition of the spreading angles, $\gamma_J$and γ_{L_p}, to calculate the shear layer half-width, δ_β.

The spreading angle computed from the experimental data is 6.06° compared to 6.8° from the RANS solution. The larger shear layer produced by RANS will result in the flow mixing faster than in the experiment. The far-field acoustic result of this will be that energy is shifted towards the nozzle exit and higher frequencies.

To see if this additional spreading happens at all scales within the flow, the flow at the nozzle exit is analysed. The boundary layer at the nozzle exit is shown below in Figures 4.1.4. The experimental boundary layer thickness, δ, is about 2mm whereas

the boundary layer for the RANS simulation is about 3mm. This would indicate that the increase in the spreading rate is due to a global parameter or equation within the k-ϵ model rather than a wall function in the CFD model. Despite this, a turbulent boundary layer profile is produced at the nozzle exit in the velocity profile and there is a reasonable agreement in the shape of the profiles shown.

When looking at the turbulence intensity profile, a reasonable match is found when $\frac{x_3}{\delta} > 0.3$. Very close to the wall, there is an error in the first two experimental data points due to the finite size of the hot-wire probes. One of the probes is effectively outside the jet stream and so a large difference is measured between the probes. Therefore, the first two experimental data points should be discounted. The turbulence should decrease to zero at the wall. RANS also predicts a large increase in turbulence when $\frac{x_3}{\delta} < 0.3$. This is thought to be due to a combination of the large y^+ (≈ 35) and the fact that damping functions are used to model the dissipative effects of viscous forces within the viscous sublayer.

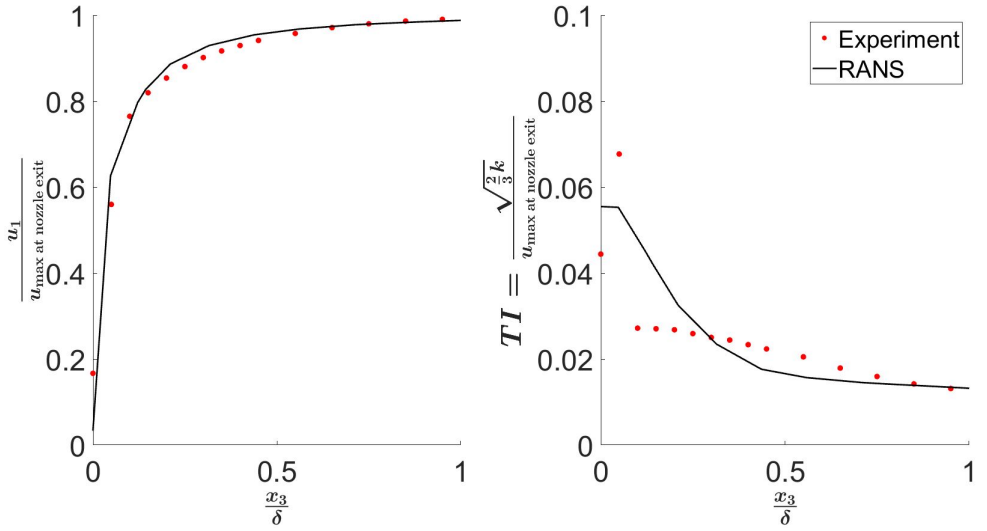

FIGURE 4.1.4: Profiles of axial velocity (left) and turbulent intensity (right) within the boundary layer for the static conical nozzle at $M_J = 0.6$ of the RANS simulation compared to experimental data.

So far, the velocity field has primarily been considered. However, the turbulence is of most interest to the noise problem. Profiles of turbulent intensity along the centre and lip-lines can be seen in Figure 4.1.5, while radial profiles can be seen in Figure 4.1.6. When looking at Figure 4.1.5, the experimental data indicates that there is a small amount of turbulence present on the centreline inside the potential core but the RANS simulation predicts very little. As the flow within the potential core can be considered

laminar in nature, this additional turbulence in the experimental data will not influence the far-field noise much. Nearing the end of the potential core, the RANS simulation predicts a sharp rise in the turbulent intensity as the laminar flow mixes with the turbulent shear layer. The peak on the centreline in the RANS simulation occurs $0.25L_p$ closer to the nozzle than in the experiment. This will certainly skew the source distribution towards the nozzle exit. The shape of the experimental data is captured much better on the lip-line compared to the centreline, although the peak magnitude is not the same. The under-prediction in peak intensity level is consistent with results found by Lyu [105].

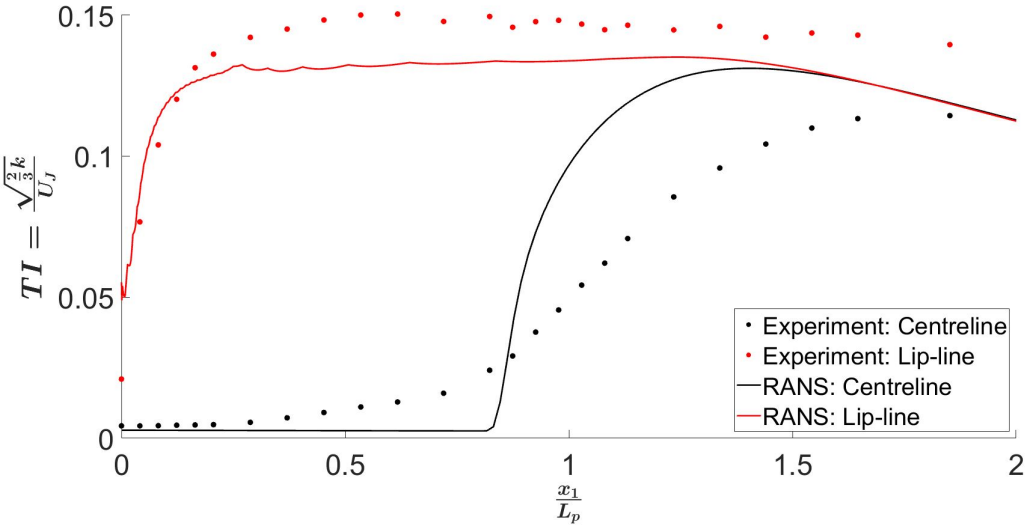

FIGURE 4.1.5: TI on the jet centre and lip-lines for the static conical nozzle at $M_J = 0.6$.

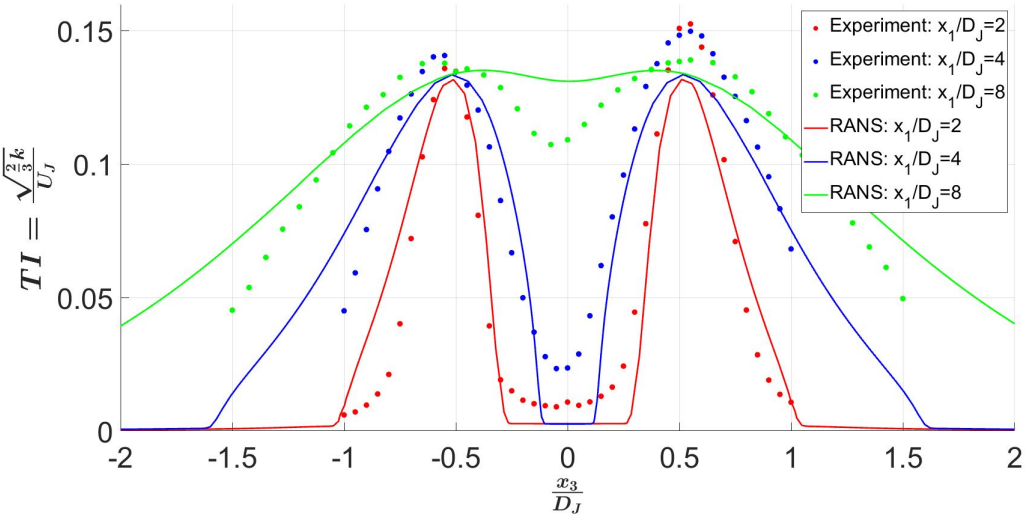

FIGURE 4.1.6: Radial profiles of TI for the static conical nozzle at $M_J = 0.6$.

In terms of the radial profiles in Figure 4.1.6, good agreement is found within the first two diameters for both the shape and the peak levels. However, due to the differences in potential core length and spreading rate, the RANS under-predicts the peak level by 1% at $\frac{x_1}{D_J} = 4$ and the shear layer is nearly fully mixed by $\frac{x_1}{D_J} = 8$. It should be noted that RANS assumes isotropic turbulence throughout the jet. This is not strictly correct for eddies close to the nozzle exit. This will be discussed in more detail in Section 4.3.3. Despite this, reasonable agreement to within 1% can still be found.

Having analysed the conical nozzle statically, in-flight results are now presented. As the flight Mach number increases, the potential core of a jet increases in length due to the reduced shear between the jet and ambient air flows. Proença [53] found, empirically from experimental data, that the change in potential core length for this nozzle when a flight-stream is present could be expressed as

$$\left[\frac{L_p}{D_J}\right]_{M_f>0} = 16M_f + \left[\frac{L_p}{D_J}\right]_{M_f=0} \tag{4.1.3}$$

The length of the potential core in-flight can be seen below in Table 4.4. Although these results indicate that the in-flight potential core length is still over-predicted by RANS by roughly 10%, a much smaller error exists compared to the results shown by Ilario [21] using the standard coefficients for the k-ϵ turbulence model. It is unclear why there is a variation in the error but further investigation of this is beyond the scope of this thesis. The main observation that can be made from Table 4.4 is the fact that RANS does not predict either the potential core length or the spreading rate correctly.

	Potential core length $\left[\frac{L_p}{D_J}\right]$			Spreading angle $\left[\text{degrees}\right]$	
M_f	Experiment	RANS	% Error	Experiment	RANS
0	4.86	5.86	20	6.06	6.8
0.1	6.46	7.03	9	3.3	4.4
0.2	8.06	8.99	12	2.09	2.4

TABLE 4.4: Variation in potential core length and spreading angle of the conical nozzle with M_f in the RANS simulations and experiment for $M_J = 0.6$.

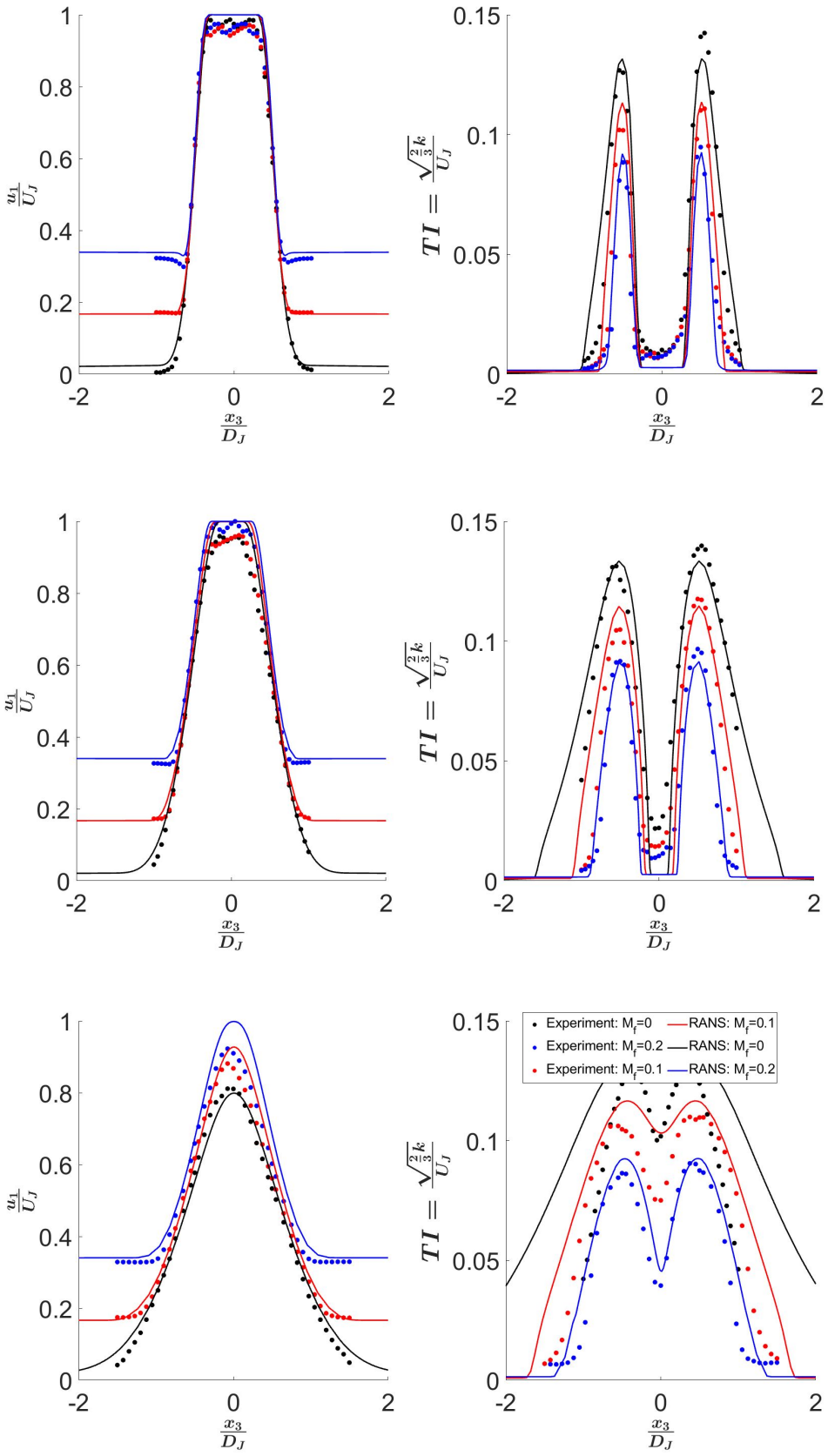

FIGURE 4.1.7: Radial profiles of $\frac{u_1}{U_J}$ (left) and turbulence intensity (right) for the conical nozzle at $M_J = 0.6$ and $M_f = 0$, 0.1 and 0.2. Each row corresponds to $\frac{x_1}{D_J} = 2$, 4 and 8, respectively.

The radial profiles of axial velocity and turbulence intensity as the flight-stream increases can be seen in Figures 4.1.7. Good predictions of axial velocity (within 5%) are made within the first four diameters and, although the peak velocity is not matched after four diameters (up to 8% error), the RANS simulations predict the correct shape. The amount of under-prediction downstream of the potential core is similar for both the static and in-flight cases. This result is not surprising given the error introduced when predicting the potential core length seen in Table 4.4. A slight negative skew can be seen in the experimental data at $\frac{x_1}{D_J} = 8$ in Figure 4.1.7, which is likely due to a compounding probe alignment error. The turbulent intensity profiles show that the in-flight data has the same trends as the static case. Both the static and in-flight data show that the shear layers mix out quicker in the RANS calculation compared to experimental data and that the turbulence exists over a wider area, due to the increased spreading angle. RANS captures the decrease in turbulent intensity which will result in a reduction in mixing noise as M_f increases.

4.2 Acoustic results

Having analysed the CFD data, far-field acoustic predictions of the static and in-flight cases are now presented. The initial results in this chapter have used an isotropic turbulence model (i.e., $\Delta = 1$ and $\beta = 0$). The impact of anisotropy on the results will be studied at the end of this chapter (Section 4.3.3).

All experimental and simulation data in this thesis are compared for a 1m lossless situation and primarily shown as 100Hz narrow band data.

Figures 4.2.1 and 4.2.2 show the results for the conical nozzle at $M_J = 0.6$ and 0.8 for $M_f = 0$, 0.1, 0.2 at three polar angles. As mentioned previously, the calibration of the LRT model was carried out at $\theta = 90°$ for the static $M_J = 0.6$ case by matching the peak frequency and SPL level. This results in the prediction being within 0.5dB of the experimental data at all frequencies. The calibration constants are kept the same for all simulations and polar angles.

Starting with Figures 4.2.1, there is an over-prediction at $\theta = 60°$ at high frequency (2dB at $St = 3$) and the peak is over-predicted by 0.75dB for the static case. At $\theta = 120°$, there is an under-prediction of 1.5dB statically. However, when one considers the in-flight predictions, more accurate predictions are generally made

compared to the static case. Similar trends are generally observed in Figure 4.2.2 for the $M_J = 0.8$ data compared to the $M_J = 0.6$ case. One thing of note is that there is an under-prediction at high frequency for the static $M_J = 0.8$ case. This point will be revisited, later in this chapter, when the topic of anisotropy is considered.

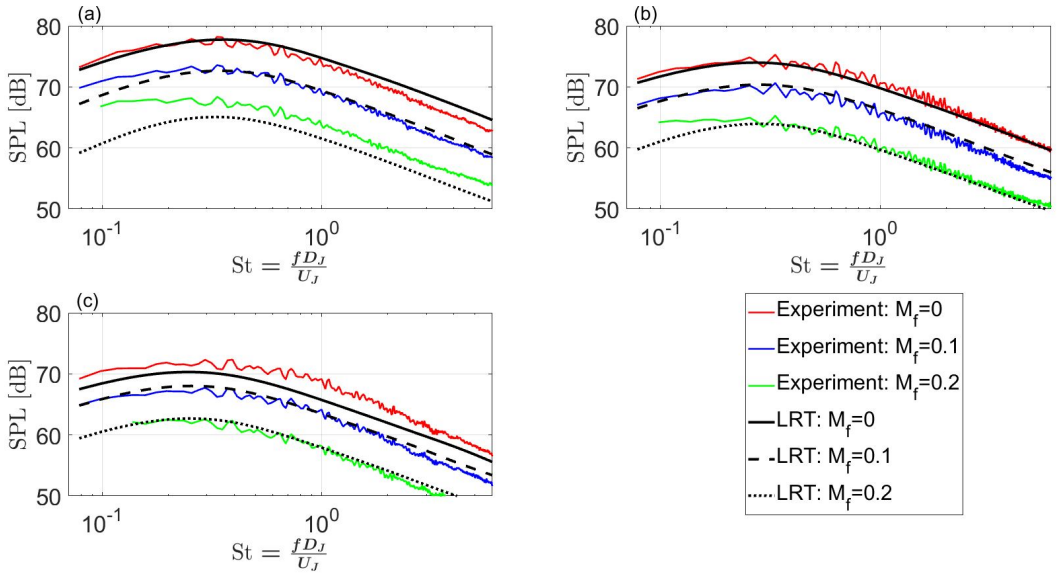

FIGURE 4.2.1: LRT predictions for the conical nozzle for $M_J = 0.6$ with experimental and simulation data at 100Hz narrow band frequencies. a). $\theta = 60°$, b). $\theta = 90°$ and c). $\theta = 120°$.

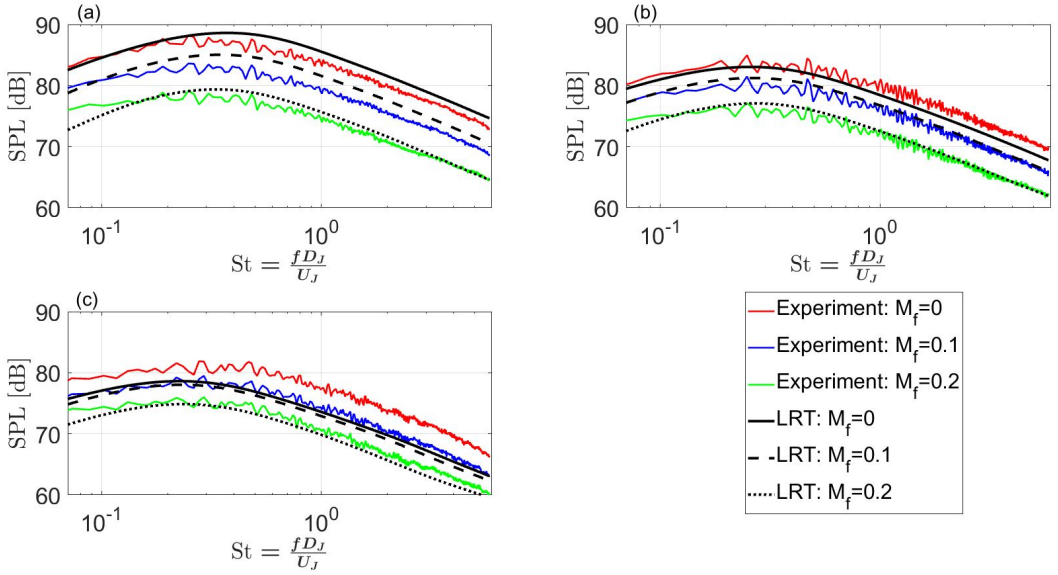

FIGURE 4.2.2: LRT predictions the conical nozzle for $M_J = 0.8$ with experimental and simulation data at 100Hz narrow band frequencies. a). $\theta = 60°$, b). $\theta = 90°$ and c). $\theta = 120°$.

Clearly, there are errors in the directivity of the model away from $\theta = 90°$. Although

Ffowc-Williams [57] corrected Lighthill's Doppler factor to an exponent of -5, Goldstein [47,116] showed that an exponent of -3 better fit the data. Making this change within the LRT source equation would reduce the variation away from $\theta = 90°$ and hence the LRT predictions would improve. This change will be left to future work in this project as the focus of this work is the change in the source distribution at $\theta = 90°$.

Data is often scaled to compare different scenarios [57,117–119]. For far-field mixing noise at $\theta = 90°$, where the effects of refraction are negligible, the OASPL of subsonic jets scales according to the Lighthill's Acoustic Analogy by U_J^8. Figure 4.2.3 shows the scaling of the conical nozzle data with jet velocity using the relationship $70 \log\left(\frac{U_{ref}}{U_J}\right)$, where U_{ref} is a reference velocity. The reference case for this figure is the static $M_J = 0.6$ case. The experimental data collapses well, but due to the under-prediction at high frequency for the $M_J = 0.8$ case, the LRT data does not. This will be revisited later in Section 4.3.3.

When considering scaling of jets with flight Mach number, there are a variety of scaling relationships proposed within the literature [54–56]. Figure 4.2.4 shows the scaling with flight Mach number at $\theta = 90°$ data using the relationship $60 \log\left(\frac{U_J}{U_J - U_f}\right)$, which matches results that found by Michalke [56]. As can be seen, there is a good match between the experimental data sets when $St \geq 0.2$.

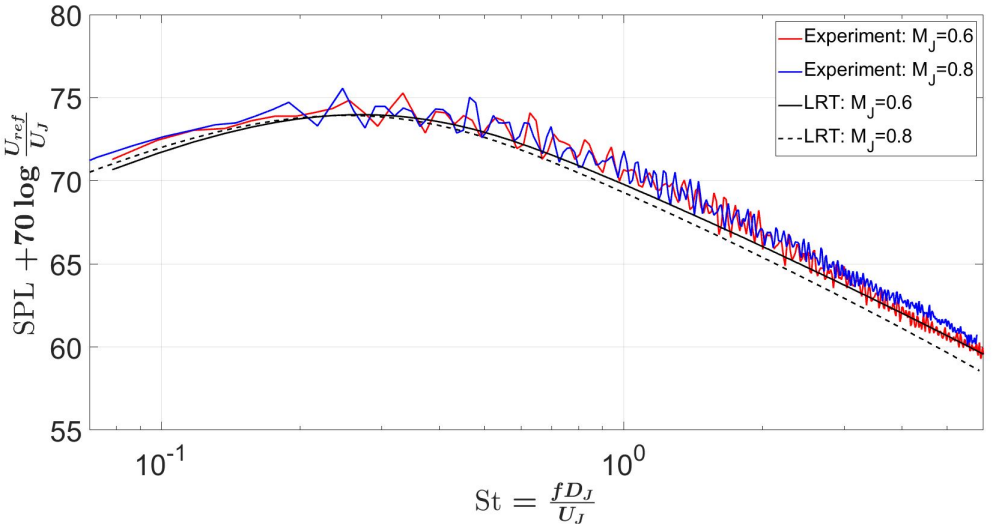

FIGURE 4.2.3: Scaling data with jet velocity using $70 \log\left(\frac{U_{ref}}{U_J}\right)$ at $\theta = 90°$.

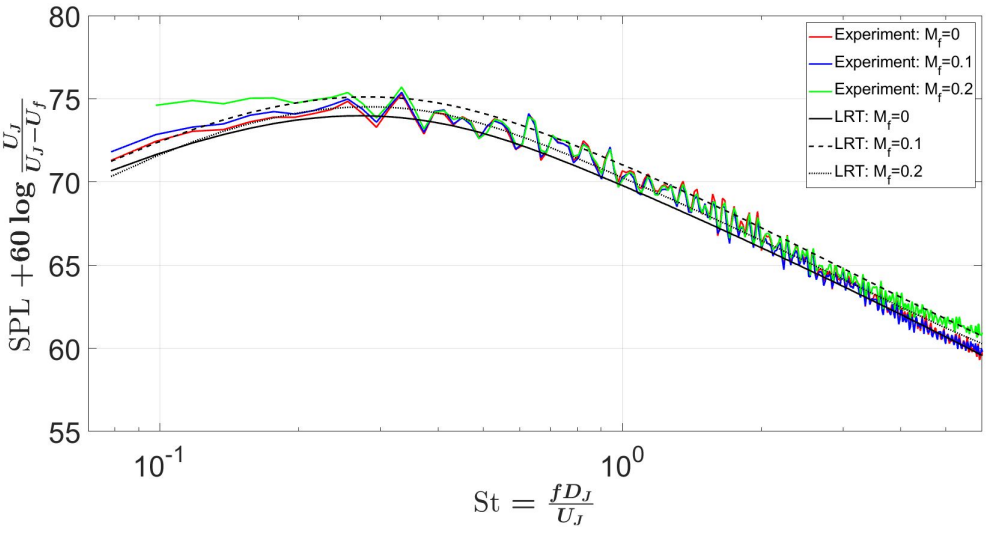

FIGURE 4.2.4: Scaling data with flight velocity using $60\log\left(\frac{U_J}{U_J-U_f}\right)$ for the $M_J = 0.6$ jet at $\theta = 90°$.

The source strength, Q, distribution for the static $M_J = 0.6$ case at $\theta = 90°$ has been analysed and can be seen in Figure 4.2.5. This has been calculated by taking radial slices down the jet and integrating the source equation (Equation 3.1.32) over each slice. The maximum energy is seen to occur at roughly $St = 0.4$, as expected. One would also expect $St = 1$ to be produced just downstream of the end of the potential core, but LRT predicts that this Strouhal number occurs upstream of this. The likely cause of this is the increased spreading rate seen in the CFD, which causes the jet to mix faster and produce stronger high-frequency sources close to the nozzle.

Further evidence of the redistribution of sources towards the nozzle exit can be seen in Figure 4.2.6, where the centroid position of each frequency is compared against the experimental data from Battaner-Moro [120]. Here, it can easily be seen that for $St > 0.4$, LRT predicts that more high-frequency energy exists closer to the nozzle exit compared to the experimental data.

There are several potential explanations for this, but it is difficult to determine which one is dominant. Firstly, it has been demonstrated that RANS over-predicts the spreading rate. Given that the shear layer width determines where different frequencies occur, it is not surprising that higher frequencies occur nearer the nozzle exit. Secondly, the choice of calibration constants will influence where frequencies occur within the jet. As these values have been chosen to match the peak SPL and

frequency at $\theta = 90°$, this will potentially cover up the errors seen in the CFD predictions.

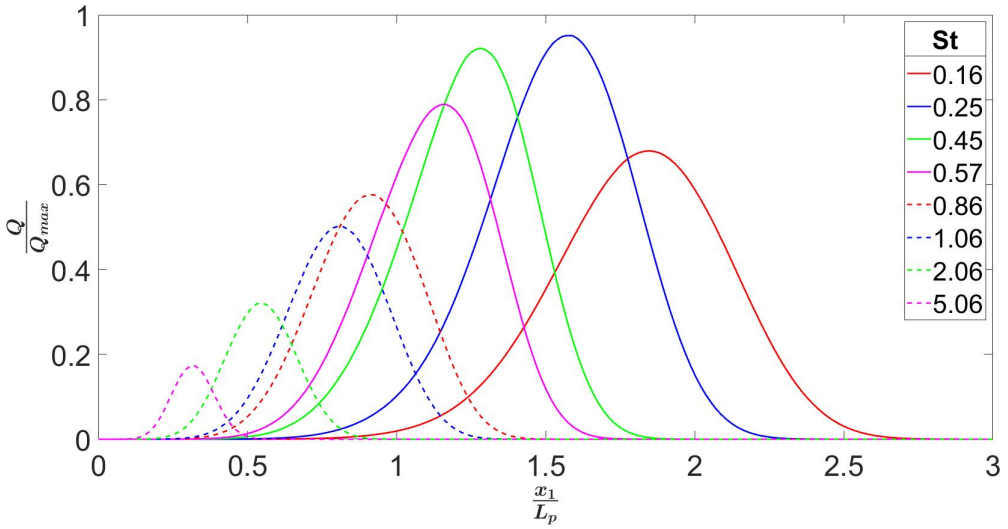

FIGURE 4.2.5: Axial distribution of source strength for the static conical nozzle at different Strouhal numbers for $M_J = 0.6$ at $\theta = 90°$.

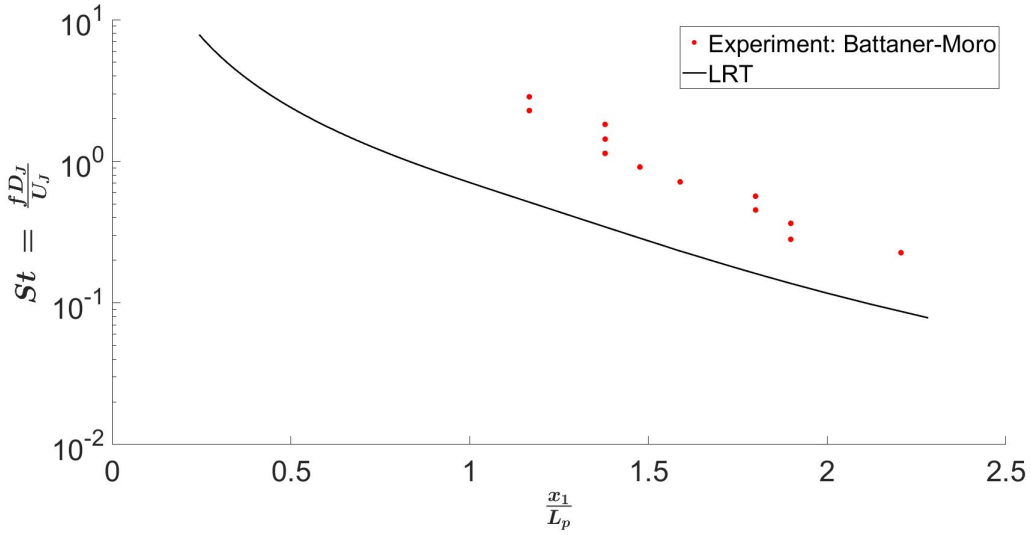

FIGURE 4.2.6: Centroid position per frequency for the static conical nozzle for $M_J = 0.6$ compared with experimental data from Battaner-Moro [120] at $\theta = 90°$.

4.3 Sensitivity studies

In this section, the sensitivity of the LRT method will be studied. There are six variables within the LRT source equation that control the amplitude and frequency response of the model. These are k, ϵ, c_l, c_t, β and Δ.

4.3.1 Turbulence intensity and dissipation rate

The source equation (Equation 3.1.32), outlined in Chapter 3, requires the mean flow variables from a RANS calculation. The obvious question, therefore, is how sensitive is the LRT model to this input data from RANS. The k-ϵ model has been shown to over-predict the potential core length and spreading rate of the conical nozzle in Table 4.4. Thus, the input data to the acoustic model is inherently inaccurate. In order to assess the impact of CFD inputs on the LRT prediction, k and ϵ were increased independently by 5% across the entire jet. The change in SPL at $\theta = 90°$ is shown below in Figure 4.3.1. As expected, the change in TKE significantly affects the low-frequency region, since these larger structures exist in the energy-containing region of the flow. They are, therefore, more susceptible to gross changes in the TKE. Above $St = 1$, there is a roughly constant 0.25dB increase in noise. In contrast to this, a 5% increase in the dissipation rate primarily affects the high frequencies. Intuitively, this makes sense as the dissipative effects have a greater impact on smaller eddies which exist where the shear layer is thinnest. These small eddies generate the high frequency noise and so the greatest change is seen for these frequencies when the dissipation rate is changed.

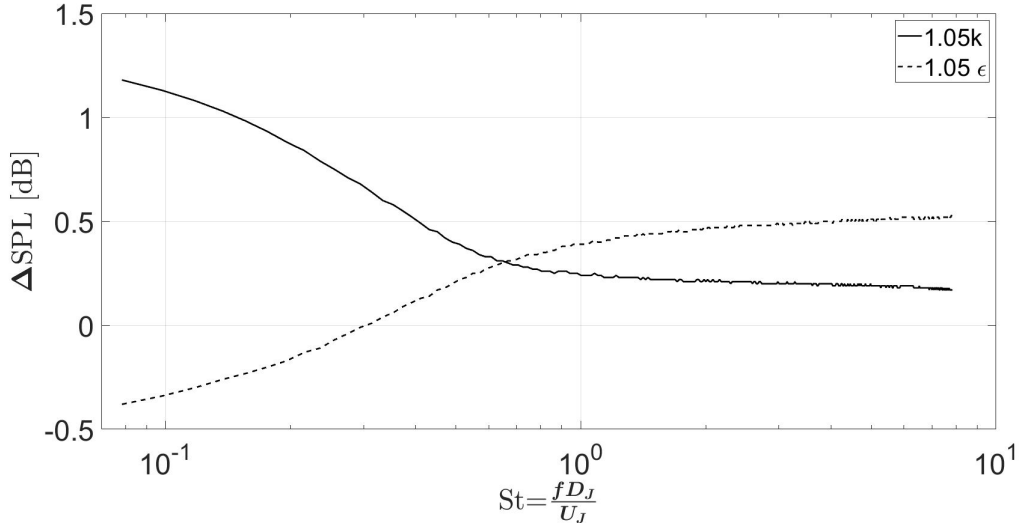

FIGURE 4.3.1: LRT predictions of the change in SPL due to 5% changes in the magnitude of k and ϵ RANS input data for a static conical nozzle at $M_J = 0.6$ and $\theta = 90°$. The values of the calibration constants are unchanged.

It has already been shown that RANS under-predicts the turbulent intensity after six D_J, which is the main noise-producing region and where the low frequencies

dominate. The LRT model is, therefore, particularly sensitive to changes in this region. For example, in Figure 4.1.6, there is an under-prediction of 0.5% for the peak turbulence intensity level at $\frac{x_1}{D_j} = 10$ which equates to a 6.5% change in the TKE level or 1.4dB at $St = 0.1$. Improving the CFD predictions downstream of the end of the potential core would, therefore, lead to a large change in the low frequency predictions. This could be done by changing the turbulence model that is used (see the end of this Chapter). Once new results are generated, the model will need to be re-calibrated. It would therefore make sense to check how sensitive the LRT model is to the values of the calibration constants.

4.3.2 Calibration constants

It was noted in Chapter 3 that it may be possible to generate the same acoustic prediction with multiple combinations of the calibration constants, c_l and c_t. To test the sensitivity of the LRT model, the calibration constants were each varied in 0.01 increments in the ranges $0.35 \leq c_l \leq 0.5$ and $0.7 \leq c_l \leq 0.9$. The root mean square (RMS) difference between the predictions and experimental data was then calculated. The RMS difference is calculated as follows

$$RMS = \sqrt{\frac{1}{N}\sum_{i=1}^{N}\left(\text{Prediction}_\text{i} - \text{Experiment}_\text{i}\right)} \tag{4.3.1}$$

where N is the number of data points.

The results are shown below in Figure 4.3.2. Two features can be seen. Firstly, a linear diagonal region of low error exists as both c_l and c_t are varied. Secondly, rather than a valley-like contour forming to indicate a single minimum, multiple local minima are present in Figure 4.3.2. These local minima will be investigated further shortly.

The calibration procedure mentioned previously matched the peak frequency and SPL level (red dot in Figure 4.3.2), but a more accurate way would be to minimise the errors between prediction and experimental data at all frequencies rather than at a single frequency. It should be noted that the calibration procedure is dependent on having accurate experimental data. However, given that the experimental data has an error of $\pm$0.25dB, the absolute values of c_l and c_t will vary by 0.01 and 0.005 within this error range.

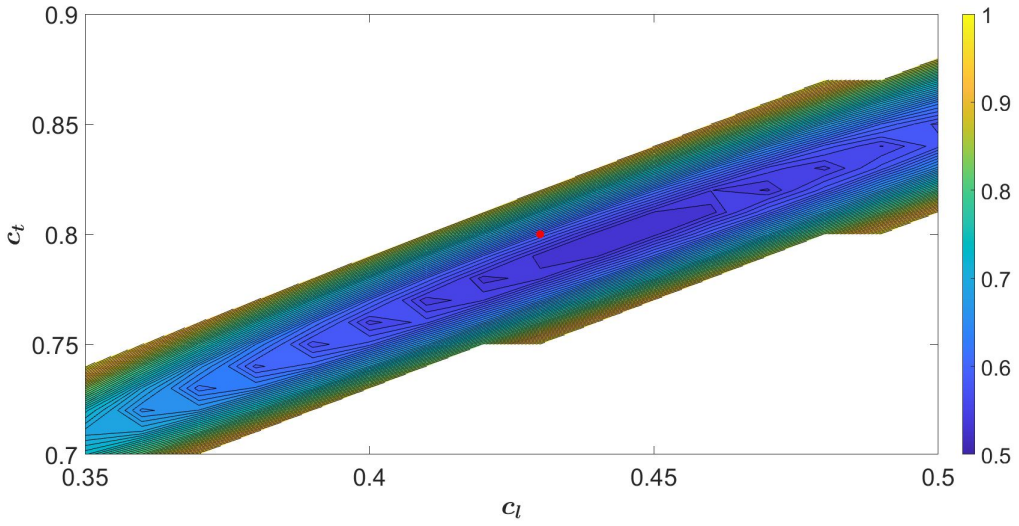

FIGURE 4.3.2: RMS difference of LRT prediction compared to experimental data as c_l and c_t are changed at $\theta = 90^\circ$ for the static conical nozzle at $M_J = 0.6$. The red dot marks the values of c_l and c_t selected through the initial calibration procedure.

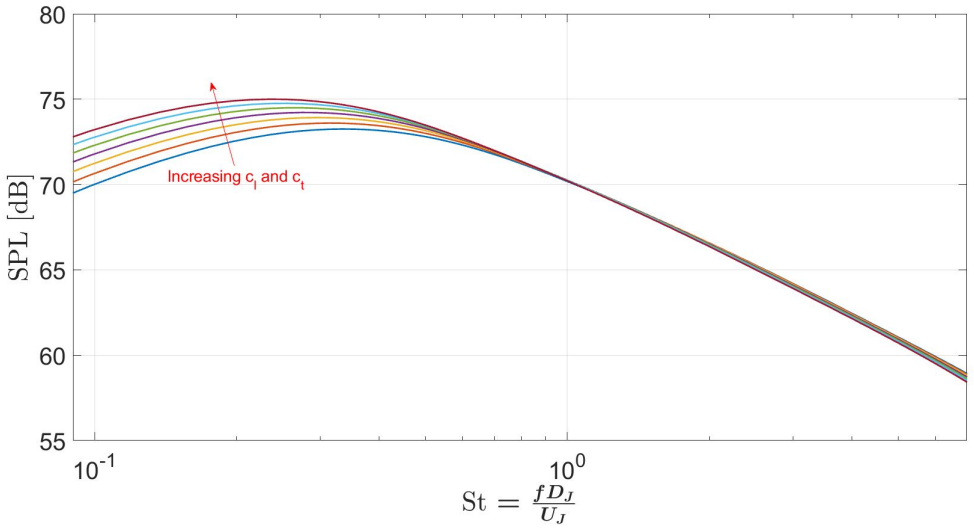

FIGURE 4.3.3: The variation in LRT prediction as c_l and c_t are changed on the diagonal of local minima values at $\theta = 90^\circ$ for the static conical nozzle at $M_J = 0.6$.

Further study of the local minima on the diagonal line in Figure 4.3.2 has been carried out and is shown in Figure 4.3.3. Here it can be seen that increasing the values of c_l and c_t has a negligible effect (< 0.5dB) at $St > 1$. However, a 3dB variation can be seen at $St = 0.1$. This highlights that the low frequency predictions are sensitive to the absolute values of the calibration constants. This should not be surprising as it was already shown that the low-frequency data was influenced more than the high frequency predictions by changes in the CFD data in Figure 4.3.1. On the other hand, the high frequency content ($St > 1$) is shown to have multiple pairs of values which

predict the high frequency content above $St = 1$ to within 0.5dB of each other. Therefore, the high frequency content is less sensitive to the absolute values of the calibration values.

The reason for the variation in sensitivity of the LRT predictions at high and low frequencies is explored in Figure 4.3.4. In this figure, the axial source strength, Q, of the jet, computed using two different pairs of c_l and c_t values, was interrogated at four frequencies. As c_l and c_t are increased (solid to dashed lines), it is clear that the peaks all move upstream. The peaks of the highest frequencies move less than $0.1L_p$ and the low-frequency peaks move by around $0.2L_p$. A change in the time scale exponential, see Figure 4.3.5, is responsible for the change in peak frequency seen in Figure 4.3.3. Although the change in both exponentials is to move frequencies upstream, the time scale exponential is the dominant factor.

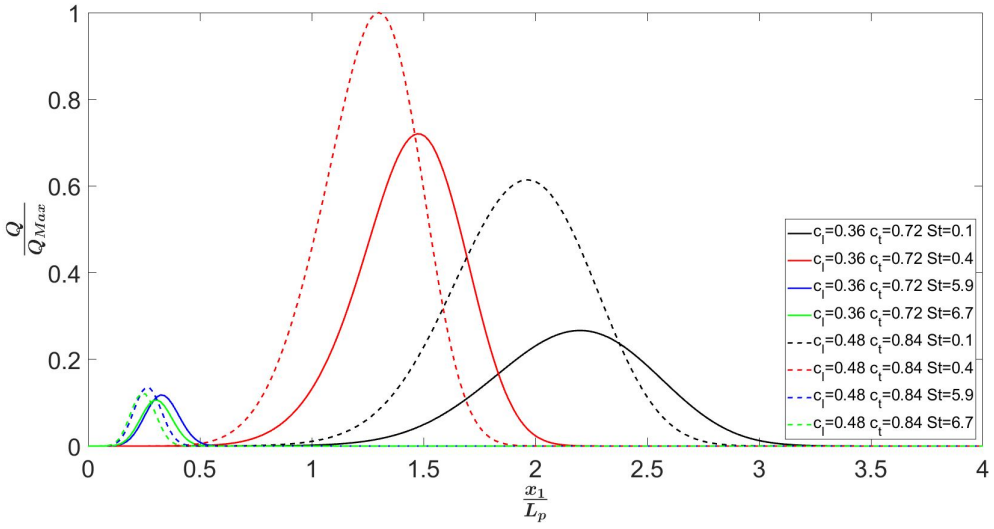

FIGURE 4.3.4: The variation in the source strength, Q, as c_l and c_t are changed at $\theta = 90°$ for the static conical nozzle at $M_J = 0.6$. Q_{max} refers to the maximum source strength in either LRT calculations.

The change in amplitude is linked to the change in peak amplitude and area under the source distribution curve. The change is much larger for the lower frequencies than for the high frequencies. At $St = 0.1$, there is a 23% increase in the area under the source distribution curve, while only a 7% increase at $St = 5.9$. Given the turbulence intensity decays after $\frac{x_1}{L_p} = 1.5$ in the RANS (Figure 4.1.5), moving the peak location of low frequencies closer to the nozzle exit means these frequencies have more energy. Thus, there is a greater change in the SPL at low frequencies.

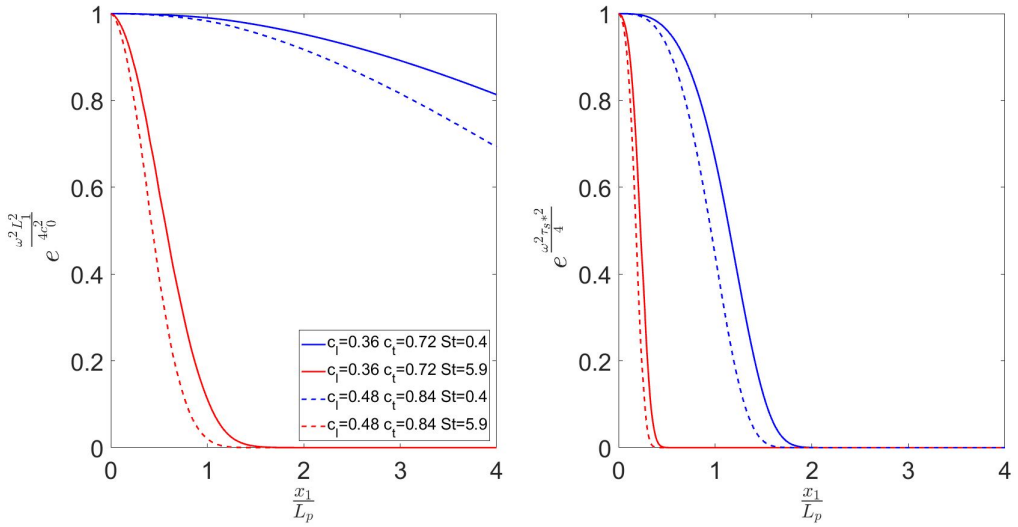

FIGURE 4.3.5: The variation in exponential terms as c_l and c_t are changed at $\theta = 90°$ for the static conical nozzle at $M_J = 0.6$.

4.3.3 Anisotropy

The next sensitivity study concerns anisotropy within a jet. Only the static case will be considered here. Anisotropy, as mentioned in Chapter 2, describes the stretching effect that eddies experience due to shear forces. Near the nozzle exit, where small eddies are typically generated, an eddy will see a large shear relative to its size, so will become distorted and anisotropic. However, as the shear layer width grows, the shear forces decrease. As lower frequencies are produced further downstream, the larger eddies will see lower shear forces and, therefore, tend to be more isotropic. Experiments have shown that the jet does not become fully isotropic until 40-50D_J downstream of the nozzle exit. Thus, some degree of anisotropy is always present within the main noise region of the jet which typically exists within the first twenty-five jet diameters [21].

Anisotropy is classically modelled using the ratio of axial and transverse velocity fluctuations, β, and the ratio of axial and transverse length scales, Δ, previously defined in Equations 3.1.22 and 3.1.25 and repeated below for convenience. Within the literature, there are a range of values reported for β $(0.37 - 0.52)$ and Δ $(\frac{1}{3} - \frac{1}{2})$ as mentioned by Almeida [88]. Experimental values by Khavaran [48] and Proença [121] can be seen in Table 4.5. Khavaran and Proença have determined similar values for Δ. However, Proença found that Δ is radially-dependent since the value changed between the lip and centreline of the jet he studied. This makes more physical sense

than Khavaran's constant values. As previously mentioned, the local shear rate is important to the degree of anisotropy present. Given that the shear layer increases in size as the jet develops, the shear rate (and therefore anisotropy) will be dependent on the axial and radial position. Hence a variable value of Δ within the jet.

$$\beta = 1 - \frac{\overline{u_2^2}}{\overline{u_1^2}} \tag{4.3.2}$$

$$\Delta = \frac{L_2}{L_1} \tag{4.3.3}$$

	Turbulence model		
Variable	Isotropic	Anisotropic [48]	Anisotropic [121]
β	0	0.4	
Δ	1	0.5	0.5 - 0.625

TABLE 4.5: Values of β and Δ used for isotropic and anisotropic turbulence models from the literature.

While Proença, does not present data for β in [121], further work has been carried out and is presented below.

The axial and transverse turbulent fluctuations of the conical nozzle were measured experimentally by Proença in the Doak laboratory and the results can be seen in Figure 4.3.6. Data was taken every diameter in the x_1 direction and every $0.05D_J$ in the x_3 direction. Here, two features can be identified. Firstly, β has a negative value close to the nozzle exit. This is interesting since it is commonly assumed that the axial turbulence is greater than the transverse component. Since this region of $-\beta$ is located inside the potential core, however, there is little turbulence and thus only a small amount of mixing noise is produced. The far-field effect, therefore, is negligible. The second interesting feature is that β remains roughly constant after the end of the potential core along the lip-line. Since this is the area of highest turbulence (and, therefore, mixing noise) within the jet, this justifies the use of a constant value of β for simulations.

Although there is not enough data to produce a similar contour plot of Δ, the difference in shear forces in the axial and transverse directions is thought to lead to a

similar effect as β. Given that the shear forces are responsible for both changes in the size of eddies and their fluctuations, a constant Δ is likely to be seen along the lip-line. Therefore, the flow can be modelled as having constant anisotropy for simple isolated round jets. This matches with results from LES simulations by Karabasov [113] who found that on the lip-line the anisotropy was independent of axial position. Further work will now be carried out using the values proposed by Khavaran.

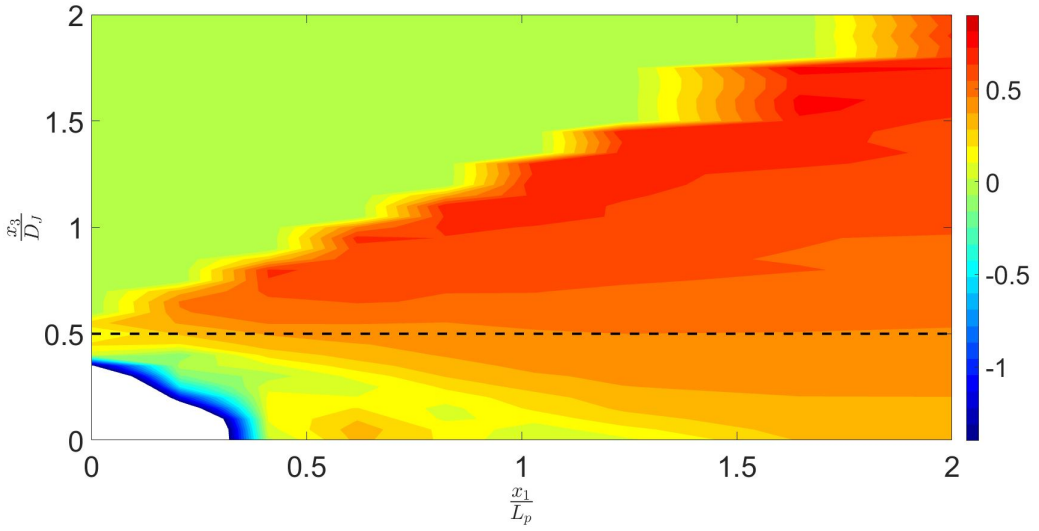

FIGURE 4.3.6: Contours of $\beta = 1 - \frac{\overline{u_2^2}}{u_1^2}$ from the experimental data of the static conical nozzle at $M_J = 0.6$. The dashed line indicates the lip-line. (Data from private communication)

In terms of the acoustic effect, the first question to ask is how much does the anisotropy affect the LRT predictions? To that end, the values of β and Δ have been changed independently from the isotropic values to those stated by Khavaran, see Figure 4.3.7. The LRT prediction results, here, are computed for the static $M_J = 0.6$ jet at $\theta = 90°$, keeping the calibration constants (c_l and c_t) constant. To explain these results, the pertinent equations from Chapter 3 are repeated below for convenience in Equations 4.3.4 - 4.3.6.

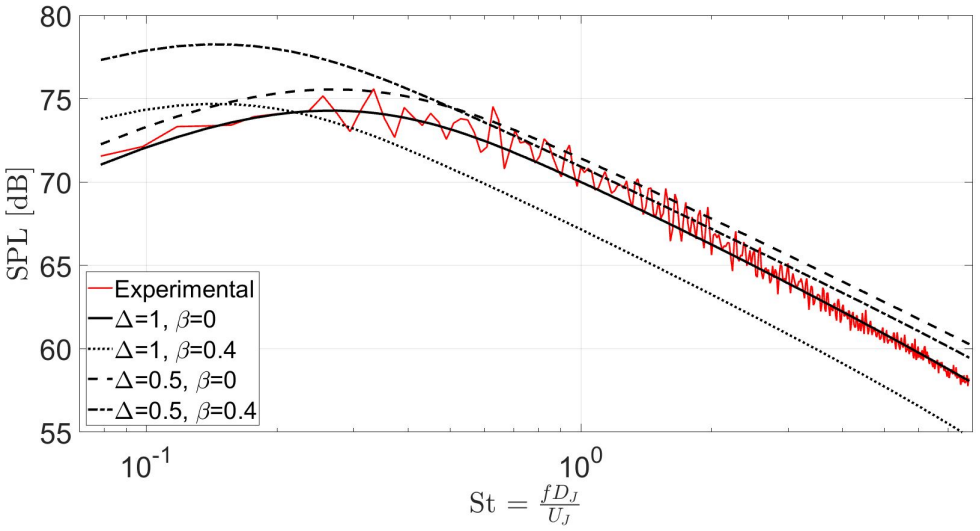

FIGURE 4.3.7: The impact of changing the values of β and Δ on the LRT prediction of the static conical nozzle at $M_J = 0.6$ and $\theta = 90°$. c_l and c_t values have remained constant.

$$P(\mathbf{x},\omega) = \frac{\rho_0^2 \Omega^4 \Pi}{16 c_0^4 r^2 D_F^5} \int_{\mathbf{y_A}} \tau_s^{*4} k^{\frac{7}{2}} \Phi(\mathbf{x},\mathbf{y}) \frac{c_l^3}{c_t^3} \frac{\Delta^2}{(\frac{3}{2}-\beta)^{\frac{7}{2}}} e^{-\frac{\omega^2 L_1^2 (\cos^2\theta + \Delta^2 \sin^2\theta)}{4c_0^2}} e^{-\frac{\omega^2 D_F^2 \tau_s^{*2}}{4}} d^3\mathbf{y_A} \tag{4.3.4}$$

$$L_1 = c_l \frac{k^{\frac{3}{2}}}{\epsilon(\frac{3}{2}-\beta)^{\frac{3}{2}}} \tag{4.3.5}$$

$$\tau_s^* = c_t \frac{k}{\epsilon(\frac{3}{2}-\beta)} \left(\frac{L_1}{D_J}\right)^{\frac{2}{3}} \tag{4.3.6}$$

Several interesting observations can be made from Figure 4.3.7. Firstly, when only β is changed (solid black to dotted black), it is clear to see that there is a large change in the frequency response of the LRT model. The change in β has shifted the curve left (by 700Hz) and slightly up (by 0.5dB) without changing its shape. β is used to calculate the length and time scale, which are used in the exponential functions within the volume integral in Equation 4.3.4. These exponential functions control the frequency-dependent decay. By increasing β, these exponential functions decay faster for all frequencies. In other words, frequencies are moved closer to the nozzle exit. Therefore, the peak frequency occurs at a lower frequency.

A different effect can be seen when only Δ is changed (solid to dashed curve). Here, there is an increase in SPL across all frequencies that ranges from 1.2dB at $St = 0.1$ and gradually increases to 2.2dB at $St = 7.6$. From Equation 4.3.4, Δ appears in three

places: the $\frac{\Delta^2}{(\frac{3}{2}-\beta)^{\frac{7}{2}}}$ term, referred to as the anisotropy amplitude term, the directivity factor, Π, and the source compactness exponential term (the first exponential term). Changing Δ from 1 to 0.5 causes the value of the anisotropic amplitude term to go from 1 to 0.25, which translates to a -6dB change in SPL. The same change in Δ results in a +7.2dB contribution from Π. However, the change in the source compactness term causes eddies to decay slower and, therefore, exist further downstream than before. There is a greater impact at higher frequencies as these frequencies are moved towards the region of the jet which contains more energy. The overall effect of these three factors is an increase in noise at all frequencies.

Finally, it can be seen that changing both the β and Δ values (solid to the dot-dashed line) combines the move towards lower frequencies and the increase in amplitude seen previously. However, the increase in amplitude is accentuated below $St = 0.6$. This is because the dominant exponential, as seen in Figure 3.1.7, is the second exponential which only contains β. Therefore, eddies decay faster and move frequencies closer to the nozzle exit as β increases. The lower frequencies, therefore, exist in a region of high turbulence intensity as the turbulence decays after $1.5L_p$.

Having seen that the introduction of anisotropy into the LRT prediction serves to redistribute too much energy to the low frequencies (by moving the source distribution towards the nozzle exit), the LRT model must be re-calibrated, by reducing the values of c_l and c_t. The re-calibrated prediction is shown below in Figure 4.3.8. It can be seen that by re-calibrating the LRT model, the shape of the spectra at low frequency is unchanged but the fall-off at high frequency (above $St = 1$) is reduced. Therefore, one can conclude by saying that anisotropy increases the high-frequency content of simple isolated jets at $\theta = 90^\circ$ if the low frequency is matched via re-calibration. Although the low frequency is not strictly speaking anisotropic, the effect on the low frequencies is mitigated by the re-calibration method.

It was previously seen in Figure 4.2.2 that there was an under-prediction of the LRT model at high frequency for the $M_J = 0.8$ jet. Since the inclusion of anisotropy has produced an increase in the SPL at high frequency (in Figure 4.3.8), the static $M_J = 0.8$ case has been recomputed. A better match to the experimental data is now obtained, see Figure 4.3.9. It is interesting to note that the isotropic and anisotropic model predictions diverge at $St = 0.5$ for the $M_J = 0.8$ case, whereas the $M_J = 0.6$ case

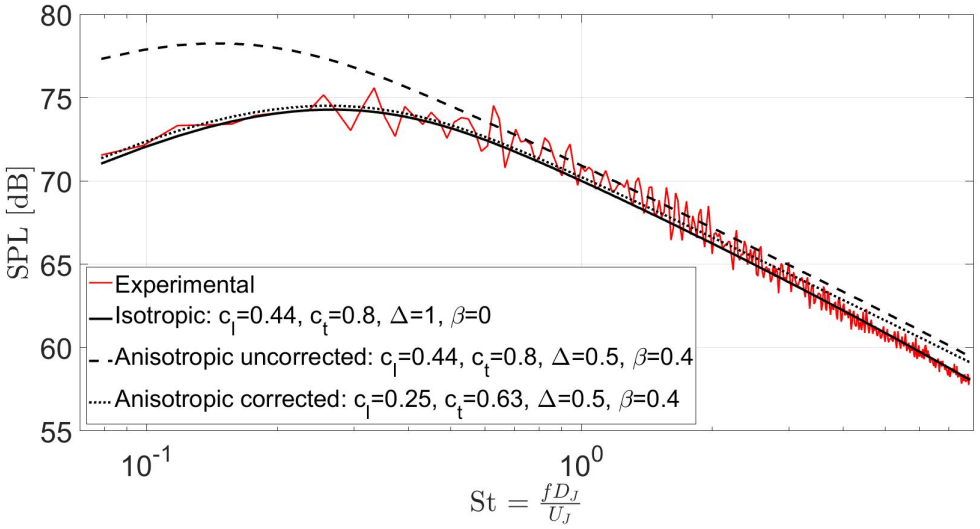

FIGURE 4.3.8: LRT prediction of the static conical nozzle at $M_J = 0.6$ and $\theta = 90°$ with and without correcting for the anisotropy.

diverged above $St = 1$. Therefore, an anisotropic model is more relevant for higher jet Mach numbers.

Although there is a lack of experimental data to explain this, let's consider what is happening physically as M_J increases. Since the spreading rate of jets does not dramatically change with increasing M_J [53], eddies will experience a greater shear over approximately the same shear layer width. Consequently, a greater stretching of the eddies is thought to occur close to the nozzle exit as M_J increases (i.e. the eddy is more anisotropic). As eddies travel downstream, they will become more isotropic but as the spreading rate is roughly constant and eddies start as being more anisotropic, a greater proportion of the frequency spectrum will be influenced by the anisotropy. There is a greater increase in the amplitude at high frequency for the $M_J = 0.8$ case as opposed to the $M_J = 0.6$ case simply because the TKE increases with jet Mach number. Therefore, the effect of anisotropy is magnified.

Further analysis was undertaken on the anisotropic data for the $M_J = 0.8$ case. It was noted in Figure 4.2.3 that the LRT predictions did not collapse when data was scaled for different jet Mach numbers. Re-plotting this data with the anisotropic data allows for the LRT prediction to collapse at high frequency and within 0.4dB at low frequency.

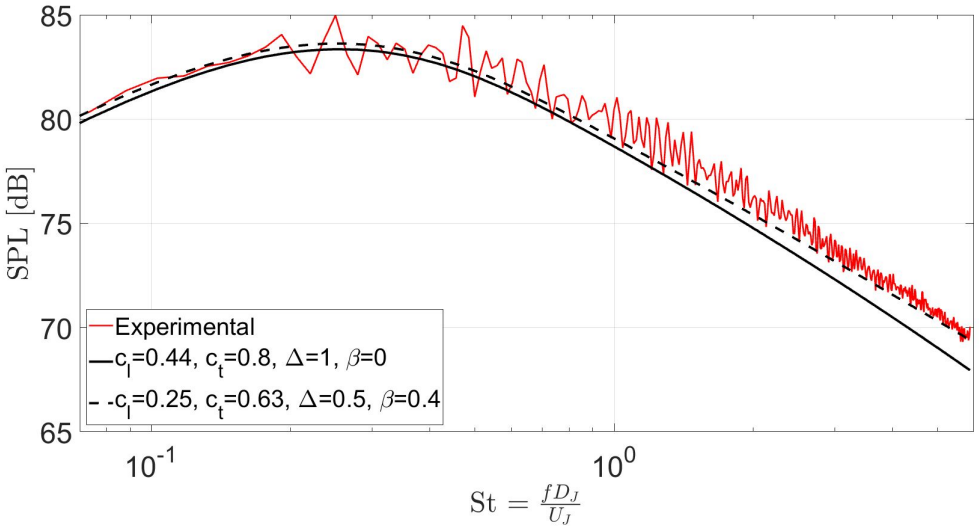

FIGURE 4.3.9: LRT prediction of the isotropic and corrected anisotropic models for the static conical nozzle at $M_J = 0.8$ and $\theta = 90°$.

With improvements in predictions seen at $\theta = 90°$, attention can be turned to other polar angles. Away from $\theta = 90°$, the $\cos^2\theta + \Delta^2 \sin^2\theta$ term within the source compactness exponential, which could be thought of as an anisotropy directivity, will introduce additional variation to the predictions. The isotropic and anisotropic LRT predictions at $\theta = 60°$ and $\theta = 120°$ are shown below in Figure 4.3.10. Here it can be seen that there is a similar level of improvement in the rear arc predictions for both jet Mach numbers. The amplitude of the peak frequency is better predicted with the anisotropic model as this has been reduced by approximately 1.5dB. Although the noise at high frequencies is still over-predicted at $\theta = 60°$, the error has been reduced in the anisotropic model. However, when looking at the results in the forward arc, the anisotropic model has reduced the LRT predictions by 0.5dB, resulting in a greater error compared to the experimental data. It has been decided that work in further chapters will use the anisotropic model. This is because better predictions are made at high frequency at $\theta = 90°$. Away from this polar angle, although there is a detriment to the accuracy of predictions in the forward arc, this is much smaller than the reduction in error in the rear arc. Therefore, the benefits of changing to the anisotropic model outweigh the drawbacks.

Given that such a large impact has been observed for a simple axisymmetric geometry, it is hypothesised that modelling the anisotropy for an asymmetric nozzle is essential. This presents a problem. Each geometry will generate a different flow field and hence,

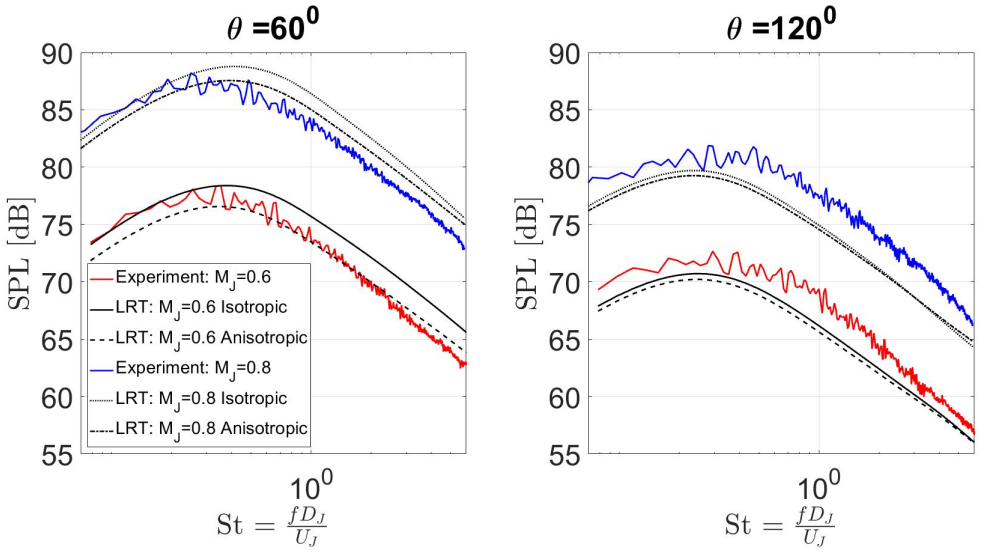

FIGURE 4.3.10: LRT prediction of the static conical nozzle at $M_J = 0.6$ and 0.8 at $\theta = 60^\circ$ and $\theta = 120^\circ$ with isotropic and anisotropic models.

a unique set of anisotropy values. While RANS will never contain the necessary data to calculate the values of β and Δ directly, approximate values could be used in the absence of further data. A small amount of experimental or LES data could help to re-calibrate the model in the future. For now, the same values of β and Δ will be used for future geometries.

4.3.4 RANS turbulence models

The final sensitivity study that has been conducted is to do with the selection of the turbulence model used within RANS. Looking at the literature, Mohan [13] found, that although the length and time scales changed when different turbulence models were used, the far-field noise data only varied by around 0.5dB. Mohan, therefore, concluded that the results were insensitive to the turbulence model used. Given that Mohan only analysed a static axisymmetric jet, it is worth looking into this further, given the fact that the analysis in future chapters will deal with asymmetric and installed jets.

Figure 4.3.11 shows the results of this study for a 2D simulation of the conical nozzle. In Figure 4.3.11, it can be seen that there is a large variation in potential core length between the different turbulence models. Therefore, the region of maximum turbulence changes position relative to the nozzle exit. As already mentioned, this will not influence the isolated far-field mixing noise greatly but will have a greater impact

on installed predictions. Moving the peak turbulence downstream would increase the cut-on frequency of reflected mixing noise as less of the source distribution will occur underneath the wing. It is also worth pointing out that the RANS models do not get the decay rate of velocity correct after the end of the potential core. Despite having the longest potential core length, the standard k-ω model actually predicts the velocity fall-off the best. However, it is the turbulence level that is most crucial for the mixing noise problem.

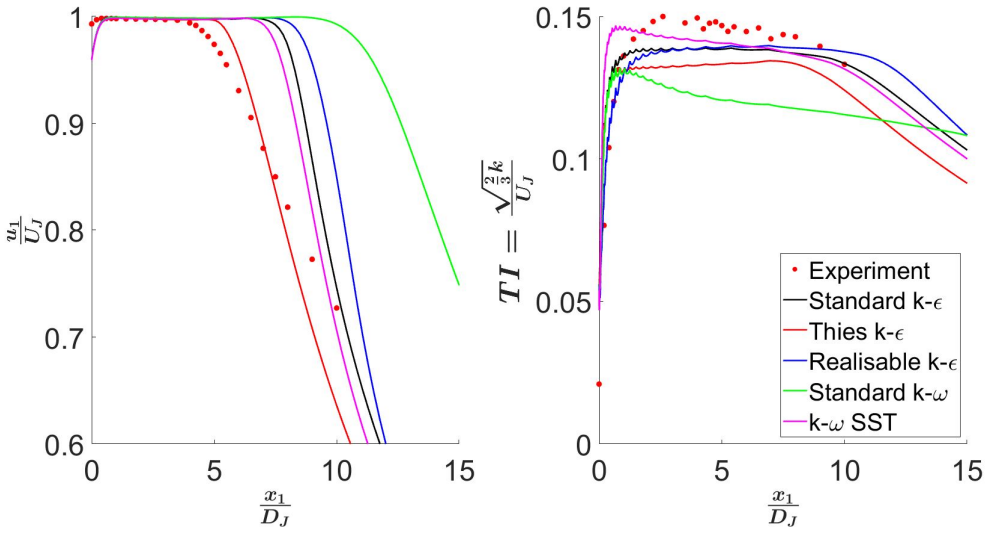

FIGURE 4.3.11: Variation in centreline axial velocity (left) and lip-line turbulence intensity (right) for different turbulence models for a 2D static conical nozzle at $M_J = 0.6$.

When looking at the turbulence levels on the lip-line in Figure 4.3.11, a small amount of variation is seen in the peak level and shape of the profiles between different turbulence models. This would suggest a small variation in isolated acoustic results between models, which is what Mohan [13] reported. It is difficult from this figure to determine the best model to use for predicting jet flows as none of the models match the experimental data perfectly. The notable exception to this is the results of the standard k-ω model which has the longest potential core length (over $10D_J$) and largest under-prediction ($\approx$2%) in turbulence intensity predictions. Therefore, it is reasonable to conclude that one should not use this turbulence model for predicting jet flows. It should be noted that as adjusting the empirical constants used within the k-ϵ model did provide improved predictions of the potential core length, it is possible that the other turbulence models could be improved by changing their empirical constants. However, that analysis is beyond the scope of this thesis.

While acoustic predictions could be made for each of the different turbulence models, several problems start to become apparent. The different turbulence intensity levels predicted in the CFD will lead to a variation in acoustic results if the same calibration constants are used. Similar predictions could likely be made by simply re-calibrating the LRT model. This would effectively cover up the variation in CFD results rather than solve the underlying issue. This subject is clearly complex and so the choice of which turbulent model to use should be considered carefully.

The work in this chapter has shown that reasonable agreement can be found close to the nozzle exit by using the k-ϵ turbulence model with Thies and Tam's coefficients compared to experimental data. Further work in this thesis will look at changes to the geometry which primarily affect the flow field close to the nozzle exit. Therefore, it seems logical to use the k-ϵ model with Thies and Tam's coefficients for these geometries.

4.4 Summary of chapter

In this chapter, the LRT method has been validated for a simple conical nozzle. The following conclusions have been made.

- It has been seen in the literature that k-ϵ RANS predictions often over-predict the potential core length of jets. To reduce this error, the turbulence model coefficients have been adjusted to those found by Thies and Tam. This reduces the over-prediction of the potential core length of the conical nozzle from 64% to 20%. Therefore, the peak turbulence region is in a more realistic position.
- Using the updated k-ϵ model, the RANS predictions of a conical nozzle are compared to experimental data. RANS predicts the axial velocity and turbulence intensity levels upstream of the end of the potential core to within 5 and 0.5% of the experimental data, respectively, but under-predicts both quantities further downstream. By ten jet diameters, RANS under-predicts the velocity by 7% and the turbulent intensity by 1%.
- It is thought that despite RANS not predicting the correct distribution of the energy after the end of the potential core, the calibration procedure of the LRT model reduces the impact of this error on the acoustic predictions.

- An isotropic turbulence model was initially used for the acoustic prediction of the conical nozzle. The LRT model predicts the acoustic response well at $\theta = 90°$ for different jet exit Mach numbers and co-flow flight Mach numbers but over-predicts the high frequency in the rear polar observer arc (by 2dB at $St = 3$ at $\theta = 60°$) and under-predicts the forward arc (by around 1dB at $\theta = 120°$ at all frequencies).

- The sensitivity of the LRT model was investigated and it was found that the low frequencies below $St = 1$ are particularly sensitive to subtle changes in the TKE and calibration values. As this is the energy-containing region of the flow, this is not a surprising result. However, this conclusion will be useful to keep in mind when looking at the results in future chapters at low frequency.

- As the effect of anisotropy can be modelled within the LRT source equation, the impact of this on the results was discussed. Although the anisotropy changes with position in the jet, it was found from experimental data of the conical nozzle that the value of the ratio turbulent fluctuations, β, on the lip-line was roughly constant. Therefore, it was proposed that a constant value of anisotropy could be applied to the entire jet. While this is not strictly true for low frequencies, it is not possible to calculate the anisotropy from the RANS data.

- The effect of including anisotropy within the LRT model was to move energy towards lower frequencies. To correct this, the LRT model was re-calibrated ($c_l = 0.25$ and $c_t = 0.63$). By doing this, it was seen that anisotropy improved the high frequency predictions of the LRT model at $\theta = 90°$, especially at $M_J = 0.8$. Away from $\theta = 90°$, the anisotropy was seen to mainly affect the rear arc predictions by reducing the over-prediction of the LRT model by 1.5dB at $\theta = 60°$. Therefore, the use of anisotropy improves the accuracy of the LRT model in predicting the mixing noise of a simple round jet.

  It should also be noted that the anisotropy has been assumed to not change with jet Mach number. There is not enough experimental data to say if this is a correct assumption to make. Despite this, improved prediction can be made at $M_J = 0.8$ with an anisotropic compared to an isotropic model.

Now that the LRT method has been validated for a simple nozzle, further work can be undertaken on more realistic geometries. Of particular interest, is the change in the

source distribution with geometry. This is due to wanting to be able to understand how noise scales with design changes, as this will be most useful at the preliminary design stage. Therefore, the rest of this thesis will primarily focus on changes at $\theta = 90°$. An anisotropic model will be used for further work as it has been shown to improve the high frequency predictions of the conical jet at this polar angle. Although the amount of anisotropy is thought to vary with jet Mach number and geometry, there is not enough experimental or numerical data to quantify the effect. Therefore, the same anisotropic values will be used to provide approximate predictions. LES could be used in the future to allow for a more in-depth study of this and to refine the LRT results.

Chapter 5

Isolated Jet Mixing Noise

In the previous chapter, the LRT method was validated against experimental results for an isolated conical nozzle. By changing the k-ϵ turbulence model coefficients from their standard values to those found by Thies and Tam, the over-prediction of the potential core length, typically seen in k-ϵ RANS models, was reduced by over 40%. The flow field was shown to be modelled to within 1% for the velocity field and 5% for the turbulence field within the first five diameters, but under-predictions were present further downstream. The acoustic predictions were calibrated at $\theta = 90^\circ$ for the static $M_J = 0.6$ case and it was found that no change in the calibration constants was needed as the jet and flight Mach numbers were varied. Although accurate predictions to within 0.5dB could be made at $\theta = 90^\circ$, over-predictions were present in the rearward arc while the mixing noise was under-predicted in the forward arc. The sensitivity of the LRT model to the CFD input, calibration constants and the effect of anisotropy on the results was then discussed. An improvement in predictions was found when the anisotropic nature of the flow was accounted for, especially in the rear arc and at higher Mach numbers.

Having validated the LRT method, one can now examine how moving towards more realistic geometries changes the isolated mixing noise. Although the LRT method has previously been used to look at isolated geometries, the geometries in this chapter have not been studied. Furthermore, LRT has not been used to look at the azimuthal variation in jet mixing noise. Finally, previous work has only considered an isotropic case, so the acoustic results presented here for the anisotropic model are new. Before

one reaches a fully installed geometry, two main geometric changes occur from the simple round nozzle studied previously. These are the bullet or centre body and the pylon. An annular nozzle with a centre-body in is studied first to provide a baseline for future comparisons. The change in the flow field and noise compared to the conical nozzle is discussed. Next, the impact of the pylon is investigated to ascertain how the asymmetric flow field impacts the mixing noise produced. This investigation is split into two parts. Firstly, a study is conducted on the internal blockage produced by the pylon. Three different internal pylon blockages are studied. This is done to see how well the LRT method can predict the asymmetric flow field and azimuthal variation in the mixing noise. Finally, the impact of the external pylon blockage surface on the flow and jet mixing noise will be considered. The same simulation conditions as used in the previous chapter are studied and are shown in Table 5.1. Some of the results in this chapter are also published in [122].

As the focus of this chapter is on how the mixing noise and source distribution change or scale with geometry, the acoustic results will focus on the changes at $\theta = 90^\circ$. This was shown in the previous chapter to be the place where the most accurate LRT predictions could be made. Therefore, the errors away from this polar angle in the LRT predictions will have a negligible impact on the results in this chapter.

M_J	M_f
0.6 and 0.8	$0.0 \rightarrow 0.2$ (0.1 intervals)

TABLE 5.1: Cases simulated for the annular nozzle and blocked nozzles.

The inclusion of the centre body and pylon presents a few problems. Firstly, the bullet will create a stagnation point at its tip. The result of this is that the maximum velocity of the jet does not occur on the centreline and so the definition of a potential core length, as used in the previous chapter, is difficult. Furthermore, the bullet and pylon reduce the flow area compared to the conical nozzle. These geometries, therefore, have different mass flow rates and momentum to each other. To be able to scale and then compare the results of these geometries, a new parameter needs to be defined. We will, therefore, use the effective diameter, D_{eff}. This is defined as the diameter of a round nozzle without a centre body or blockage, which has the same flow area as the geometry being studied.

5.1 Isolated Annular nozzle

The baseline nozzle for further studies is an isolated annular nozzle, shown below in Figure 5.1.1. The annular nozzle has an exit diameter of 40mm and a flow area of 798mm^2. This gives an effective diameter of 31.9mm. The bullet extends $0.95D_J$ past the nozzle exit. Details of the CFD mesh that was developed can be found in Section 3.1.2. One of the simplifications that was made during the generation of the CFD mesh was the removal of the struts that hold the centre body in place. This was done to reduce the complexity of the internal nozzle mesh and it was assumed that these would produce a negligible contribution to any noise produced. This point will be revisited later in this chapter.

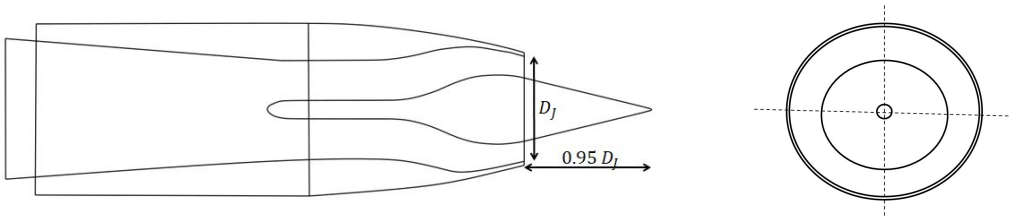

(A) Side view

(B) Front view

FIGURE 5.1.1: Schematic of the baseline annular nozzle geometry.

5.1.1 CFD results

The first analysis that was carried out on the annular nozzle was a mesh sensitivity study. Although it was shown in the previous chapter that a $y^+ \approx 35$ was sufficient to model the potential core length, the match to radial profiles down the jet was not explored.

RANS simulations have been run on two different mesh densities ($y^+ \approx 1$ and 35). The radial profiles of velocity and turbulent intensity for the static $M_J = 0.6$ jet are shown below in Figure 5.1.2. Similar to the conical nozzle results in the previous chapter, RANS can predict the peak axial velocity profiles to within 5% up to $\frac{x_1}{D_J}45$ in Figure 5.1.2. The stagnation point at the bullet tip is also captured by RANS. After four diameters, the experimental velocity data show a slight negative skew that the RANS data does not show. This is likely due to a compounding probe alignment error in the experiment. By $\frac{x_1}{D_J} = 8$, the peak velocity is under-predicted by 7%. Given that similar results were seen in Figure 4.1.2 for the conical nozzle and both meshes for the

annular nozzle under-predict the peak velocity, this result is likely due to an error in the k-ϵ turbulence model. It is thought that the under-prediction is linked to the over-prediction of the spreading rate that was highlighted in the previous chapter.

For the turbulent intensity predictions, similar trends are again seen to the conical nozzle results. After four nozzle diameters, the turbulence intensity is under-predicted by about 1%. The radial profile shape, however, appears to be well captured. Small differences can be seen in the inner shear layer, close to the jet centreline, between the RANS predictions and the experimental data up to $\frac{x_1}{D_j} = 4$. However, due to the magnitude of turbulence in the outer shear layer being much higher than the inner shear layer, it is thought that this error will not influence the far-field mixing results very much. Despite the assumption of isotropic turbulence within a k-ϵ RANS model, a surprisingly good prediction is made close to the nozzle exit, where the flow is likely to be anisotropic in nature. No experimental data was taken for this geometry that would allow the difference in anisotropy between the conical and annular nozzle to be compared. The use of LES on this nozzle could provide this information, but this will be left to the future work of the project.

The final point of note is that there is very little difference between the predictions using the coarse ($y^+ \approx 35$) and the fine ($y^+ \approx 1$) meshes in Figure 5.1.2. Minor differences can be seen at the edge of the shear layer at $\frac{x_1}{D_j} = 8$. However, due to the low-intensity levels here, this will have a negligible influence on the far-field noise. Thus, for the subsequent simulations presented in this thesis, the $y^+ \approx 35$ mesh is used to reduce the computational time.

The variation in the velocity and turbulence intensity as a flight-stream is added to the annular nozzle is seen below in Figure 5.1.3. Very close to the nozzle exit, there is very little difference in the velocity profiles but, as expected, there is a decrease in the peak turbulent intensity level as M_f increases. This trend continues at $\frac{x_1}{D_j} = 4$, with the inner shear layer taking longer to mix out with the increased flight-stream velocity. The velocity profile for the static case at $\frac{x_1}{D_j} = 8$ under-predicts the peak level by 7%. However, the magnitude of the axial velocity is more accurately predicted as the flight-stream increase as the error reduces to 5 and 0.5% for the $M_f = 0.1$ and 0.2 cases, respectively. The peak turbulence level is over-predicted by 1 and 0.7% for the $M_f = 0.1$ and 0.2 cases, respectively, at $\frac{x_1}{D_j} = 8$.

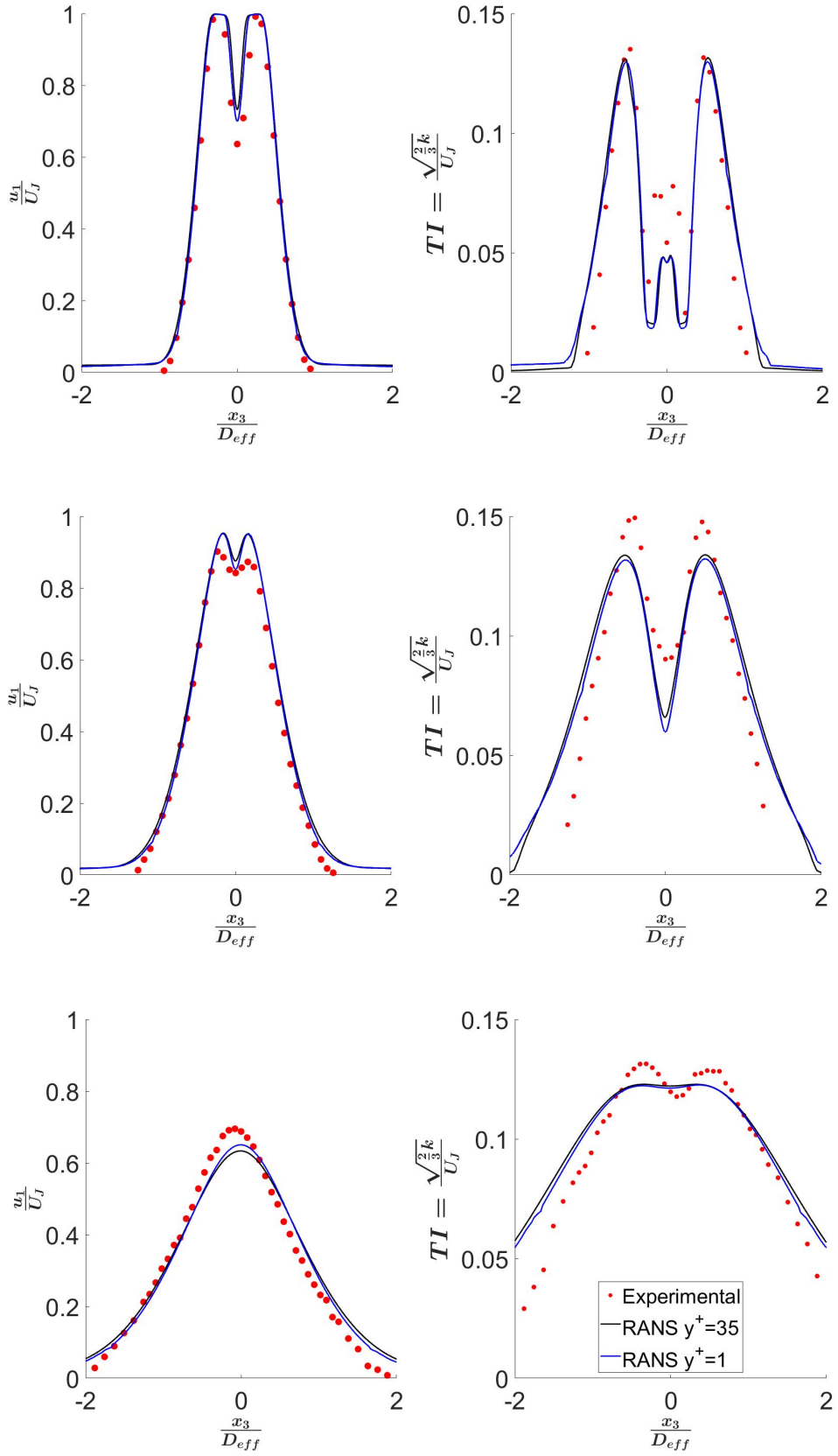

FIGURE 5.1.2: Radial profiles of $\frac{u_1}{U_J}$ (left) and turbulence intensity (right) for the static annular nozzle at $M_J = 0.6$. Each row corresponds to $\frac{x_1}{D_J} = 2$, 4 and 8, respectively.

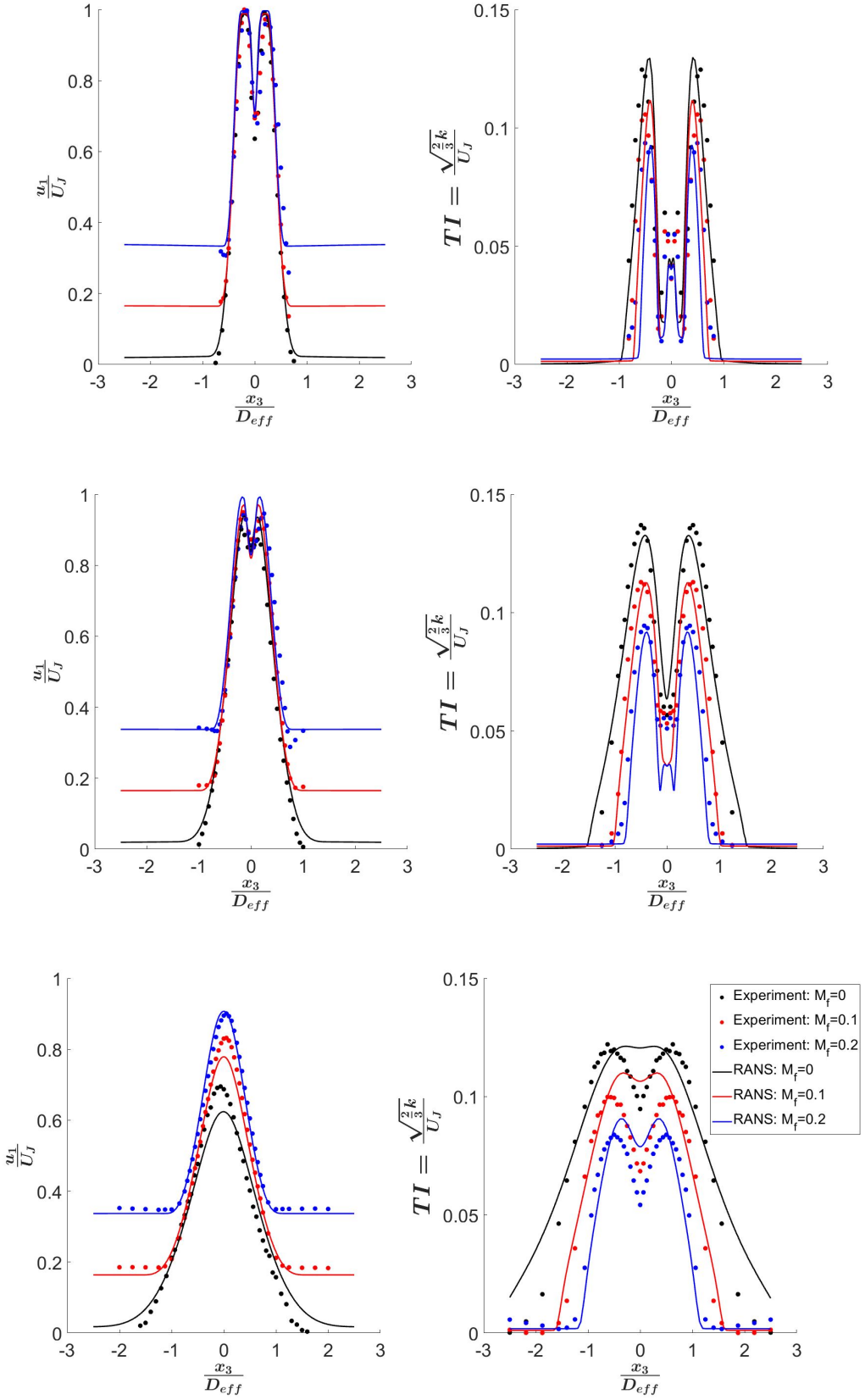

FIGURE 5.1.3: Radial profiles of axial velocity (left) and turbulence intensity (right) for the annular nozzle at $M_J = 0.6$ and $M_f = 0, 0.1$ and 0.2. Each row corresponds to $\frac{x_1}{D_J} = 2$, 4 and 8, respectively.

The results in this section have shown that accurate predictions can be made close to the nozzle exit. In this region of flow, the main difference between the conical and annular nozzle is the presence of the bullet, which extends $0.95D_J$ from the nozzle exit. The impact that this has on the shape of the jet is shown in Figure 5.1.4. To generate this data, axial velocity profiles were taken every $0.1D_J$ in the CFD simulation for the first four diameters. The experimental data for these geometries was not taken to the same spacial separation and so can not be compared. However, given the good agreement close to the nozzle exit and the small differences in spreading rate at this point in the jets, there will be a minor difference between RANS and the experimental data.

The edge of the jet is defined as the point at which the axial velocity reduces by 90% from the peak velocity to the velocity of the flight-stream. For a static jet, this results in the same definition as was used in Figure 4.1.2. From this figure, one can see that the flow from the annular nozzle follows the bullet profile after the nozzle exit, creating a vena contracta effect. On the other hand, the conical nozzle shows no contraction. This is likely because the conical nozzle has a small convergence angle ($\alpha = 2.5^\circ$), resulting in the flow being nearly horizontal at the nozzle exit. In contrast, the annular flow follows the bullet at an angle of 18° below the horizontal. This large change in the angle of the flow at the nozzle exit results in a change in the radial component of velocity. At the vena contracta point at $\frac{x_1}{D_J} = 0.5$, the annular nozzle has a radial velocity of $0.23U_J$ whereas the conical nozzle is only $0.02U_J$. However, after the vena contracta, both jets spread at the same rate and the radial velocity is roughly the same by $\frac{x_1}{D_J} = 4$. Therefore, this is a local effect close to the nozzle exit.

Looking at the in-flight data in Figure 5.1.4, the flight-stream causes the spreading rate to reduce, as expected. Again, there is no vena-contracta effect in the conical nozzle data but the vena-contracta effect of the annular nozzle moves downstream by $0.2D_J$. Similarly to the static case, the spreading rate is the same after this point. Both axis have been normalised by the jet diameter rather than an effective diameter as the difference in jet shape needs to be highlighted.

So, what does this tell us? The annular nozzle has a smaller cross-sectional area and shear layer at all points in the jet and so will generate less noise. The vena contracta

effect will become important when the mixing noise from the conical and annular nozzles is compared.

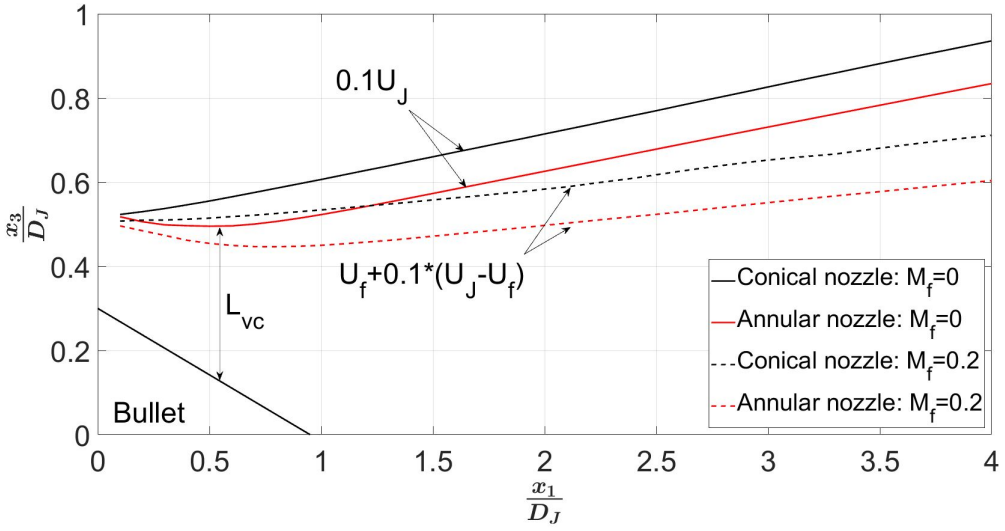

FIGURE 5.1.4: Comparison of how the edge of the jet varies between the conical and annular nozzles.

The analysis of the CFD results of the annular nozzle has shown that similar predictions to the conical nozzle studied in the previous chapter can be made. These provide a good basis for acoustic analysis.

5.1.2 Acoustic results

The largest geometric change that occurs between the conical and annular nozzles is the inclusion of the centre-body. It has been demonstrated that this produces a stagnation point in the velocity field but there are also two acoustic effects; reflection from the bullet and a change in the mixing noise due to the reduced flow area. A comparison of LRT data with and without reflections present, revealed that reflections had no impact on noise predictions below $St = 0.6$ and only made a 0.15dB difference at $St = 6$ at $\theta = 90°$. Given that the bullet only extends $0.95D_J$ from the nozzle exit, it is thought that the main impact will be on $St \geq 7$ which is above the high-frequency limit of the experimental data and LRT calculation. Therefore, the reflective noise from the bullet will not be discussed further. The rest of this analysis will focus on the change in the mixing noise.

When analysis began on this geometry, it was noticed that the experimental data contained additional noise above $St = 3$. By rotating the nozzle within the

experimental set-up, a change in the noise level was produced depending on the alignment with the struts which hold the bullet in place. The likely cause of this noise is vortex shedding from these struts. As mentioned in Section 3.1.2, these struts were removed from the CFD model to reduce the mesh density. As there is no model for vortex shedding within the LRT method, this additional noise can not be captured. Therefore, analysis in this section will be limited to below $St = 3$.

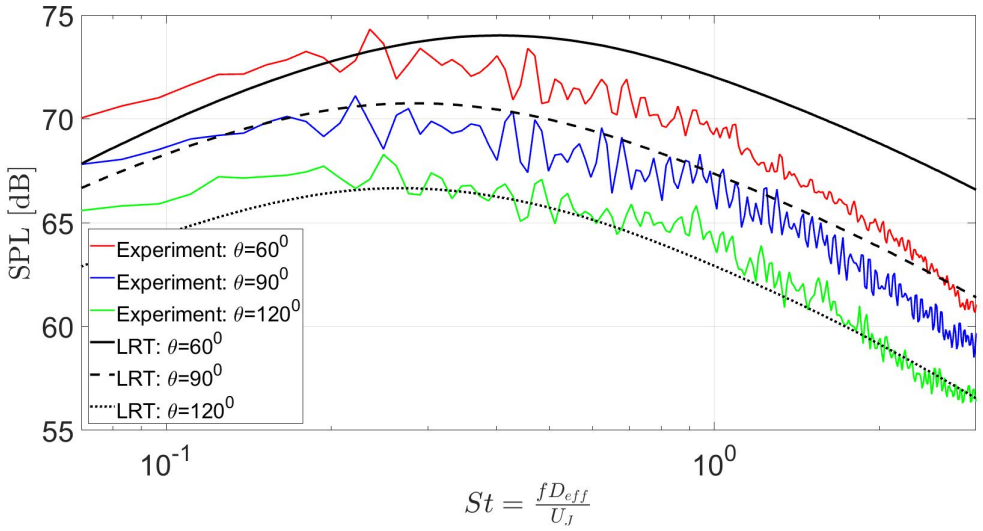

FIGURE 5.1.5: LRT predictions for the static annular nozzle for $M_J = 0.6$ at $\theta = 60$, 90 and 120° with experimental and simulation data at 100Hz narrow band frequencies.

Figure 5.1.5 shows the LRT predictions of the static annular nozzle at three different polar angles. The anisotropic model was used to generate these results with the corrected calibration values found at the end of the last chapter ($c_l = 0.25$ and $c_t = 0.63$). Here it can be seen that the LRT model over-predicts the peak SPL by 0.8dB at $\theta = 90°$. If one subtracts this delta from all polar angles, the LRT prediction gives the same trends as seen for the conical nozzle in the previous chapter, i.e. over-predict the high frequency in the rear arc and under-predict at all frequencies in the forward arc. A similar level of over-prediction at $\theta = 90°$ was found when the refined mesh was tested. Therefore, the LRT predictions are repeatable. An additional experimental data set was then examined to see if there was an error within the experimental data set being used. However, the two experimental data sets were found to be within the experimental error of the laboratory ($\pm$0.25dB). Therefore, both experiments and simulations have shown repeatable results. The next logical explanation for this difference is that there is a correction that needs to be applied but has not been.

However, this has not been identified currently. Therefore, further investigation is warranted here.

As the LRT model has been shown to have consistent errors away from $\theta = 90°$ for two geometries, the rest of this chapter will focus on results at $\theta = 90°$, where there is the greatest confidence in the model.

When looking at the in-flight experimental data for the annular nozzle, another issue with the experimental data was discovered. This is illustrated below in Figures 5.1.6 and 5.1.7 when the $\theta = 90°$ data is scaled with flight Mach number. Above $St = 0.5$, there is a bump in the experimental data (up to 5dB between $M_f = 0$ and 0.2) which increases in amplitude with increasing flight Mach number. This additional noise was not seen in the in-flight results for the conical nozzle in the previous chapter which were taken on the same rig. Therefore, this effect does not seem realistic as the flight-stream should reduce the mixing noise rather than increase it, and so is thought to be an error within the experimental data.

There are two potential causes for this additional noise. Firstly, if there was a loose part within the flight rig on the day of the experiments, vibrations from these components would generate noise. Given that this effect increases with flight Mach number, these vibrations would increase in magnitude and hence produce more noise. The effect appears to be reduced at a higher Mach number and a better collapse is achieved. However, it is more likely that the jet mixing noise is dominant in this case. The second explanation is that separation of the flight stream could be occurring on the external surface of the annular nozzle leading to additional noise generated at high frequency. No separation is seen in the CFD data and hence LRT does not predict the additional noise. It is thought that this is unlikely to be the reason because the additional mixing close to the nozzle exit by this mechanism would result in a decrease in the low-frequency content as the jet has already been mixed. However, the low frequency collapses in Figures 5.1.6 and 5.1.7. The easiest way to check which of these two explanations is correct is to retake the experimental data. If the error is repeatable for a different test day, then there is a geometric effect occurring rather than an experimental procedure error.

It is also worth noting that a scaling of 50 was used in Figure 5.1.6 to collapse data rather than 60 in Figures 4.2.4 and 5.1.7. The value of 50 was chosen as it provided a

better collapse of the experimental data than a value of 60. Given that the conical nozzle data and the higher jet Mach number data for the annular nozzle collapsed with a flight scaling value of 60, it is thought that the value of 50 at the lower jet Mach number is due to errors in the experimental procedure rather than a geometric effect, as the jet mixing noise will be dominant at the higher Mach number. This will need to be revisited once the experimental data has been retaken.

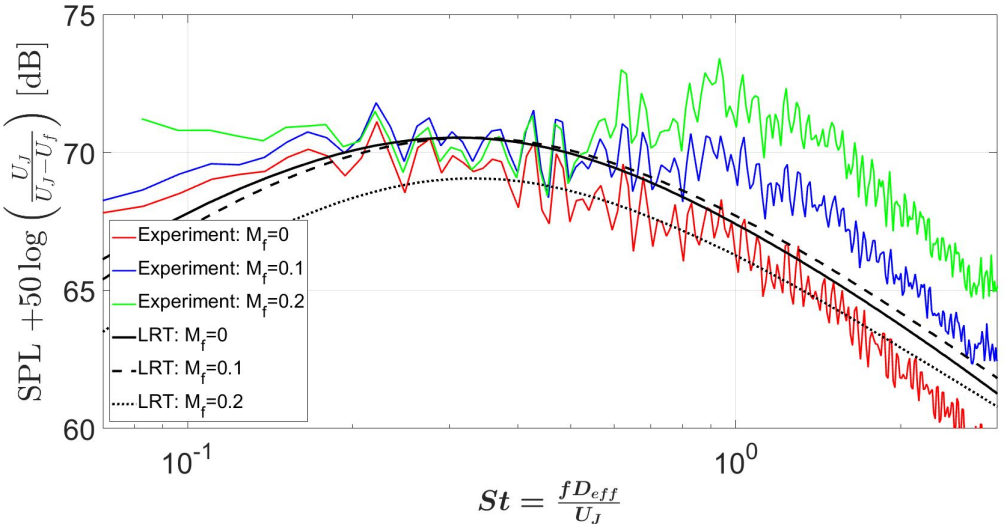

FIGURE 5.1.6: In-flight scaled data for the annular nozzle for the $M_J = 0.6$ data at $\theta = 90°$.

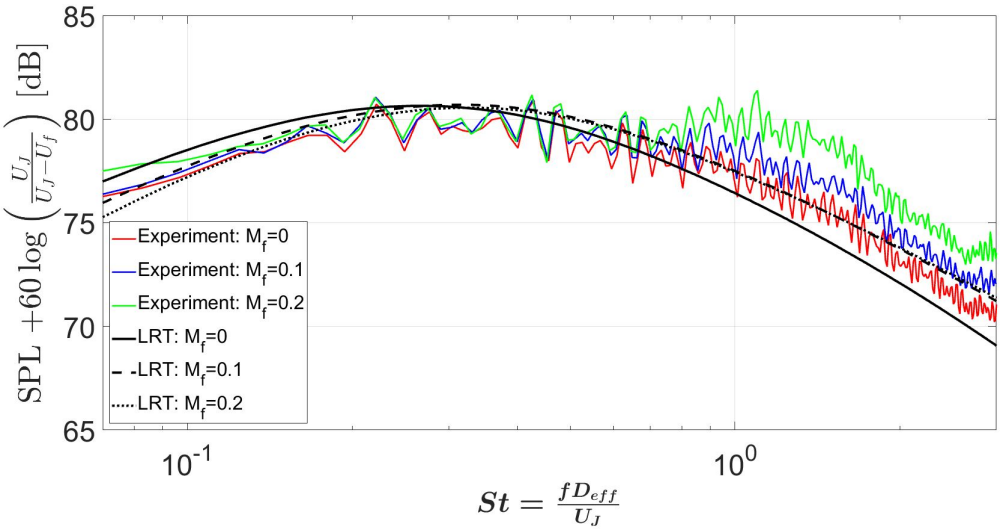

FIGURE 5.1.7: In-flight scaled data for the annular nozzle for the $M_J = 0.8$ data at $\theta = 90°$.

For the present work, the comparison of the LRT predictions to the experimental data for the in-flight cases is limited to below $St = 0.5$. Due to the small range of

frequencies that this will allow a comparison for, further analysis on this geometry will only be carried out for the static case.

With the introduction of the bullet, one would like to know how the noise scales. Although the reflective noise is minimal, the change in mixing noise is not. The centre body obviously reduces the flow area of the nozzle and introduces an additional boundary layer which reduces the overall mass flow rate. Therefore, to compare the conical and annular far-field mixing noise, the annular data needs to be scaled to account for these. This has been done by scaling by the effective diameter (a flow area correction) and accounting for the difference in mass flow rate (the additional boundary layer correction). A new jet velocity has been found based on the experimental mass flow rate and is used for this scaling. The results at $\theta = 90^\circ$ are shown below in Figure 5.1.8. An interesting feature can be observed here. One would expect the high-frequency data to collapse using the scaling outlined above. However, there is a 1dB difference between the conical and annular data above $St = 1$ in Figure 5.1.8. Effectively, the annular nozzle is behaving like a smaller nozzle than the effective diameter would suggest and hence is producing less noise. This warranted further investigation. The reader should be reminded that in Figure 5.1.4, the vena contracta effect of the bullet was discussed. This contraction of the jet generates a smaller jet than the conical nozzle. This effect is not captured by the definition of the effective diameter, which assumes that the difference in the flow area at the nozzle exit is the only change between the conical and annular nozzles. There is, therefore, an implicit assumption that the flow field after the nozzle exit is similar which has been shown to not be true. Therefore, the width of the jet at the vena contracta point, L_{vc}, as defined in Figure 5.1.4, is used to scale the jet mixing noise in Figure 5.1.9. A much better collapse is seen at high frequency using this length scale. The main conclusion that can be drawn from this is that scaling laws only hold true when the underlying physics remains the same between different cases.

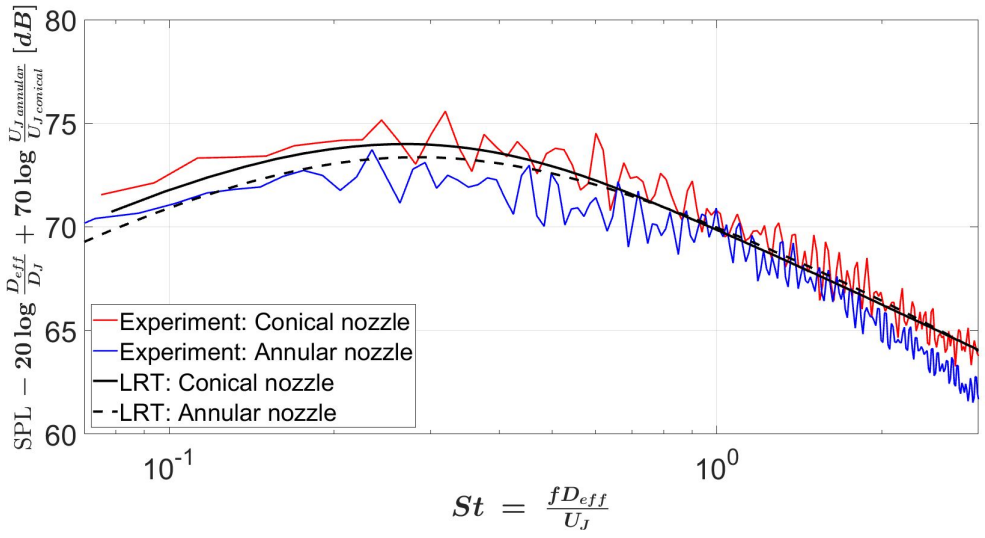

FIGURE 5.1.8: Comparison of SPL for the static conical and annular nozzles at $M_J = 0.6$ and $\theta = 90°$ using the effective diameter.

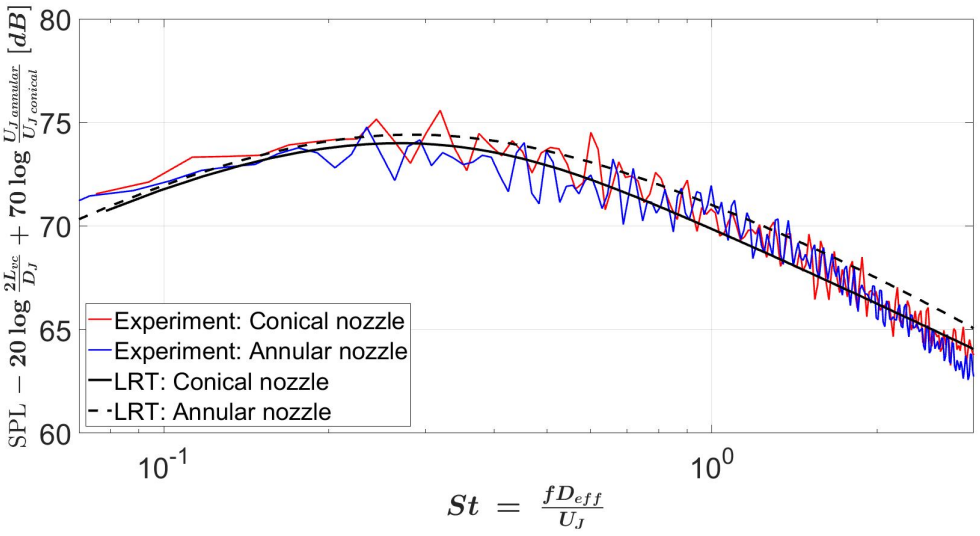

FIGURE 5.1.9: Comparison of SPL for the static conical and annular nozzles at $M_J = 0.6$ and $\theta = 90°$ using the vena contracta length.

Using the data in Figure 5.1.9, the change in SPL between the conical and annular nozzles can now be calculated. This is shown below in Figure 5.1.10. The data has been converted to $1/3^{\text{rd}}$ octave data to smooth the experimental data. The annular data is then subtracted from the conical data at a constant Strouhal number. As can be seen in Figure 5.1.10, the LRT prediction models the general trend in the change in the SPL level but does not capture the magnitude well at mid-Strouhal numbers. This is partly due to the 0.8dB over-prediction that was mentioned earlier. Nevertheless,

Figure 5.1.10 demonstrates that the LRT method is capable of predicting the general trend in the change in SPL as the nozzle geometry is changed.

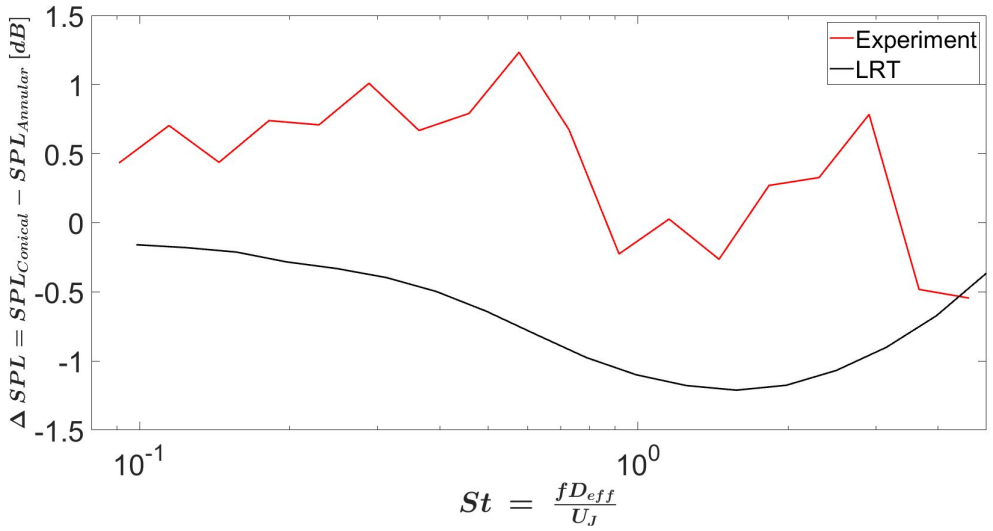

FIGURE 5.1.10: Change in SPL between the static conical and annular nozzles with a constant area at $M_J = 0.6$ and $\theta = 90°$. Data presented as $1/3^{rd}$ octave data.

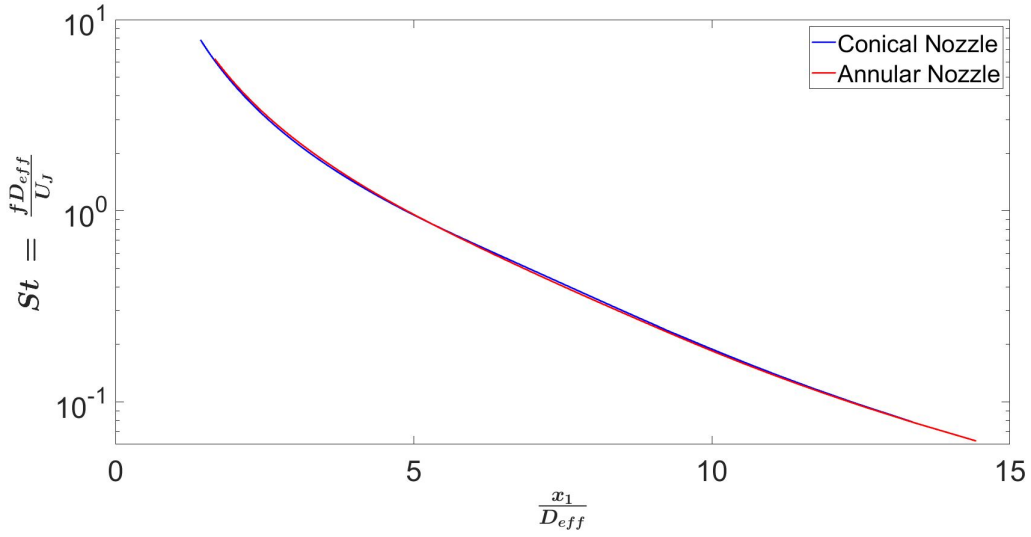

FIGURE 5.1.11: Comparison of centroid position per frequency at $M_J = 0.6$ and $\theta = 90°$ for the static conical and annular nozzles.

The source distribution of the annular nozzle has been analysed using the same method as was used for the conical nozzle in Figure 4.2.5. Figure 5.1.11 shows the centroid position for both nozzles. The jet diameter has been used to normalise the axial position of the conical nozzle results, while the effective diameter is used for the annular nozzle data. This figure confirms that using the effective diameter is the correct parameter to scale the jet mixing noise.

5.2 Isolated pylon effects

As discussed in Chapter 2, the pylon attaches the wing to the core of the engine. This creates an internal blockage within the nozzle, while the external surface of the pylon will cause a blockage of the path of the flight-stream. In both cases, a wake forms behind the pylon, causing the jet to be drawn towards the pylon, as seen in the literature. The amount of redirection of the jet will depend on the strength of the wake pressure deficit. Although the redirection will eventually be counteracted by the wing in an installed case, it is important to understand how changing the pylon design influences the flow field, to enable low-noise pylons to be designed. As the pylon surface causes the flow field to become asymmetric in nature, so will the mixing noise. Analysis of the literature in Chapter 2 has shown that the pylon causes an increase in noise levels above the pylon and at the sideline position. However, the amount by which this occurs is up for debate. It is, therefore, critical that predictions on how the pylon design changes the mixing noise can be made.

In this section, two effects will be studied. First, the impact of the internal blockage caused by the pylon will be determined. Then, the additional effect of the external pylon surface will be analysed.

5.2.1 Internal nozzle blockage effects

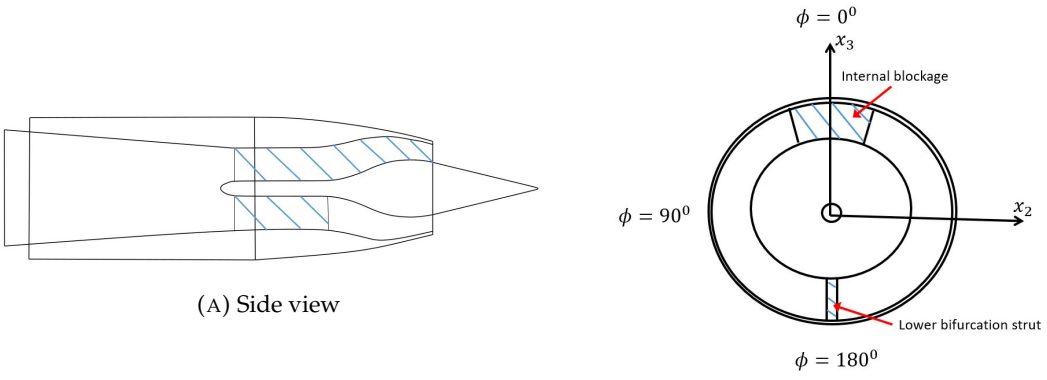

(A) Side view

(B) Front view

FIGURE 5.2.1: Geometry of 10% internally blocked nozzle.

Three different internal blockages are studied in this section to identify general trends in the changes in mixing noise. The blockages reduce the flow area of the annular nozzle by 5, 10 and 20%, giving an effective diameter of 31.1, 30.2 and 28.5mm,

respectively. While the 10% blocked nozzle is the most realistic, experimental data from the Doak laboratory suggests that the flow and noise effects are more pronounced for the 20% blocked case. The geometry for the 10% blocked nozzle is shown in Figure 5.2.1 with the pylon blockage aligned with the $+x_3$ axis.

5.2.1.1 CFD results

The first analysis that was conducted looked at the overall impact of the blockage on the velocity field, as shown below in Figure 5.2.2. This data is normalised by the jet velocity which, despite the blockage being present, only caused a variation of 0.5m/s in U_J. In Figure 5.2.2, axial slices at different locations illustrate the modifications to the shape of the jet as it develops from the blockage. As expected, the annular nozzle produces a fully axisymmetric jet. Introducing a blockage of increasing size causes the jet to become more "heart" shaped within the first effective diameter of the nozzle exit and then forms an "egg" like shape by $\frac{x_1}{D_{eff}} = 4$. After $\frac{x_1}{D_{eff}} = 4$, the blocked jets start to return to a more axisymmetric shape as the jet spreads out and the momentum diffuses. Therefore, the internal blockage will mainly affect noise sources within the first four effective diameters. The asymmetry of the jet will change the propagation of noise through this region but will have a negligible impact on the far-field mixing noise at $\theta = 90^\circ$.

Two final points can be made about the data in Figure 5.2.2. Firstly, looking at the contour plots at $\frac{x_1}{D_{eff}} = 10$, one can see that the increase in blockage leads to the jet being stretched in the $+x_3$ direction, towards the blockage. This is due to the pressure deficit introduced by the blockage wake. Secondly, for the 5% blockage case, the flow could be considered almost horizontally symmetric. The reason for this is that the blockage at the top of the nozzle is comparable in size to the supporting bifurcation strut located directly below the bullet.

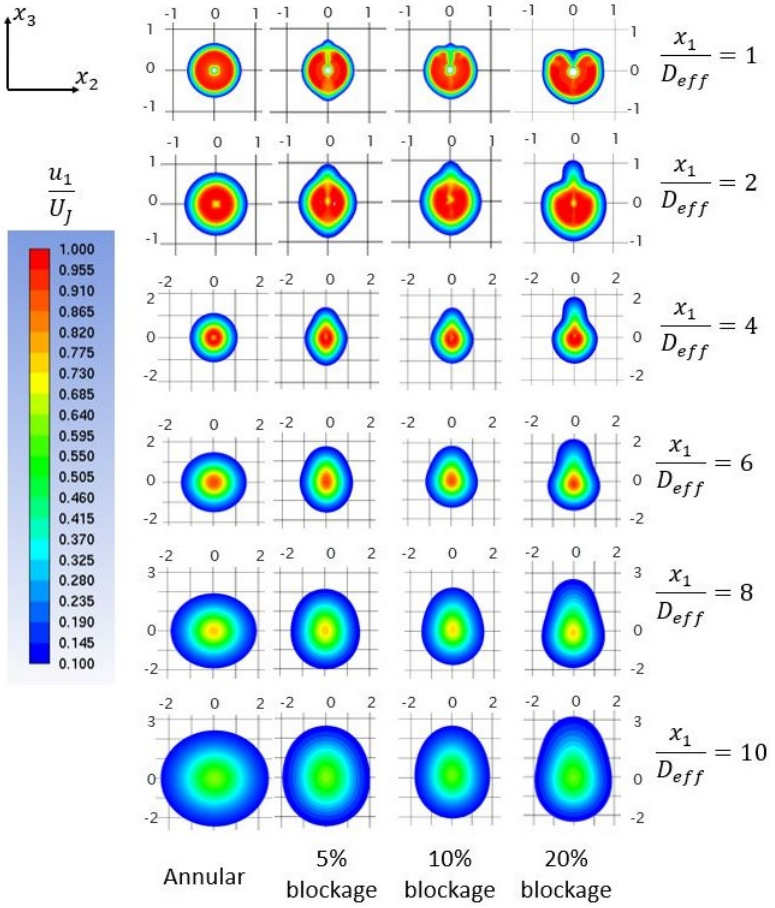

FIGURE 5.2.2: $\frac{u_1}{U_J}$ radial slices at $\frac{x_1}{D_{eff}} = 1, 2, 4, 6, 8$ and 10 for different blockages at $M_J = 0.6$ and $M_f = 0$. All scales of position are measured in effective jet diameters from the jet axis.

Given that the internal blockage induces an asymmetry in the velocity field and redirects the jet towards the blockage, the question now is how accurately does a k-ϵ RANS model predict this effect compared to experimental data? Profile of axial velocity and turbulent intensity in the vertical plane can be seen in Figure 5.2.3 for the 10% internally blocked nozzle. Similar profiles were seen for the other blockages, so those results are not presented here. Close to the nozzle exit, RANS can predict the peak velocity deficit that the blockage induces to within 0.5% at $\frac{x_1}{D_J} = 2$. The shape of the flow field around the blockage wake is matched well by the RANS simulation compared with the experimental data within the first five effective diameters. The blockage wake mixes out by $\frac{x_1}{D_J} = 4$. As with the previous RANS simulation, the slight under-prediction in the velocity profile far downstream of the nozzle exit at $\frac{x_1}{D_J} = 8$ still exists.

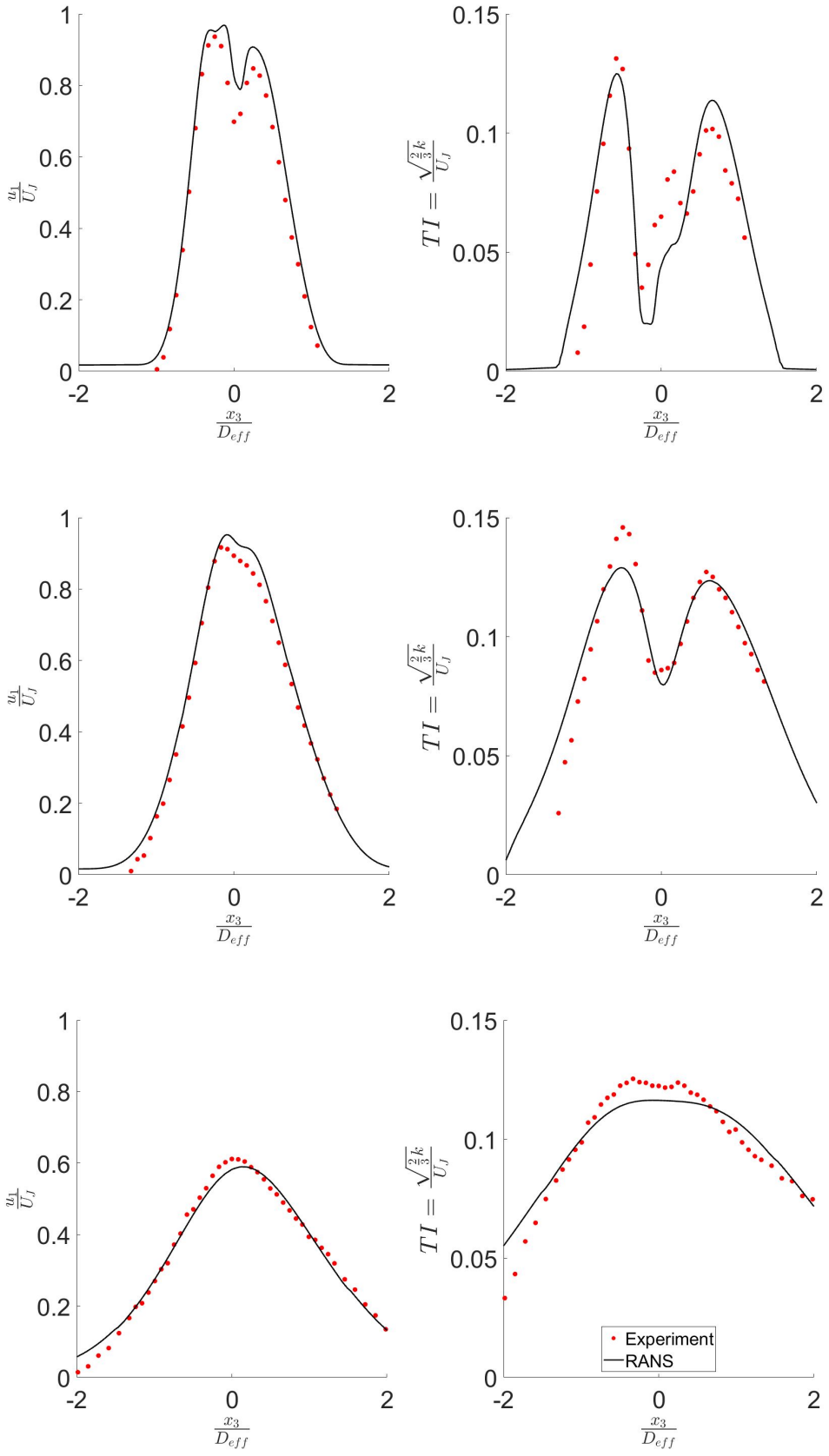

FIGURE 5.2.3: Radial profiles of $\frac{u_1}{U_J}$ (left) and turbulence intensity (right) for the static 10% internally blocked nozzle at $M_J = 0.6$. Each row corresponds to $\frac{x_1}{D_J} = 2$, 4 and 8, respectively.

In Figure 5.2.3, the general shape and amplitude of the turbulent intensity profiles are well matched in the outer shear layer. There is some discrepancy in the inner shear layer, but as mentioned previously, this should not provide a large source of error. The presence of the blockage induces a wider shear layer on the blocked side of the nozzle compared to the opposite side although the peak value is 1% lower. On the blockage side of the nozzle at $\frac{x_1}{D_j} = 2$, there is an over-prediction of around 1% TI. This is thought to be linked to the assumption of isotropic turbulence in RANS. Without LES or experimental data, it is unclear how the change in the shear forces around the blockage wake influences the anisotropy of the flow. Finally, there is an under-prediction in the peak turbulence level (0.5%) far downstream at $\frac{x_1}{D_j} = 8$ as seen with previous geometries.

When looking at flow profiles in the x_1-x_2 plane, both the experimental and RANS data sets showed a symmetrical profile about the centreline with similar trends in peak levels to those seen in the vertical plane. As this is less interesting than the results in the x_1-x_3 plane, these results have been omitted here.

The results in this section have, so far, been for the static case. For the in-flight analysis, the main question that needs answering is what effect does the flight-stream have on the wake region of the jet? One would intuitively think that the flight-stream would stretch the wake region as the rest of the jet is elongated. What is less clear, however, is how the turbulence level changes.

The first analysis that was conducted here was to look at the turbulent intensity close to the blockage at $\frac{x_1}{D_j} = 1$, as seen in Figure 5.2.4. On the opposite side to the blockage (-x_3 axis), there is a classic reduction in turbulent intensity with increasing flight Mach number (4% reduction from $M_f = 0$ to 0.2). Although a reduction is also seen on the +x_3 axis, the magnitude of change is much smaller (only 0.8%). Obviously, this is to do with the presence of the blockage wake changing the shear rate. This phenomenon is not seen one further diameter downstream which indicates that this effect decays rapidly. Acoustically, this will result in additional high-frequency noise, $St \geq 6$, that will likely prevent a collapse at high frequency when scaling noise with flight Mach number.

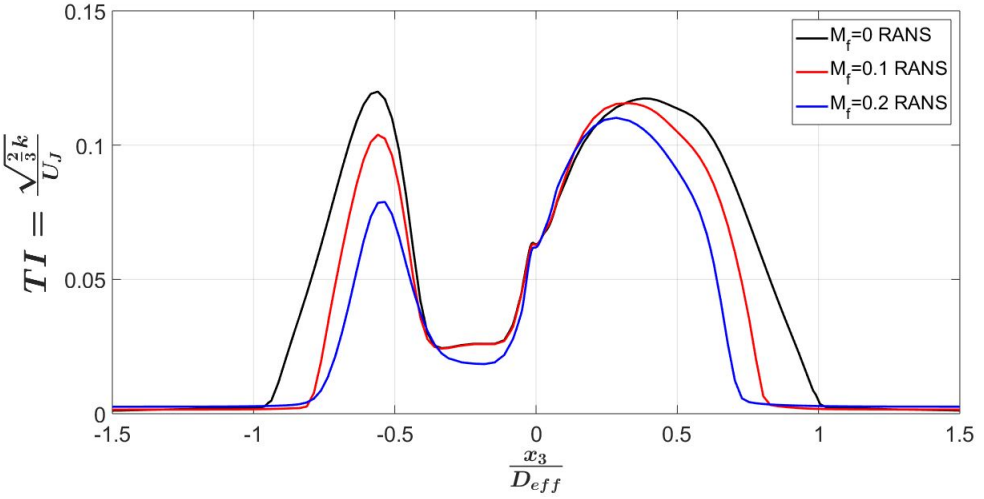

FIGURE 5.2.4: Radial profiles of turbulence intensity at $\frac{x_1}{D_j} = 1$ for the 10% internally blocked nozzle at $M_J = 0.6$ and $M_f = 0, 0.1$ and 0.2

Further analysis has been undertaken on the turbulent intensity along the lip-line of the annular and internally blocked nozzles at $+x_3$ as shown below in Figure 5.2.5. Several trends can be seen. Firstly, the change in the shape of the curves between the static and in-flight annular nozzle curves is due to the stretching of the vena-contracta effect downstream, as seen in Figure 5.1.4. Secondly, there is a change in shape close to the nozzle exit between the annular and blocked nozzles. These internally blocked nozzles do not exhibit a vena-contracta effect here as the lip-line is within the wake region and is, therefore, outside of the jet. Next, the increase in blockage results in a larger wake region as the turbulence starts to increase at 0.28, 0.51 and 0.8 effective diameters for the static 5, 10 and 20% cases, respectively. This point of increase effectively marks the end of the wake region. The end point of the wake region is extended downstream when the flight-stream velocity is increased. At $M_f = 0.2$, the point of increase in turbulence occurs at 0.65, 0.96 and 1.35 effective diameters. The next point to consider is that there is only a small variation in the turbulence level by ten effective diameters for each of the blocked nozzles. However, with increasing blockage, there is a general increase in the peak turbulence level. This is especially true for the 20% case where the change in shape of the curve between two and six effective diameters would suggest additional turbulence and, therefore, noise. This will be discussed in more detail in the acoustic results shortly.

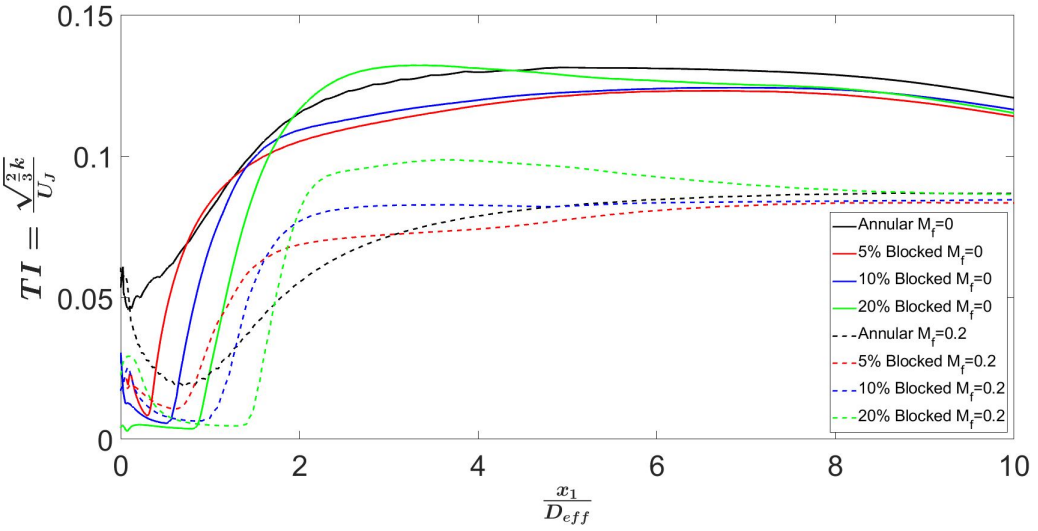

FIGURE 5.2.5: TI profiles from RANS on the nozzle lip-line on the $+x_3$ axis for different blockages at $M_f = 0$ and 0.2.

5.2.1.2 Acoustic results

The presence of the pylon is thought to primarily change the propagation of noise close to the nozzle exit and has been seen in the literature to affect the noise at the sideline and above the pylon. Below the pylon ($\phi = 180°$), there will, therefore, be limited impact of the pylon. Therefore, the difference in results of simulations with and without ray tracing at this location should be negligible. If this is the case, a simplified source equation can be used to predict the noise of these asymmetric jets.

Figure 5.2.6 shows the LRT predictions with and without ray tracing at $\theta = 90°$ and below the blockage ($\phi = 180°$) for the five geometries studied so far. All predictions are made for the static $M_J = 0.6$ case. It is clear from this figure that there is little impact of refraction at this polar angle as the results without ray tracing, when the flow factor, $\Phi = 1$, collapse on top of the full ray tracing results. The peak frequency and SPL level are captured well for the conical and blocked nozzles. This figure further emphasizes the over-prediction of the annular nozzle which does not match the trend of the other geometries. This reinforces the view point that there is a correction that has not been applied as only one of five geometries shows this error. Another observation that can be made is that the low-frequency prediction of LRT gets worse with increasing geometric complexity. The error at $St = 0.08$ starts at 0.9dB for the conical nozzle and increases to 2.4dB for the 20% blocked nozzle. This will be due to an error in the CFD calculation as the LRT prediction without ray tracing shows this

error as well. As the error occurs primarily below $St = 0.1$, this region is not of great interest to the study of jet noise, so will not be considered further.

Although the result of this analysis is not unexpected, as all that is being said is that there is no refraction at $\theta = 90°$, this shows that a simplified equation can be used to give accurate results of asymmetric nozzles at $\theta = 90°$ above the peak frequency. This simplified equation can be added to an optimisation code for analysing changes in geometry to identify potential noise risks.

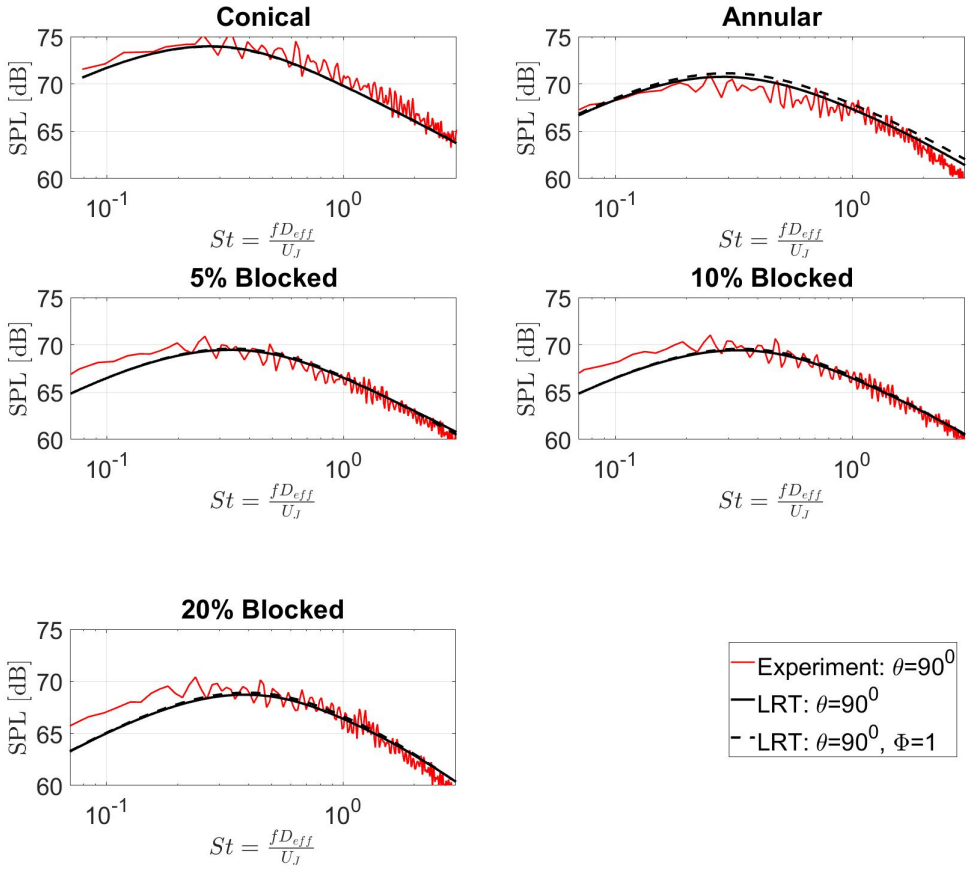

FIGURE 5.2.6: LRT predictions with and without ray tracing ($\Phi = 1$) of different geometries for the static $M_J = 0.6$ case at $\theta = 90°$ and $\phi = 180°$.

The impact of the internal blockage on the far-field mixing noise will now be considered. Figure 5.2.7 shows the azimuthal change in SPL at $\theta = 90°$ between the annular and internally blocked nozzles for certain Strouhal numbers. The SPL has been corrected for the difference in flow area to generate the values shown. The ΔSPL is defined as

$$\Delta SPL = SPL_{\text{Blocked}} - SPL_{\text{Annular}} - 20log\frac{D_{eff,\,Blocked}}{D_{eff,\,annular}} \tag{5.2.1}$$

The reader should be reminded that $\phi = 0^\circ$ refers to the position above the internal nozzle blockage and $\phi = 180^\circ$ is below the nozzle. Several observations can be made from Figure 5.2.7. Firstly, the overall effect of the internal blockage is to increase the amount of mixing noise present as the blockage increases in size. This is true for the three blockages above $St = 0.6$. Below this point, the LRT predictions of the 20% data shows a decrease in the noise level. This is thought to be linked to the increased under-prediction at low frequency mentioned in Figure 5.2.6. Secondly, the LRT predictions are consistently 0.8dB lower than the experimental data above $St = 0.6$, although the general trend is captured. This is thought to be due to the 0.8dB over-prediction of the peak level of the annular data seen in Figure 5.1.5. Next, better predictions are made at $St = 2$ and 3 compared to that at $St = 0.1$. The reason for this is difficult to discern given the intricacies of the source model but is thought to be linked to the good predictions close to the nozzle exit compared to the under-prediction of turbulence after five effective diameters. It was shown in Chapter 4 that the LRT model was sensitive to the TKE values in the main noise-producing region. Therefore, this is not an unreasonable conclusion. Finally, there is little difference between the 5 and 10% data sets. A maximum azimuthal variation of 1.6dB is seen for the 10% blocked nozzle at $St = 0.6$ and $\phi = 60^\circ$ but generally there is less than 1dB azimuthal variation for the 5 and 10% cases. The same can not be said for the 20% blockage case, however.

There are two interesting features in the experimental 20% blockage data which warrant additional discussion. Firstly, there is an increase in the ΔSPL at $St = 0.6$ and 1 which is not seen in the other geometries. The experimental data shows a 3-4dB change in the SPL for the 20% case compared to the 5 and 10% cases, whereas the LRT predicts only a 1dB increase in noise. It is intuitive that this means the 20% blockage data will not follow the normal eighth velocity scaling law and, therefore, there is an additional noise source present here. This is further confirmed by the fact that LRT predicts the jet mixing noise for other geometries well. The additional noise is not reflective noise as it occurs at too low a frequency and there is no additional solid surface present for only the 20% case.

The second feature of the 20% case is a roughly constant ΔSPL seen azimuthally in both the experimental data and LRT prediction at high frequency ($St = 2$ and 3). As these frequencies are generated close to the nozzle exit, where the effect of the blockage is seen in the flow field, this is an unusual result.

Both of these features will now be investigated in turn.

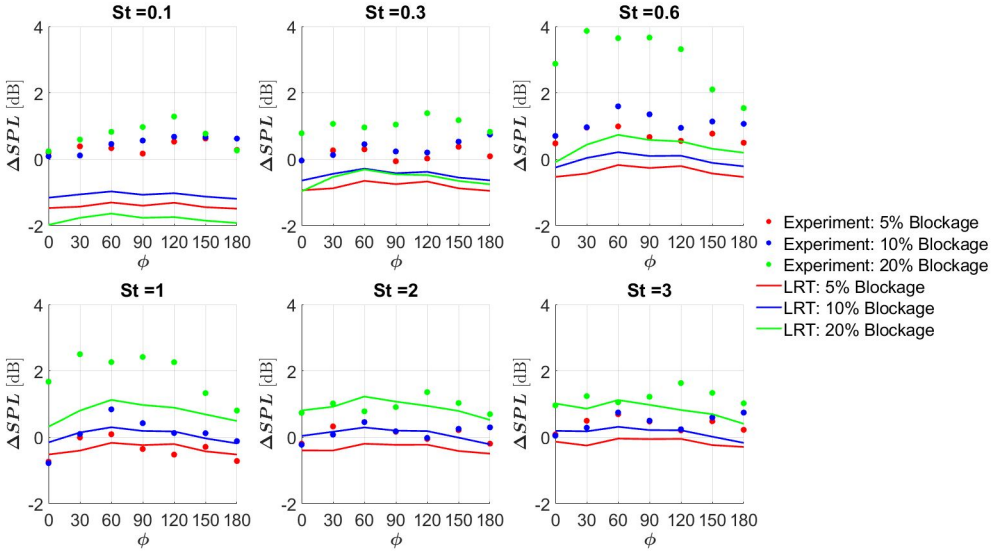

FIGURE 5.2.7: Azimuthal variation in SPL at $\theta = 90°$ for different blockages compared to the annular nozzle for $M_J = 0.6$ and $M_f = 0$. [1/3rd octave band data corrected for flow area]

Looking at the increase in noise at mid-Strouhal numbers for the 20% case, the obvious candidate for this noise would be from vortex shedding behind the blockage. More detail on this noise source can be found in the literature in [123, 124]. The CFD data was, therefore, interrogated to see if vorticity could be a likely source of the noise. A $x_1 - x_2$ plane was created halfway up the blockage, as seen in Figure 5.2.8a. Figure 5.2.8b shows the axial component of vorticity, σ_1, for the annular, 5, 10 and 20% blocked nozzles. With increasing blockage, counter-rotating axial vortices of increasing size and amplitude are created. These vortices rotate towards the centreline of the jet. The presence of these vortices would indicate that a vortex-shedding noise source is present for the blocked nozzles. Given that there is no obvious increase in the experimental data for the 5 and 10% blockage cases, it is suspected that this noise source is masked beneath the jet mixing noise and only becomes dominant in the 20% case. The derivation of the LRT source model in Chapter 3 does not include a vortex source and hence, the LRT model does not pick up on the additional noise for the 20%

case. It should be noted that the proper aerodynamic design of a full-scale pylon would mitigate the presence of such a flow feature. This point will be revisited when looking at the external pylon surface.

It should be noted that the Strouhal numbers in Figure 5.2.7 do not match the Strouhal number range for vortex shedding quoted in the literature. This is because Figure 5.2.7 uses a Strouhal number based on D_{eff} rather than the width of the blockage. At high Reynolds numbers, vortex shedding occurs over a range of Strouhal numbers ($0.2 \leq St \leq 0.5$ [125]). If one takes the middle frequency that the additional noise in Figure 5.2.7 is seen at, the average width of the blockage at the nozzle exit and the jet exit velocity, then one can obtain a Strouhal number of 0.45 for this noise, which is within the range quoted by the literature. This gives further credibility to the conclusion that the additional noise seen in Figure 5.2.7 comes from vortex shedding.

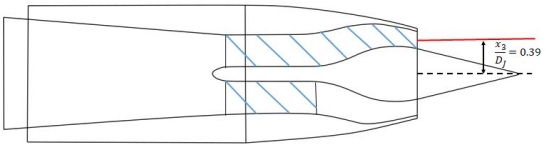

(A) Position of the mid-blockage plane.

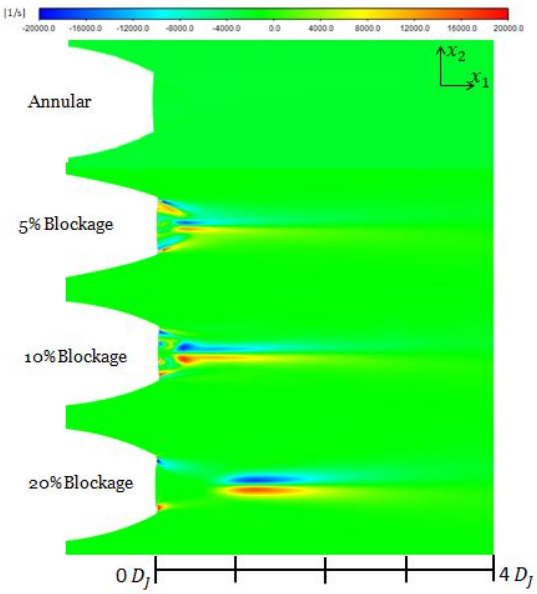

(B) Contours of axial vorticity, σ_1.

FIGURE 5.2.8: Vorticity from the internal blockage.

The second point concerning the 20% data in Figure 5.2.7 is the constant increase in SPL observed at the two highest Strouhal numbers, compared to the 5 and 10% cases. Since this result is present in both the experimental data and LRT predictions, this is believed to be a real effect. To identify the reason behind this, the acoustic source strength, Q, integrated across different axial slices at $\theta = 90°$, has been calculated for $St = 0.4$, 2 and 3 and is shown below in Figure 5.2.9. Given the maximum value of Q for a jet classically occurs at $St = 0.4$, the data has been normalised by this value. The

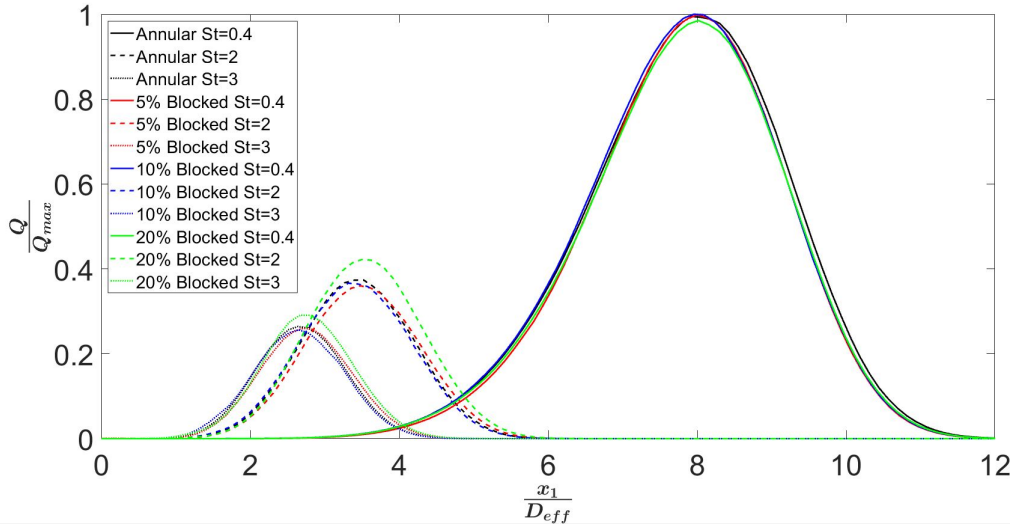

FIGURE 5.2.9: Axial source distribution at three different Strouhal numbers of the blocked nozzles.

first observation to be made is the fact that the results for all geometries collapse well at $St = 0.4$. This is likely because the influence of the blockage is not very strong after $\frac{x_1}{D_{eff}} = 6$ where this low frequency is present. Next, the annular, 5 and 10% blocked nozzle data further collapses at high frequencies as well. The green curves of the 20% blocked nozzle, however, have a significantly higher peak value. This increase in source strength, therefore, is clearly responsible for the additional high-frequency noise generation observed in Figure 5.2.7.

So, what does this mean for the jet-mixing noise? To understand this, one needs to consider the physical meaning behind Figure 5.2.9. When one scales the mixing noise from different diameter nozzles to account for the difference in flow area, a $20\log\left(\frac{D_{eff}}{D_{ref}}\right)$ correction is typically applied to measurements, where D_{ref} is a reference diameter. Physically, when this scaling is used, one is saying that eddies scale in size (and frequency) relative to the shear layer width and, therefore, the diameter of the nozzle. However, the energy content of an eddy also scales with the shear layer width up to the point of maximum turbulence. There is, therefore, a direct relationship between the maximum strength and the source strength per frequency as the diameter is changed (i.e. the $\frac{Q}{Q_{\text{Max}}}$ curves remain unchanged). This is why the annular, 5 and 10% blockage curves collapse in Figure 5.2.9. The conclusion here is that scaling laws only work while the underlying physics does not change.

To identify where the additional energy for the 20% case has come from, the results

along the nozzle lip-line above the blockage ($+x_3$) on the turbulence intensity are shown below in Figure 5.2.10 for the static case. The additional turbulence that is present between two and six effective diameters for the 20% blocked nozzle is indicative of the extra noise that will be generated in this region of flow where the vortices shown in Figure 5.2.8b are present. It is suspected that these vortices produce an increase in the mixing noise as well as introducing a vortex-shedding noise. Both of these are only prevalent in the 20% case as there is no evidence of an increase in noise in the 5 and 10% experimental and numerical data. It is also worth pointing out that there will be a decrease in the high-frequency content of the blocked nozzles within the first two diameters as the wake increases in size. This is not seen in the data presented in this thesis, as these effects will occur at $St \geq 6$.

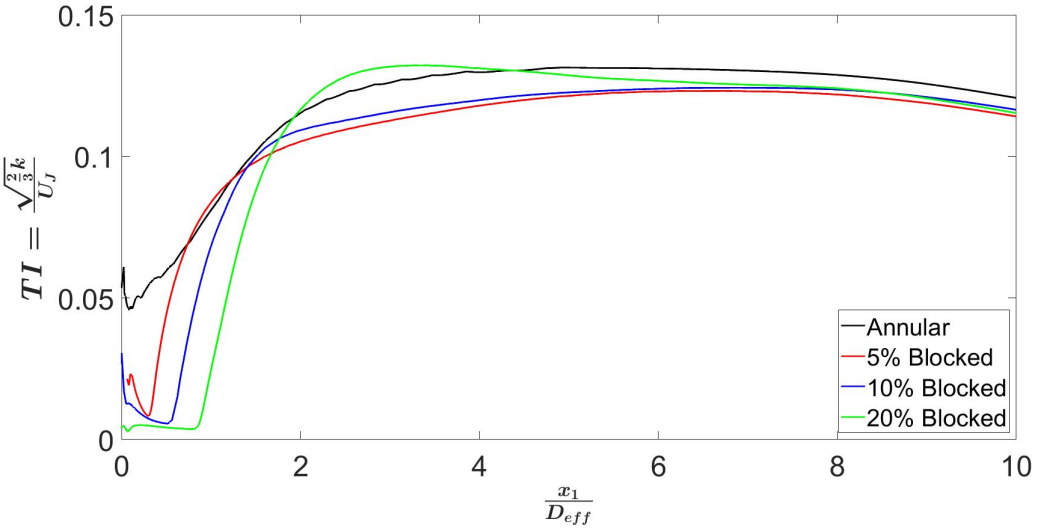

FIGURE 5.2.10: TI profiles from RANS on the nozzle lip-line on the $+x_3$ axis for the static $M_J = 0.6$ case for different blockage.

When looking at the in-flight experimental data for the internally blocked nozzles, it was noticed that the data sets had additional energy above $St = 0.5$, similar to the results for the annular nozzle results. All the in-flight data for these geometries were taken on the same day and so had the same error. Therefore, a comparison between the LRT predictions and experimental results is of limited use. The most interesting flight effects will occur, however, when the external pylon surface is included and so results for the in-flight internally blocked nozzles will not be presented here.

5.2.2 External nozzle blockage effects

The final section in this chapter looks at the impact of the external pylon surface on the flow and noise fields. An external fairing has been added to the 10% internally blocked nozzle, as seen in Figure 5.2.11.

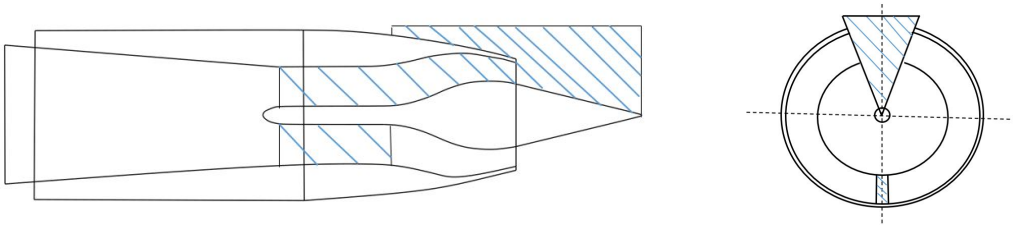

(A) Side view (B) Front view

FIGURE 5.2.11: Geometry of 10% externally blocked nozzle.

5.2.2.1 CFD Results

The results of axial velocity and turbulence intensity for the static case of the internal and external blockages are compared in Figure 5.2.12. Looking at these figures, there are only minor differences in the two profiles closest to the nozzle exit, in both the RANS and experimental data sets. This implies that the external blockage will only have an impact at very high frequencies generated near the nozzle exit. The difference in noise produced in this region will also be small which matches with the results found by Zaman [95,96]. Therefore, it can be concluded that the external pylon surface will have a minimal impact on the static far-field jet mixing noise.

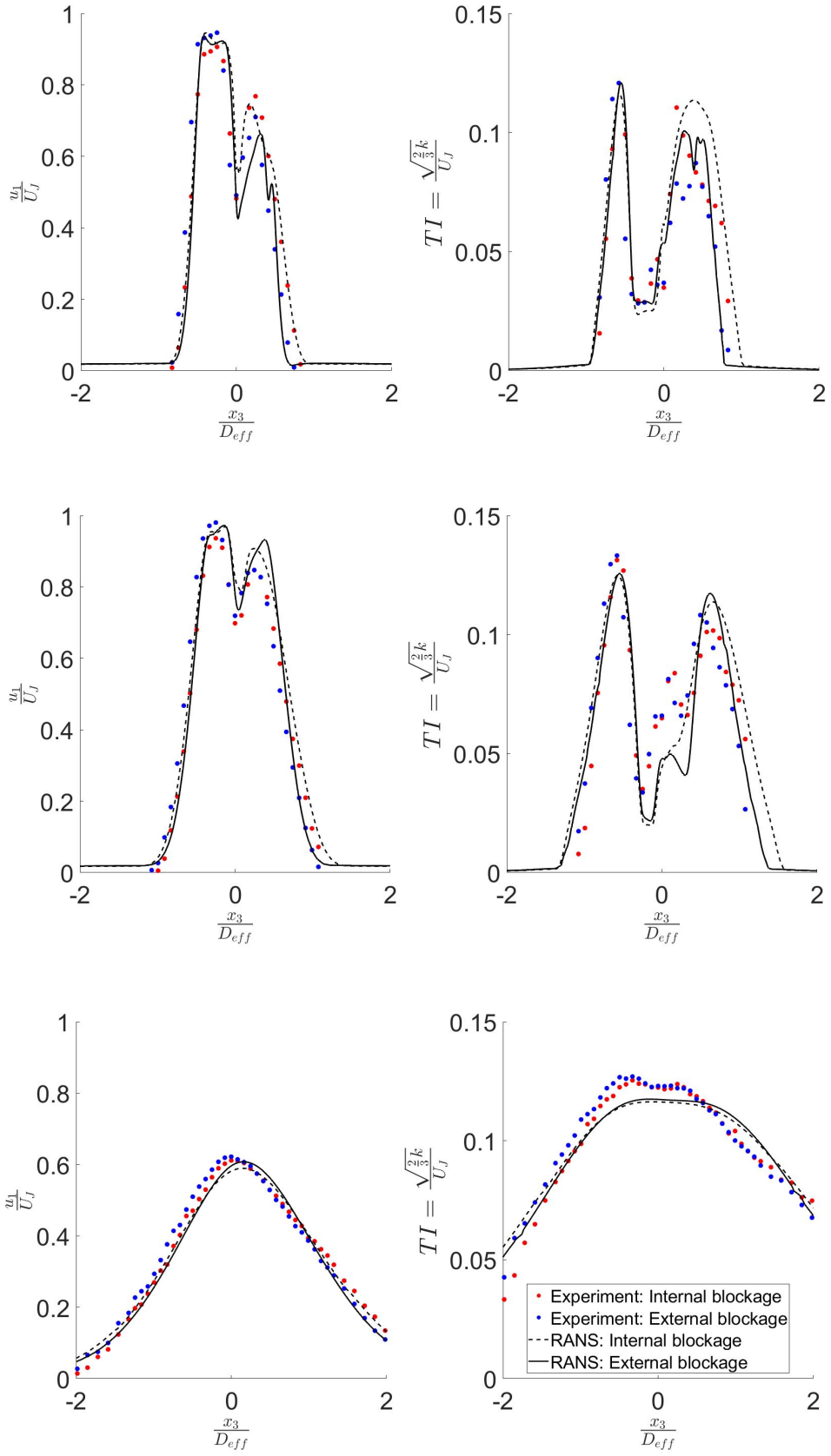

FIGURE 5.2.12: Radial profiles of $\frac{u_1}{U_J}$ (left) and turbulence intensity (right) for the static 10% internally and externally blocked nozzle at $M_J = 0.6$. Each row corresponds to $\frac{x_1}{D_J} = 1$, 2 and 8, respectively.

The more interesting question to consider is what is the impact of the external pylon surface in-flight? The CFD results for the axial velocity and turbulence intensity of the $M_J = 0.6$ jet with a flight-stream Mach number of 0.2, can be seen below in Figure 5.2.13. No aerodynamic experimental data was taken for these geometries, so comparisons will be made purely between CFD simulations. The biggest difference in axial velocity is seen at $\frac{x_1}{D_J} = 1$. Here the external surface blocks the path of the flight-stream from mixing with the wake of the pylon and so there is a reduction in the velocity just after the pylon tip on the $+x_3$ axis. This quickly mixes out as there is marginal difference present at $\frac{x_1}{D_J} = 4$.

In terms of the turbulent intensity, several differences can be observed. Firstly, there is an increase in the turbulence at $\frac{x_1}{D_J} = 1$ for the external blockage relative to the internal blockage on the -x_3 side. This will cause an increase in the high-frequency content of the mixing noise. This was an unexpected result as it was assumed that the external pylon would primarily affect the flow on the +x_3 side. As both simulations have been set up the same, converged and there is no experimental data to confirm this, one can only conclude that this is a real effect that is caused by the external fairing surface. Additional investigation is, therefore, needed in the form of more experimental data to confirm this.

Secondly, there is a small additional turbulence at $\frac{x_1}{D_J} = 1$ and $\frac{x_3}{D_{eff}} = 0.9$ for the external compared to the internal blockage. This is due to the turbulence generated by the flight-stream over the top surface of the external pylon surface. This surface would normally be touching the wing and so would see no flow across it. Due to the low magnitude of this additional energy and the fact that the external blockage geometry is unrealistic without the presence of a wing, this error will not be considered further. Finally, at $\frac{x_1}{D_J} = 8$, there is a decrease in the turbulence level at the edges of the jet, which will result in a low-frequency reduction. Given the increase in turbulence close to the nozzle exit and reduction further downstream, the external blockage acts like a chevron, by increasing the local mixing rate close to the nozzle exit. However, the key difference to a chevron is that a flight-stream is needed for this effect to be observed with the external pylon surface.

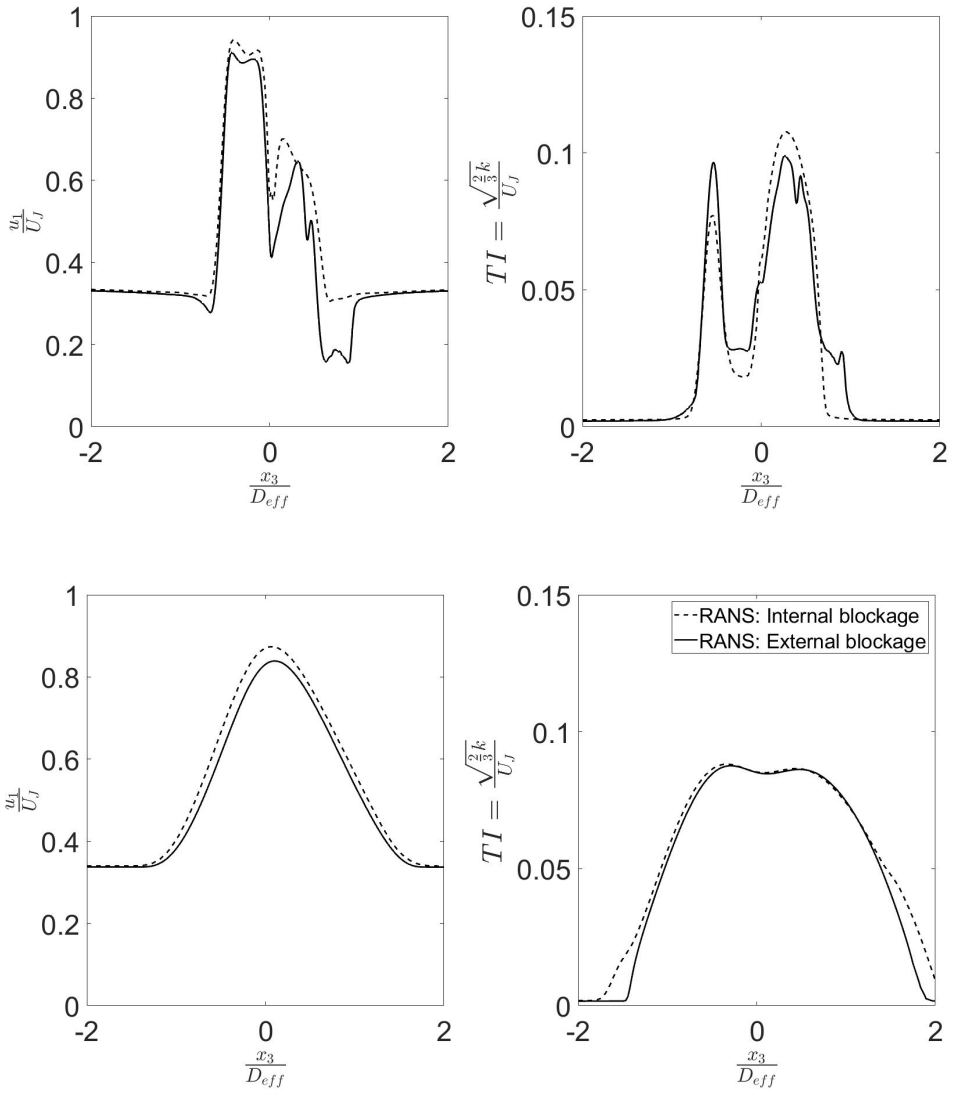

FIGURE 5.2.13: Radial profiles of $\frac{u_1}{U_J}$ (left) and turbulence intensity (right) for the 10% internally and externally blocked nozzle at $M_J = 0.6$ and $M_f = 0.2$. Top row is at $\frac{x_1}{D_J} = 1$ and the bottom at $\frac{x_1}{D_J} = 8$.

5.2.2.2 Acoustic results

Although no experimental data has been gathered for this geometry acoustically, the CFD results have demonstrated an interesting feature at $M_f = 0.2$. Therefore, analysis has been conducted using the LRT model at $\theta = 90°$ and $\phi = 180°$, to analyse the change in mixing between the internally and externally blocked nozzles, as seen in Figure 5.2.14. Statically, it can be seen that above $St = 0.15$, the mixing noise changes by less than 0.25dB, which is within the experimental error of the Doak laboratory. Therefore, it is reasonable to conclude that there is a negligible influence of the external surface statically.

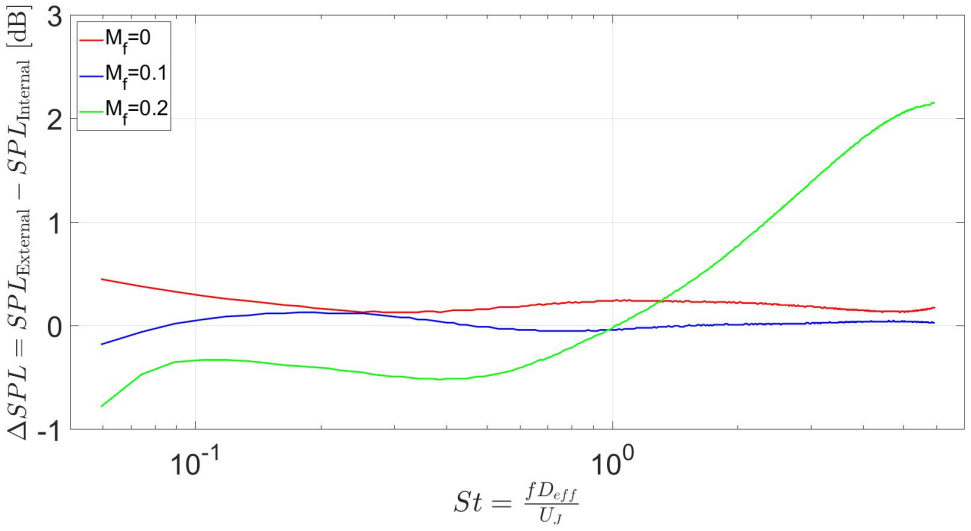

FIGURE 5.2.14: ΔSPL plots between the 10% internally and externally blocked nozzles at $\theta = 90°$, $\phi = 180°$ and $M_J = 0.6$.

Moving to the in-flight cases, at $M_f = 0.1$ there is a change in the SPL compared to the static case, but the difference is still small (less than 0.15dB). However, a large change is seen when the flight-stream is increased to $M_f = 0.2$. At $St = 6$, there is a 2.1dB increase in noise for the externally blocked nozzle compared to the internally blocked nozzle. Furthermore, there is a 0.33dB decrease at $St = 0.1$. The pylon, therefore, acts in a similar way to a chevron. It has already been noted that there is a change in the mixing rate in Figure 5.2.13 which would explain the far-field results. The interesting feature of these results is that the flight-stream needs to reach a certain velocity before the external pylon provides a benefit to the jet mixing noise.

Further evidence of this increased mixing rate can be seen if one looks at the source distribution of the $M_f = 0.2$ case, as seen in Figure 5.2.15. One can see that by increasing the mixing rate, the frequencies from the externally blocked nozzle are moved upstream. Furthermore, the increased area under the high-frequency curve is indicative of the increase in noise produced at these frequencies. One can see qualitatively that the change in area is much larger at the higher frequencies than at the lower ones.

Currently, there is no experimental data available for this geometry. However, this analysis has shown that the in-flight cases with the external pylon surface warrant further investigation.

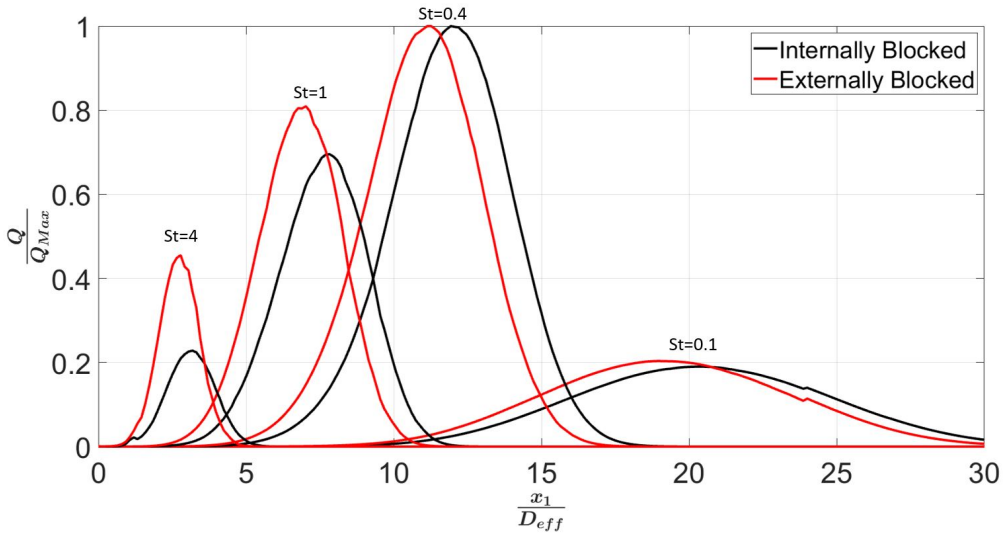

FIGURE 5.2.15: Source distribution for a select number of frequencies of the 10% internally and externally blocked nozzles at $\theta = 90°$, $\phi = 180°$, $M_J = 0.6$ and $M_f = 0.2$.

The work on the external surface has focused on the change in the mixing noise, however, there are other noise sources present. Reflective noise will be introduced by the external surface. As the external blockage surface is close to the nozzle exit (within the first jet diameter), this will primarily affect very high frequencies ($St \geq 6$) at the sideline position. As this is above the frequency range considered in this thesis, this noise source will not be studied further.

The presence of the external blockage will obviously change the bluff-body vortex shedding that was observed in the previous section. Figure 5.2.16 shows the comparison of the vorticity from the internal and external blockages on the same plane as shown in Figure 5.2.8a for the static case. Vortices are present on either side of the external surface and alternate in direction. A pair of vortices is also seen at the trailing edge of the external blockage. Although there is no source model for the vortex shedding within LRT, a hypothesis can be made on the expected impact. As the relative size of the vortices decreases when the external blockage is included, it is thought that this would result in a higher vortex shedding frequency. These vortices will also decay faster as the eddies are smaller. This would explain the increase in high-frequency content seen in the near-field results in the Doak laboratory [112]. As higher frequencies have less energy than large-scale structures, vortex noise of this nature is likely not to be important for the overall noise produced by the jet.

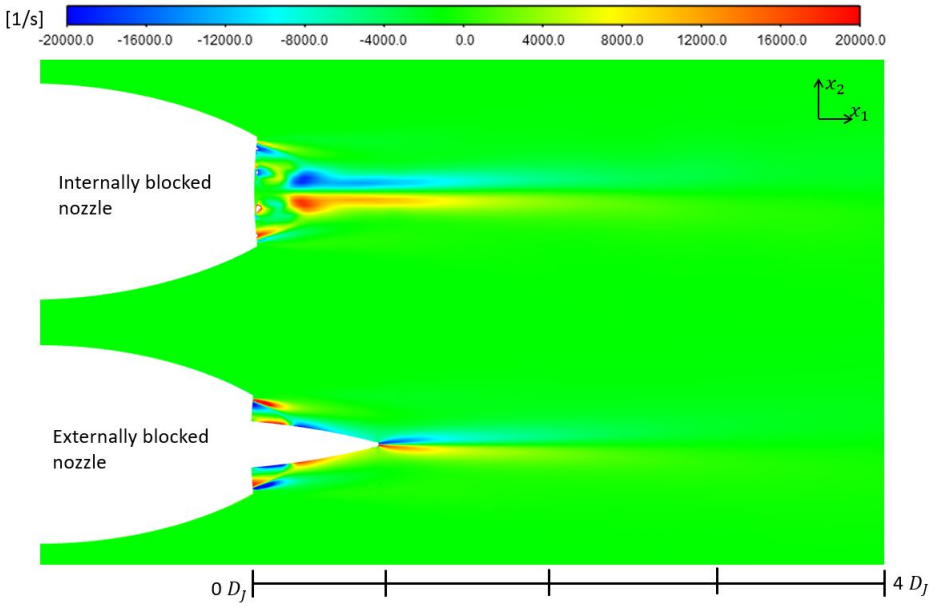

FIGURE 5.2.16: Contours of axial vorticity, σ_1, for the static 10% internally and externally blocked nozzles at $M_J = 0.6$.

5.3 Summary of chapter

In this chapter, several conclusions have been reached.

- A mesh sensitivity study was conducted on the CFD mesh for the isolated annular nozzle. It was found that a mesh with a $y^+ \approx 35$ was capable of showing the same radial profiles of axial velocity and turbulent intensity as a much finer mesh with a $y^+ \approx 1$. Therefore, further CFD simulations used the coarser mesh settings to reduce the computational cost as there was a negligible difference in accuracy.

- Similar to the CFD results for the conical nozzle in Chapter 4, it was seen that RANS produces an under-prediction of the peak axial velocity (7%) and the turbulence intensity (1%) at ten jet diameters downstream of the nozzle exit. This is thought to be due to the over-prediction of the spreading rate seen in the previous chapter. Given multiple meshes have shown this error, the k-ϵ turbulence model is the most likely root cause of the problem.

- Acoustically, it was seen that the LRT model over-predicted the static experimental results for the annular nozzle by 0.8dB at $\theta = 90°$, although the same general trends were observed as seen previously with the conical nozzle. It

was seen later in the chapter that LRT only produces this over-prediction for this geometry as a good match is obtained for four other geometries. The reason for the over-prediction is not clear as both the experimental and simulation results were seen to be repeatable. It is thought that there is a correction factor has not been applied to the data, but it is unknown what this is.

- It was noticed that the experimental data for the in-flight annular nozzle contained additional noise above $St = 0.5$ as the $\theta = 90^\circ$ data did not collapse when scaled. This was thought to be either due to vibrations in the flight rig or from flow separation from the external nozzle surface. The result of this was that there was limited experimental data to compare in-flight LRT predictions to and so the focus for the rest of the chapter was primarily on the static case.

- To scale the static far-field jet mixing noise of the annular nozzle to the conical nozzle, two corrections were needed. Firstly, an area correction using the effective diameter was used to account for the difference in flow area. Secondly, a correction was needed for the difference in mass flow rate due to the additional boundary layer around the bullet. Using both of these corrections, the conical and annular nozzle data could be scaled at $\theta = 90^\circ$ to within 0.5dB.

- The ability of the LRT method to model asymmetric jet flows and jet mixing noise was then investigated by looking at including the internal geometry of the pylon which blocks part of the flow area of the nozzle. Three different pylon blockages (5, 10 and 20% blockage of the annular nozzle) were studied to look at the general trends in results with increasing blockage. In the velocity field, the increased blockage created a more "egg"-like shape at four effective diameters downstream and the flow was drawn upwards. RANS was able to capture the decrease in velocity and turbulence in the wake region of the blockage to within 0.5% and 1%, respectively.

- Very close to the nozzle exit at $\frac{x_1}{D_j} = 1$, it was seen that the turbulence level in the wake region of the 10% internally blocked nozzle did not decrease as expected with increasing flight stream velocity. This suggests that the pylon changes the local mixing rate. However, this effect was not seen one diameter further downstream and so will only affect very high frequencies ($St \geq 7$).

- When looking at the acoustic results of the static internally blocked nozzles, it was seen that, at $\theta = 90^\circ$, the 5 and 10% blocked nozzles did not vary much azimuthally (maximum 1dB).

- When a large (20%) blockage was used, 3-4dB of additional noise was seen between $St = 0.6$ and 1 and there was a roughly constant 1dB of additional noise at $St = 2$ and 3. The first was thought to come from vortex shedding from the large blockage as axial vortices of increasing magnitude were seen in the CFD results. It was also noticed that there was an increase in the TKE around these vortices for the 20% case which would generate additional mixing noise at high frequencies.

- Perhaps the most important conclusion reached in this chapter was that the effective diameter is the correct scaling parameter to use for scaling the mixing noise of the annular and internally blocked nozzles. By using this parameter, the source distribution for the annular, 5 and 10% jets collapsed onto each other. The 20% blocked nozzle only collapsed at low frequency where the additional energy from the vortices was not present. Therefore, the scaling laws only work when the physics of the jet remains constant.

- When an external pylon fairing was added to the 10% internally blocked nozzle, it was found that there was little difference between the internal and external blockages statically. Above $St = 0.15$, the change in mixing noise was less than 0.25dB which is within the experimental error from the Doak laboratory.

- When a flight-stream ($M_f = 0.2$) is added to the externally blocked nozzle, there is an increase in the turbulence intensity close to the nozzle exit, leading to a 2.1dB increase at $St = 6$. A 0.33dB decrease in noise is seen at $St = 0.1$. Therefore, in-flight the external pylon surface acts like a chevron by creating additional mixing close to the nozzle exit. LRT suggests there is a benefit at low frequency due to the reduction in the noise here.

Chapter 6

Installed Jet Reflected Mixing Noise

In the previous chapter, the change in the flow field and mixing noise as the blockage of the pylon was included, was the main focus of the analysis. The change in the mixing noise was found to scale with the effective diameter as the flow area changed. However, having a large pylon produced additional noise which was thought to come from vortex shedding. Finally, it was shown that the external fairing of the pylon produced a negligible effect statically but acted similar to a chevron when the flight-stream was added.

This chapter is concerned with modelling installed jets. As outlined in Chapter 2, installed jet noise is made up of two main components: the jet-surface interaction (JSI) noise from near-field pressure fluctuations and the jet-surface reflection (JSR) noise from high-frequency reflected waves. Most research for installed jets has focused on JSI noise as this can generate up to 10dB of additional noise at low frequency ($St < 1$). While JSI noise has a negligible impact at high frequency ($St > 2$), JSR noise constitutes a significant increase in this frequency range. This is due to the close proximity of the wing to the jet for realistic wing positions ($\frac{l}{D_j} < 2$ and $\frac{h}{D_j} < 1$ [103]) limiting the JSR noise to those frequencies generated close to the nozzle exit.

The focus of this chapter is on the change to the high-frequency content of an installed jet. This can be split into the direct jet mixing noise (which travels straight to the observer) and the reflected mixing noise from the wing. Accurate predictions of the high-frequency JSR noise content of an installed jet can be used to interrogate installed spectra to isolate the JSI noise source. In the current work, the JSI noise is not

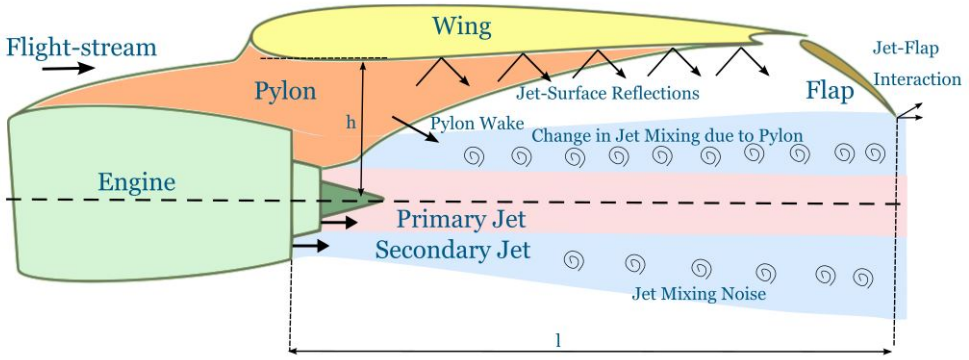

FIGURE 6.0.1: Diagram showing the geometry and acoustic sources around the engine.

modelled. This means that comparison to experimental data will be limited to high frequencies. For reference, the main problem parameters are shown again in Figure 6.0.1.

This chapter is split into four sections. Firstly, the method for calculating the path of the reflected rays is outlined. The results are then validated against experimental data. The observer angle and wing position are varied to see if the correct trends can be captured by LRT. Secondly, having validated the reflection code, attention is turned to predicting the flow field of installed geometries. A NACA4415 airfoil is added to the annular and 10% externally blocked nozzles from the previous chapter. Analysis of the installed annular nozzle allows the influence of the wing on the jet flow to be studied. Next, the combined effects of pylon and wing are studied. In the previous chapter, the isolated pylon was shown to draw the jet up towards the pylon, an effect which will, to some degree, be counteracted by the high-pressure region below the wing in-flight. Work in the previous chapters has shown that, despite the fact that the RANS solution does not provide accurate flow predictions after six effective jet diameters, good acoustic predictions can still be made. As the effects of the wing and pylon occur close to the nozzle exit, one would expect RANS to capture these adequately. This, in turn, should ensure accurate prediction of the source location, source magnitude and propagation of the high-frequency waves through the jet. However, it is not known if a k-ϵ RANS model is able to accurately predict the flow of an installed jet. It was mentioned in Chapter 2 that a known weakness of the k-ϵ model is the inability to predict the adverse pressure gradients on isolated wings. As this separation affects the wake region behind the wing, it is unknown how this will

interact with the turbulent shear layer of the jet. Finally, a theoretical situation is considered where a deployed flap redirects the jet away from the wing. The changes to both the direct mixing noise and the reflected mixing noise will be considered.

6.1 Installed jet methodology

In this chapter, CFD has not been carried out for all geometries studied. In sections 6.1.2 and 6.4, the main concern is with the acoustic response of the source equation to particular situations. These sections use the CFD data from the static conical nozzle studied in Chapter 4 at $M_J = 0.6$ as a basis for predictions. The accuracy of RANS simulations for predicting the flow of installed jets is examined when looking at the installed annular and jet-pylon-wing configurations in sections 6.2 and 6.3. Details of the meshes for these two geometries can be found in Chapter 3. When running the CFD of these meshes, it was found that for convergence to be achieved, the simulations required that the flow, kinetic energy and dissipation were solved initially with a first-order scheme and then changed to a second-order scheme later on. This was different to the isolated geometries which could be solved using a second-order scheme initially.

6.1.1 Modelling reflected mixing noise

To allow for the JSR noise to be modelled, additional code was added to calculate the change in the ray path caused by reflecting from a solid surface. For an acoustic source below a wing, one would expect the pressure to double due to the wing creating a virtual source. An increase of 3dB would, therefore, be seen. If one models this with ray tracing, one would expect twice the number of rays to arrive below the wing as in an isolated case. As the flow factor, Φ, is a measure of the number of rays that arrive at the observer location, the reflected noise can be included within the LRT model. The definition of the flow factor can be found in Appendix A.2.

To calculate the path of a reflected ray, the first step is to determine if a ray could intersect with a solid surface. If one considers that a wing with little curvature can be modelled as a flat plate, this process is relatively simple. The wing position is defined by the horizontal distance from the nozzle exit to the wing trailing edge (TE), l, and a vertical distance, h, from the centreline of the nozzle. The wing also extends $0.75D_J$

upstream of the nozzle exit. The current and previous position of a ray is compared to the position of the wing. If the line between these ray positions intersects with the wing, a reflection will take place and so the current ray position will need to be updated. A similar procedure can be taken for reflections from the flap and pylon with only the location of the solid surface changing.

As the wing is being modelled as a flat plate, a line-plane intersection calculation is required. To do so, three points on the plane are defined, as shown in Figure 6.2.4.

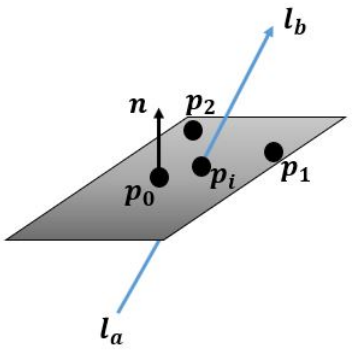

FIGURE 6.1.1: Line-plane intersection.

A point of intersection, $\mathbf{p_i}$, lies on the line between two points, $\mathbf{l_a}$ and $\mathbf{l_b}$, so that

$$\mathbf{p_i} = \mathbf{l_a} + m\mathbf{l_{ab}} \tag{6.1.1}$$

where m is a real number and $\mathbf{l_{ab}} = \mathbf{l_b} - \mathbf{l_a}$. Furthermore, $\mathbf{p_i}$ also lies on an infinite plane so that

$$\mathbf{p_i} = \mathbf{p_0} + v_1\mathbf{p_{01}} + v_2\mathbf{p_{02}} \tag{6.1.2}$$

where $\mathbf{p_{01}} = \mathbf{p_1} - \mathbf{p_0}$, $\mathbf{p_{02}} = \mathbf{p_2} - \mathbf{p_0}$ and v_1 and v_2 are real numbers. Therefore

$$\mathbf{l_a} + m\mathbf{l_{ab}} = \mathbf{p_0} + v_1\mathbf{p_{01}} + v_2\mathbf{p_{02}} \tag{6.1.3}$$

Equation 6.1.3 can be written in matrix form as

$$\begin{bmatrix} \mathbf{l_a} - \mathbf{p_0} \end{bmatrix} = \begin{bmatrix} -\mathbf{l_{ab}} & \mathbf{p_{01}} & \mathbf{p_{02}} \end{bmatrix} \begin{bmatrix} m \\ v_1 \\ v_2 \end{bmatrix} \tag{6.1.4}$$

A unique solution to Equation 6.1.4 can then be found if the determinate of the first matrix on the right-hand side is non-zero. Therefore

$$\begin{bmatrix} m \\ v_1 \\ v_2 \end{bmatrix} = \begin{bmatrix} -\mathbf{l_{ab}} & \mathbf{p_{01}} & \mathbf{p_{02}} \end{bmatrix}^{-1} \begin{bmatrix} \mathbf{l_a} - \mathbf{p_0} \end{bmatrix} \tag{6.1.5}$$

The value of m can then be calculated from

$$m = \frac{(\mathbf{p_{01}} \times \mathbf{p_{02}}) \cdot (\mathbf{l_a} - \mathbf{p_0})}{-\mathbf{l_{ab}} \cdot (\mathbf{p_{01}} \times \mathbf{p_{02}})} \tag{6.1.6}$$

Finally, the intersection point is calculated by substituting the value of m from Equation 6.1.6 back into Equation 6.1.1. It should be noted that this method calculates the intersection point for an infinite plane, so the intersection point needs to be checked to see if it falls within the finite extent of the wing.

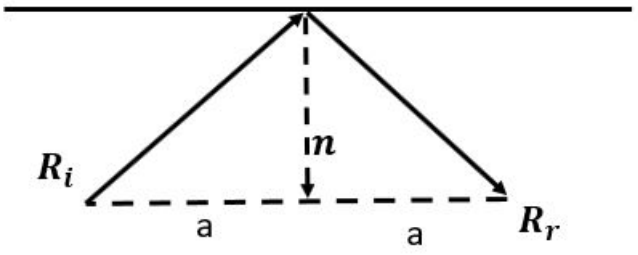

FIGURE 6.1.2: Direction of a reflected ray.

Having calculated the intersection point, one needs to calculate the direction that the reflected ray will carry on travelling in. This can be seen in Figure 6.1.2. If one describes the vector for the incident ray as $\mathbf{R_i}$, the reflected ray, $\mathbf{R_r}$, and normal to the surface, $\mathbf{n}$, then one can write

$$\mathbf{R_r} = \mathbf{n}(-\mathbf{R_i} \cdot \mathbf{n}) + a \tag{6.1.7}$$

$$-\mathbf{R_i} + a = \mathbf{n}(-\mathbf{R_i} \cdot \mathbf{n}) \tag{6.1.8}$$

where a is the horizontal distance from the ray vector to the normal vector. Eliminating a from Equations 6.1.7 and 6.1.8 gives

$$\mathbf{R_r} = \mathbf{R_i} - 2\mathbf{n}(\mathbf{R_i} \cdot \mathbf{n}) \tag{6.1.9}$$

Equation 6.1.9 determines the direction of the reflected ray and the ray tracing can continue as normal. Although Figure 6.1.2 shows a 2D case, Equation 6.1.9 applies to 3D cases as well.

The procedure for the calculation of reflections from the wing, flap and pylon is the same, although the position of the surfaces is different. The flap, which will be described in section 6.4, is assumed to be attached to the wing at the wing trailing edge. Modelling the pylon is slightly more complex than the wing or flap as two vertical planes are needed to be defined for either side. These planes meet at the bullet tip and extend back to the nozzle exit. Although this does not precisely match the outline of the pylon, it is a good enough first approximation. A more accurate description would require a line intersection with an arbitrary shape which is more complex to code and so will be left to future work.

For calculating the reflections from the bullet, a line-cone intersection calculation is carried out. By writing the surface of the cone as a parametric function, as seen above, the intersection point with the bullet can be calculated. It has already been shown in Chapter 5 that this reflection does not contribute very much to the noise within the frequency range that is being studied. Therefore, the additional description of this calculation is omitted here.

6.1.2 Validation of reflective code

With the method for calculating the reflected mixing noise outlined above, the results need to be validated. To do so, the position of the far-field observer and wing is varied

in this section to see if LRT can pick up the trends in the change in SPL. The reader should be reminded of the installed wing position parameters shown in Figure 6.1.3. The change in the SPL between the installed and isolated cases is compared to experimental data taken as part of the SYMPHONY project [103]. As this analysis is interested in the high frequency reflected noise and there is no model for the JSI noise within LRT, analysis is restricted to $St \geq 1$.

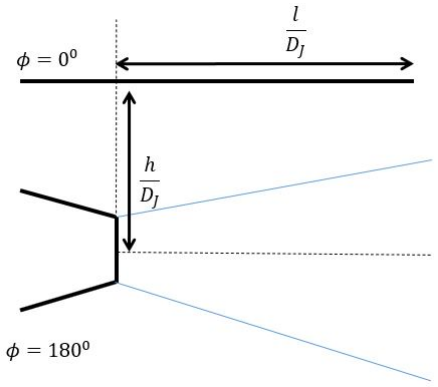

FIGURE 6.1.3: Geometry of the installed conical nozzle.

In order to make predictions using the LRT source model, some flow data is required. If the wing is placed far away from the jet, it will have a minimal influence on the flow field. Therefore, the flow field of the installed case will be identical to that of the isolated case. It was shown in Chapter 4, that RANS over-predicts the potential core length. To enable a comparison to be made, the wing length, l, has been extended within the LRT simulations in this section to provide the same ratio of wing length to potential core length as seen in the experiments.

In this analysis, the data from the isolated conical nozzle studied in Chapter 4 is used as a baseline for predictions. It was found by Lawrence [103] that the high-frequency content was independent of M_J so only the flow field for the static $M_J = 0.6$ case is studied here. A flat plate, representing the wing (span of $15D_J$), is then placed in the acoustic domain as outlined previously and the ray tracing is carried out. The position of the acoustic sources relative to the wing can be seen in Figure 6.1.4. The same number of source points (5925) and number of rays (655, 000) are used as outlined in Chapter 3. The additional reflective noise changes the number of rays received in each of the far-field bins and so will change the flow factor, ϕ, as outlined in Appendix A.2.

This is an oversimplification of the problem but will reveal if the general trends in the change in reflected mixing noise can be picked up. The accuracy of RANS in predicting installed jet flows is examined later in this chapter.

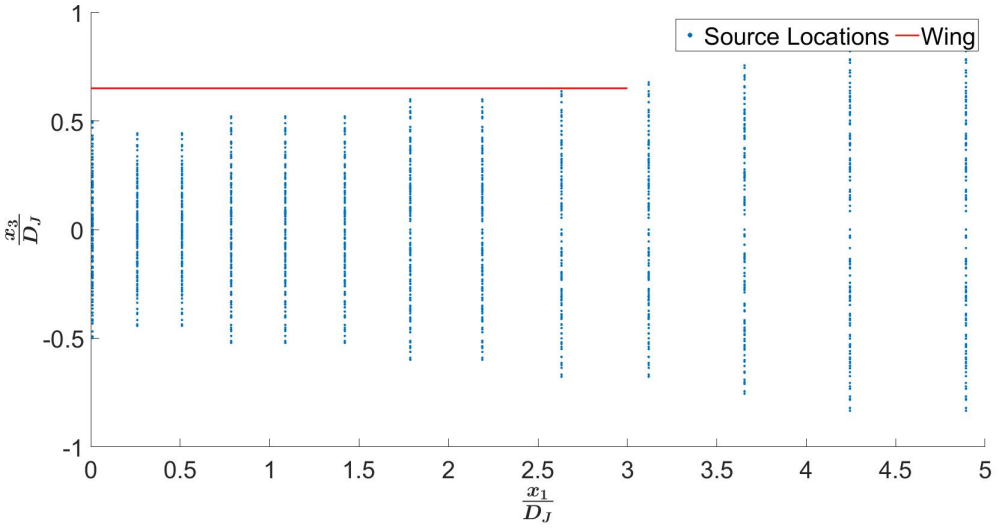

FIGURE 6.1.4: Position of sources under the wing with $\frac{l}{D_J} = 3$ and $\frac{h}{D_J} = 0.65$.

6.1.2.1 Variation with ϕ

The first analysis that was carried out was to look at whether LRT can detect the shielding effect of the wing. A reminder of the definition of the azimuthal angles can be seen in Figure 6.1.3. A flat plate has been placed at $\frac{l}{D_J} = 2$ and $\frac{h}{D_J} = 4$. This position has been selected so that there is a negligible impact on the flow field and a minimal amount of JSI is generated. Therefore, any change in the SPL can be attributed to reflected noise.

From the results in Figure 6.1.5, the LRT model predicts a decrease in noise on the shielded side ($\phi = 0°$) of the wing, as expected. Below the wing, the reflections from the wing cause an increase in the SPL observed. Although these are expected results, it confirms that the physics is being correctly modelled. At the sideline position ($\phi = 90°$), there is a small increase of 0.25dB in the experimental noise seen at high frequencies which is picked up by the LRT code. This is thought to be due to a small number of reflections from the wing reaching the observer from small angles and the semi-infinite wing. As one is mainly concerned with the noise below the wing ($\phi = 180°$), the small amount of reflected noise at the sideline is not as important.

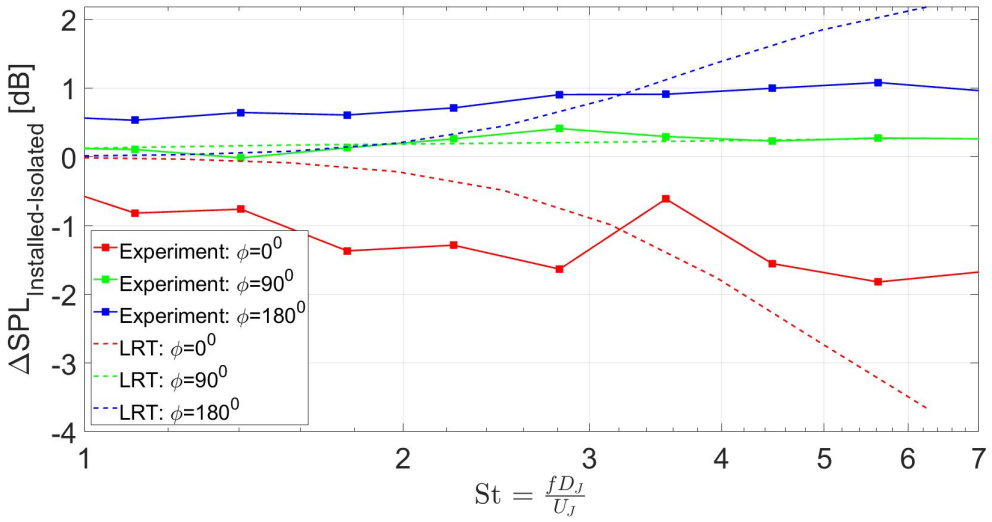

FIGURE 6.1.5: Azimuthal variation in ΔSPL for the static installed conical nozzle at $M_J = 0.6$, $\theta = 90°$, $\frac{l}{D_J} = 2$ and $\frac{h}{D_J} = 4$ compared to the isolated case. All data is presented as $1/3^{rd}$ octave data.

6.1.2.2 Variation with θ

The next analysis looks at how the reflected noise varies in terms of θ. The results for this can be seen below in Figures 6.1.6. In the rear arc, there is a 0.5dB increase in SPL as one moves from $\theta = 60° \rightarrow 80°$ experimentally. The LRT model only starts to pick up the additional energy at $\theta = 80°$. However, the reflected mixing noise at $\theta = 60°$ and 70° is less than 0.2dB which is within the experimental error, so the LRT predictions are still accurate.

More interesting results are seen in the forward arc as both the experiment and LRT indicate a larger change in SPL compared to the rear arc. The experimental data shows a roughly constant peak ΔSPL at high frequencies but a decrease in the peak Strouhal number as θ increases. This change in the peak Strouhal is reflected in the LRT simulation, although the amplitude and peak location are not captured. The change in the peak Strouhal number is thought to be due to lower frequencies occurring further down the jet. Rays from these low-frequency sources will be reflected towards higher polar angles due to the source's position relative to the wing. It is thought that the over-prediction in SPL comes from not modelling the outside surface of the nozzle. This will mean that rays that would be reflected off the outside of the nozzle will instead be traced through the nozzle wall to the far field. Adding the reflection from the external surface of the nozzle will be future work of this project.

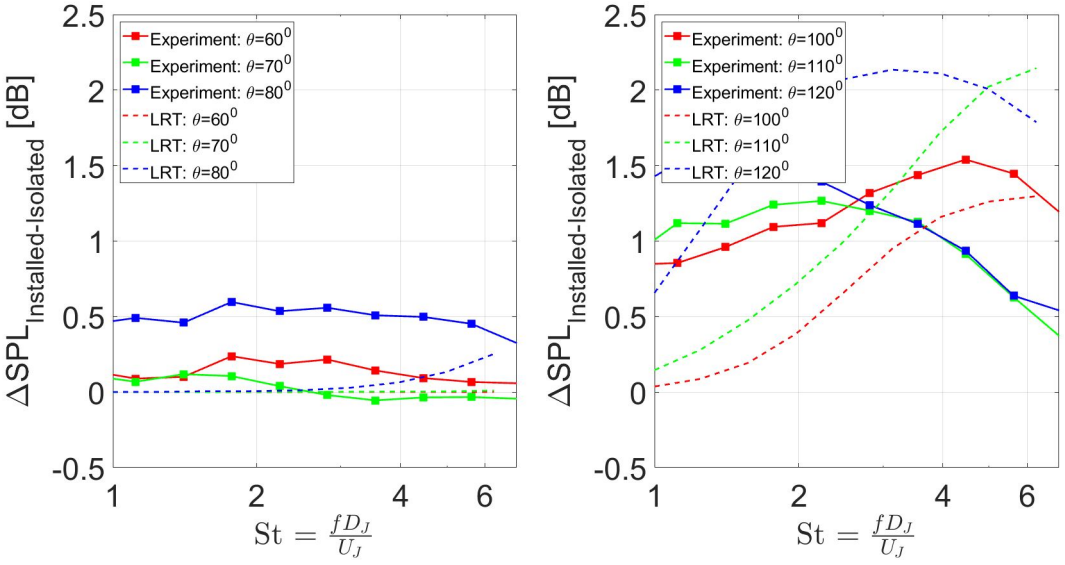

FIGURE 6.1.6: θ variation in the rearward (left) and forward arcs (right) in ΔSPL for the static installed conical nozzle at $M_J = 0.6$, $\phi = 180°$, $\frac{l}{D_J} = 2$ and $\frac{h}{D_J} = 4$ compared to the isolated case. All data is presented as $1/3^{rd}$ octave data.

One interesting point of note is that there is a decrease in the ΔSPL at high frequencies with increasing θ in the forward arc. One would think that the ΔSPL would plateau rather than decrease. As LRT picks up on this trend, it is thought that this trend is due to the path that high-frequency rays take. As the higher frequencies occur closer to the nozzle exit, it could be that these have fewer possible paths to the far-field observer due to the narrow region in which the frequencies exit.

To conclude, the main influence of reflected mixing noise as θ varies is seen, both experimentally and in the LRT results, in the forward arc.

6.1.2.3 Variation with l

The previous two analyses focused on how the reflected mixing noise changed with the far-field observer position. More interesting results were found by Lawrence [103] when the wing position was changed. As mentioned in Chapter 2, Lawrence found a large variation in the JSI noise when the horizontal distance to the wing TE, l, was varied. To minimise this effect in the analysis, the wing is placed at $\frac{h}{D_J} = 4$. The results for varying l on the high-frequency noise can be seen in Figure 6.1.7. There are two points of interest here. Firstly, the LRT predictions show that the cut-on frequency of reflected noise decreases as $\frac{l}{D_J}$ increases. This makes intuitive sense as one can describe that more of the source distribution lies underneath the wing as l increases.

Secondly, LRT predicts that there is a maximum ΔSPL of reflected noise which does not change with l. However, the experimental data shows a gentle increase in the ΔSPL with frequency until $\frac{l}{D_J} = 7$ and then remains roughly constant. This is an unexpected result. As the wing is placed away from the jet ($\frac{h}{D_J} = 4$), it is unlikely that there is any flow interaction around the wing. More likely, there is some feedback mechanism that is dependent on the wing length which causes this trend. However, the nature of this mechanism is unknown and so will need to be investigated further in future work.

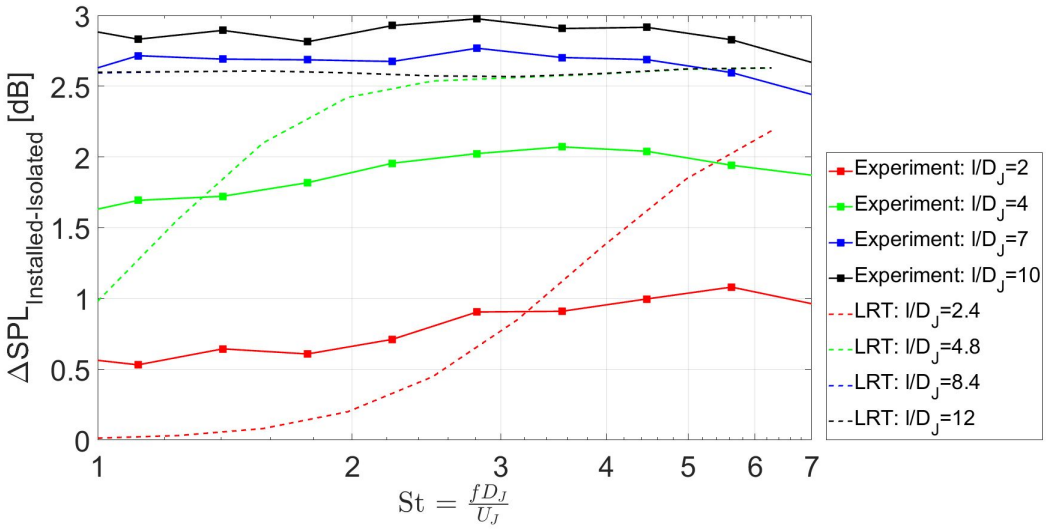

FIGURE 6.1.7: $\frac{l}{D_J}$ variation in ΔSPL for the static installed conical nozzle at $M_J = 0.6$, $\theta = 90°$, $\phi = 180°$ and $\frac{h}{D_J} = 4$ compared to the isolated case. All data is presented as $1/3^{rd}$ octave data.

6.1.2.4 Variation with h

The next analysis looks at how the reflected mixing noise varies with vertical separation, h, between the nozzle centreline and the wing. For this analysis, $\frac{l}{D_J} = 4$. As the wing is being moved closer to the jet, the original assumption that the flow field is not influenced by the wing needs to be revisited. Wang [126] found that for this value of l and when $\frac{h}{D_J} = 1$, the jet was not altered by the plate despite being at the edge of the shear layer. Therefore, the isolated flow field is representative of the installed flow field when $\frac{h}{D_J} \geq 1$.

The results of this analysis can be seen in Figure 6.1.8. As can be seen from the figure below, LRT does predict a small amount of variation with h (0.2dB), but not as much as is seen experimentally (0.4dB). The experimental data suggests that as h decreases,

the ΔSPL increases, which makes sense as the rays have less time to refract and a shorter distance to travel. Therefore, rays are focused towards the observer's position as the wing moves closer to the jet. Although LRT only predicts a small variation in the ΔSPL, the opposite trend can be seen i.e. a decrease of 0.2dB as the wing moves closer to the jet. This would imply that more refraction is taking place within the ray tracing which is diverting rays away from the far-field observer. Further investigation is required here to understand what is happening within the ray tracing.

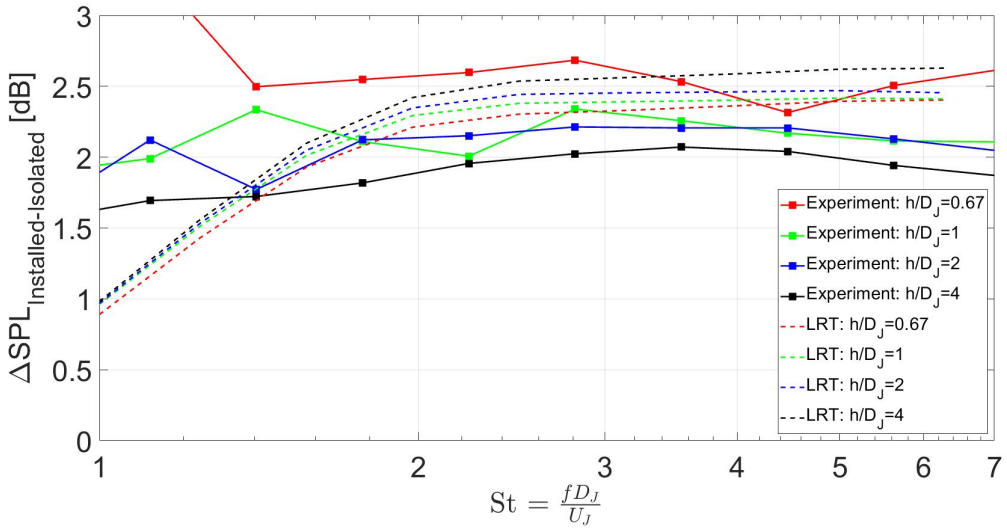

FIGURE 6.1.8: $\frac{h}{D_J}$ variation in ΔSPL for the static installed conical nozzle at $M_J = 0.6$, $\theta = 90°$, $\phi = 180°$ and $\frac{l}{D_J} = 4$ compared to the isolated case. All data is presented as $1/3^{rd}$ octave data.

It should be noted that there is a cross-over region between $St = 1$ and 2 of the JSI and JSR noise sources [103]. Above $St = 2$ where only the JSR noise is present, the LRT model generally predicts the change in noise level to within 0.5dB. Therefore, despite not predicting the correct general trend, reasonable predictions can still be made.

6.1.2.5 Variation with M_f

The final analysis that has been carried out in this section, is how the variation in the flight Mach number affects the reflection noise. The results can be seen below in Figure 6.1.9. Here, experimental data for a flat plate of 300mm at $\frac{h}{D_J} = 0.67$ and $\frac{l}{D_J} = 3$ was taken in the Doak laboratory. As can be seen from Figure 6.1.9, there is little variation in ΔSPL with M_f. A quick check of other polar angles confirmed that this result was consistent and so results for only one polar angle are presented here. The

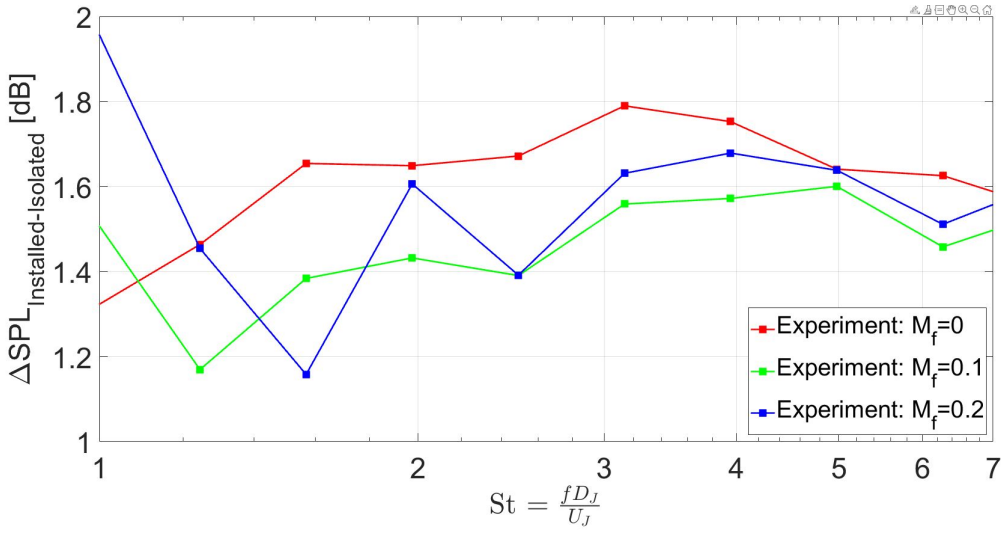

FIGURE 6.1.9: M_f variation in ΔSPL for the installed conical nozzle at $M_J = 0.6$, $\theta = 90°$ and $\phi = 180°$ at $\frac{h}{D_J} = 0.67$ and $\frac{l}{D_J} = 3$ compared to the isolated case. All data is presented as $1/3^{rd}$ octave data. (Data from private communication)

peak in the experimental data at $St = 2$ for the $M_f = 0.2$ case is thought to be due to vortex shedding from the flat plate in the flight-stream. Therefore, the conclusion is that the reflected mixing noise does not depend on the flight Mach number and so the LRT simulations for these scenarios were not run.

The consequence of the reflected noise not varying with M_f, or indeed with M_J as Lawrence [103] showed, is that the same scaling laws can be used for the high-frequency content of the installed noise as are used for isolated noise. Therefore, installed spectra can be collapsed at $\theta = 90°$ with $60 \log\left(\frac{U_J}{U_J - U_f}\right)$ for in-flight cases and with $70 \log \frac{U_J}{U_{ref}}$ for varying jet Mach number. This has been confirmed by studying experimental data from the Doak laboratory, although the data are not presented here.

This conclusion may seem fairly trivial, as all that is being said is that the wing does not impact the jet mixing noise source, but this may not be true for installed pylon cases. The pylon wake connects the two regions of flow and the isolated data in the previous chapter would suggest a dependency on the flight Mach number.

The analyses in this section have shown that the reflected mixing noise is a function of the wing position, l and h, as well as the observer position. LRT has been shown to pick up the general trends in changes with the observer position. More analysis is needed to understand the physics of the wing position on the reflected noise. It should be noted that these analyses have mainly been carried out on wing positions where

there is limited jet impingement. Obviously, additional turbulent energy will be generated for an impinged jet (for example when there is a deployed flap) and so additional mixing noise will be generated downstream of this point. It is suspected that this will prevent a collapse of the installed spectra with the scaling laws mentioned above.

6.2 Installed annular nozzle

Having verified the reflection code in the previous section, attention can now be turned to whether RANS can accurately predict the flow field of an installed jet. In this section, a NACA4415 airfoil has been placed above the annular nozzle studied in the previous chapter, as seen in Figure 6.2.1. The airfoil is positioned at $\frac{l}{D_J} = 3$ and $\frac{h}{D_J} = 0.65$ with an AOA of 3.1°. As mentioned in the previous section, the wing is modelled in the ray tracing code as a flat plate. This assumption is valid due to the limited curvature of the NACA4415 airfoil. Given that the reflected mixing noise does not change with M_J [103], it has been decided that only the $M_J = 0.6$ case will be studied as seen in Table 6.1.

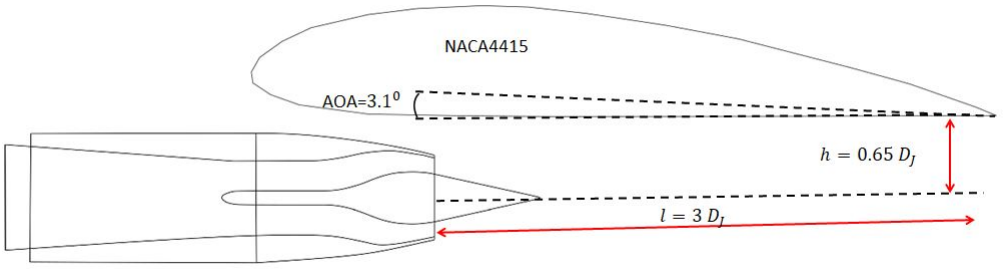

FIGURE 6.2.1: Geometry of the installed annular nozzle

M_J	M_f
0.6	$0.0 \rightarrow 0.2$ (0.1 intervals)

TABLE 6.1: Cases simulated for the installed annular nozzle.

6.2.1 CFD results

In this section, we are concerned with the impact of the wing on the flow. For a static case, one would expect there to be a minimal difference between the isolated and installed geometries as the wing will not generate much lift. This comparison can be

seen below in Figure 6.2.2, which shows the velocity and turbulence profiles at three axial locations. If one looks at the velocity profiles at $\frac{x_1}{D_j} = 2$ and 4, which are underneath the wing and just after the trailing edge, there is very little difference between the isolated and installed cases. Although the entrainment of the jet will draw flow through the small gap between the wing and nozzle, thus accelerating the flow, this effect is small as there is a negligible difference in the results. However, looking further downstream at $\frac{x_1}{D_j} = 8$, the wing has introduced a coanda effect into the flow field as the velocity profile is no longer symmetric about the centreline. Furthermore, the wing reduces the mixing rate of the jet as the installed peak velocity is higher than the isolated case. This effect is seen in both the experimental and CFD data although a greater difference in peak velocity is seen experimentally (5%) than in the RANS simulation (1.2%). Finally, both RANS profiles at this location have a much lower peak velocity than the experiment would suggest, thought to be due to the turbulence model as mentioned in the previous chapter.

Looking at the TI profiles in the right-hand column of Figure 6.2.2, RANS captures the reduction in TI close to the wing ($+x_3$) at $\frac{x_1}{D_j} = 2$ and 4. However, further downstream of the wing TE at $\frac{x_1}{D_j} = 8$, RANS suggests an increase in turbulence of 0.2% while experimentally there is a decrease of 1%. As this trend was not seen in the isolated results in the previous two chapters, the wing is the cause of the problem. This is not a physical effect as the general trend in RANS does not match the experimental data. Therefore, RANS is not predicting the effect of the wing correctly. It is known that the k-ϵ turbulence models over-predict the turbulence from isolated wings [26], so this result is not entirely unexpected. Although good acoustic predictions of the high-frequency content may be possible due to the excellent match between RANS and experimental data underneath the wing, an over-prediction of the low-frequency mixing noise will occur due to the additional turbulence after the wing trailing edge. It is unclear currently whether this additional mixing noise will be relevant as the low-frequency noise of installed jets is dominated by the JSI noise. This point will be revisited when looking at the acoustic results.

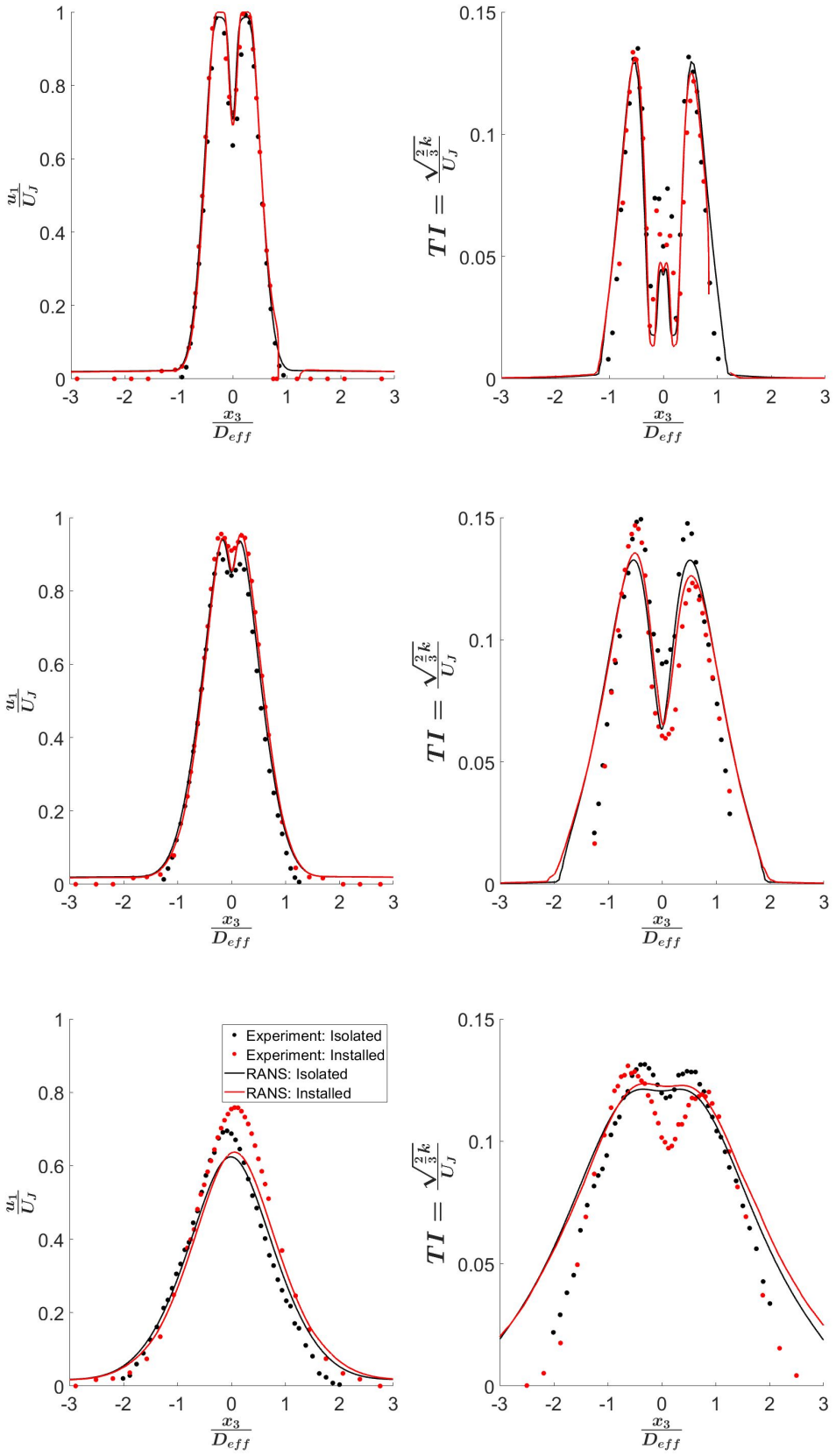

FIGURE 6.2.2: Radial profiles of $\frac{u_1}{U_J}$ (left) and turbulence intensity (right) for the static isolated and installed annular nozzles at $M_J = 0.6$. Each row corresponds to $\frac{x_1}{D_J} = 2$, 4 and 8, respectively.

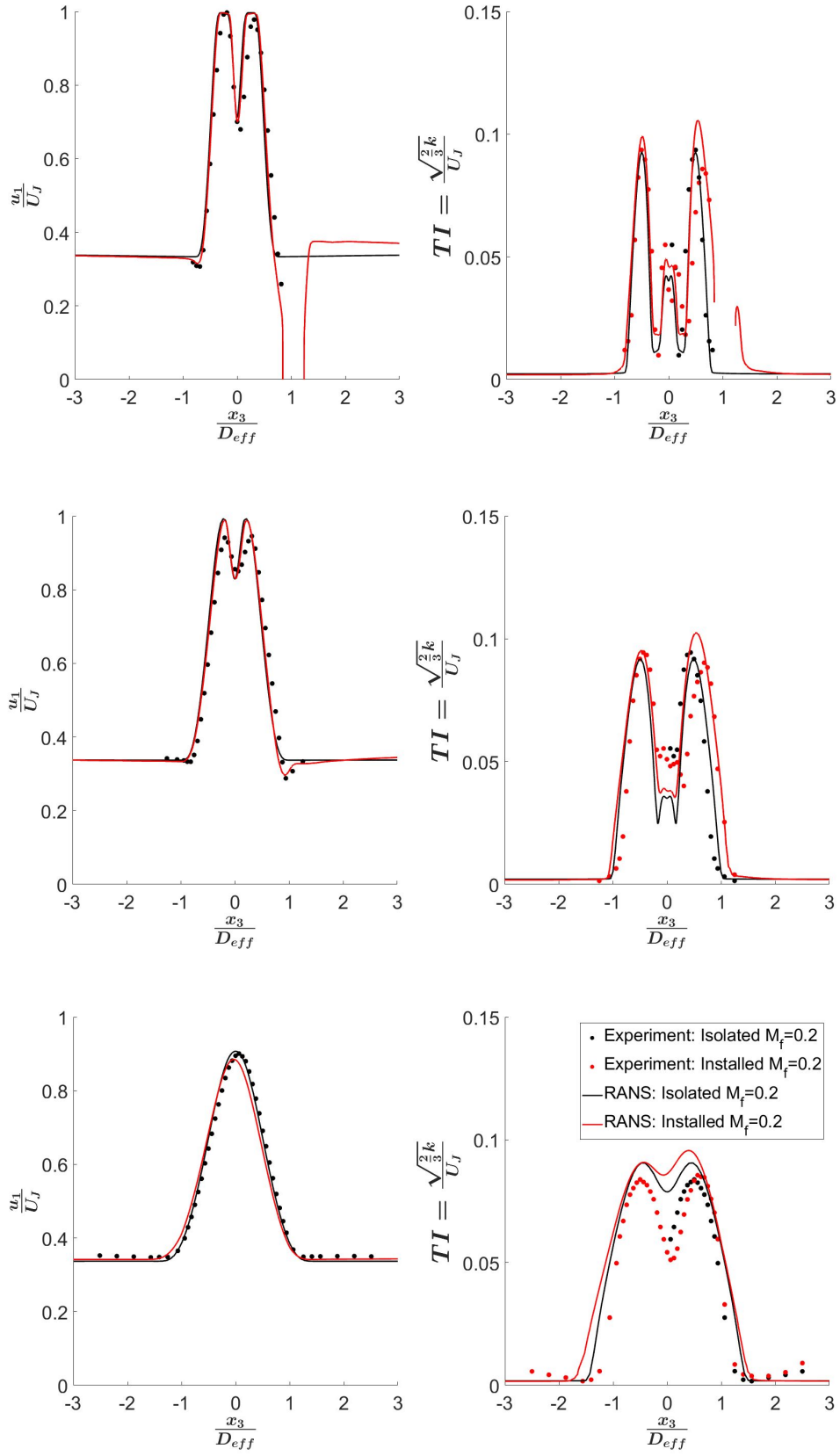

FIGURE 6.2.3: Radial profiles of $\frac{u_1}{U_J}$ (left) and turbulence intensity (right) for the isolated and installed annular nozzles at $M_J = 0.6$ and $M_f = 0.2$. Each row corresponds to $\frac{x_1}{D_J} = 2$, 4 and 8, respectively.

If one now considers an in-flight case where the wing is generating some lift a slightly different set of conclusions is reached. The data for this analysis is shown in Figure 6.2.3. Similar to the static results, close to the wing at $\frac{x_1}{D_j} = 2$ and 4 there is little difference between the velocity profiles in the RANS simulations. The acceleration of the flow above the wing can be seen in the velocity profile at $\frac{x_1}{D_j} = 2$. However, travelling downstream to $\frac{x_1}{D_j} = 8$, RANS predicts that the jet flow is slightly deflected away from the wing as expected but has a lower peak velocity than the isolated case. Comparison can not be made to the experimental data for the installed case, as the velocity data was not taken. This is due to there being little of interest within said data.

Experimental data has been taken, however, for the turbulence levels around the wing in-flight. Around the wing, there is a decrease in the turbulence level experimentally, although this is not picked up by the RANS model at $\frac{x_1}{D_j} = 2$ and 4. RANS does pick up on the fact that the turbulent shear layer is drawn slightly towards the wing, however. The result of these two factors will mean that acoustic predictions in-flight are likely to over-predict the mixing noise levels at all frequencies. This again is thought to be linked to the turbulence model, but there is a greater impact for the in-flight cases.

The previous figures have highlighted the fact that a k-ϵ turbulence model produces errors when modelling installed jets, but it has been shown in the previous chapters to be good for isolated cases. It is already known that the k-ϵ model does not predict isolated wings well and researchers have turned to the SST model, as mentioned in Chapter 2. This blends the k-ω model near the wall with a k-ϵ model far away from the wall. By doing this, researchers have produced better predictions for isolated wings. The question that arises, is can an SST model be more accurate in predicting installed jet flows?

This question is studied in Figures 6.2.4, where the k-ϵ model has been compared to the SST model for the static installed case. At $\frac{x_1}{D_j} = 2$ and 4, there is little difference in the axial velocity profiles. However, when the turbulence intensity is examined, the SST model produces a thinner shear layer at these axial locations. While this does produce a better fit compared to the experimental data, due to the low levels of turbulence at the edge of the shear layer, it is expected that there will only be a small difference in the acoustic response at high frequency. In terms of peak turbulence

predictions, which would impact the acoustic results the most, it is difficult to tell if the SST model is more accurate. At $\frac{x_1}{D_J} = 4$, the SST model provides a more accurate prediction on the $-x_3$ side (under-prediction of 0.4% rather than 1% for k-ϵ) but is worse on the wing side (an under-prediction of 1.2% as opposed to an over-prediction of 0.3%). Given that there is not a clear improvement in the turbulence predictions of the high-frequency content which would result in a large change in the acoustic results, further work will continue with the k-ϵ model. A more detailed analysis could be carried out to understand the sensitivities of the SST model, but this will be left for future work.

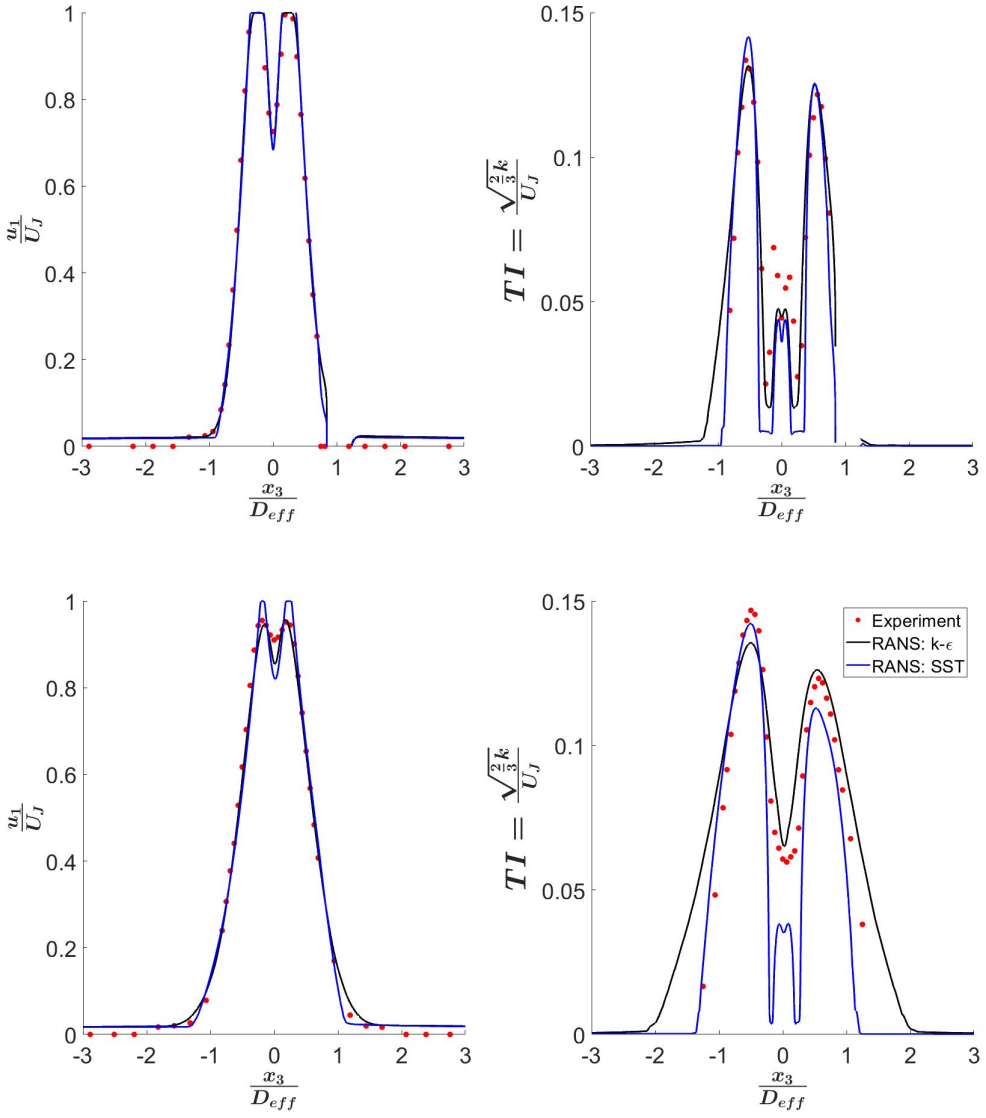

FIGURE 6.2.4: Radial profiles of $\frac{u_1}{U_J}$ (left) and turbulence intensity (right) for the static installed annular nozzles at $M_J = 0.6$ with a k-ϵ and SST turbulence models. Each row corresponds to $\frac{x_1}{D_J} = 2$ and 4, respectively.

6.2.2 Acoustic results

There are three main noise sources within the far-field spectra for installed jets: the direct jet mixing noise, reflected mixing noise and the JSI. The first two of these are accounted for within the LRT model, but the final one is not. Given that the JSI noise is dominant at low frequencies, the LRT predictions are only expected to match the high-frequency region, $St \geq 2$. A cross-over region between the JSI and the reflected noise exists between $St = 1$ and 2 [103], so an under-prediction is expected here.

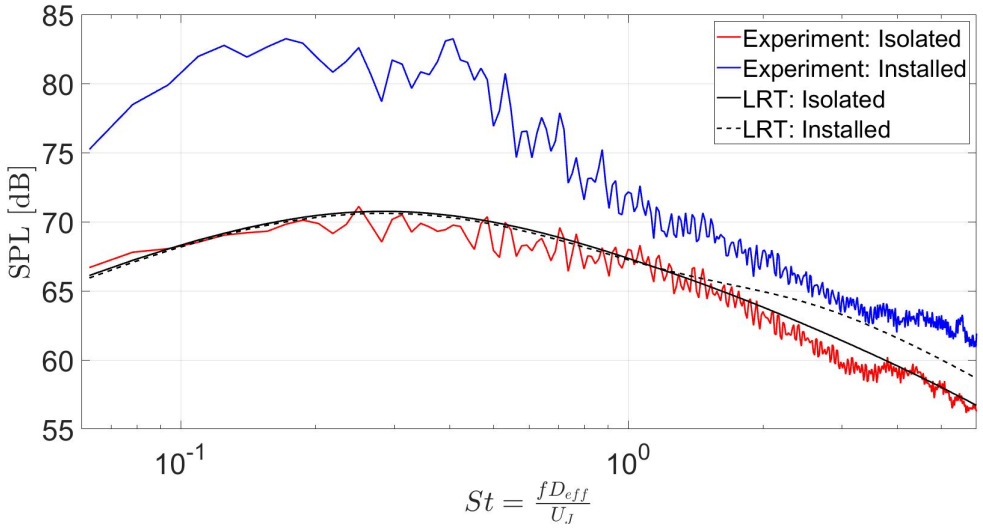

FIGURE 6.2.5: LRT predictions at $\theta = 90°$ and $\phi = 180°$ for the static installed annular nozzle at $M_J = 0.6$. All data is shown at 100Hz narrowband frequencies.

The LRT prediction for the static installed annular nozzle using a k-ϵ turbulence model is shown in Figure 6.2.5 on the unshielded side ($\phi = 180°$). Here, one can see that below $St = 1$, the isolated and installed data collapse to within 0.15dB of each other. Above this point, the reflected noise starts to contribute to the overall noise level. By $St = 3$, the LRT prediction is within 1dB of the experimental noise level. Above $St = 3$, the additional noise from the bullet struts that was mentioned in Chapter 5 prevents a collapse of the experimental data with the LRT prediction. It is suspected that if this noise source were removed, then the LRT prediction would be within 1dB of the experimental data. It is surprising that the low frequency data for the isolated and installed cases collapse, given that additional TKE was seen after the wing TE within the CFD results (Figure 6.2.2). Further analysis on the change in the low-frequency content above and below the wing is shown in Figure 6.2.6. As the reflected mixing noise is negligible below $St = 1$, the change in noise seen in this figure is entirely due

to the mixing noise. A maximum change of 0.69dB is seen at $St = 0.55$. The only way this is possible is if the jet is shielding the additional turbulence behind the wing TE from the far-field observer below the wing. Therefore, despite having inaccurate CFD predictions downstream of the wing trailing edge, there is a negligible impact on the mixing noise predictions on the unshielded side of a static installed jet at $\theta = 90°$.

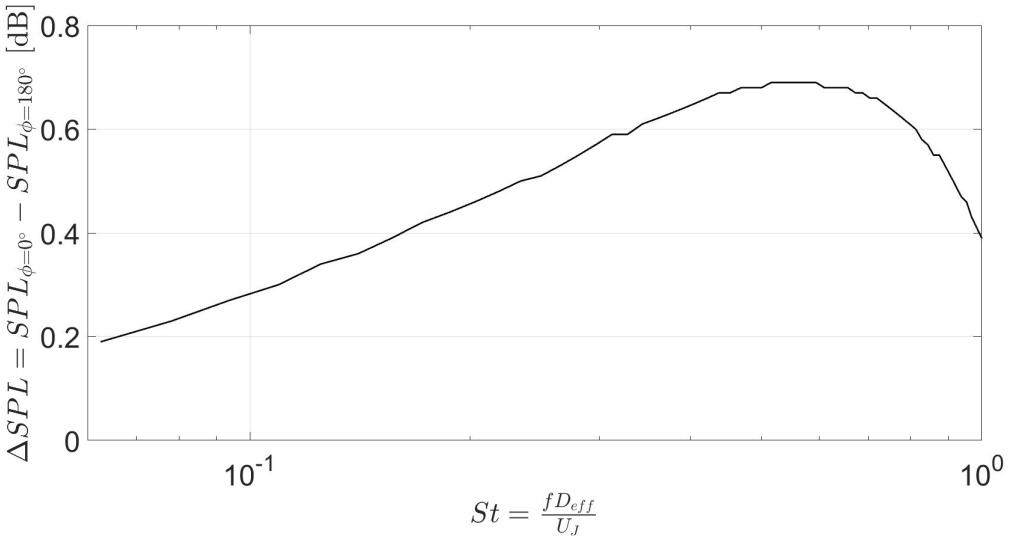

FIGURE 6.2.6: The change in SPL in the LRT predictions at $\theta = 90°$ for the static installed annular nozzle at $M_J = 0.6$ between the shielded and unshielded side of the wing. All data is shown at 100Hz narrowband frequencies.

In-flight acoustic predictions have been made for the installed annular nozzle and the change in SPL between the installed and isolated cases can be seen below in Figure 6.2.7. One would like to verify how much the errors seen in Figure 6.2.3 around the wing have influenced the acoustic results. From the results in Figure 6.1.8, we know that the reflected mixing noise is independent of the flight-stream velocity. Therefore, any change in the acoustic prediction from the static to in-flight cases can be linked to errors within the CFD. From Figure 6.2.7, one can see that at $M_f = 0.1$, there is negligible change in the noise below $St = 1$ between the static and in-flight case and a maximum of 0.5dB above $St = 1$. The data at low frequencies converges to a difference of 0dB due to the fact that the low frequencies exist far downstream of the wing and so there is no reflected noise at the polar angle from these frequencies due to the relative angles between the source and the wing. However, a larger change is seen for the $M_f = 0.2$ case where there is a maximum error of 1dB at $St = 0.07$ and $St = 6$. This is not realistic and so is thought to come from errors in the CFD. Therefore,

further acoustic predictions of installed jets will be limited to the static case to limit the errors from the CFD data.

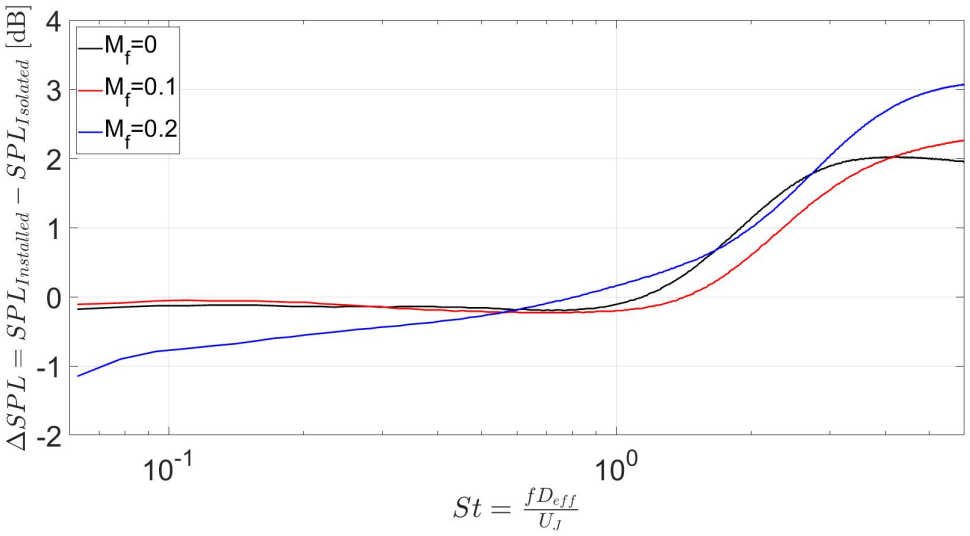

FIGURE 6.2.7: The change in SPL in the LRT predictions at $\theta = 90°$ and $\phi = 180°$ for the isolated and installed annular nozzles at $M_J = 0.6$. All data is shown at 100Hz narrowband frequencies.

6.3 Jet-pylon-wing configuration

The final geometric change that has been investigated is the inclusion of the pylon to an installed jet. In this section, the NACA4415 airfoil is added to the 10% externally blocked nozzle, as shown in Figure 6.3.1. The same wing position is studied here as for the installed annular case (i.e. $\frac{l}{D_J} = 3$ and $\frac{h}{D_J} = 0.65$). The cases studied are outlined in Table 6.2.

This geometry is being studied to observe how the pylon affects the installed flow field. In the isolated case, the wake from the pylon blockage was shown to draw the jet upwards. The point of interest is how this effect interacts with the wing, which will push the jet away from the wing for in-flight cases.

Similar to the study in Chapter 5 with the external pylon surface, although the addition of the pylon will provide an additional surface for reflective noise, this will be confined to very high frequencies ($St > 6$) and predominantly occur at the sideline. Therefore, as this effect is above the frequency range of the current analysis, the reflected mixing noise from the pylon will not be discussed further.

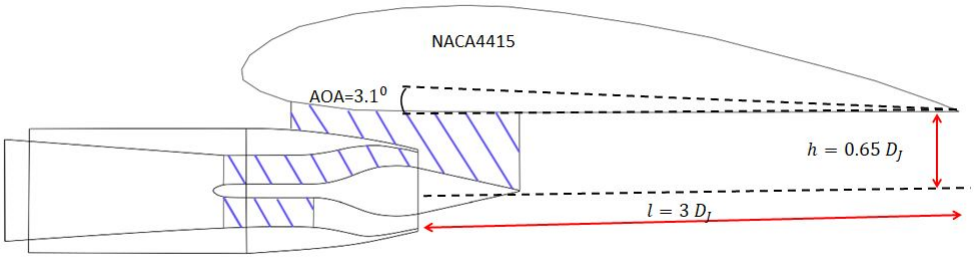

FIGURE 6.3.1: Geometry of jet-pylon-wing configuration

M_J	M_f
0.6	$0.0 \rightarrow 0.2$ (0.1 intervals)

TABLE 6.2: Cases simulated for the installed annular nozzle.

6.3.1 CFD results

The radial profiles of velocity and turbulence intensity at different flight Mach numbers for the $M_J = 0.6$ case can be seen below in Figures 6.3.2. The profiles are taken at $\frac{x_1}{D_J} = 2, 4$ and 8. Similar to the installed annular nozzle, experimental velocity data for the $M_f = 0.2$ case were not taken. The RANS data has been included to show the general trend in the data. Like with the installed annular nozzle, the peak velocity and shape are well captured beneath the wing and just after the trailing edge. As expected, the pylon wake produces a decrease in the peak velocity (3%) on the wing side of the jet ($+x_3$) at $\frac{x_1}{D_J} = 2$.

From the experimental data, it is clear to see that the combination of the pylon and wing causes the jet to bend away from the wing at $\frac{x_1}{D_J} = 8$, even in the static case. This is not picked up, however, by the RANS simulation. The CFD shows that the flow is drawn towards the wing. This coanda effect does reduce slightly as M_f increases, which will be due to an increase in pressure below the wing generating some lift and the flight-stream convection. Clearly, there is some additional physics that the RANS model is not capturing in terms of the velocity flow field. The obvious difference that this will make acoustically is the fact that the refraction of noise after the trailing edge of the wing will be different between the experiment and LRT predictions, introducing a further source of error away from $\theta = 90°$. While lower frequencies are generated further downstream and are less affected by refraction, it is suspected that mid-frequencies ($St \approx 1$) will be affected.

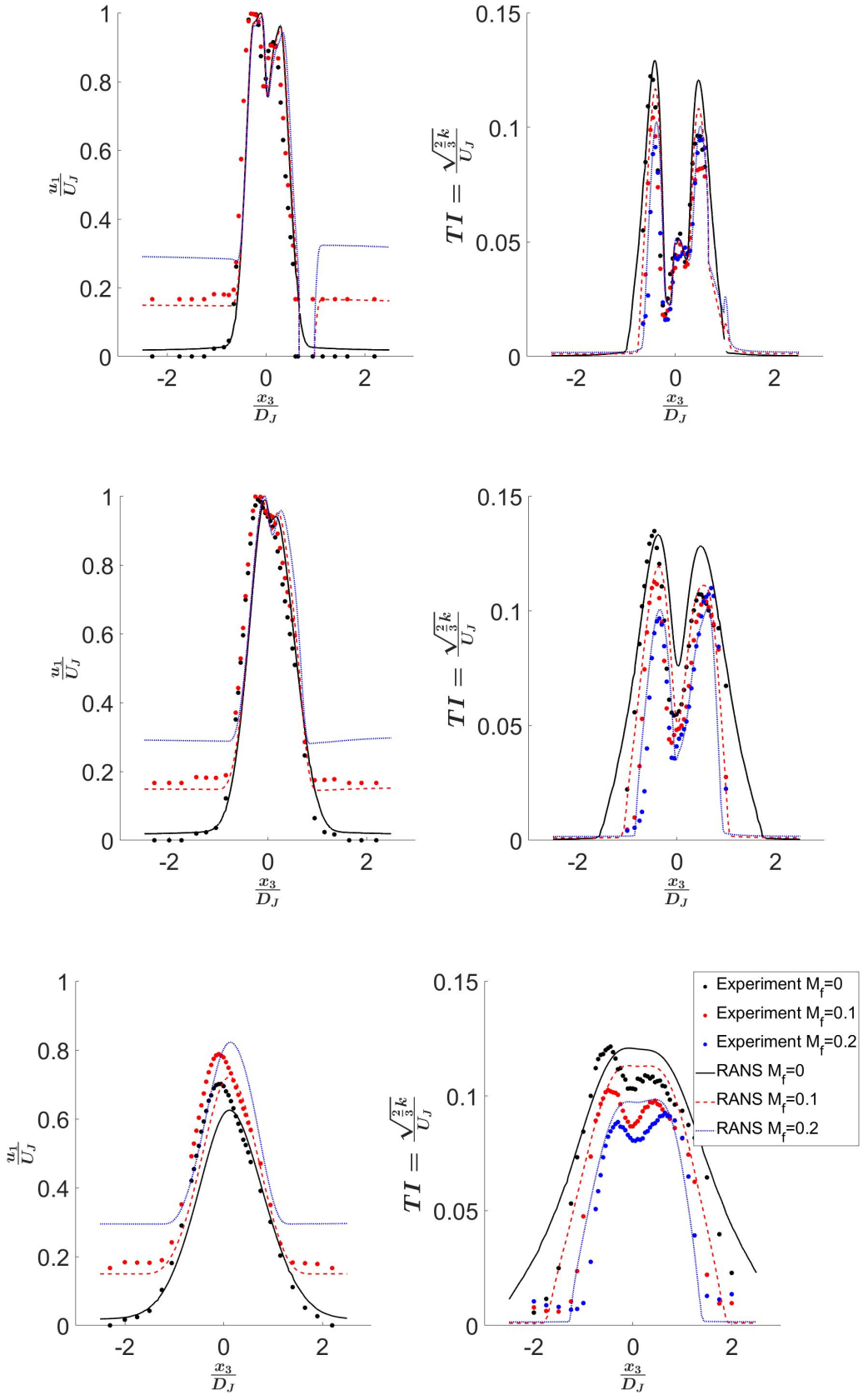

FIGURE 6.3.2: Radial profiles of $\frac{u_1}{U_J}$ (left) and turbulence intensity (right) for the jet-pylon-wing configuration at $M_J = 0.6$ and $M_f = 0, 0.1$ and 0.2. Each row corresponds to $\frac{x_1}{D_J} = 2$, 4 and 8, respectively.

Looking now at the turbulence intensity plots in Figures 6.3.2, a reasonable agreement to experimental data in terms of amplitude and shape can be seen on the $-x_3$ side at $\frac{x_1}{D_j} = 2$ and 4. However, there is an over-prediction of the RANS at all values of M_f on the $+x_3$ near the wing at $\frac{x_1}{D_j} = 2$. The experimental data also shows an increase in the TI in the $M_f = 0.2$ case near the wing which is not picked up by the k-ϵ RANS simulation and was also seen in the isolated pylon data. Therefore, there is some additional physics that the CFD is not capturing.

The previous results for the installed annular case showed good agreement below and just after the wing, however, the addition of the pylon makes a large difference to the accuracy of the k-ϵ RANS predictions. The real physics is more complex than what RANS can handle and so it appears that the limit of modelling jets with RANS using a k-ϵ turbulence model has been discovered.

6.3.2 Acoustic results

Given the errors seen in the CFD results in this chapter downstream of the wing TE, it is difficult to believe that acoustic predictions at low frequencies are accurate. Therefore, analysis in this section will be limited to looking at the high-frequency data above $St = 1$, which occurs primarily within the first six diameters. This will minimise the influence of errors from the CFD on the acoustic results.

As the change in mixing noise that occurs between geometries is of interest, the LRT prediction of the ΔSPL between the static jet-pylon wing and installed annular nozzle is shown in Figure 6.3.3 for the static case. The change in mixing noise is calculated using the following equation

$$\Delta SPL = SPL_{\text{jet}-\text{pylon}-\text{wing}} - SPL_{\text{installed annular}} - 20\log\left(\frac{\mathrm{D}_{\text{eff, pylon}}}{\mathrm{D}_{\text{eff, annular}}}\right) \tag{6.3.1}$$

It can be seen that above $St = 2.6$, there is less than a 0.2dB change in the mixing noise between the two geometries. This implies that there is little difference in the reflected mixing noise below the wing. Therefore, similar to the static isolated cases, the pylon is having a negligible impact on the static far-field results.

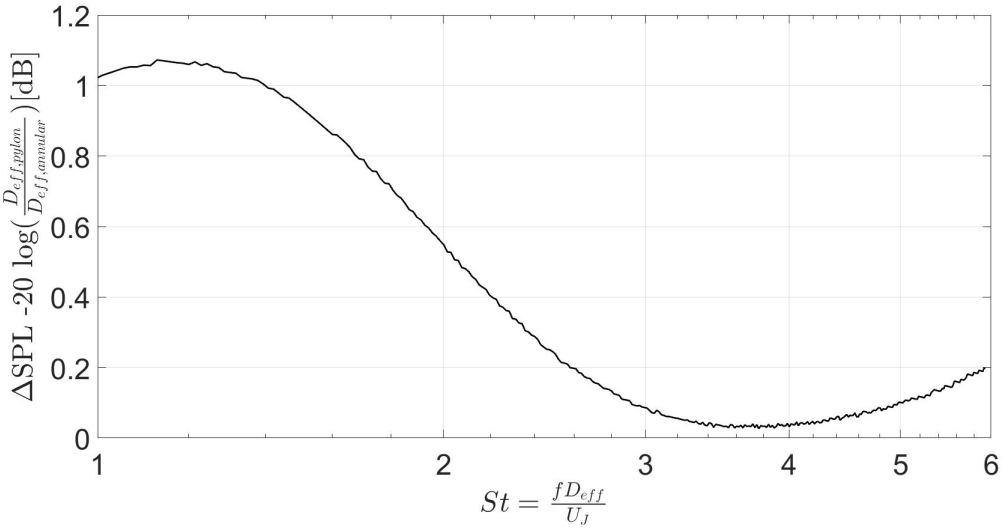

FIGURE 6.3.3: LRT prediction of the ΔSPL at $\theta = 90°$ and $\phi = 180°$ from the static jet-pylon-wing configuration to the installed annular nozzle at $M_J = 0.6$.

While further analysis is certainly possible with this geometry, the problem that is faced is that the errors within the CFD data are likely to lead to inaccurate conclusions being made. It has been seen with the installed annular nozzle that even more errors are introduced when the in-flight case was studied. As this is likely to be the point where the pylon in the installed case has a large effect as seen for the isolated case, it will be difficult to separate the pylon effect from CFD error. Therefore, acoustic analysis has not been run on the in-flight jet-pylon-wing case.

6.4 Installed jet with a deployed flap

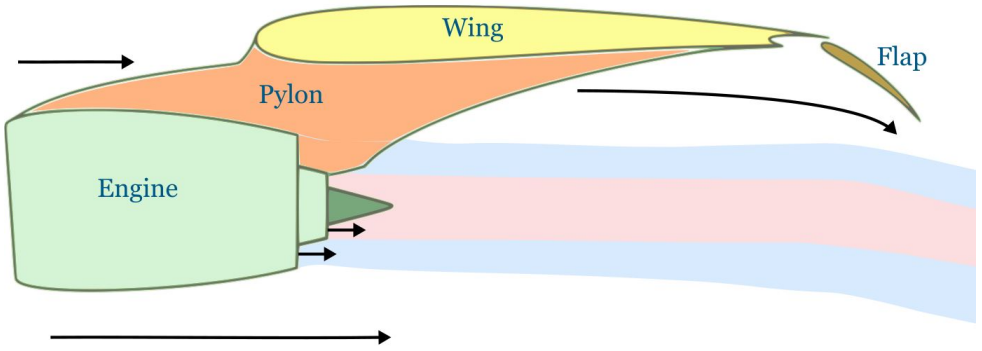

FIGURE 6.4.1: Flow around an installed jet with a deployed flap.

One of the most complex situations that one would like to study for an installed jet would involve modelling a wing with a deployed flap. During take-off and approach,

the flaps on aircraft are deployed to increase lift and drag, respectively. By deploying the flaps, there is an increase in the high pressure underneath the wing which bends the jet away from the nozzle axis, as seen in Figure 6.4.1. This will change the directivity of the mixing noise produced downstream of the flap. Furthermore, the increased flap angle will increase the JSR noise in the forward arc and the JSI. The questions that now arise are how much does the jet deflect and then by how much do the various noise mechanisms change as the flap angle varies?

Some authors within the literature have studied this scenario. One of the main conclusions that researchers have reached is that a jet is deflected by a smaller angle than the flap is deployed at [127–130]. For example, Tyacke [129] analysed a wing with a 8° and 14° deployed flap, which resulted in a jet deflection of 0° and 2°, respectively. Tyacke thought this was due to the wing position being too far away from the jet, resulting in little jet impingement. The convection of the flight-stream will also help to reduce the overall amount of jet deflection. In terms of acoustic effects, Tyacke showed that the flap introduced noise sources at either end of the flap due to trailing edge noise and flow through the gap between wing and flap leading to a slat-like noise source. The increase of the flap angle was seen to increase the noise in the forward arc. Perrino [130] also showed that there was a large increase in both the JSI and JSR when the flap was aggressively deployed (45°) but was less significant at 22.5°. The jet impingement results in a large increase in the turbulence in the upper shear layer from the flap wake [131].

The authors mentioned above have used LES simulations to provide details of the flow field. One would like to be able to run analysis on this scenario during the preliminary design stage as this configuration will occur at take-off when the public and airport workers are close to the aircraft. However, work in this chapter has shown that more work is needed to understand how to model installed jets with RANS. However, the LRT acoustic model has shown that the general trends in the change in jet mixing and reflected noise can be captured for simpler jets. Therefore, one can use this knowledge to perform a series of acoustic analyses on a hypothetical flow field for this complex situation. By comparing the predicted trends in the acoustic data to hypotheses about the expected results, this analysis is a proof of concept to show if ray tracing can be used for these complex situations.

6.4.1 Case set-up

A diagram of an installed jet with a deployed plain flap can be seen in Figure 6.4.2. The flap, of length W, is deployed at an angle, $\theta_{deployed}$. W is assumed to be $0.5D_J$, which is similar to that used in the SYMPHONY project [132]. $\theta_{deployed}$ is set at $-10, -20$ and $-30°$ from the horizontal.

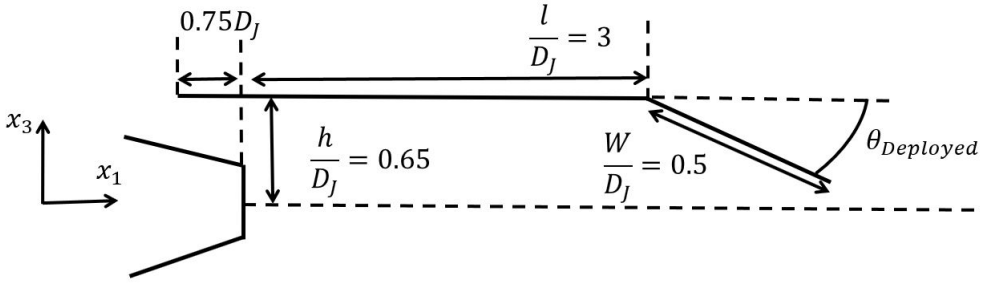

FIGURE 6.4.2: Geometry for an installed jet with deployed flap.

As this chapter has shown that RANS does not accurately predict the flow field for installed jets, RANS has not been run for this scenario.

While some flow data is shown within the literature, details of the velocity gradients and dissipation rate in the jet are not given. There is, therefore, insufficient data to conduct analysis with the LRT method based on accurate data from the literature. Consequently, several assumptions need to be made for the flow field based on the available RANS data. This will, by necessity, be an inaccurate flow field but will give initial insights into this complex problem.

Firstly, the baseline flow field for the work in this section is the static $M_J = 0.6$ conical nozzle jet, studied in Chapter 4. This is referred to as the $0°$ deflected jet. This is an oversimplification of the problem as in reality a flight-stream is needed to generate enough lift for an appreciable jet deflection to occur. In-flight data has not been used for this analysis as the convection of the flight-stream will reduce the deflection angle of the jet. However, without CFD data to back up the amount of reduction, the choice of how much deflection would occur would be arbitrary.

Secondly, to mimic the effect of the jet deflection by the flap, a rotation matrix has been applied to several CFD variables after the end of the wing (assumed to be $\frac{l}{D_J} = 3$). The following vector quantities have been rotated by the flap deflection angle: x_1, x_3, u_1, u_3, $\frac{du_1}{dx_1}$, $\frac{du_1}{dx_3}$, $\frac{du_3}{dx_1}$ and $\frac{du_3}{dx_3}$. An example of the rotation of a variable can be seen below in

Figure 6.4.3. By doing this, the author is effectively assuming that there is no flap impingement or wake effects. Analysis of the literature has shown this is incorrect, however, there is no simple way to quantify these effects without running the CFD.

The rotation of the flow data after the end of the wing introduces a new problem. Part of the flow in the deflected jet region will lie outside the acoustic domain if the same x_3 limits are used as in previous chapters. Therefore, the vertical dimensions of the acoustic domain have been adjusted to allow the majority of the deflected jet to be within the acoustic domain. Small errors are, therefore, expected below frequencies of 200Hz ($St < 0.04$). As this is below the minimum frequency of the acoustic grid, there will be no impact on the results. While generating the new acoustic grid, the gradients of the speed of sound in each direction are calculated from the rotated CFD data.

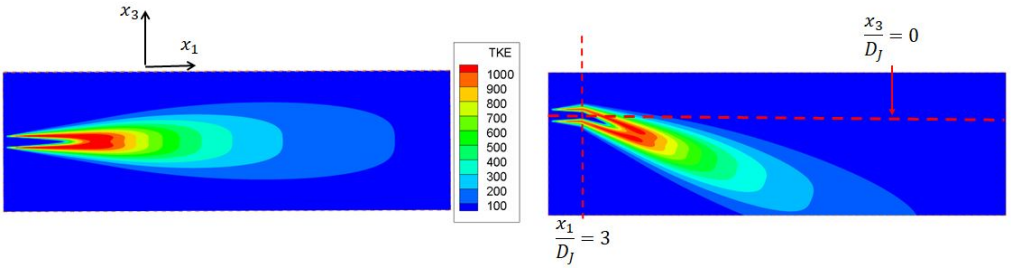

FIGURE 6.4.3: TKE distribution for the isolated 0° deflected jet (left) and a 20° rotated jet to mimic a 20° deployed flap (right).

The next assumption that is made is the fact that the flap does not change the decay rate of the mixing noise. This will certainly be true for low frequencies which exist far downstream of the flap trailing edge, but may not be true close to the flap. Again, without CFD data of this situation, this effect cannot be quantified and so this fact must simply be acknowledged.

This is linked to another assumption that has been made. If one assumes that the mixing rate in the deflected region of flow after the wing TE is not changed by the flap, then the quadrupole sources will not change their directivity. However, the orientation of the flow means that quadrupole directivity is no longer in sync with the definition for the global polar angle. Therefore, one needs to correct for this. As there is no change in the mixing rate, it can be assumed that the directivity of any quadrupole sources in the deflected region of the jet will be offset from the nozzle axis by the angle of the deployed flap, $\theta_{deployed}$. For example, a source downstream of a 20° deflected

flap will produce an SPL with $\theta = 70^\circ$ directivity at a global polar angle of $\theta = 90^\circ$. This assumption will be true for low frequencies far downstream of the trailing edge, but as the flap will impact frequencies generate close to it, there is some degree of uncertainty for mid-range frequency over the applicability of this assumption.

The final assumption that has been made is that the wing and flap are not highly curved and so can be modelled as flat plates. This means the method outlined at the beginning of this chapter can be used and is simply for ease of analysis.

With the assumptions of this work outlined, several hypothesise can be made based on expected results. These are listed below. The goal of this analysis is to see if the LRT prediction matches these expected results.

- Increasing the deployed flap angle will increase the overall noise produced. The change in noise at low frequency will primarily be down to the change in the mixing noise, while the change at high frequency will be due to reflected noise.
- The flap reflections will cause an increase in the high-frequency content, primarily in the forward arc, compared to only having a wing present.
- The peak frequency of reflected noise will change with the flap angle at a particular observer angle.
- Due to the size of the flap and wing, it is expected that the flap will produce a smaller amount of reflected noise than the wing.

It should be noted that as there is no JSI model within LRT, the changes at low frequency ($St \leq 1$) are likely unimportant due to the JSI being the dominant noise source in this frequency range.

6.4.2 Acoustic results

The presence of the flap obviously changes the noise sources within the jet. The question now is, how do the noise mechanisms change as the flap angle is varied? To study this, the spectra from different cases can be subtracted from each other. These cases are outlined below in Tables 6.3 and 6.4. All predictions in this section are carried out on the unshielded side of the wing ($\phi = 180^\circ$).

Case	Deflected / Undeflected jet	Isolated / Installed	Flap present
A	Undeflected	Isolated	No
B	Deflected	Isolated	No
C	Undeflected	Installed	No
D	Deflected	Installed	No
E	Deflected	Installed	Yes

TABLE 6.3: Cases simulated.

	Noise source
$B - A$	Change in jet mixing noise
$C - A$	Reflection from wing
$E - D$	Reflection from flap
$E - A$	Total change

TABLE 6.4: Cases being subtracted to isolate noise mechanisms.

To start with, the change in the spectra of the isolated jet mixing noise is considered in Figure 6.4.4. Here, the spectra of the 20° deflected jet at $\theta = 90°$ is compared to the 0° deflected jet at $\theta = 70°$ and 90°. The 20° deflected jet tends to the low frequency prediction of the 0° deflected jet at $\theta = 70°$ below $St = 1$ ($\Delta SPL = 0.6$dB at St=1) and has a transition region between $St = 1$ and 4. Above $St = 4$, the deflected jet follows the 0° deflected jet $\theta = 90°$ prediction. Looking into the source distribution curves of the 0° deflected jet, it was found that when part of the distribution curve crossed the transition point at the end of the wing ($\frac{x_1}{D_j} = 3$), then the SPL will be in the transition between the two 0° deflected jet curves. Similar trends are seen at $\theta = 90°$ with the 10 and 30° deflected jets matching the $\theta = 80°$ and 60° predictions for the 0° deflected jet, respectively, but are not shown here.

When the isolated cases are subtracted from each other (Case B-A), the change in the jet mixing noise due to the presence of the flap is revealed. Figure 6.4.5 shows the change in the OASPL from the 0° deflected jet. It is clear to see that increasing $\theta_{deployed}$ increases the overall noise at $\theta \geq 80°$ for all flap angles. At $\theta = 70°$, the 30° deflected jet shows a 0.7dB increase in noise compared with the data at $\theta = 80°$ but then shows a large decrease of 5.2dB going to $\theta = 60°$. The 20° deflected jet also shows a decrease

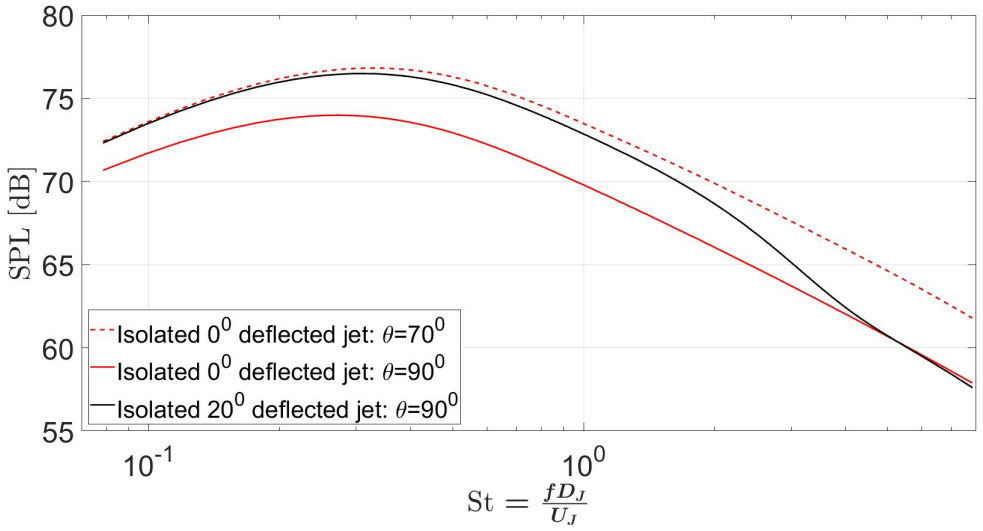

FIGURE 6.4.4: SPL spectra of the static isolated 20° deflected jet at $\theta = 90°$, $\phi = 180°$ and $M_J = 0.6$ at compared to the isolated 0° deflected jet. Plot of Case B versus Case A.

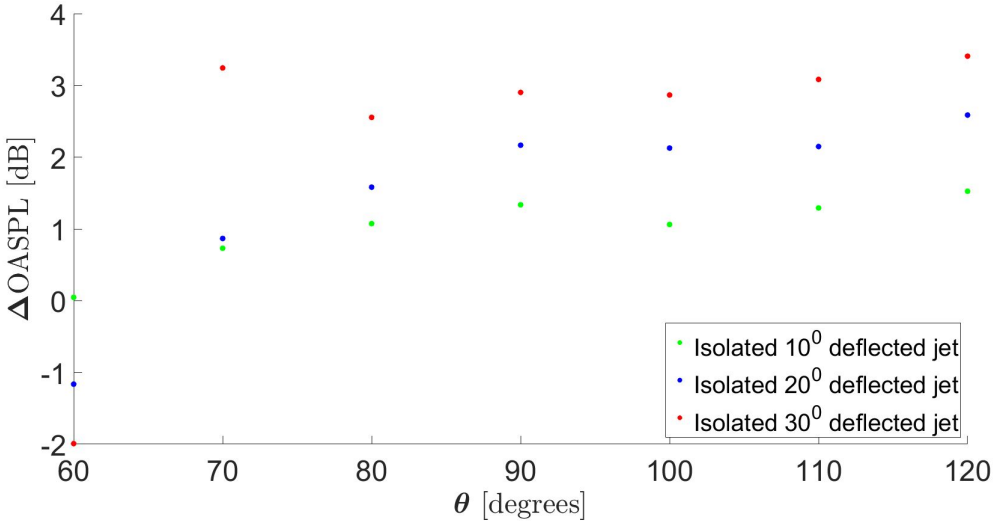

FIGURE 6.4.5: The ΔOASPLs due to the change in jet mixing noise between the isolated deflected jets compared to the isolated 0° deflected jet at $\phi = 180°$ (Case B-A).

of 1.15dB at $\theta = 60°$ but produces a positive change in noise at $\theta = 70°$. As there is no wing for reflections of rays to occur from, it is thought that rays are entering the cone of silence of the deflected region of the jet. Rays are, therefore, being diffracted away from the rotated centreline of the jet. Hence, a lower OASPL is generated.

Figure 6.4.6 shows the reflected mixing noise from the wing (Case C-A). As the wing position has been shown to affect the reflected noise amplitude earlier in this chapter, the reflected mixing noise at this particular wing position is shown in Figure 6.4.6. When looking at Figure 6.4.6, it can be seen that the peak and cut-on frequencies

decrease as θ increases. As explained earlier, this is due to the position of each of these frequencies relative to the wing, with lower frequencies existing further downstream and so being reflected to higher polar angles. The amplitude shown in Figure 6.4.6 is higher at all polar angles than those shown for the SYMPHONY data set in Figure 6.1.6. This is due to an increase in l resulting in a greater proportion of the source distribution beneath the wing.

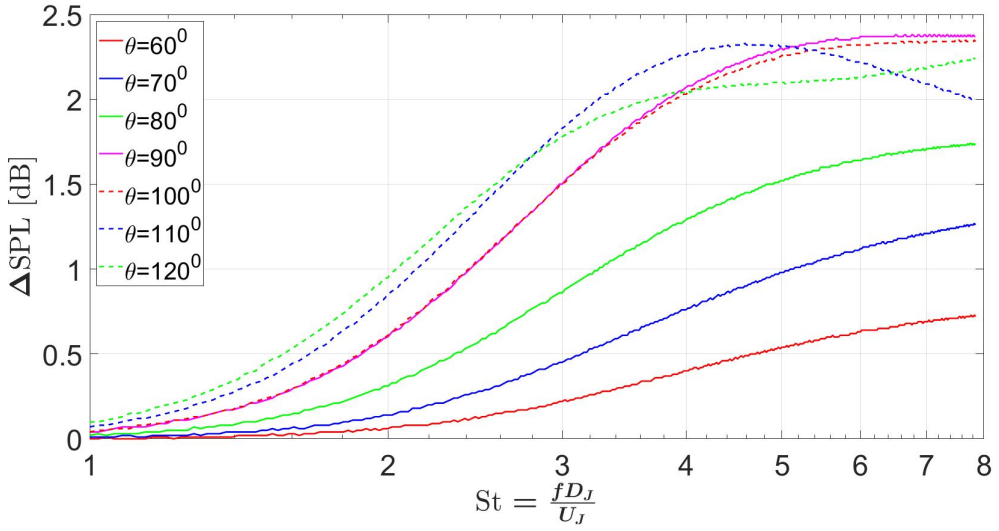

FIGURE 6.4.6: The ΔSPLs of the reflected mixing noise from the wing with a 0° deflected jet at different polar angles at $\phi = 180°$ (Case C-A).

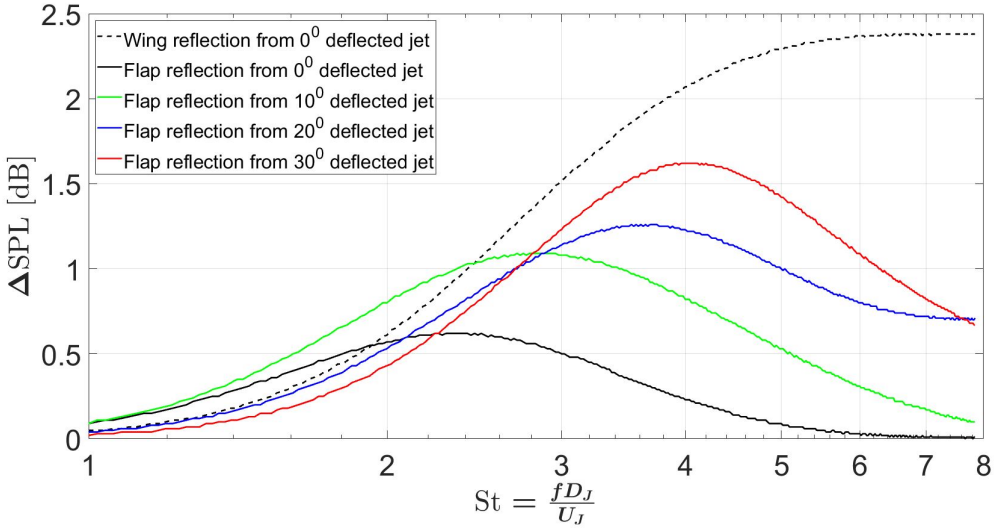

FIGURE 6.4.7: The ΔSPL of the reflected mixing noise from the flap at $\theta = 90°$ and $\phi = 180°$ (Case E-D).

The reflected mixing noise from the flaps can be isolated by subtracting the case with the wing from the case with the wing and flap (Case E-D). Due to the physical size of

the flap being smaller than the wing, it is expected that the reflections from the flap will be smaller than that from the wing. These results are shown in Figure 6.4.7. Here, one can see that the wing does indeed generate a larger amount of reflective noise than the flap. Furthermore, there is an increase in the peak frequency of the reflection by 8700Hz as $\theta_{deployed}$ increases from 0 to 30°. A focal point for reflections is, therefore, created by the flap. This focal point changes position as the flap angle increases, which explains the change in peak frequency. The increase in the amplitude of that peak frequency (1dB from 0 to 30° deflected) with increasing flap angle is more complicated to understand. As the flap angle changes the path that rays travel through the jet, the rays will experience a different amount of refraction. On top of this, each frequency has a different amount of energy. The combination of these two factors results in a different virtual source strength being created by the flap.

Having analysed the individual sources of noise, one can now collate this information to look at the total change in noise from the isolated 0° deflected jet to each of the fully installed deflected jets (Case E-A). This is shown below in Figures 6.4.8-6.4.10 for the 20% deflected jet at three different polar angles. Similar trends were observed for the other deflected jets and so are not shown here. As mentioned previously, the JSI noise is not modelled and so results below $St = 1$, where the JSI is dominant, need to be considered with this in mind.

The total change in noise is separated into the noise from the jet mixing noise and that from reflections. The reflected noise is then further split into that from the wing and the contribution from the flap. In Figure 6.4.8, being inside the cone of silence of the 20° deflected jet results in a decrease in the mixing noise at $\theta = 60°$ (as seen in Figure 6.4.5). There is a small amount of reflection from the wing present at $St \geq 1.5$ but this only produces a maximum increase of 0.67dB in noise at $St = 7.8$. The flap has no effect on the noise produced. Moving to higher polar angles in Figures 6.4.9 and 6.4.10, each noise source produces more noise compared to the rear-arc predictions. As expected at high frequency, the reflected mixing noise dominates whereas the direct mixing noise is responsible for the change at low frequency. Between $St = 1$ and 2, there is a cross-over region similar to the JSI and JSR noise sources mentioned earlier. However, as the reflected noise and jet mixing noise sources are within 3dB of each other, the overall noise is still affected by the mixing noise above $St = 2$.

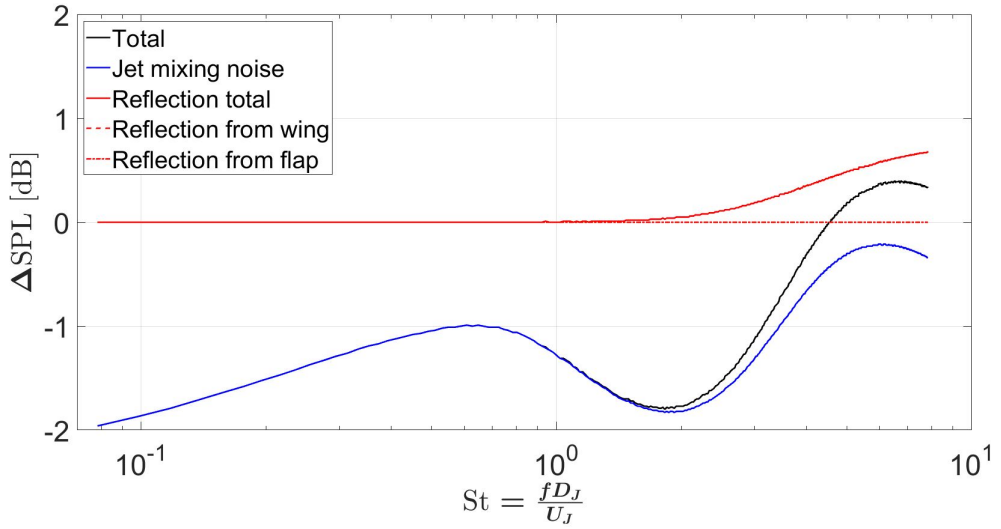

FIGURE 6.4.8: The ΔSPL from each of the noise mechanisms at $\theta = 60°$ for the installed 20° deflected jet at $\phi = 180°$ (Case E-A).

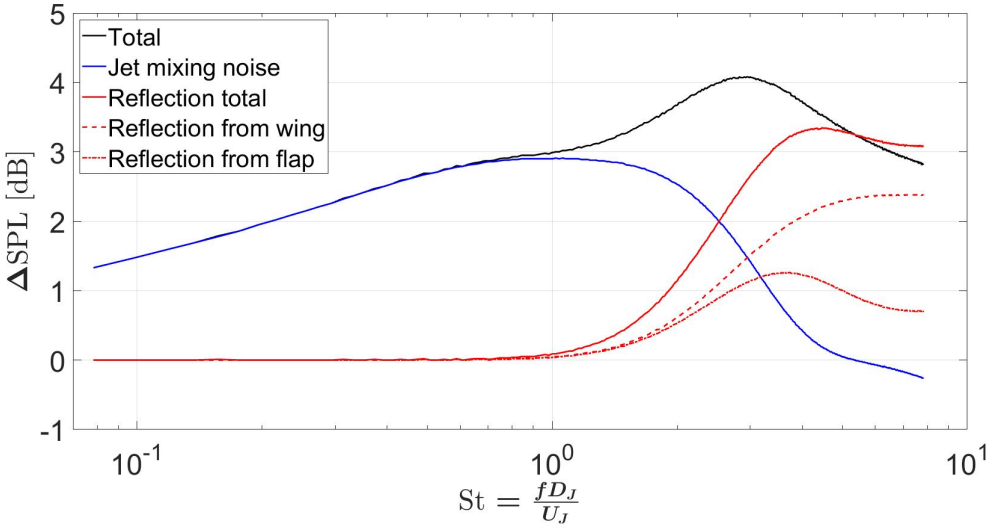

FIGURE 6.4.9: The ΔSPL from each of the noise mechanisms at $\theta = 90°$ for the installed 20° deflected jet at $\phi = 180°$ (Case E-A).

The main findings of this analysis can be summarised when looking at the change in the OASPL between the installed deflected jet and the isolated undeflected jet (Case E-A). The contribution that each noise source provides can be seen in Figure 6.4.11. Here only the results for the 20% deflected case are shown. At low polar angles, the mixing noise dominates. It should be noted that in reality, the JSI noise source will dominate at low frequencies, but this noise source has not been modelled here. The cone of silence effect can be seen at $\theta = 60°$. As θ increases, there is a general increase in noise from all sources. In the forward arc, the reflected mixing noise provides a

larger contribution to the change in noise compared to the rear arc but the flap does not produce as much noise as the wing.

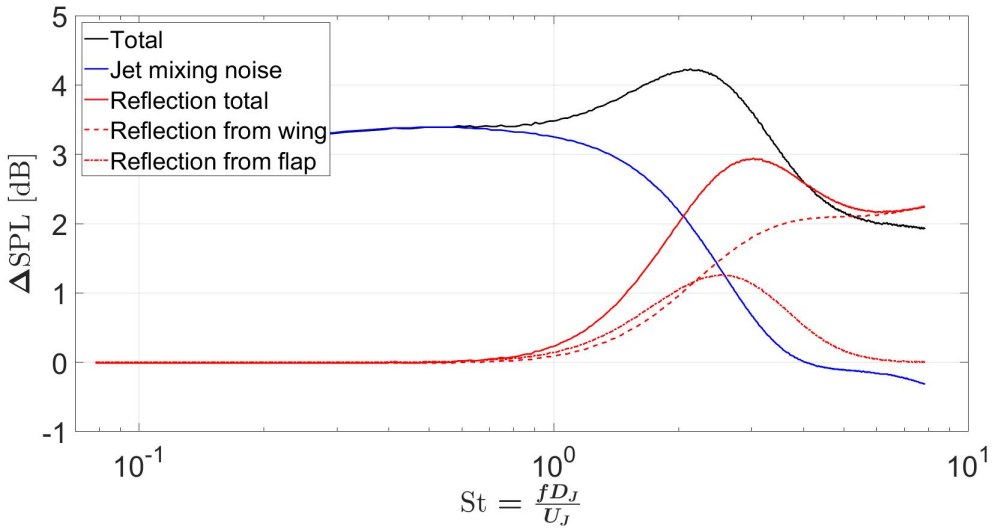

FIGURE 6.4.10: The ΔSPL from each of the noise mechanisms at $\theta = 120°$ for the installed 20° deflected jet at $\phi = 180°$ (Case E-A).

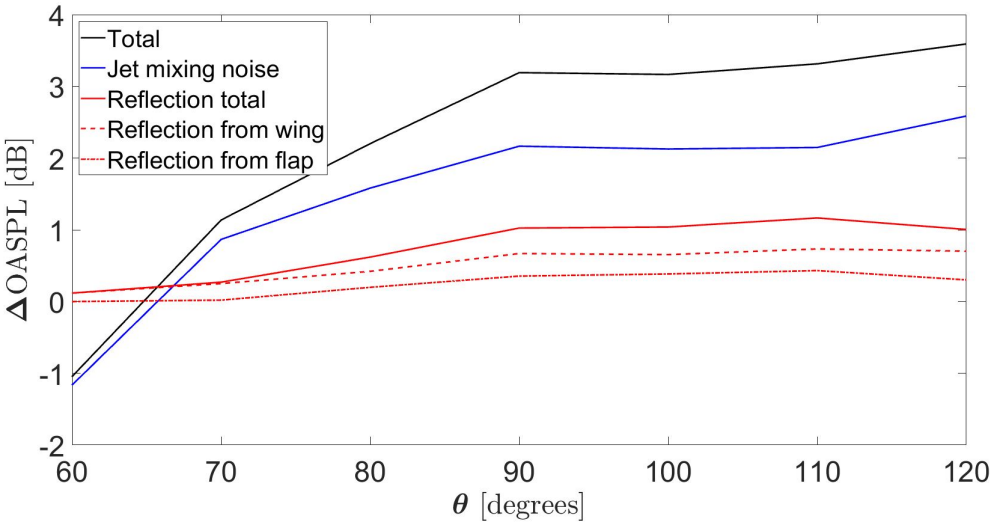

FIGURE 6.4.11: The ΔOASPL of the different source mechanisms for the 20° deflected jet at $\phi = 180°$ (Case E-A).

From this analysis, it is clear to see that frequencies within the range $St = 1 - 3$, provide the greatest contribution to the increase in noise produced by a deployed flap. It should come as no surprise that these frequencies are those that exist closest to the flap. Despite several large assumptions that have been used in this analysis, it is clear that the ray tracing method can be used to investigate complex situations. Now,

further work is needed to improve the accuracy of CFD models to catch up with the acoustic modelling.

6.5 Summary of chapter

In this chapter, it has been shown that:

- A method for calculating the reflection of mixing noise from solid surfaces has been outlined. The wing, flap and pylon can be modelled as flat plates to enable easy calculation within the ray tracing code. This code was then validated by studying the change in reflected mixing noise as the observer and wing position were varied.
- LRT was able to predict the shielding and amplification effects of noise on opposite sides of the wing.
- LRT correctly shows that there is a greater influence of reflection in the forward arc than in the rear arc. The general trend in the reduction of peak frequency with increasing θ was also captured.
- When the horizontal position of the wing trailing edge, l, is increased, LRT predicts a reduction in the cut-on frequency of reflections. This occurs as more of the source distribution lies underneath the wing. However, the experimental data predominately shows an increase in the amplitude of reflected noise as l increases. As the wing was positioned vertically far away from the jet, it is thought that there was little JSI noise. There is, therefore, some feedback mechanism, that is not fully understood, occurring.
- When the vertical distance to the wing trailing edge, h, was varied, the experimental data showed a small decrease of around 0.5dB with increasing h. The wing, therefore, focuses the reflected rays towards the far-field observer as it is moved closer to the jet. However, LRT predicts a small increase in noise as h increases. It is unclear why this occurs. It should be noted that despite this, LRT captures the rough magnitude of the ΔSPL to within 0.5dB.
- Experimental data showed that the reflected mixing noise was insensitive to changes in the flight Mach number. Since Lawrence [103] showed that the

high-frequency noise of an installed jet is also not dependent on the jet Mach number, the high-frequency region of installed spectra can be scaled with jet and flight Mach number in the same way as isolated jets.

- With the reflective code validated, attention was turned to how accurately RANS could model installed jets. Analysis of an installed annular jet showed that, statically, a k-ϵ RANS model can predict the velocity and turbulence intensity underneath the wing well but over-predicts the turbulence level downstream of the trailing edge of the wing. This causes additional mixing noise at $St < 1$ on the shielded side of the wing. However, this additional noise was shielded from observers at $\phi = 180^\circ$ and will likely be hidden when the JSI noise is included.

- In-flight, the k-ϵ turbulence model was seen to over-predict the turbulence on the wing side of the installed annular nozzle at all axial locations in the jet. However, acoustically this only changed the LRT predictions below the wing by a maximum of 1dB.

- The most complex geometry studied with CFD was the jet-pylon-wing configuration. Experimental data suggested that the flow would be deflected away from the wing, but this was not seen in the RANS results. General agreement was obtained below the wing, however. Therefore, the interaction between the pylon and wing is not being correctly modelled within RANS which will primarily affect the refraction of noise after the wing trailing edge.

- A hypothetical case was studied to determine if ray tracing could pick up on the expected trends of an installed jet with a deployed flap. It was seen that having a deployed flap mainly increased the high-frequency content within the forward arc. It was assumed that the mixing noise directivity would change due to the jet deflection, however, this would likely be covered by the JSI noise in reality.

- The flap produced a smaller amount of reflective noise than the wing and changed the focal point of reflected noise with changing flap angle.

The work in this chapter has shown that, although the ray tracing code is capable of modelling reflected mixing noise, additional work is needed to improve the accuracy of RANS calculations for installed geometries. This is suggested as future work for this project.

Chapter 7

Conclusions

7.1 Summary of background

The topic of research in this thesis has been the jet noise that commercial aircraft generate. This primarily affects the local communities and workers around airports and can have negative impacts on health. With a growing demand for air travel, reducing the noise of aircraft needs to be considered during the design cycle of new engines.

The background to modelling the turbulent scales in a jet and the noise that this generates is outlined in Chapter 2. Most of the research carried out in this area has been on isolated axisymmetric jets although there is interest in the design of low-noise pylons. The pylon attaches the engine to the wing. Despite the impact on the flow of the pylon being agreed on, results in the azimuthal variation in mixing noise range between 0 and 3dB of additional noise at the sideline compared to an axisymmetric jet. The pylon primarily affects high frequencies and so will be important in an installed situation. Numerical studies are, therefore, needed to quantify the change in the mixing noise from the pylon. The literature review highlighted the fact that many acoustic models assume that jets can be modelled as being axisymmetric which is not accurate for realistic jets. Hence, there is a gap in our understanding of how realistic asymmetric jets can be modelled. This is the focus of the work in this thesis.

Chapter 3 provided the methodology of a numerical procedure called Lighthill's Acoustic Analogy with Ray Tracing (LRT), developed at the University of

Southampton. The mean flow field is first modelled using a k-ϵ RANS calculation. Rays are then traced from acoustic source points in the jet shear layer using a ray tracing code. **An improved source equation allows the mixing noise to be calculated and includes the effects of source compactness and anisotropy, which are primarily high-frequency effects.** This is one of the novel contributions of this work, as previous work using the LRT method has focused on isotropic turbulence. Although no experimental data has been gathered as part of this project, data from the Doak laboratory at the University of Southampton has been used to verify numerical predictions.

7.2 Summary of results: Chapter 4

The LRT method was first validated against a simple conical nozzle in Chapter 4. **It was found that by adjusting the coefficients of the k-ϵ turbulence model to those found by Thies and Tam [25], the over-prediction of the potential core length was reduced from 64% to 20%**. Therefore, the region of maximum turbulence is in a more realistic position, which is thought to be important for the installed case. The peak velocity and turbulence levels are predicted to be within 5% and 0.5%, respectively, before the end of the potential core. However, after this point, RANS begins to under-predict both the velocity and turbulence levels, which was thought to be linked to the over-prediction of the spreading rate. Despite this, RANS captures the overall shape of the velocity and turbulent flow fields, both statically and in-flight, providing a good basis for acoustic predictions to be made.

The LRT acoustic predictions were calibrated by changing the values of c_l and c_t to match the peak frequency and SPL level at $\theta = 90^\circ$ for the static conical nozzle at $M_J = 0.6$. The same calibration values were then used to predict the results at other jet and flight Mach numbers. In general, predictions could be made to within 0.5dB at $\theta = 90^\circ$ using an isotropic turbulence model. Away from this polar angle, the high-frequency content was over-predicted (by 2dB at $St = 3$) at $\theta = 60^\circ$ while there was an under-predicted of 1dB at all frequencies at $\theta = 120^\circ$. Further analysis was conducted on the sensitivity of the LRT acoustic predictions to several inputs and it was found that the low-frequency prediction below $St = 0.7$ was particularly sensitive to the turbulence intensity and absolute values of the calibration constants. Therefore, results at low frequency need to be interrogated cautiously.

One of the important conclusions that have been reached in this work is that the anisotropy of the jet needs to be accounted for. It was shown that an improved set of predictions at high frequency can be made using an anisotropic model, especially for higher jet Mach numbers. Furthermore, a reduction of 1.5dB in the rear arc noise at $\theta = 60^\circ$ provided closer agreement with experimental data, while little change was observed in the forward arc. Therefore, for the rest of the thesis, an anisotropic model was used.

7.3 Summary of results: Chapter 5

More complex isolated geometries were studied in Chapter 5. Of particular interest was how the source distribution changes with the geometry and how the mixing noise scales accordingly. The first geometry studied in this chapter was an annular nozzle. Similar to the conical nozzle data, good predictions of the velocity could be made within the first five diameters (within 5%) but under-predictions of 7% occurred by ten diameters downstream. Acoustic analysis was limited to the static case, due to additional noise in the in-flight experimental data. In terms of acoustic predictions, LRT predicted that the peak noise of the annular nozzle at $\theta = 90^\circ$ was 0.8dB higher than the experimental data. Results shown later in the chapter indicated that this was unusual as other geometries predicted the peak SPL well. Despite this, the LRT method was able to capture the general change in the SPL level between these geometries at $\theta = 90^\circ$ to within 1.5dB at all frequencies given the over-prediction already mentioned. A correction for the vena-contracta effect and mass flow rate was needed to achieve this.

The main part of Chapter 5 dealt with the impact of the pylon on the mixing noise. Three increasingly internally blocked nozzles (5, 10 and 20% of the flow area of the annular nozzle) were studied. The increasing blockage was seen to create a more "egg" shaped flow field in the first four effective jet diameters whilst drawing the jet towards the blockage. RANS was able to correctly predict the reduction in velocity and turbulent intensity to within 1 and 0.5%, respectively. Four interesting conclusions were drawn while studying the far-field mixing noise of these blocked nozzles. Firstly, increasing the pylon blockage increased the mixing noise. Secondly, there was little difference in the mixing noise when the blockage of the pylon was small (for the 5 or 10%). However, having a 20% blockage introduced additional noise at mid-Strouhal

numbers which was thought to come from vortex shedding. As no additional noise was seen for the 5 and 10% blocked cases, it was thought that this noise source only becomes dominant for the 20% case. These vortices are thought to also increase the local mixing and generate around 1dB of additional high-frequency mixing noise.

The final section of Chapter 5 looked at the influence of the external fairing of the pylon on the flow and mixing noise. Little difference was observed statically in the flow field or noise level (less than 0.25dB) compared to the internally blocked nozzle. However, at a flight Mach number of 0.2, the external pylon surface was seen to increase the mixing rate close to the nozzle exit. This generated an increase in the high-frequency content of the flow (2.1dB at $St = 6$) and a decrease at low frequency (0.33dB at $St = 0.1$). No experimental data was generated for the external pylon geometry in-flight, so these results can not be confirmed currently.

The key point from Chapter 5 was that the effective diameter, which accounts for the variation in flow area between nozzles, was the appropriate parameter to scale the mixing noise with the introduction of the pylon. However, this only worked when the underlying physics of the jets remains constant. The additional noise that was generated by the vortices in the 20% blocked case prevented a collapse of the source distribution at high frequencies. It should be noted that only one parameter was varied in this pylon study; namely the flow area of the pylon blockage. There are other geometric variations for the pylon design which will influence the mixing noise and so a comprehensive study would be needed to validate if the conclusions reached in this chapter can be applied generally.

7.4 Summary of results: Chapter 6

The final chapter of this thesis investigated the direct mixing and reflected mixing noise generated from an installed geometry. Firstly, a new piece of code was added to the ray tracing code to enable the reflections to be modelled. This code was validated against experimental data from the SYMPHONY project. **LRT was able to pick up the increase in mixing noise below the wing and in the forward arc.**

Having validated the reflective code, attention was turned to looking at the accuracy of RANS in predicting installed jets. A NACA4415 airfoil was added above the isolated annular nozzle studied in Chapter 5. It was found that the wing caused very

little difference in the velocity and turbulence profiles underneath the wing but RANS over-predicts the amount of turbulence after the end of the wing, statically. This is a known error with the k-ϵ turbulence model for isolated wings, but the additional mixing noise is unlikely to be seen once the JSI noise is included. However, in-flight analysis showed that the reflected noise changed with flight Mach number, contrary to that seen in results earlier in the chapter. This was put down to errors in the CFD data from the k-ϵ model. Acoustic analysis was, therefore, restricted to the static case for the final installed geometry.

To take the CFD analysis a bit further, a complex situation with a jet, pylon and wing was analysed. Similar to the installed annular nozzle, good predictions could be made below the wing, but after the wing trailing edge, differences were again observed between the experimental data and RANS predictions. RANS indicated that the flow was drawn towards the wing, but the experimental data suggested that the flow was deflected away from the wing. Clearly, the interaction between the pylon and wing is not being modelled correctly within RANS. **Therefore, there is a limit to what RANS can accurately model**. Acoustic comparisons were only made above $St = 1$ and the installed pylon was seen to increase the high-frequency content by less than 0.2dB above $St = 2.5$. Therefore, the installed pylon has a negligible impact on the static case, similar to the isolated result.

The final part of Chapter 6 dealt with one of the most complex situations that one would like to be able to study: an installed jet with a deployed flap. As the results have indicated that there are errors within RANS for complex flow scenarios, a hypothetical case was considered. A wing with a deployed flap at three different angles was modelled above the flow of the static conical nozzle from Chapter 4 and the flow after the wing trailing edge was rotated by the angle of the flap. The point of this analysis was to see if ray tracing could pick up on the expected trends in the reflected noise that including a deflected flap would bring. The impact of the JSI was not considered. It was seen that the wing created more reflected noise than the flap due to being larger. However, the flap was found to change the focal point of the reflected noise. **As the ray tracing results matched the expected results, one can say that ray tracing and the LRT method are thought to be able to predict complex installed scenarios, provided improvements can be made to the RANS modelling.**

7.5 Recommendations

From this work, there are several recommendations for future work with the LRT method.

- From the isolated geometries studied in this thesis, a mesh with a $y^+ \approx 35$ was selected as this was sufficient to capture the overall flow features. It is recommended that initial future meshes of isolated geometries are generated at this mesh density, but mesh sensitivity studies should still be performed to check their suitability, especially for complex geometries.
- A k-ϵ turbulence model is used within the CFD model for isolated jets that uses the coefficients found by Thies and Tam. More analysis is needed to determine the best turbulence model to use for installed cases.
- In this work, an anisotropic acoustic model with values of β and Δ that do not change with position has been used. Whilst this is not realistic, improved predictions can be made compared to an isotropic model. The anisotropy is expected to vary with geometry and jet Mach number, but until this is quantified, the anisotropic values used in this thesis should be used to provide initial estimates of jet mixing noise. LES could be used in the future to provide the detail needed to refine the values of β and Δ.
- Due to the additional turbulence that is generated downstream of the wing TE for installed cases, LRT predictions below $St = 1$ should be treated with caution. However, below the wing accurate predictions have been shown for two static installed geometries. Therefore, this would lead one to conclude that static predictions on the unshielded side of the wing and above $St = 1$ are accurate to within 0.5dB at $\theta = 90°$.

7.6 Future work

There are several avenues for potential research in the future on this project. For predicting isolated jet noise, additional work needs to be carried out on improving the accuracy of the LRT predictions away from $\theta = 90°$. There are three terms in the LRT source equation that affect the noise level as the polar angle changes: the Doppler

factor, D_f, the flow factor, Φ, and the jet directivity factor, Π. Due to the complex nature of the source equation, it is not clear which of these is the principal reason for the errors away from $\theta = 90°$.

Next, a study of how the anisotropy changes within a jet as the geometry, flight and jet Mach numbers are changed would allow for a greater understanding of jet physics. It is expected that anisotropy is highly important for asymmetric geometries but there is a lack of both experimental and numerical data for a quantitative assessment to be made. Numerically, this is not possible with RANS and so several LES studies would be needed for this work to be carried out. Although the results are likely to be case and geometry-dependent, this would give confidence and validation for the use of the values of β and Δ within the LRT acoustic predictions.

When looking at the noise of installed jets, there are two areas for future work. Firstly, it is clear that the k-ϵ turbulence model generates errors downstream of the wing TE and for in-flight cases. While this was seen to not impact the results of the static installed annular nozzle at $\theta = 90°$, it is expected that incorrect predictions would be made away from this polar angle for the jet-pylon-wing case. This introduces a further error on top of that seen already in the LRT predictions away from $\theta = 90°$. Further analysis is, therefore, needed into whether the use of an SST model would improve the flow field predictions downstream of the wing TE. If this is not possible, it would likely mean that it is best to use LES modelling for installed geometries. This would obviously take longer to solve but may be needed for accurate predictions of installed geometries.

Finally, the obvious issue with the current LRT predictions of installed geometries is the lack of modelling of the large JSI noise source. Therefore, including a model of this, for example, the method used by Dawson [106], would allow for the full frequency range of an installed jet to be studied. The other option is to subtract the LRT prediction away from installed spectra which would allow for a more detailed analysis of the JSI noise source.

Appendix A

A.1 Axisymmetric directivity

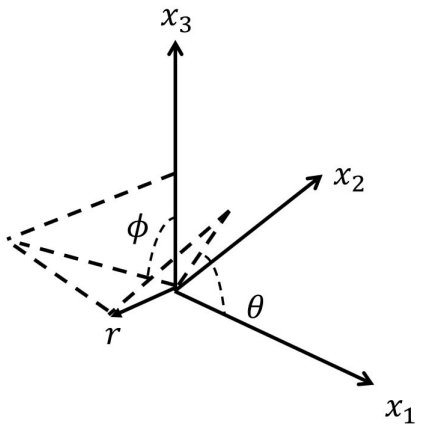

FIGURE A.1.1: Diagram of the co-ordinate system.

The directivity of the jet, Π_{ijkl}, is given by

$$\Pi_{ijkl} = \frac{1}{2\pi} \int_0^{2\pi} \frac{x_i x_j x_k x_l}{\mathbf{x}^4} d\phi \tag{A.1.1}$$

and was shown by Ribner [65] to contain nine non-zero components that contribute to self noise. These occur when i, j, k and l are equal in pairs. Given that

$$x_1 = r\cos\theta \tag{A.1.2}$$

$$x_2 = r\sin\theta\cos\phi \tag{A.1.3}$$

$$x_3 = r\cos\theta\sin\phi \tag{A.1.4}$$

where x_1, x_2 and x_3 are the axis as defined in Figure A.1.1, r is the distance to the far field observer, θ is the polar angle and ϕ is the azimuthal angle. The directivity components of self noise are

$$\Pi_{1111} = \cos^4\theta \tag{A.1.5}$$

$$\Pi_{1212} = \Pi_{1122} = \Pi_{1313} = \Pi_{1133} = \frac{1}{2}\cos^2\theta\sin^2\theta \tag{A.1.6}$$

$$\Pi_{2222} = \Pi_{3333} = \frac{3}{8}\sin^4\theta \tag{A.1.7}$$

$$\Pi_{2323} = \Pi_{2233} = \frac{1}{8}\sin^4\theta \tag{A.1.8}$$

As Equations A.1.5 to A.1.8 do not contain a variation in ϕ, a axisymmetric directivity is derived. Ilario [21] showed that the acoustic field could be written as

$$\begin{aligned} P(\mathbf{x},\omega) = {} & I_{1111}(\cos^4\theta) + 4I_{1212}(\frac{1}{2}\cos^2\theta\sin^2\theta) + 2I_{1122}(\frac{1}{2}\cos^2\theta\sin^2\theta) \\ & + I_{2222}(\frac{3}{8}\sin^4\theta) + 4I_{1313}(\frac{1}{2}\cos^2\theta\sin^2\theta) + 2I_{1133}(\frac{1}{2}\cos^2\theta\sin^2\theta) \\ & + 2I_{2233}(\frac{1}{8}\sin^4\theta) + 4I_{2323}(\frac{1}{8}\sin^4\theta) + I_{3333}(\frac{3}{8}\sin^4\theta) \end{aligned} \tag{A.1.9}$$

Khavaran [48] found that the directivity of an axisymmetric jet could be expressed in terms of the directivity component along the jet axis, Π_{1111}. He found that

$$\begin{aligned} \Pi_{2222} &= \Pi_{3333} = C_1\Pi_{1111} \\ \Pi_{1122} &= \Pi_{1133} = C_2\Pi_{1111} \\ \Pi_{2233} &= C_3\Pi_{1111} \\ \Pi_{1212} &= \Pi_{1313} = C_4\Pi_{1111} \\ \Pi_{2323} &= C_5\Pi_{1111} \end{aligned} \tag{A.1.10}$$

where the coefficients of C_i can be found using the following equations

$$C_1 = \frac{3}{2}\beta^2 + \frac{1}{32}\left[9(\Delta+\Delta^{-1})^4 - 48(\Delta+\Delta^{-1})^2 + 80\right] - \frac{\beta}{4}(6-\Delta^2+3\Delta^{-2})$$

$$C_2 = \frac{\Delta^2}{8}$$

$$C_3 = \frac{1}{8}\Big[\frac{3}{4}(\Delta+\Delta^{-1})^4 - 4(\Delta+\Delta^{-1})^2 + 7 - 2\Delta^2 + 4\beta^2 + 2\beta(\Delta^2 - 2 - \Delta^{-2})\Big]$$
$$C_4 = \frac{1}{16}\Big[2(\Delta+\Delta^{-1})^2 - \Delta^2 - 8\beta\Big]$$
$$C_5 = \frac{1}{2}(C_1 - C_3) \tag{A.1.11}$$

Δ and β are defined in Equations 3.1.22 and 3.1.25. The summation of components of directivity can now be written

$$\begin{aligned}\Pi_{ijkl} = {} & \cos^4\theta + 2C_4(\cos^2\theta\sin^2\theta) + C_2(\cos^2\theta\sin^2\theta) + \frac{3}{8}C_1(\sin^4\theta) \\ & + 2C_4(\cos^2\theta\sin^2\theta) + C_2(\cos^2\theta\sin^2\theta) + 4C_3(\sin^4\theta) + 2C_5(\sin^4\theta) + \frac{3}{8}C_1(\sin^4\theta)\end{aligned} \tag{A.1.12}$$

This directivity factor, Π_{ijkl}, is an axisymmetric directivity and it is assumed that any variation azimuthally of the self noise is accounted for in the flow factor.

A.2 Flow factor derivation

The flow factor allows for the impact of the shear layer and solid surfaces on the propagation of a ray to be calculated. There is no assumption over whether the jet is symmetric or static. The flow factor is defined within the LRT model as

$$\Phi(\mathbf{x},\mathbf{y}) = \frac{\overline{p^2}|_{\mathbf{x},\,\text{jet}}}{\overline{p^2}|_{\mathbf{x},\,\text{free field}}} \tag{A.2.1}$$

where $\mathbf{x}$ and $\mathbf{y}$ are the observer and source locations respectively and $\overline{p^2}$ is the average acoustic pressure. As $\overline{p^2}|_{\mathbf{y},\,\text{jet}} = \overline{p^2}|_{\mathbf{y},\,\text{free field}}$, Equation A.2.1 can be written as

$$\Phi(\mathbf{x},\mathbf{y}) = \frac{\overline{p^2}|_{\mathbf{x},\,\text{jet}}}{\overline{p^2}|_{\mathbf{y},\,\text{jet}}}\,\frac{\overline{p^2}|_{\mathbf{y},\,\text{free field}}}{\overline{p^2}|_{\mathbf{x},\,\text{free field}}} \tag{A.2.2}$$

The Blokhintzev invariant can then be used, which says that along a given ray path

$$\frac{\overline{p^2}|u_i|A}{(1-u_i s_i)\rho c^2} = \text{const} \tag{A.2.3}$$

where $|u_i| = |\frac{dx_{ray}}{dt}|$ is the magnitude of the velocity vector of the ray, A the ray tube area, ρ the density and c is the speed of sound. Therefore, the ratio of the observer to source location can be written as

$$\frac{\overline{p^2}|_{\mathbf{x}}}{\overline{p^2}|_{\mathbf{y}}} = \frac{\left.\frac{|u_i|}{(1-u_i s_i)\rho c^2}\right|_{\mathbf{y}}}{\left.\frac{|u_i|}{(1-u_i s_i)\rho c^2}\right|_{\mathbf{x}}} \frac{A|_{\mathbf{y}}}{A|_{\mathbf{x}}} \tag{A.2.4}$$

Equation A.2.4 can now be substituted into Equation A.2.2 to give

$$\Phi(\mathbf{x},\mathbf{y}) = \frac{\left.\frac{|u_i|}{(1-u_i s_i)\rho c^2}\right|_{\mathbf{y},\,\text{jet}}}{\left.\frac{|u_i|}{(1-u_i s_i)\rho c^2}\right|_{\mathbf{x},\,\text{jet}}} \frac{A|_{\mathbf{y},\,\text{jet}}}{A|_{\mathbf{x},\,\text{jet}}} \frac{\left.\frac{|u_i|}{(1-u_i s_i)\rho c^2}\right|_{\mathbf{x},\,\text{free field}}}{\left.\frac{|u_i|}{(1-u_i s_i)\rho c^2}\right|_{\mathbf{y},\,\text{free field}}} \frac{A|_{\mathbf{x},\,\text{free field}}}{A|_{\mathbf{y},\,\text{free field}}} \tag{A.2.5}$$

In order to simplify Equation A.2.5, it is assumed that:

- There is no change in the Blokhintzev invariant between the source and observer in the free field.
- The area of the ray tube does not change at the source location when the jet is added to the analysis.
- The area of the ray tube at the observer can be estimated based on the number of rays, N, present in the far-field bin at that location. As the pressure is inversely proportional to the area, the area is also inversely proportional to the number of rays present.

Using these simplifications, Equation A.2.5 becomes

$$\Phi(\mathbf{x},\mathbf{y}) = \frac{\left.\frac{|u_i|}{(1-u_i s_i)\rho c^2}\right|_{\mathbf{y},\,\text{jet}}}{\left.\frac{|u_i|}{(1-u_i s_i)\rho c^2}\right|_{\mathbf{x},\,\text{jet}}} \frac{N|_{\mathbf{x},\text{jet}}}{N|_{\mathbf{x},\,\text{free field}}} \tag{A.2.6}$$

Equation A.2.6 now allows the effect of refraction and reflection within the ray tracing domain to be calculated for each far-field bin. Any azimuthal variation can be calculated by looking at how many rays are in each far-field bin. Therefore, the calculation of the flow factor is applicable to asymmetric jets.

References

[1] Clark C. "Aircraft noise effects on health". Technical report, Queen Mary, University of London, 2015. Prepared for the Airports Commission.

[2] International Civil Aviation Organization. "Air transport, passengers carried". https://data.worldbank.org/indicator/IS.AIR.PSGR?end=2017&start=1970&view=chart, 2018.

[3] International Civil Aviation Organization. "Air transport, registered carrier departures worldwide". https://data.worldbank.org/indicator/IS.AIR.DPRT?end=2017&start=1970&view=chart, 2018.

[4] Heathrow. "Night flights". https://www.heathrow.com/company/local-community/noise/operations/night-flights, 2019.

[5] Heathrow. "Noise insulation schemes". https://www.heathrow.com/company/local-community/noise/what-you-can-do/apply-for-help/noise-insulation-schemes.

[6] Smith M.J. *"Aircraft Noise"*. Cambridge University Press, 1989.

[7] International Civil Aviation Organization. "ICAO environmental report". 2007.

[8] Berglund B., Lindvall T., and Schwela D.H. "Guidelines for community noise". Technical report, World Health Organisation, 1999.

[9] Kumar S., Forster H.M, Bailey P., and Griffiths T.D. "Mapping unpleasantness of sounds to their auditory representation". *Journal of the Acoustical Society of America*, 124(6):3810–3817, 2008.

[10] Skagerstrand A., Köbler S., and Stenfelt S. "Loudness and annoyance of disturbing sounds- perception by normal hearing subjects". *International Journal of Audiology*, 56:775–783, 2017.

[11] Dickson N. *"Aircraft Noise Technology and International Noise Standards"*, 2015.

[12] Bridges J. and Brown C.A. "Parametric testing of chevrons on single flow hot jets". *AIAA*, pages 1–17, 2004.

[13] Mohan N.K.D., Dowling A.P., Karabasov S.A., Xia H., Graham O., Hynes T.P., and Tucker P.G. "Acoustic sources and far-field noise of chevron and round jets". *AIAA*, 53(9):2421–2435, 2015.

[14] Thomas R.H. and Kinzie K.W. "Jet-pylon interaction of high bypass ratio separate flow nozzle configurations". AIAA/CAES Aeroacoustics Conference, 2004.

[15] Eschricht D., Panek L., Yan J., Michel U., and Thiele F. "Jet noise prediction of a serrated nozzle". *AIAA*, pages 1–18, 2008.

[16] Papamoschou D. and Debiasi M. "Directional suppression of noise from a high-speed jet". *AIAA*, 39(3):380–387, 2001.

[17] Bauer A.B., Kibens V., and Wlezien R.W. "Jet noise suppression by porous plug nozzles". Technical report, NASA, 1982.

[18] Viswanathan K. and Lee I.C. "Investigations of azimuthal and flight effects on noise from realistic turbofan exhaust geometries". *AIAA journal*, 51(6):1486–1505, 2013.

[19] Czech M.J., Thomas R.H., and Elkoby R. "Propulsion airframe aeroacoustic integration effects for a hybrid wing body aircraft configuration". *AIAA*, 2010.

[20] White D.R. "Studies into the noise effects due to pylons in unmixed engines". Technical report, DEFENCE RESEARCH AGENCY, 1994.

[21] Ilario C. *"Development of a novel RANS-based method for the computational aeroacoustics of high speed jets"*. PhD thesis, University of Southampton, 2011.

[22] Jyeshtharaj B.J and Nayak A.K. *"Advances of Computational Fluid Dynamics in Nuclear Reactor Design and Safety Assessment"*. Woodhead Publishing, 2019.

[23] Davidson L. and Dahlström S. "Hybrid LES-RANS: An approach to make LES applicable at high Reynolds number". *International Journal of Computational Fluid Dynamics*, 19(6):415—427, 2007.

[24] Launder B.E. and Spalding D.B. "The numerical computation of turbulent flow". *Computer Methods in Applied Mechanics and Engineering*, 3:269–289, 1974.

[25] Thies A.T and Tam C.K.W. "Computation of turbulent axisymmetric and nonaxisymmetric jet flows using the k-epsilon model". *AIAA Journal*, 34(2):309–316, 1996.

[26] Casey M. and Wintergerste T. "Quality and trust in industrial CFD". Technical report, Sulzer Innotec, 2000. Best Practice Guidelines.

[27] Kolmogorov A.N. "Equations of turbulent motion of an incompressible fluid". *Izvestiya Academii Nauk USSR: Physics*, 6(1–2):56–58, 1942.

[28] Weaver D.S. and Miškovi S. "Formulation of the k-ω turbulence model revisited". *AIAA Journal*, 46(11):2823–2838, 2008.

[29] Kok J.C. "Resolving the dependence on freestream values for the k–ω turbulence model". *AIAA Journal*, 38(7):1292–1295, 2000.

[30] Menter F.R. "Two-equation eddy-viscosity turbulence models for engineering applications". *AIAA Journal*, 32(8):1598–1605, 1994.

[31] Douvi E.C., Tsavalos A.I., and Margaris D.P. "Evaluation of the turbulence models for the simulation of the flow over a national advisory committee for aeronautics (NACA) 0012 airfoil". *Journal of Mechanical Engineering Research*, 4(3):100–111, 2012.

[32] Suvanjumrat C. "Comparison of turbulence models for flow past NACA0015 airfoil using openfoam". *ENGINEERING JOURNAL*, 21(3):207–221, 2017.

[33] Yao J., Yuan W., Wang J., Xie J., Zhou H., Peng M., and Sun Y. "Numerical simulation of aerodynamic performance for two dimensional wind turbine airfoils". *Procedia Engineering*, 31:80–86, 2012. International Conference on Advances in Computational Modeling and Simulation.

[34] Abramovich G. *"The Theory of Turbulent Jets"*. 1963.

[35] Wygnanski I. and Fiedler H. "Some measurements in the self-preserving jet". *Journal of Fluid Mechanics*, 38(3):577–612, 1969.

[36] Hussein H.J., Capp S.P., and George. W.K. "Velocity measurements in a high-reynolds-number, momentum-conserving, axisymmetric, turbulent jet". *Journal of Fluid Mechanics*, 258:31–75, 1994.

[37] Witze P.O. "Centreline velocity decay of compressible free jets". *AIAA Journal*, 12(4):417–418, 1974.

[38] Fisher M.J and Preston G.A. "A modelling of the noise from simple coaxial jets, part 1: With unheated primary flow". *Journal of Sound and Vibration*, 209(3):385–403, 1998.

[39] Tester B.J. and Morfey C.L. "Jet mixing noise: A review of single stream temperature effects ". *International Journal of Aeroacoustics*, pages 1–41, 2009.

[40] Fisher M.J and Preston G.A. "A modelling of the noise from simple coaxial jets, part 2: With heated primary flow". *Journal of Sound and Vibration*, 209(3):405–417, 1998.

[41] Ko N.W.M. and Kwan A.S.H. "The initial region of subsonic coaxial jets". *Journal of Fluid Mechanics*, 73(3):305–332, 1976.

[42] Kwan A.S.H. and Ko N.W.M. "The initial region of subsonic coaxial jets. part 2". *Journal of Fluid Mechanics*, 82(2):273–287, 1977.

[43] Lighthill M.J. "On sound generated aerodynamically. I - General Theory". *Proceedings of the Royal Society of London, Series A, Mathematical and Physical Sciences*, 211:564–587, 1952.

[44] Lighthill M.J. "On sound generated aerodynamically. II - Turbulence as a source of sound". *Proceedings of the Royal Society of London, Series A, Mathematical and Physical Sciences*, 222:1–32, 1954.

[45] Curle N. "The influence of solid boundaries upon aerodynamic sound". *Proceedings of the Royal A*, 231:505–514, 1955.

[46] Ffowc-Williams J.E and Hawkings D.L. "Sound generation by turbulence and surfaces in arbitrary motion". *Philosophical Transactions of the Royal Society of London. Series A Mathematical and Physical Sciences*, 264:321–342, 1969.

[47] Goldstein M. *"Aeroacoustics"*. McGraw-Hill International Book Company, 1976.

[48] Khavaran A. "Role of anisotropy in turbulent mixing noise". *AIAA Journal*, 37(7):832–841, 1999.

[49] Khavaran A and Krejsa E.A. "On the role of anisotropy in turbulent mixing noise". *AIAA*, 1998.

[50] Lush P.A. "Measurement of subsonic jet noise and comparison with theory". *Journal of Fluid Mechanics*, 46(3):477–500, 1971.

[51] Harper-Bourne M. "AIAA 99-1838: Jet near-field noise prediction". 05 1999.

[52] Harper-Bourne M. "Jet noise turbulent measurements". AIAA/CAES Aeroacoustics Conference, 2003.

[53] Proença A.R. *"Aeroacoustics of Isolated and Installed Jets under Static and In-Flight Conditions"*. PhD thesis, University of Southampton, 2018.

[54] Viswanathan K. "Scaling laws and a method for identifying components of jet noise". *AIAA journal*, 44(10):2274–2285, 2006.

[55] Viswanathan K. and Czech M.J. "Measurement and modeling of effect of forward flight on jet noise". *AIAA journal*, 1(49):216–234, 2011.

[56] Michalke A. and Michel U. "Prediction of jet noise in flight from static tests". *Journal of Sound and Vibration*, 67(3):341–367, 1979.

[57] Ffowcs-Williams J.E. "The noise from turbulence convected at high speed". *Philosophical Transactions of the Royal Society A Mathematical, Physical and Engineering Sciences*, 255(1061):469–503, 1963.

[58] Laughlin Mc P. *"A Contribution to the Jet Noise Installation"*. PhD thesis, University of Southampton, 2010.

[59] Agarwal A., Dowling A.P., Shin H., Will G., and Sandy S. "A ray tracing approach to calculate acoustic shielding by the silent aircraft airframe". In *12th AIAA/CEAS Aeroacoustics Conference (27th AIAA Aeroacoustics Conference)*, 2006.

[60] Pierce A.D. *"Acoustics: An Introduction to Its Physical Principles and Applications"*. 1981.

[61] Stone J.T. *"Cones of Silence, Complex Rays, Catastrophes: Novel Sources of High-Frequency Noise in Jets"*. PhD thesis, University of Southampton, 2016.

[62] Stone J.T., Self R.H., and Howls C.J. "Cones of silence, complex rays and catastrophes: high frequency flow acoustic interaction effects". *Journal of Fluid Mechanics*, 853:37–71, 2018.

[63] Gabard G. *"Aeroacoustics: Geometric Acoustics"*, 2019.

[64] Lilley G.M. "The radiated noise from isotropic turbulence with applications to the theory of jet noise". *Journal of Sound and Vibration*, 190(3):463–476, 1996.

[65] Ribner H.S. "Quadrupole correlations governing the pattern of jet noise". *Journal of Fluid Mechanics*, 38(1):1–24, 1969.

[66] Batchelor G. K. *"The Theory of Homogeneous Turbulence"*. Cambridge University Press, 1953.

[67] Batchelor G. K. "Pressure fluctuations in isotropic turbulence". *Mathematical Proceedings of the Cambridge Philosophical Society*, 47:359–374, 1951.

[68] Azarpeyvand M. *"Some Aspects of RANS Based Jet Noise Prediction"*. PhD thesis, University of Southampton, 2008.

[69] Khavaran A. and Bridges J. "Modelling of fine-scale turbulence mixing noise". *AIAA*, 279:1131–1154, 2005.

[70] Lilley G.M, Morris P., and Tester B.J. "On the theory of jet noise and its applications". AIAA/CAES Aeroacoustics Conference, 1973.

[71] Balsa T.F, Mani R., and Gliebe P.R. "High velocity jet noise reduction. task 2 theoretical developments and basic experiments". 1978.

[72] Khavaran A., Krejsa E.A., and Kim C.M. "Computation of supersonic jet mixing noise for an axisymmetif CD nozzle using a k-ϵ turbulence model". *AIAA*, 1992.

[73] Tam C.K.W, Golebiowski M., and Seiner J.M. "On the two components of turbulent mixing noise of supersonic jets". *AIAA Conference proceedings*, 1996.

[74] Tam C.K.W, Viswanathan K., Ahuja K.K, and Panda J. "The sources of jet noise: experimental evidence". *Journal of Fluid Mechanics*, 615:253–292, 2008.

[75] Tam C.K.W and Auriault L. "Jet mixing noise from fine-scale turbulence". *AIAA Journal*, 37(2):145–153, 1999.

[76] Morris P. and Farassat F. "The acoustic analogy and alternative theories for jet noise prediction". *AIAA Journal*, 40, 02 2002.

[77] Goldstein M. and Rosenbaum B. "Effect of anisotropic turbulence on aerodynamic noise". *The Journal of the Acoustical Society of America*, 54(3):630–645, 1973.

[78] Samanta A., Freund J.B., Wei M., and Lele S.K. "Robustness of acoustic analogies for predicting mixing-layer noise". *AIAA Journal*, 44(11):2780–2786, 11 2006.

[79] Bryce W.D and Chinoy C.B. "A method for predicting static-to-flight effects on coaxial jet noise". *Journal of Sound and Vibration*, 375:132–161, 2016.

[80] Bechara W., Lafon P., Bailly C., and Candel S.M. "Application of a k-ϵ turbulence model to the prediction of noise for simple and coaxial free jets". *Journal of The Acoustical Society of America*, 97:3518–3531, 06 1995.

[81] Bailley C., Bechara W., and Lafon P. "Jet noise predictions using a k-epsilon turbulence model". *AIAA*, pages 1–8, 1993.

[82] Bailley C., Lafon P., and Candel S. "Subsonic and supersonic jet noise predictions from statistical source models". *AIAA*, 35(11):1688–1696, 1997.

[83] Morris P.J and Boluriaan S. "The Prediction of Jet Noise From CFD Data". AIAA/CAES Aeroacoustics Conference, 2004.

[84] Ilario C.R.S, Azarpeyvand M., Rosa V., Self R.H., and Meneghini Julio.R. "Prediction of jet mixing noise with Lighthill's acoustic analogy and geometrical acoustics". *Acoustical Society of America*, 2017.

[85] Townsend A.A. *"The structure of turbulent shear flow"*. Cambridge University Press, 1976.

[86] Proudman I. "The generation of noise by isotropic turbulence". *Proceedings of the Royal Society of London. Series A, Mathematical and Physical Sciences*, 214(1116):119–132, 1952.

[87] Lilley G.M. "The radiated noise from isotropic turbulence". *Theoretical ComputationalFluid Dynamics*, 6:281–301, 1994.

[88] Almeida O., Barbosa J.R., Azarpeyvand M., and Self R.H. *"Revisiting the Role of Anisotropy for Jet Noise Modelling"*, May 2009.

[89] Jordan P. and Gervais Y. "Modelling self- and shear-noise mechanisms in inhomogeneous, anisotropic turbulence". *Journal of Sound and Vibration*, 279:529–555, 2005.

[90] Self R.H. "Jet noise prediction using Lighthill acoustic analogy". *Journal of Sound and Vibration*, 275:757–768, 2004.

[91] Doty M.J., Henderson B.S., and Kinzie K.W. "Turbulent flow field measurements of separate flow round and chevron nozzles with pylon interaction using particle image velocimetry". *AIAA journal*, 45(6):1281–1288, 2007.

[92] Vuillot F., Lupoglazoff N., and Huet M. "Effect of a pylon on double stream jet noise from hybrid CAA computations". AIAA/CAES Aeroacoustics Conference, 2010.

[93] Hunter C.A., Thomas R.H., Abdol-Hamid K.S., Pao S.P., Elmiligui A.A., and Massey S.J. "Computational analysis of the flow and acoustic effects of jet-pylon interaction". AIAA/CAES Aeroacoustics Conference, 2005.

[94] Massey S.J., Thomas R.H., Abdol-Hamid K.S., and Elmiligui A.A. "Computational and experimental flow field analyses of separate flow chevron nozzles and pylon interaction". AIAA/CAES Aeroacoustics Conference, 2003.

[95] Zaman K.B.M.Q. and Papamoschou D. "Effect of a wedge on coannular jet noise". *AIAA*, pages 1–8, 2006.

[96] Zaman K.B.M.Q. "An investigation of noise reduction for the 3BB nozzle with a pylon using external flaps". Technical report, NASA, 2008.

[97] Bhat T.R.S. "Experimental study of acoustic characteristics of jets from dual flow nozzles". AIAA/CAES Aeroacoustics Conference, 2001.

[98] Meloni S., Proenca A.R., Lawrence J.L.T., and Camussi R. "An experimental investigation into model-scale installed jet–pylon–wing noise". *Journal of Fluid Mechanics*, 929(4), 2021.

[99] Papamoschou D. "Pylon-based jet noise suppressors". *AIAA*, 47(6):1408–1420, 2009.

[100] Birch S.F, Khritov K.M, Maslov V.P, Mironov A.K., and Secundov A.N. "An experimental study of flow asymmetry in coaxial jets". AIAA/CAES Aeroacoustics Conference, 2005.

[101] Tam C.K.W and Pastouchenko N.N. "Noise from fine-scale turbulence of nonaxisymmetric jets". *AIAA Journal*, 40(3):456–464, 2002.

[102] Semiletov V.A., Karabasov S.A., Lyubimov D.A., Faranosov G.A., and Kopiev V.F. "On the effect of flap deflection on jet flow for a jet-pylon-wing configuration: near-field and acoustic modelling results". pages 1–9, AIAA/CAES Aeroacoustics Conference, 2013.

[103] Lawrence J.L.T. *"Aeroacoustic Interactions of Installed Subsonic Round Jets"*. PhD thesis, University of Southampton, 2014.

[104] Amiet R.K. "Noise due to turbulent flow past a trailing edge". *Journal of Sound and Vibration*, 47(3):387–393, 1976.

[105] Lyu B., Dowling A.P., and Naqavi I. "Prediction of installed jet noise". *Journal of Fluid Mechanics*, 811:234–268, 2017.

[106] Lawrence J.L.T. Dawson M.F., Self R.H., and Kingan M.J. "Validation of a jet-surface interaction noise model in flight". *AIAA*, pages 1–14, 2019.

[107] Rosa V. *"RANS-based prediction of noise from isothermal and hot subsonic jets"*. PhD thesis, University of Southampton, 2017.

[108] III Dippold V.F. *"Generating a Grid for Unstructured RANS Simulations of Jet Flows"*, August 2018.

[109] Azarpeyvand M. and Self R.H. "Improved jet noise modelling using a new time-scale". *Journal of Acoustical Society of America*, 126:1015–1025, 2009.

[110] Proença A.R, Lawrence J., and Self R. "Experimental investigation into the turbulence flow field of in-flight jets". 25th AIAA/CAES Aeroacoustics Conference, 2019.

[111] Proença A.R. and Lawrence J.L.T. "Experimental flowfield analyses of installed subsonic jet-pylon interaction". *AIAA*, 60(3):1630–1642, 2022.

[112] Proença A.R. and Lawrence J.L.T. "Blocakge effects on the pressure field of 3D-printed small-scale jet nozzles". pages 1–17, AIAA/CAES Aeroacoustics Conference, 2021.

[113] Karabasov S.A, Afsar M.Z., Hynes T.P., and Dowling A.P. "Jet noise: Acoustic analogy informed by large eddy simulation". *AIAA*, 48(7):1312–1325, 2010.

[114] Morris P.J. and Zaman K.B.M.Q. "Velocity measurements in jets with application to noise source modeling". *Journal of Sound and Vibration*, 329:394–414, 2010.

[115] Weaver D.S. and Miškovi S. "A study of RANS turbulence models in fully turbulent jets: A perspective for CFD-DEM simulations". *Fluids*, 6(271):1–19, 2021.

[116] Goldstein M.E. "Aeroacoustics of turbulent shear flows". *Annual Review of Fluid Mechanics*, 16:263–285, 1984.

[117] Harper-Bourne M. "Jet noise measurements: past and present". *International journal of aeroacoustics*, 9(4 and 5):559–588, 2010.

[118] Kandula M. "On the scaling laws for jet noise in subsonic and supersonic flow". AIAA/CAES Aeroacoustics Conference, 2003.

[119] Khavaran A. and Bridges J. "Development of jet noise power spectral laws using SHJAR data". AIAA/CAES Aeroacoustics Conference, 2009.

[120] Battaner-Moro J. "Report on automated source breakdown for coaxial and single jet noise measurements". Technical report, 2003.

[121] Proença A.R, Lawrence J., and Self R. "Measurements of the single-point and joint turbulence statistics of high subsonic jets using hot-wire anemometry". *Experiments in Fluids*, 60(63), 2019.

[122] Wellman M., A.R. Proença, Lawrence J.L., and Self R.H. "The effects of internal nozzle blockage in a single stream jet on far-field jet mixing noise". AIAA/CAES Aeroacoustics Conference, 2022.

[123] Roshko A. "On the drag and shedding frequency of two-dimensional bluff bodies". Technical report, NATIONAL ADVISORY COMMITTEE FOR AERONAUTICS, 1954.

[124] Rienstra S.W. "On the acoustical implications of vortex shedding from an exhaust pipe". *Transactions of the ASME*, 103:378–384, 1981.

[125] Kaneko S., Nakamura T., Inada F., Kato M., Ishihara K., Nishihara T., and Langthjem M.A. "Flow-induced Vibrations (Second Edition)". pages 1–28. Academic Press, Oxford, second edition edition, 2014.

[126] Wang Z., Proenca A., Lawrence J., Tucker P., and Self R. "LES study of noise and its sources of closely installed jets". AIAA/CAES Aeroacoustics Conference, 2022.

[127] Faranosov G., Kopiev V, Ostrikov, and Kopiev V. "The effect of pylon on the excess jet-flap interaction noise". AIAA/CAES Aeroacoustics Conference, 2016.

[128] Kopiev V., Belyaev I., Faranosov G., Kopiev V., Ostrikov N., Zaytsev M., and Paranin G. "Numerical and experimental study of JFI effect on swept wing". *AIAA jounral*, pages 1–16, 2014.

[129] Tyacke J.C., Wang Z., and Tucker P.G. "LES-RANS of installed ultra-high-bypass-ratio coaxial jet acoustics with flight stream ". *AIAA*, 57(3):1215–1236, 2019.

[130] Perrino M. *"An Experimental Study into Pylon, Wing, and Flap Installation Effects on Jet Noise Generated by Commercial Aircraft"*. PhD thesis, University of Cincinnati, 2014.

[131] Xia H., Tucker P.G., Eastwood S., and Mahak M. "The influence of geometry on jet plume development". *Progress in Aerospace Sciences*, 2012.

[132] Wrighton C.M. and Lawrence J.L. "Test conduct report for SYMPHONY WP3.2 installation effects –acoustic tests". Technical report, Qinetiq, 2010.